THE UNIVERSITY of ADELAIDE

Constraints on the fluid enhanced eclogitisation of granulite domains in the Bergen Arcs, Norway.

Kamini Bhowany

Earth Sciences
School of Physical Sciences
University of Adelaide

This thesis is submitted in fulfilment of the requirements
for the degree of Doctor of Philosophy

30th June 2020

High-pressure (HP) and ultra-high-pressure (UHP) terranes are often associated with the presence of fluids (e.g. hydrous mineral assemblages, pegmatite veins or melts). However, examples of progressive conversion of anhydrous mineral assemblages, to hydrous ones, are rare. Holsnøy Island is host to a unique setting whereby hydrous eclogite domains are perfectly preserved juxtaposing anhydrous granulite domains. The structural evolution of the system on Holsnøy Island can be observed via different stages, each indicated by an increase in fluid availability and degree of ductile deformation.

This thesis identified 5 stages of deformation, based on structural cross-cutting relationships, and *P–T* condition estimations for four of the stages (1, 3, 4 and 5), using forward phase equilibria modelling. Stage 1 is the formation of pseudotachalytes and fractures in the granulite domains, which provide the initial pathway for the infiltration of fluid. The metamorphic overprint of the pseudotychylytes limit the occurrence of stage 1 of deformation to maximum *P–T* conditions of 15.2–15.7 kbar and 675–685 °C. Stage 2 of deformation is the formation of small-scale discrete shear zones along the partially hydrated domains. Mineralogically, this stage of deformation is indicated by the breakdown of garnet grains to form omphacite–kyanite–zoisite–plagioclase symplectites. Stage 3 of deformation is the formation of peak, sheared eclogite domains at *P–T* conditions of 21–22 kbar and 670–690 °C. Stage 4 of deformation is the formation of a retrogressed-eclogite (R-eclogite), a phengite-rich domain at *P–T* conditions 16–17 kbar and 680–700 °C. Lastly, is stage 5 of deformation, which is the retrogression of the system to amphibolite-facies at *P–T* conditions 11.8–12.8 kbar and 720–732 °C. Combined, these different stages of deformation illustrate the first calculated *P–T* path experienced by the Holsnøy domains (presented in Chapters 2 and 5).

Systematic sampling of altered domains and their closest granulite protolith provided a comparative study, thus allowing the geochemical characterisation of the fluid infiltrating the Holsnøy granulites. Stage 3 of deformation has been interpreted to be rock-buffered based on whole-rock $\delta^{18}O$ analyses, trace element chemistry, and Sm–Nd chemistry. In contrast, a fluid-buffered system was interpreted for stage 4 of deformation. Calculated $\delta^{18}O$ and δD values for the fluid based on measured mineral isotopic values are consistent with a metamorphic fluid reservoir, interpreted in Chapter 2. Trace element analyses and Sm–Nd systematics, presented in Chapter 3, suggest the possibility of a sedimentary unit, with mafic components as a likely source of fluids for the eclogitisation of granulite domains on Holsnøy Island.

Lastly, this thesis investigated the exhumation rates of the peak eclogite-facies altered domain (stage 3 of deformation). Calculated minimum exhumation rates of 41– 6122 mm/yr were obtained based on diffusion durations in zoned garnet grains, and constraints on pressure decrease from eclogite-facies to amphibolite-facies (stage 5). These extreme exhumation rates experienced by the HP terranes on Holsnøy Island cannot be explained by known exhumation mechanisms. Therefore, this highlights the need to reassess the general scientific consensus that pressure can be used as a proxy for depth in the Earth's crust, and propose new mechanisms for the emplacement of HP and UHP terranes.

Combined, the chapters provide a series of new datasets for the eclogitisation process on Hoslnøy Island. This ulstimately contributes to the better understanding of deep crustal metamsomatism and metamorphic processes at HP and UHP conditions.

I certify that this work contains no material which has been accepted for the award of any other degree or diploma in my name, in any university or other tertiary institution and, to the best of my knowledge and belief, contains no material previously published or written by another person, except where due reference has been made in the text. In addition, I certify that no part of this work will, in the future, be used in a submission in my name, for any other degree or diploma in any university or other tertiary institution without the prior approval of the University of Adelaide and where applicable, any partner institution responsible for the joint-award of this degree.

I acknowledge that copyright of published works contained within this thesis resides with the copyright holder(s) of those works.

I also give permission for the digital version of my thesis to be made available on the web, via the University's digital research repository, the Library Search and also through web search engines, unless permission has been granted by the University to restrict access for a period of time.

Kamini Bhowany
30 June 2020

The completion of this PhD would not have been possible without the invaluable support and contribution of many people and groups of people- apologies if I miss out on anyone, but there were that many of you.

An enormous thank you to Dr. Dave Kelsey, who supported me through my lowest of lows and celebrated my achievements with a big smile and simple 'nice' while nodding. My deepest gratitude to Dr. Morgan Blades, who became an unofficial supervisor overnight. Your friendship and guidance has helped me overcome more than I thought I could.

Thank you to Prof. Chris Clark (and the Curtin Crew) for always making me feel welcome at Curtin University and supporting me since we first met during my Honours year. Ass Prof. Tom Raimondo, thanks for always being there when I needed help (it probably happened more often than you would have liked). Thank you to Prof. Alan Collins for his constant support and welcoming me in his research group. And last, but not least, thank you so very much to Ass Prof. Ros King—you took me under your wing when I most needed it and for that I will always be grateful.

This project would not have been possible without the funding of the Australian Research Council and the Core to Crust Fluid Systems ARC. It is also a product of the input and guidance of many collaborators: Prof. Martin Hand, Prof. Steve Reddy, Dr. Mark Pearce, Dr. Naomi Tucker, Dr. Laura Morrisey, Dr. Richard Tylor and Ass Prof. Mark Caddick. Thank you all for your invaluable help.

A special acknowledgement to everyone who helped me with data collection in the labs and in the field: David Bruce, Dr. Sarah Gilbert, Luke Hersey, Prof. Pete Kenny, Prof. Steve Reddy, Dr. Alex Prent, Dr. Dennis Fourgerouse and Miss Sophie Reddy. A particular mention to Dr. Ben Wade, EPMA wizard: you would have seen my ups, but mostly my downs in the basement of AM.

I would not be here without the support of all the close friends who kept me sane. To the Friday night market friends who listened: Varun, Steph, Nigel, Anton, Raj, Urvashi and Khoa- you have made life outside uni the best one could ask for. To the uni friends who always understood: The Hot Choc Crew (Briony, Kiara and Alicia), Drew, Richard, Dingo Jack, Morgan. To every officemate I ever had from CERG (old and new), S3 (special mention to old mates John, Furph, Finn and Coopers- Drew and I had the best times with you, and you kept us going through the late nights!) and to TES 2020. To Briony, thank you for being the best friend anyone can ask for and helping me english when i needd it. And lastly, an enormous thanks to my volleyball friends (way too many of you), but most specially Andy and Mani my two adopted brothers.

My deepest and most heartfelt gratitude goes Daniel, my partner. You had to put up with moody, grumpy and emotional Kam ever since I started Honours. You have been my greatest support through it all. And thank you to all the Lanes for being family away from home. I guess I should also thank my brothers Hari and Ashwi, for being my brothers.

Lastly, I would like to dedicate this PhD to two educators who taught me the importance of being grateful and the value of education: my parents Meeken and Ram who sacrificed a lot for the three of us. Mam you taught me to be resilient and this is the product of very resilient/ stubborn me.

And I will finish on this: Pap, you always wanted a doctor in the family… so here goes!

CHAPTER 1

Introduction and thesis outline

1. INTRODUCTION

Deep-seated processes in the Earth's crust are crucial as they affect its dynamics, rendering them important in geology. While it is not possible to sample the present deep crust, exhumed high-pressure (HP) and ultra-high-pressure (UHP) terranes and their mineral assemblages (i.e. blueschist and eclogites) help geologists understand the possible processes that occur at great depths in different tectonic settings. These understandings can then be applied to tectonic and geodynamic models to predict the displacement of specific crustal unit, which is especially important in industries such as mining and petroleum where locating targeted units/beds in the crust is critical to their success.

This thesis focuses on metasomatism owing to fluid infiltration — a process that potentially affects domains at crustal scales (Oreskes & Einaudi, 1992; Smit & Van Reenen, 1997; Tumiati *et al.*, 2007; Raimondo *et al.*, 2011). The understanding of deep crustal metasomatism is crucial as this process changes the geochemistry, rheology, geodynamics, and as later demonstrated, the interpretation of tectonic settings for an area (Austrheim, 1987; Engvik *et al.*, 2000; Jolivet *et al.*, 2005; Pollok *et al.*, 2008; Centrella *et al.*, 2016; Petley-Ragan *et al.*, 2018). The presented chapters focus on the progressive conversion of an anhydrous granulite to eclogites, enhanced by fluid infiltration on Holsnøy Island. This study area is an ideal natural laboratory to study the process of fluid infiltration in a comparatively anhydrous crust, as the granulite and altered domains are perfectly preserved next to each other. Moreover, the stage-wise evolution of the system can be observed in the field, only a few kilometres apart (Boundy *et al.*, 1992; Jolivet *et al.*, 2005; Austrheim, 2013; Chapter 2), thus providing an ideal framework for any geological studies.

There are three main foci to the following chapters and overall thesis. Firstly, a pressure – temperature (*P–T*) framework is set up by identifying the significant stages of deformation in the structural evolution on Holsnøy Island. Robust constraints on the *P–T* conditions for the different stages of deformation provides the first *P–T* path for the domains. Second, is to investigate the most likely source for the fluid that infiltrated the granulite domain. While multiple previous studies have characterised the potential signatures of the fluid that infiltrated the Holsnøy system (e.g. Andersen *et al.*, 1989; Andersen *et al.*, 1990; Jamtveit *et al.*, 1990; Andersen *et al.*, 1991; Andersen *et al.*, 1993; Mattey *et al.*, 1994; Van Wyck *et al.*, 1996), the provenance of the fluid remains unknown. The addition of dataset to the literature can assist in further constraining the provenance of fluids in the Holsnøy system. Lastly, the overpressure hypothesis is investigated as an alternative model for the formation of the eclogite domains on Holsnøy Island. Furthermore, the validity of the current tectonic model for the Lindås Nappe and emplacement of the Holsnøy HP terrane is evaluated.

2. GEOLOGICAL SETTING AND BACKGROUND

Each chapter in this thesis includes its individual detailed geological background. However, below is a summary of previous findings related to this study.

Holsnøy Island is situated in western Norway, approximately 45 km north-west of Bergen (Figure 1a). The rocks that are observed on Holsnøy Island form part of the Lindås Nappe, which along with the Bergen Minor and Major Arcs

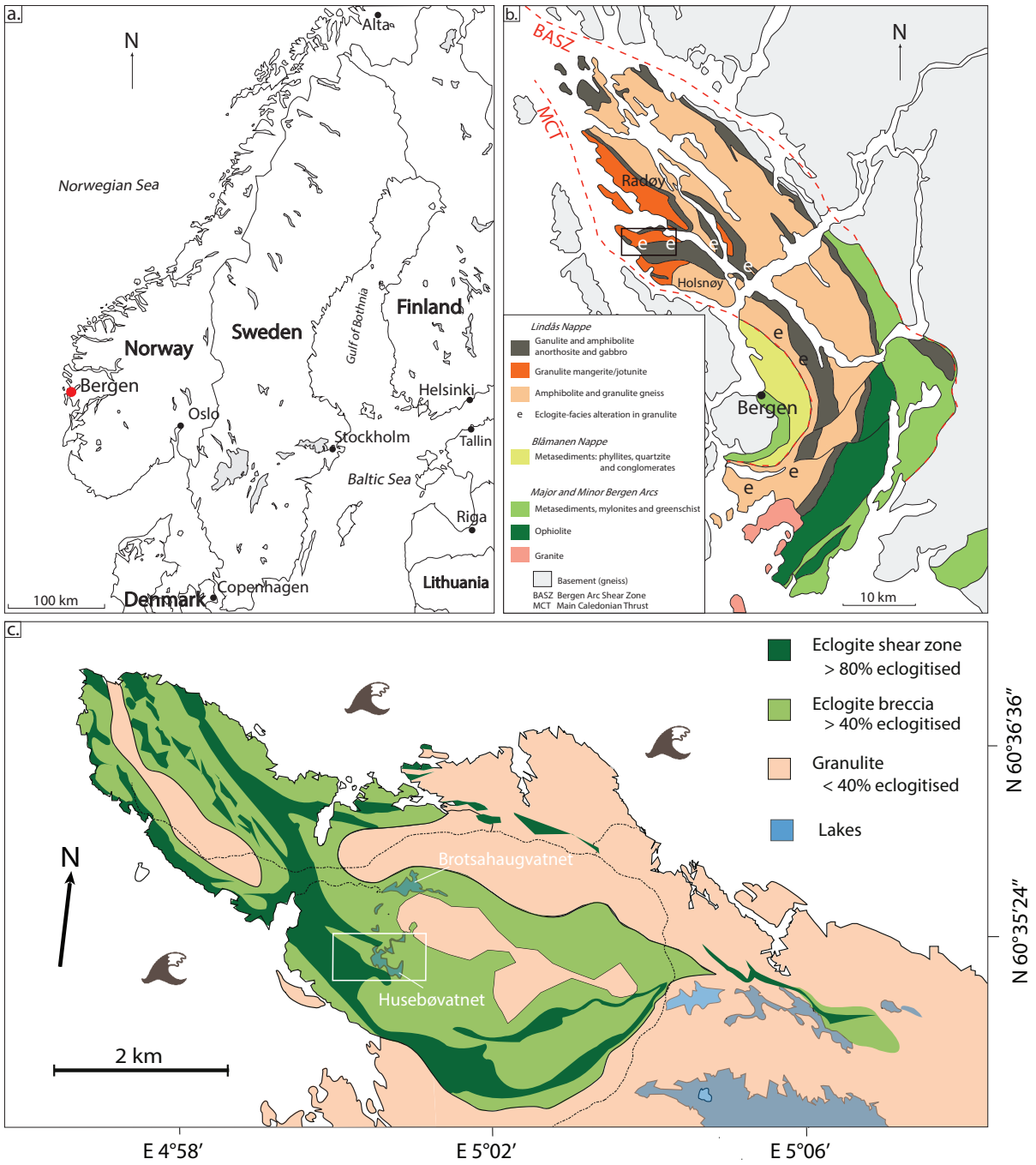

Figure 1. a) Location of Bergen, Norway. b) Location of Holsnøy Island relative to Bergen. c) Modified geological map (from and Boundy *et al.* 1992 and Austrheim *et al.* 1996) of northern Holsnøy island. White box indicates the approximate location of the field area for this thesis.

form the Bergen Arcs, an arcuate structure around Bergen (Figure 1b). The study area for this thesis is located in the north of Holsnøy Island (Figure 1c). The main domain that outcrops on Holsnøy Island is an anorthosite granulite composed of an anhydrous interpreted peak metamorphic mineral assemblage of garnet–plagioclase–clinopyroxene ± orthopyroxene, with garnet, clinopyroxene and orthopyroxene forming eye-shaped coronae or bands. The metamorphism of the anorthosite to granulite-facies mineral assemblages occurred during the Scandonorwegian Orogeny at c. 950 Ma (Austrheim & Griffin, 1985), at interpreted peak metamorphic conditions of 10 kbar and

800–900 °C (Austrheim, 1987; Boundy *et al.*, 1997). The granulite then cooled and was subsequently buried during the Caledonian Orogeny at c. 450 Ma, during the collision of Baltica and Laurentia (Austrheim, 1987; Boundy *et al.*, 1997; Bingen *et al.*, 2004). Two generations of fluid have previously been identified for the modification of the granulite to hydrous mineral assemblages. A first instance of infiltration of a H_2O-rich fluid resulted in the formation of eclogite-facies mineral assemblages (Jamtveit *et al.*, 1990; Andersen *et al.*, 1993; Kühn, 2002), and a succeeding H_2O-poor fluid initially infiltrated at eclogite-facies and continued throughout the amphibolite-facies (Andersen *et al.*, 1991; Mattey *et al.*, 1994; Kühn, 2002). While the formation of hydrous mineral assemblages is enhanced by fluid availability, the preservation of the different stages of rehydration in the system's evolution is due to the shortage of fluid (Austrheim, 2013).

The rehydration of the granulite to form eclogite-facies mineral assemblages is progressive and can be observed stage-wise in different locations on Holsnøy Island (Boundy *et al.*, 1992; Austrheim, 2013; Chapter 2). The petrology for the eclogite domains has been described in detail by multiple previous authors (Boundy *et al.*, 1992; Kühn, 2002; Raimbourg *et al.*, 2007; Austrheim, 2013; Chapter 2). Briefly, the interpreted peak metamorphic mineral assemblage for the peak eclogite consists of garnet, omphacite, zoisite, phengite and depending on the rock compositions, varying abundances of kyanite, rutile and quartz. The peak metamorphic conditions for the eclogite domains has previously been estimated to occur at 15–21 kbar and 650–800 °C, based on conventional thermobarometry (Austrheim, 1987; Boundy *et al.*, 1992). These peak metamorphic conditions are interpreted as the burial of the domains on Holsnøy Island, to depths > 70 km in a subduction zone (Austrheim, 2013), based the current tectonic model. The amphibolite-facies retrogression due to the second pulse of fluid resulted in an interpreted peak mineral assemblage of garnet–plagioclase–hornblende–muscovite–zoisite ± quartz ± rutile. The peak metamorphic conditions for this alteration have previously been constrained by conventional thermobarometry, with estimates of 8–12 kbar and 600–700 °C (Kühn, 2002; Glodny *et al.*, 2008).

A number of previous authors have investigated the potential source of the fluids that infiltrated the Holsnøy system. Understanding the fluid provenance has important implications for the overall understanding of the tectonic setting of the area. Previous authors used different isotopic systems to deduce the potential fluid signatures, and fluid provenance responsible for the rehydration of the granulite. Using O, C and N in fluid inclusions in garnet, Andersen *et al.* (1991; 1993) and Kühn (2002) concluded that the first fluid pulse was likely derived from the granulite protolith. Andersen *et al.* (1990) and Mattey *et al.* (1994) used C, N and Ar isotopic constraints in fluid inclusions and mineral separates to suggest the devolitilisation of metasediments as the likely source of the second pulse of fluid. This thesis adds to the existing literature the systematic isotopic analyses of $\delta^{18}O$ and δD within the *P–T* framework depicted in Chapter 2, as well as whole-rock and mineral trace elements and Sm–Nd systematics. Innovative methods such as *in–situ* $\delta^{18}O$ analysis and trace element mapping in garnet grains are also employed to investigate grain-scale isotopic variations caused by fluid infiltration.

Another aspect of the HP terrane on Holsnøy Island, which is investigated,in this thesis is the exhumation rates of the Lindås Nappe from

eclogite-facies to amphibolite-facies. Raimbourg *et al.* (2007) previously used forward diffusion modelling on zoned garnet grains in peak eclogite samples to determine rapid exhumation rates for Holsnøy Island. While no quantitative estimates was given in the study for the exhumation rates, the durations obtained by Raimbourg *et al.* (2007) would result in a minimum rate of 10344 mm/yr, for an ascension of 30 km (i.e. eclogite to amphibolite-facies) in the Earth's crust. Chapter 5 of this thesis quantifies a series of minimum exhumation rates experienced by the eclogite domains on Holsnøy Island, and uses the extreme decompression rates as a test for the overpressure hypothesis for the emplacement of this HP terrane.

Combined, the studies in this thesis provides an insight in the feasibility of the current tectonic model for the Bergen Arcs. Moreover it highlights the necessity for alternative interpretations and explanations for pressure changes recorded by HP/UHP terranes.

Details of each chapter are outlined below.

3. THESIS OUTLINE

Chapter 2: Structural and *P–T* evolution of the Holsnøy Island system.

Chapter 1 presents a series of detailed maps of the key structural deformation stages during the progressive eclogitisation of the granulite domains during fluid infiltration. Four stages of deformation (stages 1, 2, 3 and 4) depict the evolution of the system from brittle deformation to ductile deformation, as fluid became increasingly more available. Moreover, *P–T* conditions are estimated for samples from stages 1, 3 and 4 of deformation, using forward phase equilibria modelling, to establish the first framework for the burial and decompression of the domains. These are then combined to depict the *P–T* path experienced by the Holsnøy system.

Chapter 3: $\delta^{18}O$ and δD isotopic constraints on the fluid infiltrating the system.

This chapter focuses on the most fluid affected domains; i.e. stages 3 (eclogite) and 4 (a retrogressed-eclogite). Systematic sampling and analysis of the fluid altered domains and their corresponding closest anhydrous protolith granulite provide constraints on isotopic shifts that occurred owing to fluid infiltration. Whole-rock and mineral separates $\delta^{18}O$ and δD analyses, as well as *in-situ* $\delta^{18}O$ analyses in garnet grains, are used to constrain the isotopic signatures of fluid that infiltrated the granulite. The dataset from this chapter constrains the type of fluid that triggered the conversion of the anhydrous granulite to the hydrous eclogite.

Chapter 4: Radiogenic (Sm–Nd) and REE evolution of the Holsnøy eclogites.

This chapter builds onto both Chapters 2 and 3 and utilises the same samples from Chapter 3. However, in this chapter, trace element and Sm–Nd analyses were performed on the samples to constrain shifts that occurred during the influx of fluid. Combined with Chapter 3 this provides a potential constraint on the source of the fluid. Moreover, the first trace element mapping of garnet grains for the Holsnøy eclogites were acquired to observe potential changes in the distribution during fluid infiltration.

Chapter 5: Constraints on the exhumation rate of the eclogite on Holsnøy Island.

Chapter 5 builds onto the *P–T* framework presented in Chapter 1. To constrain the exhumation rate experienced by the peak metamorphic eclogite (stage 3) on Holnøy Island, a pressure

decrease is calculated based on *P–T* constraints obtained from a fifth stage of deformation (added in this chapter), using forward phase equilibria modelling for the amphibolite-facies domain. This pressure decrease is then combined with exhumation durations, determined by the forward diffusion modelling between zoned garnet cores and rims, to obtain the minimum exhumation rates for the Holsnøy system.

Chapter 6: Discussion and conclusion

This chapter provides a summary of the findings in this thesis. Moreover, a short discussion linking chapters 2, 3, 4 and 5 is presented, highlighting the necessity of considering the feasibility of tectonic models and processes when dealing with pressure in the Earth's crust. Final comments and conclusions are also included in this chapter.

REFERENCES

Andersen, T., Austrheim, H. & Burke, E. A. J., 1990. Fluid inclusions in granulites and eclogites from the Bergen Arcs, Caledonides of W. Norway. *Mineralogical Magazine*, **54**, 145-158.

Andersen, T., Austrheim, H. & Burke, E. A. J., 1991. Fluid-induced retrogression of granulites in the Bergen Arcs, Caledonides of W. Norway: Fluid inclusion evidence from amphibolite-facies shear zones. *Lithos*, **27**, 29-42.

Andersen, T., Austrheim, H., Burke, E. A. J. & Elvevold, S., 1993. N 2 and CO 2 in deep crustal fluids: evidence from the Caledonides of Norway. *Chemical Geology*, **108**, 113-132.

Andersen, T., Burke, E. & Austrheim, H., 1989. Nitrogen-bearing, aqueous fluid inclusions in some eclogites from the Western Gneiss Region of the Norwegian Caledonides. *Contributions to Mineralogy and Petrology*, **103**, 153-165.

Austrheim, H., 1987. Eclogitization of lower crustal granulites by fluid migration through shear zones. *Earth and Planetary Science Letters*, **81**, 221-232.

Austrheim, H., 2013. Fluid and deformation induced metamorphic processes around Moho beneath continent collision zones: Examples from the exposed root zone of the Caledonian mountain belt, W-Norway. *Tectonophysics*, **609**, 620-635.

Austrheim, H. & Griffin, W. L., 1985. Shear deformation and eclogite formation within granulite-facies anorthosites of the Bergen Arcs, western Norway. *Chemical Geology*, **50**, 267-281.

Bhowany, K., Hand, M., Clark, C., Kelsey, D., Reddy, S., Pearce, M., Tucker, N. & Morrissey, L., 2018. Phase equilibria modelling constraints on P–T conditions during fluid catalysed conversion of granulite to eclogite in the Bergen Arcs, Norway. *Journal of Metamorphic Geology*, **36**, 315-342.

Bingen, B., Austrheim, H., Whitehouse, M. J. & Davis, W. J., 2004. Trace element signature and U–Pb geochronology of eclogite-facies zircon, Bergen Arcs,

Caledonides of W Norway. *Contributions to Mineralogy and Petrology*, **147**, 671-683.

Boundy, T. M., Fountain, D. M. & Austrheim, H., 1992. Structural development and petrofabrics of eclogite facies shear zones, Bergen Arcs, western Norway: implications for deep crustal deformational processes. *Journal of metamorphic geology*, **10**, 127-146.

Boundy, T. M., Mezger, K. & Essene, E. J., 1997. Temporal and tectonic evolution of the granulite-eclogite association from the Bergen Arcs, western Norway. *Lithos*, **39**, 159-178.

Centrella, S., Austrheim, H. & Putnis, A., 2016. Mass transfer and trace element redistribution during hydration of granulites in the Bergen Arcs, Norway. *Lithos*, **262**, 1-10.

Engvik, A. K., Austrheim, H. & Andersen, T. B., 2000. Structural, mineralogical and petrophysical effects on deep crustal rocks of fluid-limited polymetamorphism, Western Gneiss Region, Norway. *Journal of the Geological Society*, **157**, 121-134.

Glodny, J., Kühn, A. & Austrheim, H., 2008. Geochronology of fluid-induced eclogite and amphibolite facies metamorphic reactions in a subduction–collision system, Bergen Arcs, Norway. *Contributions to mineralogy and petrology*, **156**, 27-48.

Jamtveit, B., Bucher-Nurminen, K. & Austrheim, H., 1990. Fluid controlled eclogitization of granulites in deep crustal shear zones, Bergen arcs, Western Norway. *Contributions to mineralogy and petrology*, **104**, 184-193.

Jolivet, L., Raimbourg, H., Labrousse, L., Avigad, D., Leroy, Y., Austrheim, H. & Andersen, T. B., 2005. Softening trigerred by eclogitization, the first step toward exhumation during continental subduction. *Earth and Planetary Science Letters*, **237**, 532-547.

Kühn, A., 2002. The influence of fluid on the granulite to eclogite and amphibolite facies transition: a study in the anorthositic rocks from the Lindås Nappe, Bergen Arcs, West Norway. *Unpub. PhD Thesis, University of Oslo*.

Mattey, D., Jackson, D. H., Harris, N. B. W. & Kelley, S., 1994. Isotopic constraints on fluid infiltration from an eclogite facies shear zone, Holsenøy, Norway. *Journal of metamorphic geology*, **12**, 311-325.

Oreskes, N. & Einaudi, M. T., 1992. Origin of hydrothermal fluids at Olympic Dam; preliminary results from fluid inclusions and stable isotopes. *Economic Geology*, **87**, 64-90.

Petley-Ragan, A., Dunkel, K. G., Austrheim, H., Ildefonse, B. & Jamtveit, B., 2018. microstructural records of

earthquakes in the lower crust and associated fluid-driven metamorphism in plagioclase-rich granulites. *Journal of Geophysical Research: Solid Earth*.

Pollok, K., Lloyd, G. E., Austrheim, H. & Putnis, A., 2008. Complex replacement patterns in garnets from Bergen Arcs eclogites: a combined EBSD and analytical TEM study. *Chemie der Erde-Geochemistry*, **68**, 177-191.

Raimbourg, H., Goffé, B. & Jolivet, L., 2007. Garnet reequilibration and growth in the eclogite facies and geodynamical evolution near peak metamorphic conditions. *Contributions to Mineralogy and Petrology*, **153**, 1-28.

Raimondo, T., Clark, C., Hand, M. & Faure, K., 2011. Assessing the geochemical and tectonic impacts of fluid–rock interaction in mid-crustal shear zones: a case study from the intracontinental Alice Springs Orogen, central Australia. *Journal of Metamorphic Geology*, **29**, 821-850.

Smit, C. & Van Reenen, D., 1997. Deep crustal shear zones, high-grade tectonites, and associated metasomatic alteration in the Limpopo Belt, South Africa: Implications for deep crustal processes. *The Journal of Geology*, **105**, 37-57.

Tumiati, S., Godard, G., Martin, S., Klötzli, U. & Monticelli, D., 2007. Fluid-controlled crustal metasomatism within a high-pressure subducted mélange (Mt. Hochwart, Eastern Italian Alps). *Lithos*, **94**, 148-167.

Van Wyck, N., Valley, J. W. & Austrheim, H., 1996. Oxygen and carbon isotopic constraints on the development of eclogites, Holsnøy, Norway. *Lithos*, **38**, 129-145.

CHAPTER 2

This chapter has been publised in *Journal of Metamorphic Geology* as:
Bhowany, K., Hand, M., Clark, C., Kelsey, D., Reddy, S., Pearce, M., Tucker, N. & Morrissey, L., 2018. Phase equilibria modelling constraints on *P–T* conditions during fluid catalysed conversion of granulite to eclogite in the Bergen Arcs, Norway. Journal of Metamorphic Geology, 36, 315-342.

Statement of Authorship

le of Paper	Phase equilibria modelling constraints on *P–T* conditions during fluid catalysed conversion of granulite to eclogite in the Bergen Arcs, Norway.
Publication Status	☑ Published ☐ Accepted for Publication ☐ Submitted for Publication ☐ Unpublished and Unsubmitted w ork w ritten in manuscript style
Publication Details	Pulised in the Journal of Metamorphic Geology as: Bhowany, K. and Hand, M. and Clark, C. and Kelsey, D. and Reddy, S. and Pearce, M. and Tucker, N. et al. 2017. Phase equilibria modelling constraints on P-T conditions during fluid catalysed conversion of granulite to eclogite in the Bergen Arcs, Norway. Journal of Metamorphic Geology. 36 (3): pp. 315-342.

Principal Author

	Kamini Bhowany		
Contribution to the Paper	Project fieldwork, detailed mapping, sample collection and preparation, data acquisition and analysis, figure making and manuscript writing.		
Overall percentage (%)	80		
Certification:	This paper reports on original research I conducted during the period of my Higher Degree by Research candidature and is not subject to any obligations or contractual agreements with a third party that would constrain its inclusion in this thesis. I am the primary author of this paper.		
Signature		Date	29/08/19

Co-Author Contributions

By signing the Statement of Authorship, each author certifies that:

i. the candidate's stated contribution to the publication is accurate (as detailed above);
ii. permission is granted for the candidate in include the publication in the thesis; and
iii. the sum of all co-author contributions is equal to 100% less the candidate's stated contribution.

Name of Co-Author	Prof. Martin Hand		
Contribution to the Paper	Fieldwork guidance, sample collection, guidance in manuscript structure and writing and manuscript review.		
Signature		Date	21/08/19

Name of Co-Author	Prof. Chris Clark		
Contribution to the Paper	Fieldwork guidance, sample collection, guidance in manuscript structure and writing and manuscript review.		
Signature		Date	4/07/19

Name of Co-Author	Dr. David E. Kelsey
Contribution to the Paper	Guidance in phase equilibria modelling and troubleshooting, guidance in sample collection and manuscript writing, manuscript reviewing.
Signature	Date: 29/6/19

Name of Co-Author	Prof. Steven Reddy
Contribution to the Paper	EBSD collection and manuscript reviewing.
Signature	Date: 07 June 2019

Name of Co-Author	Dr. Mark A. Pearce
Contribution to the Paper	Guidance in TCInvestigator setup and troubleshooting, manuscript reviewing.
Signature	Date: 11/06/2019

Name of Co-Author	Dr. Naomi M. Tucker
Contribution to the Paper	Guidance in phase equilibria modelling, manuscript structure and review.
Signature	Date: 11/06/2019

Name of Co-Author	Dr. Laura J. Morrissey
Contribution to the Paper	Guidance in phase equilibria modelling, manuscript structure and review.
Signature	Date: 11/6/19

ABSTRACT

Exhumed eclogitic crust is rare and exposures that preserve both protoliths and altered domains are limited around the world. Nominally anhydrous Neoproterozoic anorthositic granulites exposed on the island of Holsnøy, in the Bergen Arcs in western Norway, preserve different stages of progressive prograde deformation, together with the corresponding fluid-assisted metamorphism, which record the conversion to eclogite during the Ordovician-Silurian Caledonian Orogeny. Four stages of deformation can be identified: 1) brittle deformation resulting in the formation of fractures and the generation of pseudotachylites in the granulite; 2) development of mesoscale shear zones associated with increased fluid–rock interaction; 3) the complete large-scale replacement of granulite by hydrous eclogite with blocks of granulite sitting in an eclogitic 'matrix'; and 4) the break-up of completely eclogitised granulite by continued fluid influx, resulting in the formation of coarse-grained phengite-dominated mineral assemblages. *P–T* constraints derived from phase equilibria forward modelling of mineral assemblages of the early and later stages of the conversion to eclogite document burial and partial exhumation path with peak metamorphic conditions of ~ 21–22 kbar and 670–690 °C. The *P–T* models, in combination with existing *T–t* constraints, imply that the Lindås Nappe underwent extremely rapid retrogressive pressure change. Fluid infiltration began on the prograde burial path and continued throughout the recorded *P–T* evolution, implying a fluid source that underwent progressive dehydration during subduction of the granulites. However, in places limited fluid availability on the prograde path resulted in assemblages largely consuming the available fluid, essentially freezing snapshots of the prograde evolution. These were carried metastably deeper into the mantle with strain and metamorphic recrystallisation partitioned into areas where ongoing fluid infiltration was concentrated.

1. INTRODUCTION

A number of studies have explored the way in which fluids can be generated during prograde dehydration accompanying subduction (e.g. Groppo & Castelli, 2010; Liu, Bohlen, & Ernst, 1996; Peacock, 1990, 1993; Schmidt & Poli, 1998; Spandler, Hermann, Arculus, & Mavrogenes, 2003). Using calculated mineral modal proportions and compositions, Hacker, Abers, and Peacock (2003) demonstrated that subducted (and exhumed) lithologies generally retain less water than their less buried equivalents. It follows that for the most part, the record of fluid expulsion is an inverse one, where the formation of comparatively anhydrous co-product assemblages are the record of fluid generation and loss (Baxter & Caddick, 2013; Guiraud, Powell, & Rebay, 2001). For example, Dragovic, Samanta, Baxter, and Selverstone (2012) and Baxter and Caddick (2013) showed that the formation of garnet-bearing assemblages during subduction could be used to make estimates of the amount fluid released during increasing temperature, and demonstrated that rates of fluid generation are not steady state, but rather are punctuated around prograde mineral reactions. More generally, similar models have been formulated for fluid release during prograde metamorphic dehydration in non-subduction settings (e.g. Philippot, 1993; Stüwe, 1998; Vry, Powell, Golden, & Petersen, 2010). A consequence of punctuated fluid generation is that fluid flow events in subducting systems are probably also punc-

tuated, resulting in comparatively short-lived fluid–rock interactions.

While recrystallisation and dehydration of subducted fluid-bearing rocks leads to predictable mineral assemblages and fluid generation, the fate of subducted, nominally anhydrous, rocks such as continental granulites is less predictable. From an equilibrium thermodynamic standpoint, the conversion of granulite across a wide range of compositions to compositionally equivalent eclogite should occur in response to changes in pressure and temperature (Ghent, Dipple, & Russell, 2004; Lardeaux & Spalla, 1991; Ridley, 1984). However, studies have shown that anhydrous granulitic rocks are relatively stable, and hence their conversion to eclogite is not kinetically favourable, with the result that large tracts of dry granulitic crust can be transported into the mantle and returned to the surface with little mineralogical modification (e.g. Austrheim, Erambert, & Engvik, 1997; Ellis & Maboko, 1992; Jackson, Austrheim, McKenzie, & Priestley, 2004). On the other hand, the conversion of dry granulite to eclogite can be catalysed by interaction with fluids (e.g. Austrheim & Griffin, 1985; Erambert & Austrheim, 1993; Jolivet *et al.*, 2005; Martin, Rubatto, Brovarone, & Hermann, 2011; Terry & Heidelbach, 2006). Such catalysis leads to the development of hydrous mineral assemblages that may result in changes in the rheology and bulk density of the deeply buried crust (e.g. Connolly, 2009; Engvik, Austrheim, & Andersen, 2000; Erambert & Austrheim, 1993; Pollok, Lloyd, Austrheim, & Putnis, 2008; Rockow, Haskin, & Fountain, 1997). While the generation of fluids in hydrous subducted rocks will leave a dehydrated mineralogical record, anhydrous granulites can potentially record fluid release events via the formation of hydrous mineralogies that mark the absorption of fluid released elsewhere by dehydration. Given the importance of fluid in catalysing reactions in previously anhydrous rocks, the product mineral assemblages are likely to be frozen in when the fluid pulse is exhausted or consumed by the product assemblages. These hydrous mineral assemblages, therefore, have the potential to record the pressure–temperature (*P–T)* conditions at which fluid was able to migrate from a dehydrating source region(s) during the subduction and exhumation of granulitic crust and the *P–T* path of otherwise unreactive rocks.

In the Lindås Nappe in the Bergen Arcs, western Norway, white mica- and epidote-group-bearing (i.e. hydrous) high-*P* amphibolite and eclogite occur extensively within granulitic protolith (Figure 1). The granulites are early Neoproterozoic in age (c. 950 Ma), whereas the eclogites are Ordovician-aged (c. 450 Ma; Austrheim, 2013; Bingen, Austrheim, Whitehouse, & Davis, 2004; Bingen, Davis, & Austrheim, 2001; Van Wyck, Valley, & Austrheim, 1996). The formation of the high-*P* mineral assemblages is interpreted to have occurred during H_2O-rich fluid infiltration—a form of deep crustal metasomatism—along fractures and shear zones during the Caledonian Orogeny (Andersen, Austrheim, & Burke, 1990; Austrheim, 2013; Austrheim & Griffin, 1985;

Boundy, Fountain, & Austrheim, 1992). Mineralogically and geochemically, the evidence for fluid infiltration is confirmed by the presence of potassium-rich mica, epidote-group minerals and the presence of quartz veins within the host plagioclase–clinopyroxene–orthopyroxene–garnet anorthositic granulite (Andersen *et al.*, 1990; Andersen, Austrheim, & Burke, 1991b; Austrheim, 2013; Austrheim & Griffin, 1985; Boundy *et al.*, 1992; Raimbourg, Jolivet, Labrousse, Leroy, & Avigad, 2005).

Numerous studies have investigated the development of the fluid–rock system in the Lindås Nappe (e.g. Andersen *et al.*, 1991b; Austrheim, 2013; Austrheim & Griffin, 1985; Bingen *et al.*, 2001; Raimbourg *et al.*, 2005; Russell *et al.*, 2012). However, there are comparatively few robust constraints on the *P–T* conditions at which fluid–rock interaction occurred. Existing constraints of 15–21 kbar and 650–800 °C have been derived from conventional thermobarometry (Fe–Mg exchange between garnet and omphacite and garnet and amphibole; Austrheim & Griffin, 1985; Boundy, Essene, Hall, Austrheim, & Halliday, 1996; Boundy, Mezger, & Essene, 1997; Jamtveit, Bucher-Nurminen, & Austrheim, 1990). More recently, Raimbourg, Goffé, and Jolivet (2007) used Gibbs energy minimisation methods to derive rudimentary phase diagrams in concert with average *P–T* calculations (Holland & Powell, 1990, 1998; Powell & Holland, 1988), and derived *P–T* conditions of 20 kbar and 720 °C. However, there are little systematic *P–T* information for the different stages of fluid–rock interaction recorded in the Lindås Nappe, particularly the stages that led to the development of the eclogitic assemblages. Better constrained *P–T* information will provide a framework in which to understand the origins of the

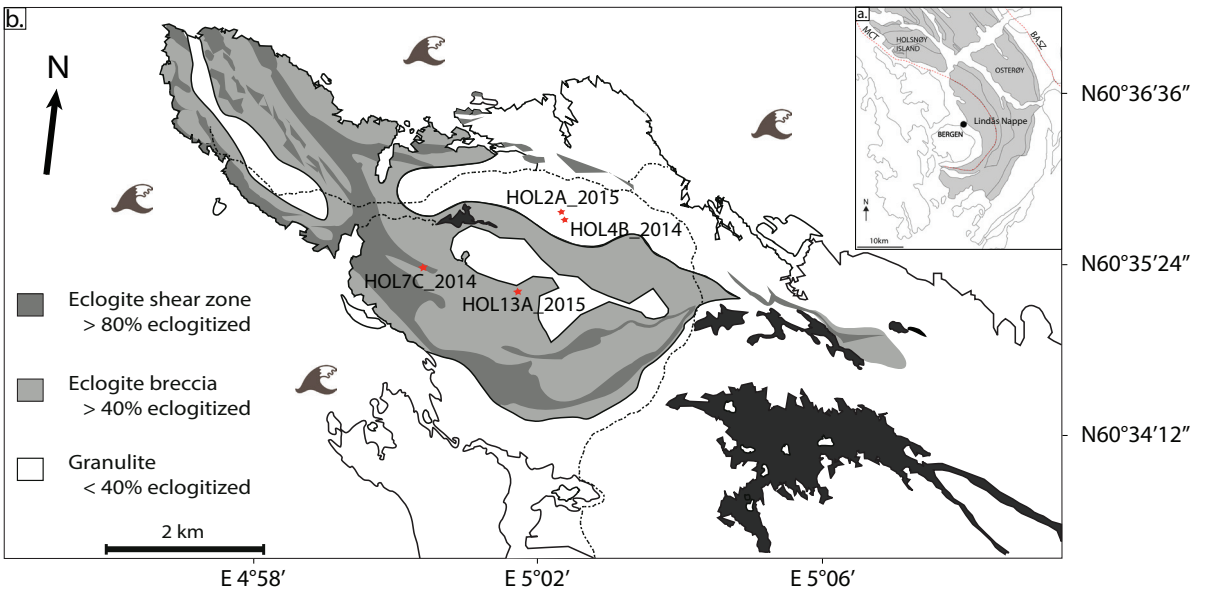

Figure 1. (a) Location of Holsnøy Island relative to Bergen in western Norway. The Lindås Nappe is also highlighted in grey. (b) Geological map of northern Holsnøy island, modified from Austrheim *et al.* (1996) and Boundy *et al.* (1992). Sample locations are indicated as red stars.

metasomatising fluids. In this study, field structural relationships on the island of Holsnøy were used to identify different stages of deformation and recrystallization during modification of the granulite protolith to eclogite. Samples from these different stages were then used in phase equilibria forward modelling to constrain the framework for the evolving *P–T* conditions under which eclogitisation occurred.

2. GEOLOGICAL SETTING

2.1 Study area

Holsnøy is located in south-western Norway, approximately 45 km north-west of Bergen. The outcropping rocks on Holsnøy form part of the Lindås Nappe, which is one of the major domains of the Bergen Arcs (Austrheim, 2013; Centrella, Austrheim, & Putnis, 2015). It is arguably one of the best locations in the world to study metasomatism in deeply buried crust, as both the protolith (granulite) and metasomatic product (eclogite) are superbly preserved, and a number of studies have documented the fluid–rock interactions in this area (e.g. Austrheim, 2013; Centrella *et al.*, 2015; Jolivet *et al.*, 2005; Mattey, Jackson, Harris, & Kelley, 1994; Raimbourg *et al.*, 2005). This study focuses on north-eastern Holsnøy (Figure 1), where the main eclogitised granulite can be found along with distinct stages of deformation and mineral assemblage development associated with the transformation of granulite to eclogite.

2.2 Structural features and stages of deformation

The granulite facies anorthositic protolith was metamorphosed at approximately 950 Ma (Austrheim & Griffin, 1985; Krogh, 1977; Pollok *et al.*, 2008) during the Grenvillian-aged Sveconorwegian Orogeny (Austrheim, 1987; Austrheim & Griffin, 1985). The granulite is dominated by plagioclase with lesser clinopyroxene, garnet and orthopyroxene. Garnet and clinopyroxene commonly form coronae around orthopyroxene, and are aligned with the foliation in the granulite (Austrheim, 2013; Raimbourg *et al.*, 2005). *P–T* estimates from conventional thermobarometry for the granulite facies peak metamorphic conditions are 10 kbar and 800–900 °C (Austrheim, 1987, 2013; Boundy *et al.*, 1997).

The anorthositic granulites were subsequently deeply buried during the Caledonian Orogeny at c. 450 Ma and partially to completely converted to high-*P* amphibolite and eclogite (Austrheim & Griffin, 1985; Boundy *et al.*, 1996; Glodny, Kühn, & Austrheim, 2008; Van Wyck *et al.*, 1996). There has been less focus on the high-*P* amphibolite facies assemblages that preceded the eclogite assemblage. However, petrology of the eclogite has been previously described in detail (Austrheim *et al.*, 1997; Austrheim & Griffin, 1985; Bingen *et al.*, 2001; Boundy *et al.*, 1992; Jamtveit *et al.*, 1990; Pollok *et al.*, 2008; Raimbourg *et al.*, 2005). The essential mineralogy of the eclogites consists of garnet, omphacite and zoisite. Depending on rock

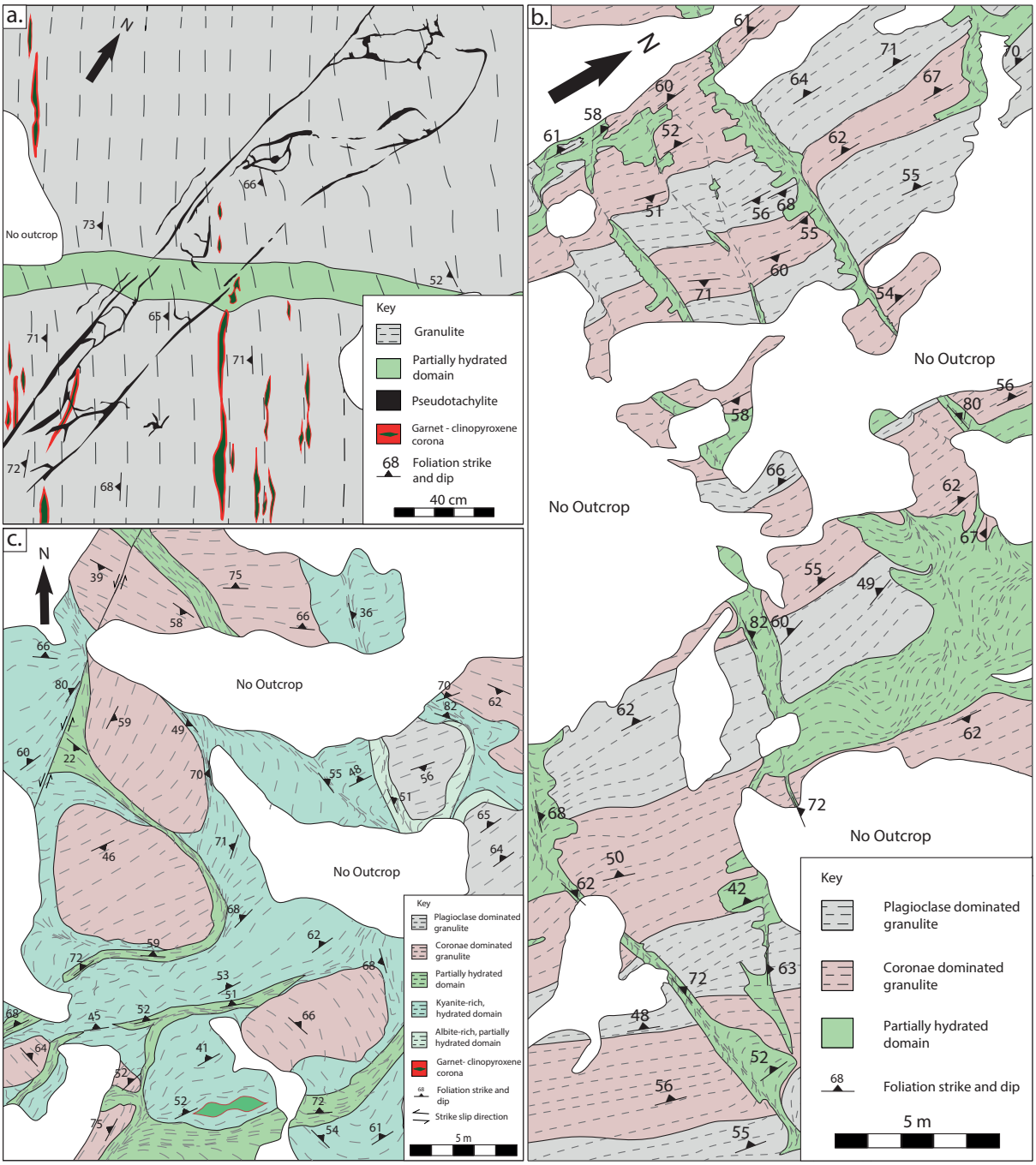

Figure 2. Detailed outcrop-scale maps showing the relationship between different lithological domains on Holsnøy Island. (a) Pseudotachylite veins cross-cutting the foliation of granulite in stage 1 and later overprinted by partially hydrated shear zone. (b) Structural features in stage 2 of deformation, namely the formation of fractures and discrete shear zones which are both accompanied by fluid alteration. (c) The formation of granulite blocks (previously described as the granulite 'breccia') enclosed by highly sheared eclogite in stage 3 of deformation. Map details are provided Table S1.1.

composition, the eclogites may also contain varying amounts of phengite, kyanite, rutile and quartz as well as retrograde amphibole. Previous *P–T* constraints for their formation (15–21 kbar and 650–800 °C) suggest burial depths of approximately 50–70 km, assuming no deviatoric stress contribution (Austrheim, 1987, 2013; Boundy *et al.*, 1996; Boundy *et al.*, 1997; Jamtveit *et al.*, 1990; Pollok *et al.*, 2008). Later reworking of the eclogite is interpreted to be associated with partial exhumation at amphibolite facies conditions

of 8–12 kbar and 600–700 °C (Glodny *et al.*, 2008; Kühn, 2002).

The transition from granulite to eclogite on Holsnøy has been described by a number of workers (Austrheim, 1987; Boundy *et al.*, 1992; Boundy *et al.*, 1997; Jamtveit *et al.*, 1990; Jolivet *et al.*, 2005; Kühn, Glodny, Austrheim, & Raheim, 2002; Raimbourg *et al.*, 2007), and can be tracked via stages of deformation that progressively increase the degree of transformation of the protolith.

Stage 1 involves the formation of pseudotachylite arrays and veins. These have been described in detail by Austrheim and Boundy (1994), Austrheim, Erambert, and Boundy (1996) and Austrheim *et al.* (2017). The pseudotachylites now occur in the granulites as recrystallised pale grey veins and injection structures. They either cross-cut the granulite foliation (Figure 2a) or follow its trend (Figure 3a). Where the veins follow the granulitic foliation, they form thin (2–4 cm) dyke-like structures that can be traced continuously for

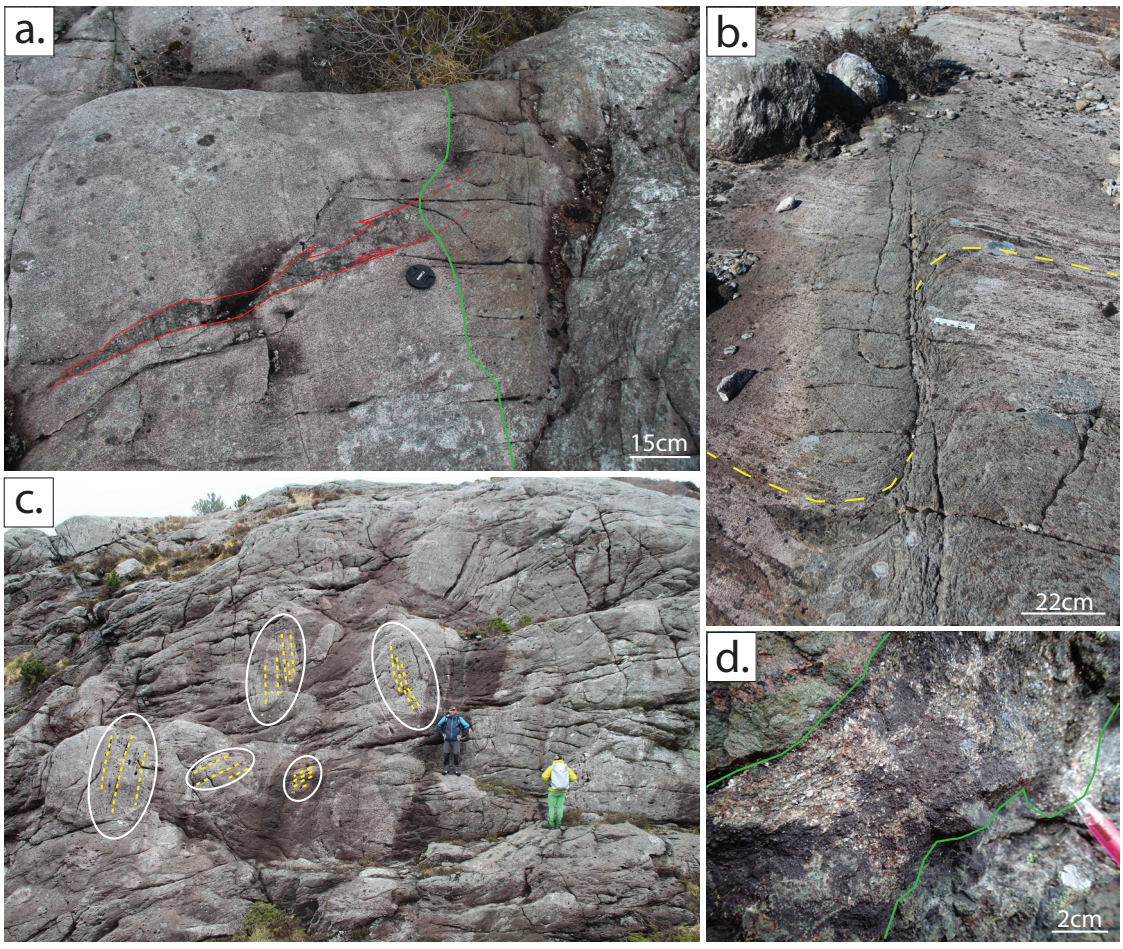

Figure 3. Field photographs illustrating the different stages of deformation. (a) Pseudotachylite outline in red overprinted by a partially hydrated shear zone (grey zone on right of the picture) during stage 1 of deformation. The boundary between the granulite and partially hydrated zone is outlined in green. Camera cap as scale is 60 mm (b) Small-scale partially hydrated shear zone (denoted grey zone) in stage 2. Displacement of coronitic bands by up to 1 m shown by the yellow dashed lines in and out of the shear zone. Scale bar in the photograph is 11 cm. (c) Granulite blocks (circled) sitting in extensively sheared eclogite formed during stage 3 of deformation. Foliation in individual granulite blocks cannot be followed from one block to another one (highlighted in yellow dashed line). (d) Retrogressive phengite-rich eclogite (pale strip in the middle of photo) overprinting eclogite (dark green domain on top left of photo). Pink pen tip at bottom right of picture for scale.

up to 20 m. These dyke-like veins have irregularly shaped injection veins that branch off and transect the enclosing granulitic foliation. In other instances the pseudotachylites form arrays within foliation-discordant domains up to 1 m wide (Figure 3a), within which numerous irregular centimetre-scale pseudotachylite veins occur. In places rotation and disruption of the granulite foliation has occurred, creating zones that also contain cataclasites and ultramylonites (Austrheim & Boundy, 1994; Austrheim *et al.*, 1996). The pseudotachylites have been overprinted by high-*P* amphibolite and eclogite assemblages that formed during fluid infiltration. The formation of the pseudotachylites is probably linked to the Caledonian Orogeny due to their consistent proximity to eclogitised shear zones (Austrheim & Boundy, 1994).

Stage 2 involved the formation of discrete shear zones that range from centimetre- to metre- scale within metasomatised granulite (Figure 2b). The metasomatism is marked by a darkening of the granulite to form grey–green regions with a diffuse and gradational transition to the granulite (Figure 2b). These regions of alteration and associated plastic deformation overprint the stage 1 pseudotachylite (Figure 3a). The alteration comprises polygonal recrystallised plagioclase grains, together with zoisite, kyanite, omphacite and phengite. Garnet grains inherited from the granulite protolith have been partially consumed, with modal proportion reductions of ~ 50% compared to the granulite protolith, and form relict grains in the stage 2 assemblage. The domains of altered granulite typically flank the shear zones and contain structurally reworked granulite (Figure 3b). However, in some instances the granulite is altered without any associated deformation, with the pre-existing foliation passing smoothly through the region of alteration. Where stage 2 deformation and alteration are volumetrically minor, the pre–existing granulite facies structures can be traced continuously through the outcrops and are only modified where they are deflected into discrete shear zones (Figure 3b).

Stage 3 involved a significant increase in ductile deformation, indicated by shear zones that are tens to hundreds of metres in width and kilometres in length. Within these zones, the protolithic granulite is completely replaced by eclogite. This is indicated by the complete disappearance of plagioclase, and the formation of a new coarse-grained assemblage that contains omphacite–zoisite–phengite–kyanite–garnet. This omphacite-rich eclogite is strongly foliated and forms a 'matrix' that encloses relict granulite blocks (Figure 2c). The granulite blocks vary in size, ranging from metre to tens-of-metre scale, and the relict foliation usually cannot be traced smoothly between adjacent blocks. Deflection of the granulite fabric into the foliated eclogite occurs at the margins of the granulite blocks, indicating that plastic deformation was associated with eclogite formation. The stage 3 domains are organised into deformation belts that principally trend 110/20NE, with a subordinate conjugate that trends 050/20SE. Within the ESE trending eclogite belts, the relict granulite blocks com-

Table 1. Bulk-rock composition of chosen samples for phase modelling expressed in wt %.

Sample	HOL2A_2015 (stage 1)	HOL4C_2014 (stage 2)	HOL7C_2014 (stage 3)	HOL13A_2015 (stage 4)
SiO_2	50.81	50.54	46.51	48.33
TiO_2	0.08	0.10	0.61	0.64
Al_2O_3	24.72	24.92	18.65	20.69
MnO	0.09	0.07	0.20	0.21
MgO	4.72	5.49	6.60	7.10
CaO	10.02	8.54	10.93	7.70
Na_2O	4.06	3.92	3.34	3.02
K_2O	0.57	0.45	0.79	2.49
P_2O_5	0.07	0.03	0.03	0.04
LOI	0.91	0.74	1.36	2.44
FeO	2.80	3.68	7.23	6.22
Fe_2O_3	1.41	1.31	3.35	2.63
Total	**99.66**	**99.79**	**99.60**	**99.76**

*HOL4C_2014 was not modelled as it is only partially modified.

monly have sigmoidal shapes with east–west elongation that suggests bulk dextral top-to-the-east non-coaxial flow (Jolivet *et al.*, 2005; Raimbourg *et al.*, 2005).

Stage 4: In places the strongly foliated eclogite has been overprinted by localised, coarse-grained phengite-rich domains (~40 cm wide at outcrop scale; Figure 3d) locally associated with small pegmatites, in which earlier formed stage 3 omphacite-rich eclogite has been broken into fragments. These omphacite-rich domains contain euhdral garnet and disseminated omphacite and amphibole, whereas the phengite-rich domains contain minor garnet, omphacite and zoisite. These phengite-rich domains may form the early stages of the amphibolite facies overprint that occurred during exhumation of the eclogites (Boundy *et al.*, 1992; Glodny *et al.*, 2008; Kühn, 2002; Kühn *et al.*, 2002).

3. METHODS

3.1 Bulk-rock and mineral chemistry

Whole-rock geochemistry for implementation in phase equilibria forward modelling was done at the Department of Earth and Environment, Franklin and Marshall College, Lancaster PA, using Wavelength Dispersive X-ray Fluorescence (WD–XRF) spectrometry. Major elements were analysed on fused disks prepared using a lithium tetraborate flux. Ferric vs ferrous iron content was determined by titration. Whole rock geochemistry in wt% is provided in Table 1.

Mineral compositions and elemental X-ray maps were acquired using a CAMECA SXFive electron microprobe at Adelaide Microscopy, University of Adelaide. For elemental analyses, a beam current of 20 nA and accelerating voltage of 15 kV was used. Prior to analysis, calibration was done on an andradite standard, and wavelength dispersive spectrometers (WDS) were used for the analyse of SiO_2, ZrO_2, TiO_2, ZnO,

Table 2. Un-normalised bulk-rock composition in the system NCKFMASHTO expressed in mol % as input to THERMOCALC.

Sample	HOL2A_2015 (stage 1)	HOL7C*_2014 (stage 3)	HOL7C_2014 (stage 3)	HOL13C_2015 (stage 4)
SiO_2	55.47	48.91	48.55	48.98
TiO	0.07	0.48	0.53	0.49
Al_2O_3	15.50	11.56	10.88	12.35
FeO*	3.71	9.01	6.87	7.28
MgO	7.98	10.35	9.15	10.73
CaO	11.72	12.31	12.84	8.36
Na_2O	4.29	3.4	3.85	2.97
K_2O	0.40	0.53	0.60	1.61
H_2O	0.18	4.77	5.39	8.25
O	0.58	1.33	1.35	1

HOL7C* designates the original bulk composition for this sample (including relict garnet inherited from the granulitic protolith) whereas HOL7C is the modified bulk composition derived from removing the relict granulitic garnet from the whole-rock composition. The composition of the relict garnet is on the basis of electron micrprobe-measured mineral composition data (see Table 3).
FeO* = FeO(original) + 2×O as 'O' specifies the amount of excess oxygen required to oxidise FeO to create Fe2O3.

Al_2O_3, Cr_2O_3, FeO, MnO, MgO, CaO, BaO, Na_2O, K_2O, P_2O_5, Cl and F. Element maps were obtained using a beam current of 200 nA and accelerating voltage of 15 kV. Step sizes and dwell times were chosen based on the size of the area mapped and the grain size of the minerals to maximise the resolution. Elements Ca, Fe, Mn and Mg were mapped using WDS, and Al, Si, Ti, K, Na, Zr, Cl, Ce and F were mapped using energy dispersive spectrometers (EDS). Electron backscatter diffraction (EBSD) was used to identify minerals in fine-grained symplectites that formed during stage 2 replacement of garnet. EBSD mapping was undertaken at the John De Laeter Centre at Curtin University using a Tescan $MIRA_3$. For EBSD analysis samples were polished using 60 nm colloidal silica solution. EBSD maps were collected via the software Aztec (Oxford Instruments). An acceleration voltage and beam current of 20 kv and 15 nA, respectively, were used during acquisition with 50 ms dwell time per pixel. Proportions of minerals were completed by processing the collected EBSD maps of reaction rims of omphacite and garnet. Phengite did not index during EBSD collection and modal proportions have been estimated by EDS phase mapping. Image J was used to calculate the relative modal proportions by colour thresholding.

3.2 Phase equilibria forward modelling

3.2.1 Bulk-rock composition determination

Bulk compositions used for phase equilibria forward modelling were determined from whole-rock geochemistry. The whole-rock sample is a slice of rock ~ 2mm thick taken from the thin section rock block adjacent to the surface that was glued to the thin section glass. Hence, this whole-rock composition closely approximates the integrated mineralogical composition of the minerals observed in thin section. Weight percent data from whole-rock geochemical analyses (Table 1) were recast in terms of mole percent-

age of oxide components (e.g. MgO, SiO_2; Table 2) for phase equilibria modelling using THERMOCALC. For samples that had completely recrystallised (e.g. HOL2A_2015), the forward modelling calculations used the recast values directly from bulk-rock composition and titration analyses. However, for samples that still contained relicts from the granulitic mineralogy (e.g. HOL7C_2014), it was necessary to derive an effective reactive bulk composition prior to forward modelling. The removal of garnet cores was done in the admittedly simple way of determining the proportion of the samples that consists of garnet cores (19%). This was done via pixel counting using Adobe Photoshop, taking advantage of the colour contrast of the garnet cores and rims. Because the garnet cores are mostly unzoned (see section 4.2 Mineral chemistry), it is straight forward to determine the integrated bulk composition of the garnet cores and subtract it from the measured XRF whole-rock composition.

3.2.2 P–T pseudosections

Phase equilibria calculations were undertaken using the software program THERMOCALC v.3.33 in the geologically realistic chemical system Na_2O–CaO–K_2O–FeO–MgO–Al_2O_3–SiO_2–H_2O–TiO_2–O (NCKFMASHTO), where 'O' is a proxy for Fe_2O_3, using the internally-consistent thermodynamic dataset 'ds5' (filename ds55.txt, 22nd Nov 2003 update of Holland & Powell, 1998). The activity–composition (*a–x*) models used were: amphibole (Diener & Powell, 2012; Diener, Powell, White, & Holland, 2007); clinopyroxenes (Diener & Powell, 2012; Green, Holland, & Powell, 2007); chlorite, talc and epidote–clinozoisite (Holland & Powell, 1998); garnet and biotite (White, Powell, & Holland, 2007); plagioclase and K-feldspar (Holland & Powell, 2003); ilmenite and chloritoid (White, Powell, Holland, & Worley, 2000); muscovite and paragonite (Coggon & Holland, 2002).

Based on the low abundance of hydrous minerals in the recrystallised pseudotachylite, the measured LOI (0.91 wt %) was interpreted to be too high to represent the water content at metamorphic conditions for stage 1 of deformation. To determine an effective water content for this particular sample (HOL2A_2015), a $T–M_{H2O}$ was calculated (Figure S1.1). An appropriate water content in the peak field was then constrained by the use of garnet and omphacite compositions isopleths. Samples HOL7C_2014 and HOL13A_2015 did not require the use of $T–M_{H2O}$ models to determine effective water contents as both samples have significantly high abundances of hydrous minerals (e.g. phengite and zoisite). The LOI was interpreted as the maximum possible water content that was present in the system. To investigate the effect of decreasing water content, the *P–T* position of the peak assemblage in both samples was calculated with different percentages of the LOI. The peak field boundaries in sample HOL7C_2014 are not affected by decreasing water content (Figure S1.2). However, the peak field for HOL13A_2015 is significantly affected by decreasing water content as it is bound by the water-out line. Decreasing the LOI causes the water-out line to migrate up

pressure and temperature, causing the peak field to disappear at 80% LOI (Figure S1.3). This indicates that the peak field for HOL13A_2015 only appears at water contents between 6.60–8.25 mol %. Hence for both samples, the maximum possible amount of water was used (i.e. the measured LOI) as it best corresponds with the observed mineral assemblage.

To investigate the effect of varying Fe_2O_3 content in our samples, $P–M_O$ were calculated for stage 3 and stage 4 mineral assemblages (Figure S1.4). The stage 3 (HOL7C_2014) and stage 4 (HOL13A_2015) $P–M_O$ models reveal that the peak assemblages are stable over a wide range of M_o at high pressures, which suggest that varying Fe_2O_3 content does not significantly affect the peak assemblage at such pressures. Moreover, for both samples, the measured M_O values (recast from measured Fe_2O_3 by wet chemistry) plot in the interpreted peak field (Figure S4). The measured Fe_2O_3 values were hence used to calculate the respective *P–T* pseudosections.

Throughout the construction of the different *P–T–X* models, Matlab-based, automated software programme TCInvestigator v2.0 was used to check that the calculated assemblages validly satisfy Gibbs Energy minimisation.

3.2.3 Contouring mineral chemistry and modal proportion

Mineral composition isopleths and normalised modal abundance contours ('mode') were calculated for the forward model using TCInvestigator v2.0 for *P–T* pseudosections. The method used for contouring models is detailed by Pearce, White, and Gazley (2015). Step sizes used for contouring were 0.1 kbar and 1 °C.

4. RESULTS

4.1 Petrography

Four samples were selected to encompass the structural evolution outlined earlier (Table S1.1). Of these, three samples were subsequently chosen to evaluate the *P–T* evolution of the eclogitisation process on Holsnøy. Representative photomicrographs of all samples are presented in Figure 4.

4.1.1 HOL2A_2015 (stage 1)

This sample is from a recrystallised pseudotachylite vein that formed during stage 1. The vein is 4 cm wide and is parallel to the enclosing granulite foliation, and has associated small scale (3 cm by 0.5 cm) injection veins that branch off the main vein. The recrystallised pseudotachylite is fine-grained (<0.1 mm; Figure 4a) and contains kyanite, omphacite, plagioclase, K-feldspar, zoisite and minor amounts of quartz, rutile and poikiolitic garnet. Clusters of kyanite needles are intergrown with omphacite (Figure 4a). The matrix also contains domains dominated by K-feldspar that incorporate abundant fine-grained kyanite (Figure 4a, 5a and b). Both in the matrix and within the K-feldspar domains, the kyanite is unoriented. Garnet

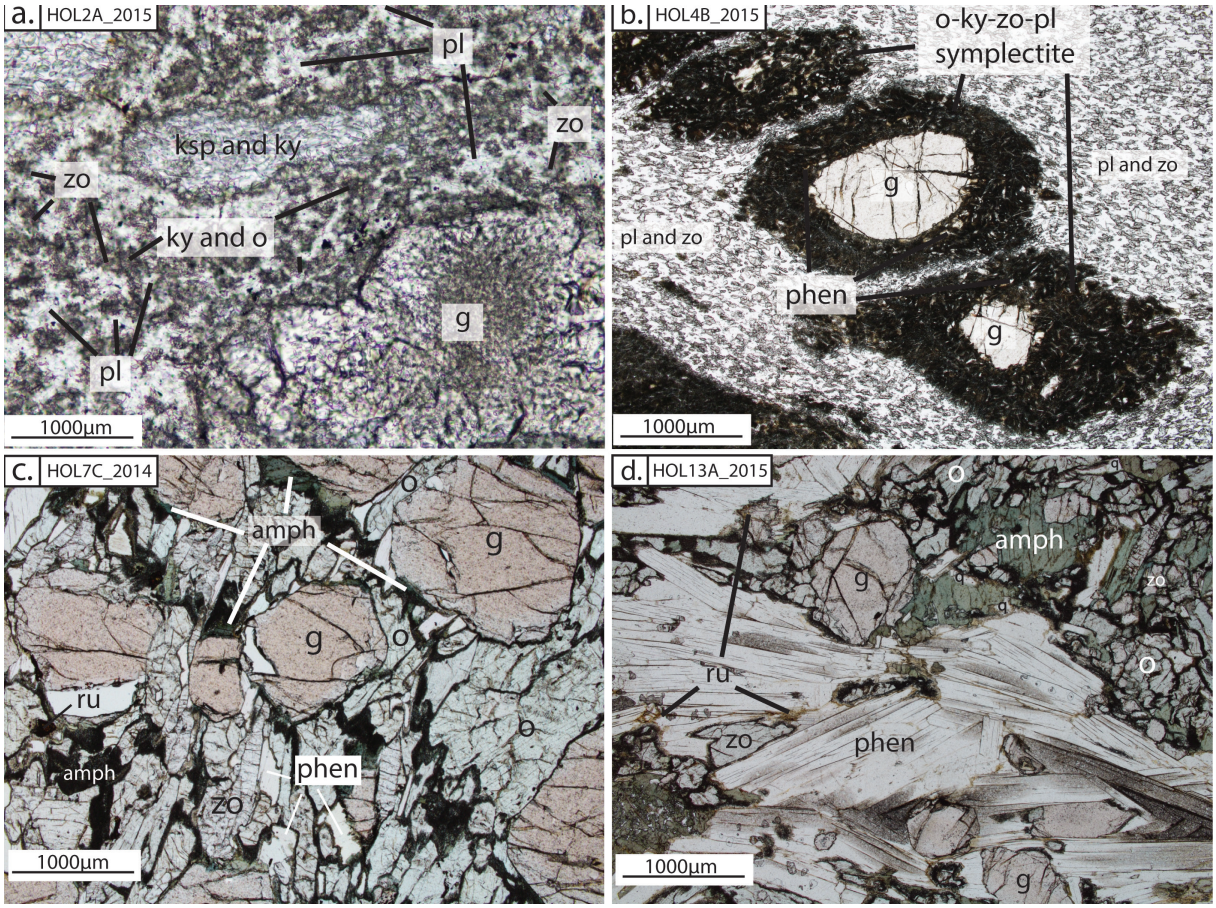

Figure 4. Photomicrographs showing the textures and mineral relationships in the different samples. (a) Sample HOL2A_2015 is a recrystallised pseudotachylite that represents stage 1 of deformation. The matrix comprises very fine-grained light-coloured plagioclase and darker omphacite and kyanite intergrowths enclosing garnet poikiloblasts and lens-shaped domains of intergrown K-feldspar and kyanite. (b) Sample HOL4B_2014 represents stage 2 of deformation. Relict granulitic garnet grains are enclosed by fine-grained plagioclase kyanite, omphacite and phengite-bearing symplectites replacing garnet grains. The light-coloured matrix comprises plagioclase and zoisite. (c) Sample HOL7C_2014 represents stage 3 deformation. Garnet with apparent zoning sits in a matrix of omphacite, zoisite and phengite with growth of amphibole-rich symplectites at garnet-omphacite grain boundaries. (d) Sample HOL13A_2015 represents stage 4 of deformation. A coarse-grained phengite matrix separates amphibole–omphacite–zoisite–garnet–quartz–bearing domains into isolated aggregates.

occurs in minor amounts as highly poikiloblastic grains (Figure 5c, d) that contain inclusions of plagioclase, K-feldspar, quartz, clinopyroxene and rare rutile. Plagioclase forms abundant polygonal grains (<0.1 mm) in the matrix. Texturally, plagioclase is part of the recrystallised assemblage and is not inferred to be a relict mineral pre-existing from the granulite protolith. The interpreted metamorphic assemblage in the recrystallised pseudotachylite is garnet–kyanite–plagioclase–K-feldspar–omphacite–zoisite–quartz–rutile.

4.1.2 HOL4B_2014 (stage 2)

This sample contains a fine-grained foliated matrix consisting of plagioclase, kyanite, clinopyroxene, phengite and minor quartz (Figure 4b, 6). The matrix encloses relict garnet and clinopyroxene derived from the granulite protolith. The modal percentage of garnet has been reduced from ~ 18% in the pristine granulite to ~10% in the recrystallised assemblage and there is no evidence of new garnet growth. Garnet is enclosed by thick coronae of fine-grained reaction prod-

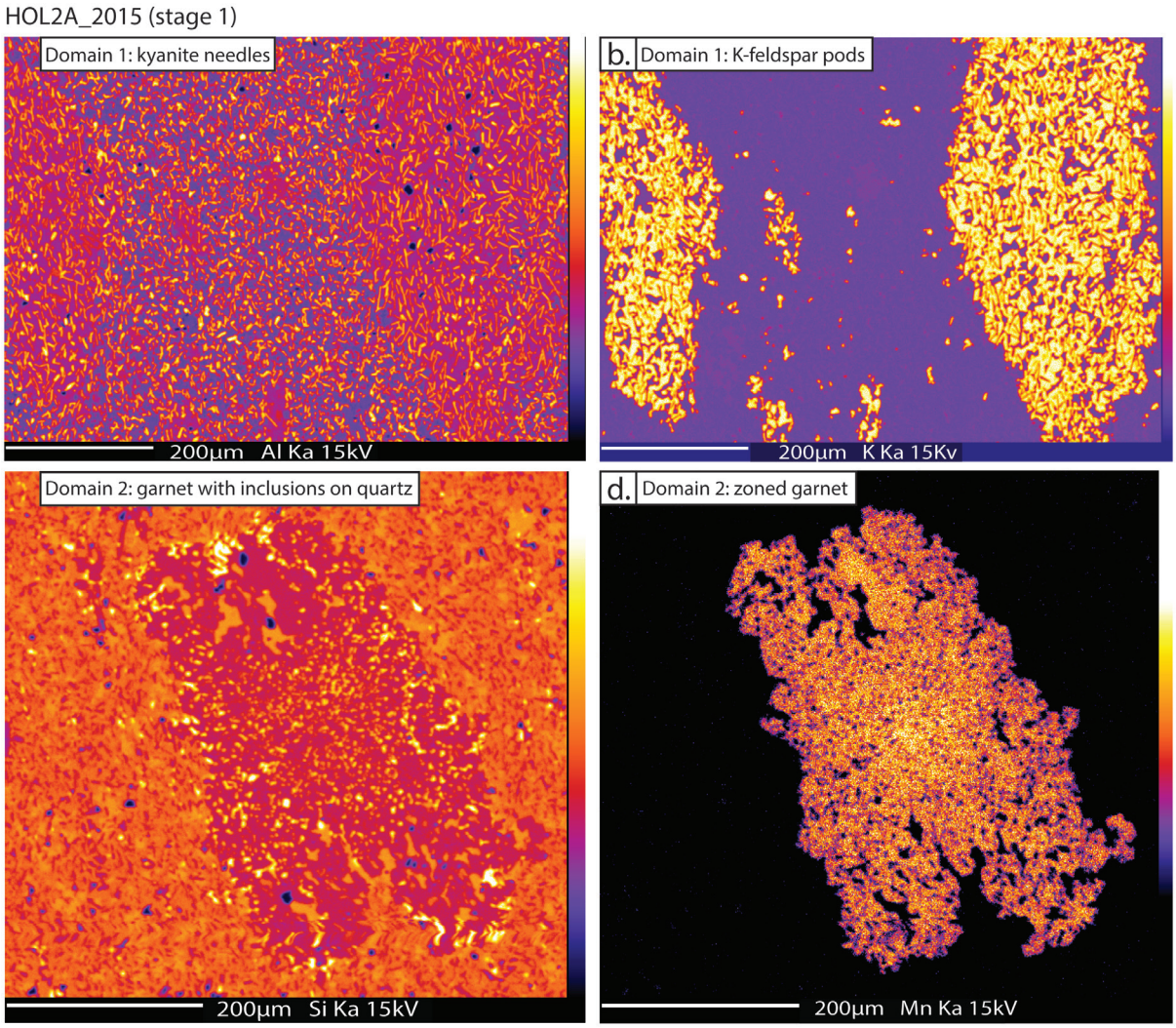

Figure 5. Representative electron microprobe X-ray maps of two regions in sample HOL2A_2015. Scalebar at the bottom of all maps is 200µm. On the colour scale, white represents relatively high abundance of an element whereas black represents relatively low abundance. (a) Aluminium map highlighting kyanite, which appears as bright yellow needles. (b) Potassium map highlighting K-feldspar, which formed the two bright pods, with inclusions of kyanite needles. (c) Silicon map of a garnet in sample HOL2A_2015, showing small grains of quartz in the matrix and as inclusions in the garnet rim. (d) Manganese map of a garnet HOL2A_2015 showing minor Mn zonation with relative enrichment in the core compared to rim.

ucts that comprise finely intergrown omphacite–kyanite–zoisite–plagioclase, with coarser individual crystals of kyanite, phengite and omphacite (Figure 6). The symplectite reaction halos are typically ellipsoidal with the longest axis parallel to the local stage 2 foliation.

4.1.3 HOL7C_2014 (stage 3)

This sample contains a well-defined stage 3 foliation defined by alignment of zoisite (14%), phengite (7%), elongate omphacite (24%) and minor rutile. Hand specimens from the sample location contain sparse, blue, millimetre-sized kyanite grains (Figure S1.5), and X-ray mapping reveals trace amounts of kyanite in HOL7C_2014. The foliation encloses garnet grains that range in size from 0.5–2 mm (Figure 4c). The garnet grains are equant and subhedral and display subtle colour variation from relatively pink cores to lighter pink rims (8%) (Figure

4c). Garnet cores may contain inclusions of coarse-grained and euheral spinel (Figure S1.6). These inclusions are identical to those that can be found in the garnet grains in the granulitic protolith, implying the garnet in the eclogite was relict from the granulite protolith. Phengite, omphacite and garnet are commonly rimmed by very fine-grained symplectites consisting of amphibole, albitic plagioclase and zoisite (Figure 4c). The symplectites are typically better formed at grain boundaries that occur at a high angle to the stage 3 foliation. The interpreted peak stage 3 mineral assemblage is zoisite–phengite–omphacite–garnet rim–rutile–kyanite.

4.1.4 HOL13A_2015 (stage 4)

This sample is from a phengite-rich schist that overprints the omphacite–garnet rich eclogite that formed during stage 3. The sample contains medium-grained (0.2–1 mm) garnet, omphacite (0.2–0.4 mm), zoisite (0.1–0.3 mm), green amphibole (0.2–1 mm) and quartz (0.1–0.2 mm), which are all in contact. These minerals form domains that are isolated by very coarse phengite grains (Figure 4d). Garnet and zoisite also occur within the coarse-grained phengite matrix. The interpreted peak metamorphic assemblage is phengite–garnet–omphacite–rutile–amphibole–quartz–zoisite. The abundance of minerals in volume % is: phengite = 36%; omphacite = 17%; amphibole = 17%; garnet = 11%; zoisite = 8% quartz = 4%; rutile = 0.6%, determined by using pixel counts in Photoshop (Appendix S1.1)

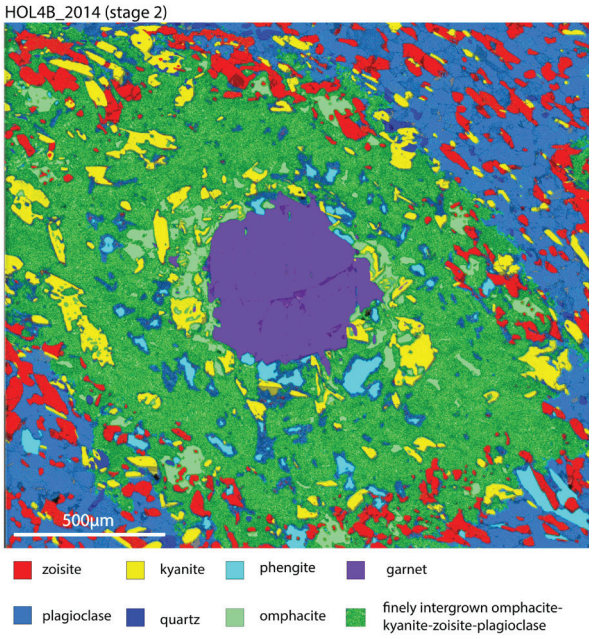

Figure 6. EBSD image of garnet breakdown texture in HOL4A_2014, representing stage 2 of deformation. In this sample, garnet breaks down owing to fluid infiltration to form a symplectite rim comprising omphacite, kyanite, zoisite, phengite and plagioclase. The matrix is predominantly made up of plagioclase, zoisite, kyanite and minor quartz. Zoisite, kyanite and plagioclase define the foliation, wrapping around the garnet and symplectite.

4.2 Mineral chemistry

Mineral compositional data were collected from the stage 1 recrystallised pseudotachylite, stage 3 peak eclogite and stage 4 retrogressed eclogite. Representative mineral compositions are provided in Table 3, and ranges in mineral chemistry are provided in Table 4.

4.2.1 Garnet

Garnet grains in HOL2A_2015 have weak zoning, with slight core to rim increases in X_{grs} (0.39 to 0.41) and X_{py} (0.12 to 0.16), and corresponding slight decreases in X_{alm} (0.43 to 0.41) and X_{sps} (0.00 to 0.02) (Table 4).

Garnet grains have a well-defined zonation in sample HOL7C_2014. The core domains,

Table 3. Representative electron microprobe data of peak minerals in three samples used for phase equilibria modelling: HOL2A_2015, HOL7C_2014 and HOL13A_2015.

	HOL2A-2015 (stage 1)						HOL7C-2014 (stage 3)					HOL13A-2015 (stage 4)						
	g rim	g core	pl	o	ksp	zo	g rim	g core	phen	o	zo	g rim	g core	phen	o rim	o core	amph	zo
SiO_2	38.32	38.39	54.05	53.97	62.88	37.99	37.76	37.93	46.94	54.36	38.59	39.24	40.11	46.79	55.23	54.68	43.64	38.45
TiO_2	0.07	0.20	0.02	0.15	0.02	0.10	0.11	0.11	0.52	0.24	0.09	0.06	0.16	0.87	0.19	0.19	0.41	0.04
Al_2O_3	21.59	21.40	26.40	12.37	19.38	30.87	21.28	20.75	31.63	11.68	31.02	22.01	22.73	31.85	10.85	11.16	15.25	31.11
Cr_2O_3	0.00	0.00	0.04	0.00	*0.01*	*0.01*	0.00	0.00	0.00	0.01	*0.01*	0.03	0.03	*0.01*	0.01	0.00	0.00	0.02
FeO	19.79	20.10	*0.03*	5.63	0.18	2.98	22.31	23.30	2.34	5.33	3.23	20.70	17.55	1.87	4.63	4.25	11.32	2.98
MnO	0.75	1.02	*0.01*	0.05	0.00	0.00	0.51	0.76	0.00	0.02	0.00	0.68	0.41	0.00	*0.02*	0.03	0.20	0.00
MgO	3.88	4.25	*0.01*	7.38	0.00	0.00	7.79	9.84	2.11	8.31	0.04	8.45	13.56	2.21	9.11	8.97	12.26	*0.02*
ZnO	0.00	0.02	0.00	0.00	0.00	0.07	0.00	0.03	0.00	0.00	0.09	0.00	0.00	0.00	0.03	0.00	*0.01*	0.09
CaO	15.00	14.30	8.93	14.02	0.24	*0.01*	8.77	5.50	0.01	13.21	23.54	8.30	5.76	0.01	14.19	14.33	9.39	23.86
Na_2O	0.01	0.05	6.00	6.28	1.53	23.38	0.06	0.02	0.91	6.68	0.00	0.03	0.01	1.55	6.09	6.22	3.86	0.04
K_2O	0.11	0.01	0.28	0.03	13.53	*0.01*	0.00	0.00	8.80	0.00	0.02	0.00	0.00	8.76	0.01	0.01	0.76	0.02
Cl	0.01	0.00	0.01	0.00	0.00	0.00	0.00	0.00	*0.01*	0.02	0.00	0.01	0.01	*0.01*	*0.01*	0.02	0.06	0.00
F	0.01	0.00	0.00	0.00	*0.01*	0.00	0.01	0.00	0.00	0.00	0.00	0.00	0.01	0.00	0.00	0.00	0.09	0.00
TOTAL	99.55	99.75	95.76	99.87	97.78	95.42	98.62	98.32	94.28	99.89	96.63	99.52	100.4	94.86	100.4	99.86	97.28	96.63
No. oxygens	12	12	8	6	8	13	12	12	11	6	13	12	12	11	6	6	23	13
Si	2.98	2.98	2.54	1.93	2.95	2.98	2.93	2.94	3.20	1.94	2.99	3.00	2.96	3.15	1.96	1.96	6.85	2.97
Ti	0.00	0.01	0.00	0.00	0.00	0.01	0.01	0.01	0.03	0.01	0.01	0.00	0.01	0.04	0.01	0.01	0.05	0.00
Al	1.98	1.95	1.46	0.52	1.07	2.85	1.95	1.90	2.54	0.49	2.83	1.98	1.98	2.53	0.45	0.47	2.82	2.84
Cr	0.00	0.00	0.00	0.00	0.00	0.00	0.00	0.00	0.00	0.00	0.00	0.00	0.00	0.00	0.00	0.00	0.00	0.00
Fe^{3+}	0.07	0.08	0.00	0.04	0.07	0.18	0.19	0.21	0.00	0.08	0.18	0.02	0.09	0.04	0.03	0.00	0.00	0.22
Fe^{2+}	1.21	1.22	0.00	0.13	0.00	0.01	1.25	1.30	0.13	0.07	0.03	1.31	1.00	0.06	0.10	0.13	1.49	0.00
Mn^{2+}	0.05	0.07	0.00	0.00	0.00	0.00	0.03	0.05	0.00	0.00	0.00	0.04	0.03	0.00	0.00	0.00	0.03	0.00
Mg	0.45	0.49	0.00	0.39	0.00	0.00	0.90	1.14	0.21	0.44	0.00	0.96	1.49	0.22	0.48	0.48	2.87	0.00
Zn	0.00	0.00	0.00	0.00	0.00	0.00	0.00	0.00	0.00	0.00	0.01	0.00	0.00	0.00	0.00	0.00	0.00	0.01
Ca	1.25	1.19	0.45	0.54	0.11	1.96	0.73	0.46	0.00	0.50	1.95	0.68	0.45	0.00	0.54	0.55	1.58	1.98
Na	0.00	0.01	0.55	0.44	0.20	0.00	0.01	0.00	0.12	0.46	0.00	0.00	0.00	0.20	0.42	0.43	1.17	0.01
K	0.01	0.00	0.02	0.00	0.46	0.00	0.00	0.00	0.77	0.00	0.00	0.00	0.00	0.75	0.00	0.00	0.15	0.00
Cl	0.00	0.00	0.00	0.00	0.00	0.00	0.00	0.00	0.00	0.00	0.00	0.00	0.00	0.00	0.00	0.00	0.02	0.00
F	0.00	0.00	0.00	0.00	0.00	0.00	0.00	0.00	0.00	0.00	0.00	0.00	0.00	0.00	0.00	0.00	0.05	0.00
Total cations (S)	8.00	8.00	5.02	3.99	4.86	8.00	8.00	8.01	7.00	3.99	8.05	7.99	8.01	6.99	3.99	4.03	17.08	8.06

*Values in italic are under detection limit

Table 4. Representative mineral chemistry for samples used in forward phase equilibria modelling.

Sample	HOL2A_2015 (stage 1)	HOL7C_2014 (stage 3)	HOL13A_2015 (stage 4)
Garnet rim			
X_{alm}	0.41–0.42	0.45–0.46	0.30–0.38
X_{py}	0.15–0.16	0.29–0.30	0.45–0.46
X_{grs}	0.40–0.41	0.22–0.28	0.15–0.16
X_{sps}	0.01–0.02	0.00–0.01	0.00–0.01
Garnet core			
X_{alm}	0.41–0.43	0.47–0.49	0.43–0.47
X_{py}	0.12–0.16	0.35–0.38	0.27–0.34
X_{grs}	0.39–0.40	0.14–0.16	0.16–0.23
X_{sps}	0.00–0.02	0.01–0.02	0.01–0.02
Phengite			
X_{Mg}	–	0.65–0.71	0.59–0.70
Omphacite			
X_{jad}	0.36–0.43	0.42–0.49	0.37–0.39
X_{diop}	0.47–0.53	0.46–0.50	0.48–0.50
X_{hed}	0.11–0.18	0.01–0.06	0.07–0.10
X_{aeg}	0.00–0.05	0.08–0.12	0.03–0.06
Zoisite			
X_{Fe3+}	0.15–0.18	0.18–0.21	0.15–0.19
Plagioclase			
X_{Ab}	0.51–0.54	–	–
K-feldspar			
X_{or}	0.84–0.88	–	–
Amphibole			
X_{Mg}	–	–	0.63–0.71

X_{alm}= $Fe^{2+}/(Fe^{2+}+Mg+Ca+Mn)$; X_{py}= $Mg/(Fe^{2+}+Mg+Ca+Mn)$; X_{grs}= $Mg/(Fe^{2+}+Mg+Ca+Mn)$; X_{sps}= $Mn/(Fe^{2+}+Mg+Ca+Mn)$; X_{Fe}=$Fe^{2+}/(Fe^{2+}+Mg)$; X_{Mg}= $Mg/(Fe^{2+}+Mg)$; X_{ab}= Na/(Na+Ca+K); X_{or}=K/(Na+Ca+K)
For omphacite: X_{jad}= j(1-f); X_{diop}= 1-j-x+jx; X_{hed}=x-jx; X_{aeg}=fj where x(cpx)= $Fe^{2+}/(Fe^{2+}+Mg)$; j(cpx)= Na cations (omphacite 0.35< j <0.7) and f(cpx)=$Fe^{3+}/(Fe^{3+}+Al+Cr)$.

which are interpreted to be derived from the protolith, are compositionally homogeneous, with X_{grs} ranging between 0.12 and 0.16; X_{py} of 0.35–0.38; X_{alm} of 0.47–0.49 and X_{sps} of 0.02. The cores are enclosed by a well-defined compositionally contrasting rim that is best expressed by X_{grs} (Figures 7a and 8a). The rims show slight zoning with X_{grs} decreasing from 0.29 to 0.24 from the interior of the rim to the exterior while X_{py} in the rim increases from 0.22 to 0.27 (Figure 8a). X_{alm} (0.44) and X_{sps} (0.01) are essentially unzoned (Table 4).

Garnet grains in HOL13A_2015 show well-defined compositional zoning (Figure 7c, d) similar to that in HOL7C_2014, expressed by a core domain of garnet derived from the protolith, and a rim of new garnet (Figure 8b). The cores are compositionally homogenesous with X_{grs} of 0.13–0.16, X_{py} of 0.46–0.52, X_{alm} of 0.30–0.32 and X_{sps} of 0.02–0.03 (Table 4). The rims are enriched in X_{grs} and X_{alm} with respect to the cores, showing relative increases of around 38 and 20% respectively, and are depleted in X_{py} (Figure 8b). The X_{py} in the rims ranges between 0.33 and 0.31 and shows zoning to lower

X_{py} towards the outer margin of the garnet overgrowth. In contrast with X_{py}, X_{alm} in the garnet rims is homogeneous. Compositional gradients between cores and overgrowths are steeper for X_{grs} than for X_{py} and X_{alm} (Figure 8b), suggesting the outer regions of the core domains may have undergone more extensive diffusional modification in Fe and Mg .

4.2.2 Phengite

HOL2A_2015 does not contain phengite, however, it is present in the other two samples.

HOL7C_2014 contains phengite in the matrix which defines the foliation, together with zoisite and omphacite. Phengite grains in

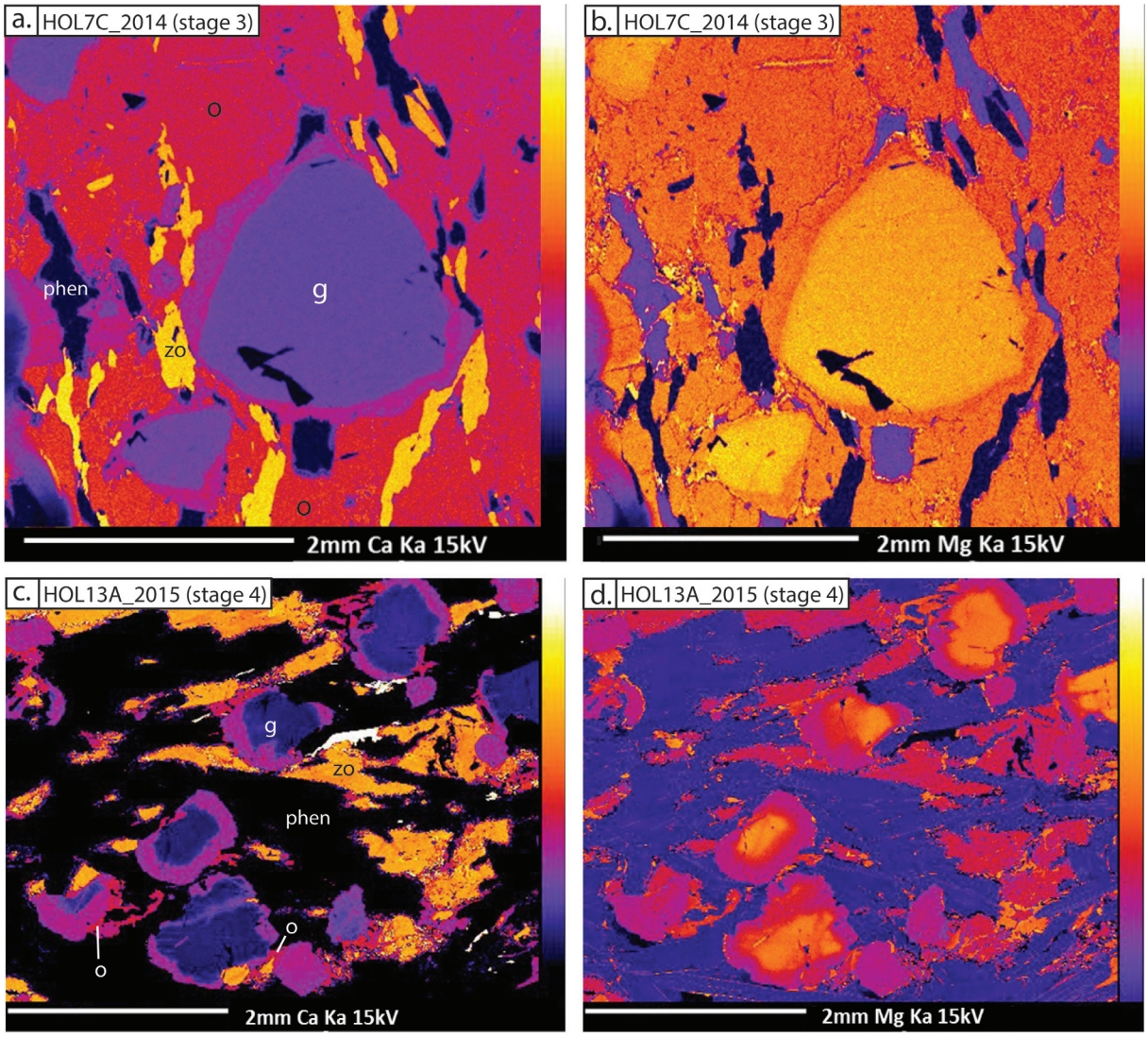

Figure 7. Electron microprobe X-ray maps of garnets in HOL7C¬_2014 (top) and HOL13A_2015 (bottom). Scalebar at the bottom of each map is 2mm. On the colour scale, white represents relatively high abundance of an element while black represents relatively low abundance. (a) X-ray map of calcium in HOL7C¬_2014. There is a very sharp boundary between the core and rim, with a distinct enrichment in Ca in the rim of garnet grains. Garnet cores are interpreted to be relict from the granulite and make up approximately 75 vol. % of garnet grains. (b) Magnesium X-ray map of garnet in HOL7C_2014. Garnet grains show a general decrease in Mg content from core to rim. (c) Calcium X-ray map of garnet grains in HOL13A_2015, which have smaller cores than those in HOL7C_2014, but show similar increase in Ca content at the rims. (d) Magnesium X-ray map of garnet grains in HOL13A_2015. As in HOL7C_2014, there is a general decrease of Mg content from core to rim, however, the core-rim boundary is less sharp.

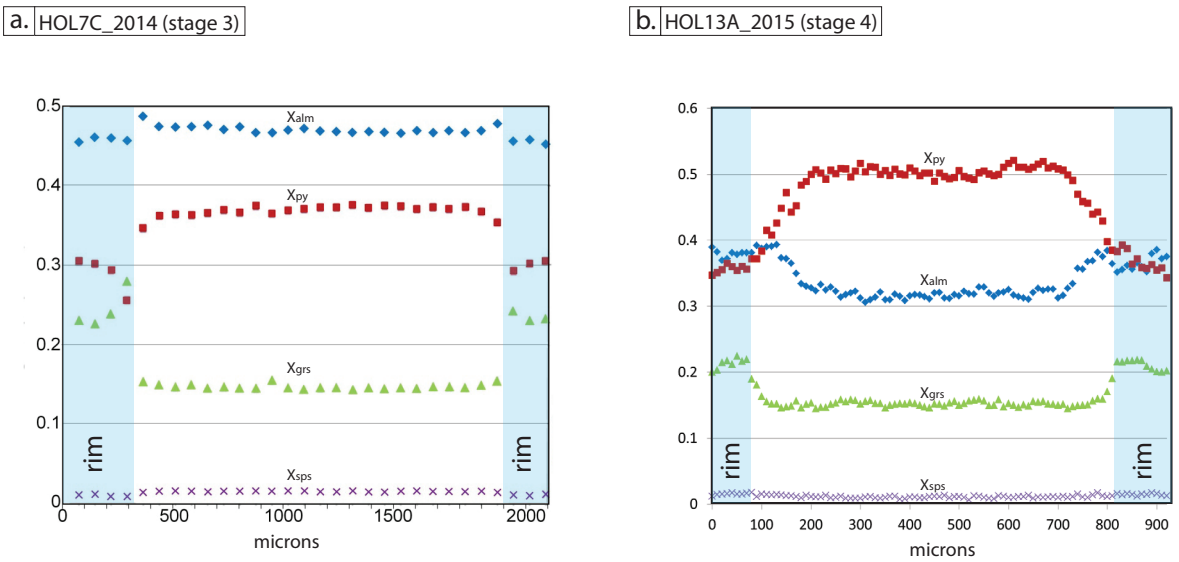

Figure 8. Zonation profile of garnet grains in (a) HOL7C_2014 and (b) HOL13A_2015. In both samples, Xgrs content increases from core to rim, Xpy decreases and Xsps increases. Xalm decreases from core to rim in HOL7C_2014, whereas it increases in HOL13A_2015.

this sample are unzoned, with XMg ranging from 0.65 to 0.71 (Table 4). Phengite in HOL13A_2015 is abundant in the matrix as coarse grains, but shows no zonation. XMg for phengite in this sample range from 0.59 to 0.70.

4.2.3 Omphacite

Omphacite grains in HOL2A_2015 occur as intergrowths with kyanite in the matrix. The grain size is too small to identify compositional zoning. They have Xjad of 0.36–0.43; Xdiop of 0.47–0.53; Xhed of 0.11–0.18 and Xaeg of 0–0.050 (Table 4).

Compared to HOL2A_2015, HOL7C_2014 contains much coarser (up to 1.5 mm) omphacite grains. The Xjad and Xdiop values range from 0.36–0.41 and 0.46–0.50 respectively. The sample shows significantly lower Xhed (0.01–0.06) and a relative enrichment in Xaeg (0.08–0.12) compared to HOL2A_2015 (Table 4).

Omphacite grains in HOL13A_2015 occur predominantly associated with garnet and amphibole and less commonly in the phengite dominated domains. Grains in proximity to the phengite-rich domains usually show slight zonation in both Ca and Na, increasing from 0.39 to 0.54 c.pfu and 0.27 to 0.42 c.pfu, from core to rim, respectively, compared with those in the garnet-amphibole domains which are homogeneous. In general, HOL13A_2015 has Xjad of 0.37–0.39 and Xdiop of 0.48–0.50, and is relatively enriched in Xhed (0.07–0.10) while depleted in Xaeg (0.03–0.06; Table 4).

4.2.4 Feldspar

HOL2A_2015 is the only sample to contain feldspars. Plagioclase occurs in the matrix intergrown with kyanite–omphacite clusters and fine-grained zoisite, and has XAb from 0.11 to 0.15 (Table 4). In the same sample, K-feldspar occurs with kyanite needles in

lense-shaped domains in the matrix (Figure 5b). The Xor of K-feldpar ranges from 0.84 to 0.88, whereas the Na is ~ 0.20 c. pfu and Ca is ~ 0.11c. pfu (Table 3).

4.2.5 Amphibole

HOL2A_2015 does not contain any amphibole. Amphibole occurs in HOL7C_2014 as very fine-grained symplectites on the margins of garnet and omphacite grains but was too fine-grained to analyse without overlapping the surrounding minerals.

In HOL13A_2015, the amphibole grains are unzoned. The XMg ranges from 0.63 to 0.71 (Table 4) and Ca and Na contents are 1.58 c. pfu and 1.17 c. pfu, respectively (Table 3).

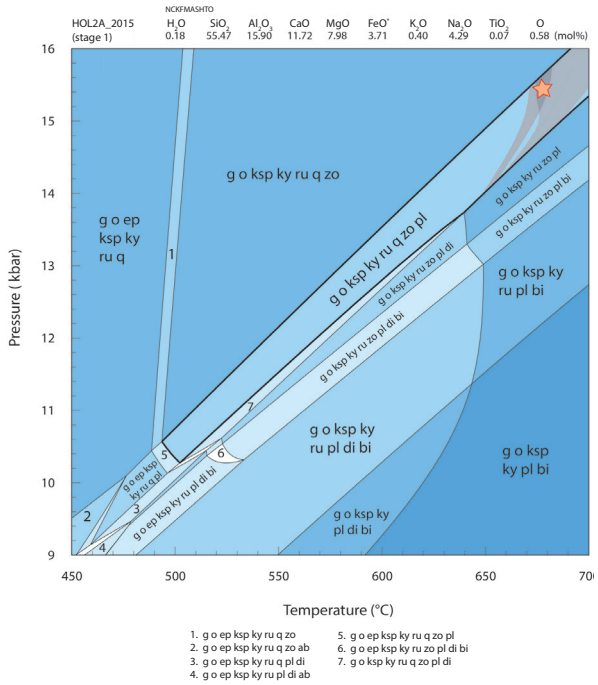

Figure 9. (a) Calculated *P–T* pseudosection for sample HOL2A_2015. The bulk composition at the top of the model is expressed as mol %. The white fields have a variance of two whereas the darkest shade of blue indicates variance of six. Mineral abbreviations are from Holland and Powell (1998).
Note: very small fields are not labelled.The bold outline indicates the peak mineral assemblage and the red star designates approximate *P–T* conditions. The grey shaded regions represent the contour ranges for garnet composition (x(g) of 0.71-0.73) and K-feldspar ranges (XNa ~ 0.140-0.145), used to further constrain the peak conditions. Peak conditions were selected where the two contours overlap, as indicated by the red star.

4.5.6 Zoisite

In sample HOL2A_2015, zoisite occurs as fine-grained clusters with plagioclase, kyanite and omphacite in the matrix and has XFe3+ in the range 0.15–0.18. HOL7C_2014 contains elongate zoisite grains in the matrix that defines the foliation along with phengite and omphacite. The XFe3+ is in the range 0.18–0.21 (Table 4). In HOL13A_2015, zoisite grains display no zonation and have XFe3+ in the range 0.15–0.18 (Table 4).

4.3 Pressure–Temperature conditions

P–T pseudosections were calculated for sample HOL2A_2015, HOL7C_2014 and HOL13A_2015 which represent stages 1, 3 and 4 assemblages, respectively. These samples collectively span the recorded metamorphic evolution leading up to and immediately post-dating the formation of eclogite on Holsnøy. Thus, they provide a *P–T* framework for the deformation stages and associated fluid–rock interaction.

4.3.1 HOL2A_2015 (recrystallised pseudotachylite; stage 1)

The assemblage within the recrystallised pseudotachylite that formed during stage 1 is garnet–kyanite–plagioclase–K-feldspar–zoisite–quartz–omphacite. The phase equilibria model is shown in Figure 9 and was calculated using the composition presented in Table 2. The observed assemblage is not well constrained by equilibria modelling

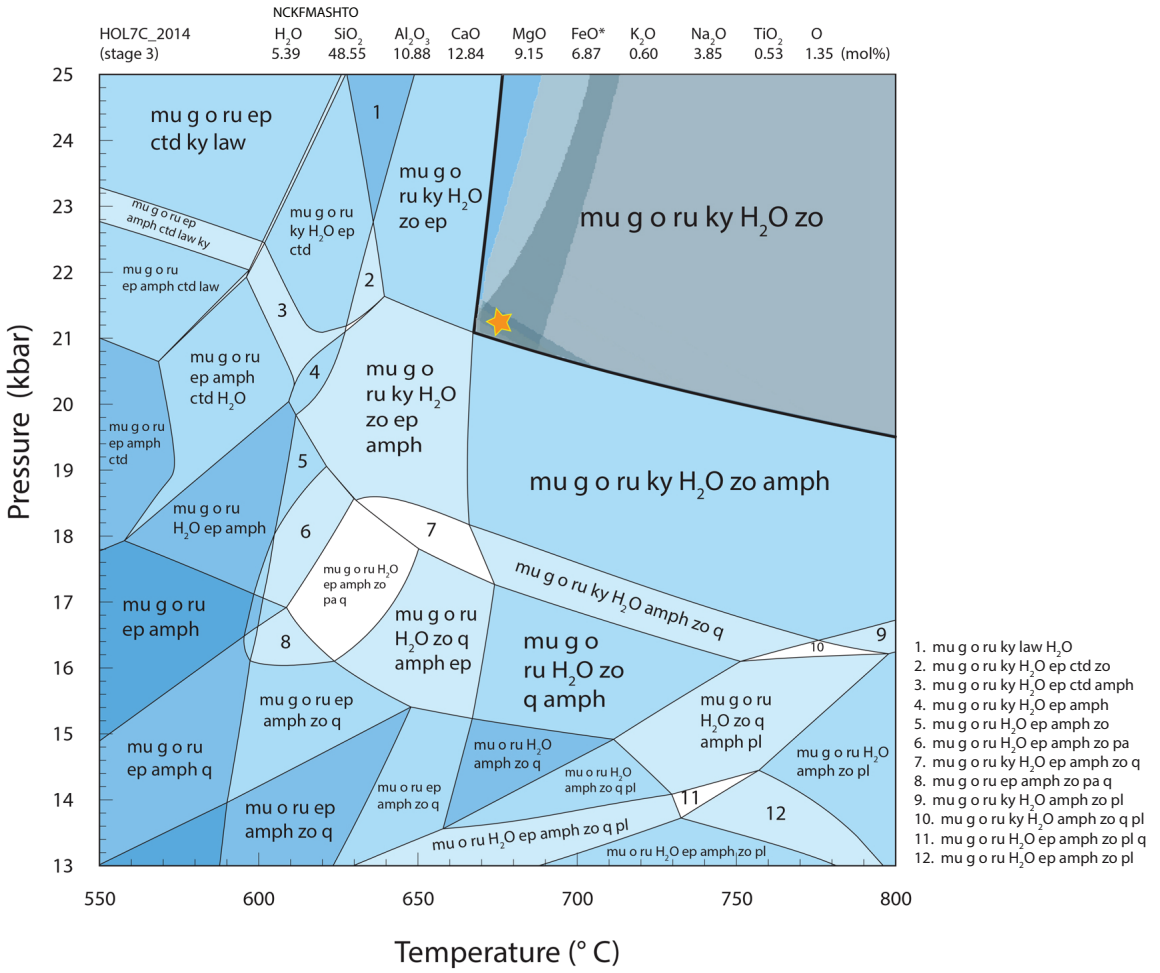

Figure 10. Calculated *P–T* pseudosection for modified bulk composition (relict granulitic garnet removed) of sample HOL7C_2014 (Table 2). The bulk composition at the top of the model is expressed as mol %. The white fields have a variance of two whereas the darkest shade of blue indicates variance of six. Mineral abbreviations are from Holland and Powell (1998).

Note: very small fields were not labelled.The bold outline indicates the peak mineral assemblage. For further constraints, contours for the following measured mineral chemistry were plotted in grey: garnet compositional contours for z(g) with measured range of 0.26¬¬–0.29; 2) omphacite compositional contours for x(o) with measured range 0.10–0.13; omphacite compositional contours for j(o), measured range of 0.48–0.50 and lowest abundance of kyanite in the peak field.

The peak conditions are more tightly constrained to 21–22 kbar and 670–690 °C, where the different isopleth ranges coincide in the peak field, as indicated by the orange star.

as it occupies a large part of *P–T* space. In the modelled *P–T* window, the peak assemblage occurs at conditions above 10 kbar and 490°C. In an attempt to further constrain the peak field, mineral modes and compositional contours for different minerals were calculated. In this case, the use of mineral abundance isopleths was not useful as they parallel the field boundary of the interpreted peak mineral assemblage (Figure S1.7). However, garnet and feldpsar compositions can be used to provide an upper limit on the potential *P–T* conditions at which the pseudotachylite recrystallised. Garnet in the assemblage is essentially unzoned, and while this may reflect post growth re-equilibration, the *x*(g) value range of ~0.71–0.73 occurs, within the modelled peak assemblage field and suggests conditions of around 13.3–15.7 kbar and 630–780 °C. This estimate can be coupled with K-feldspar composition (X_{Na} ~ 0.14-0.15) to obtain more tightly constrained

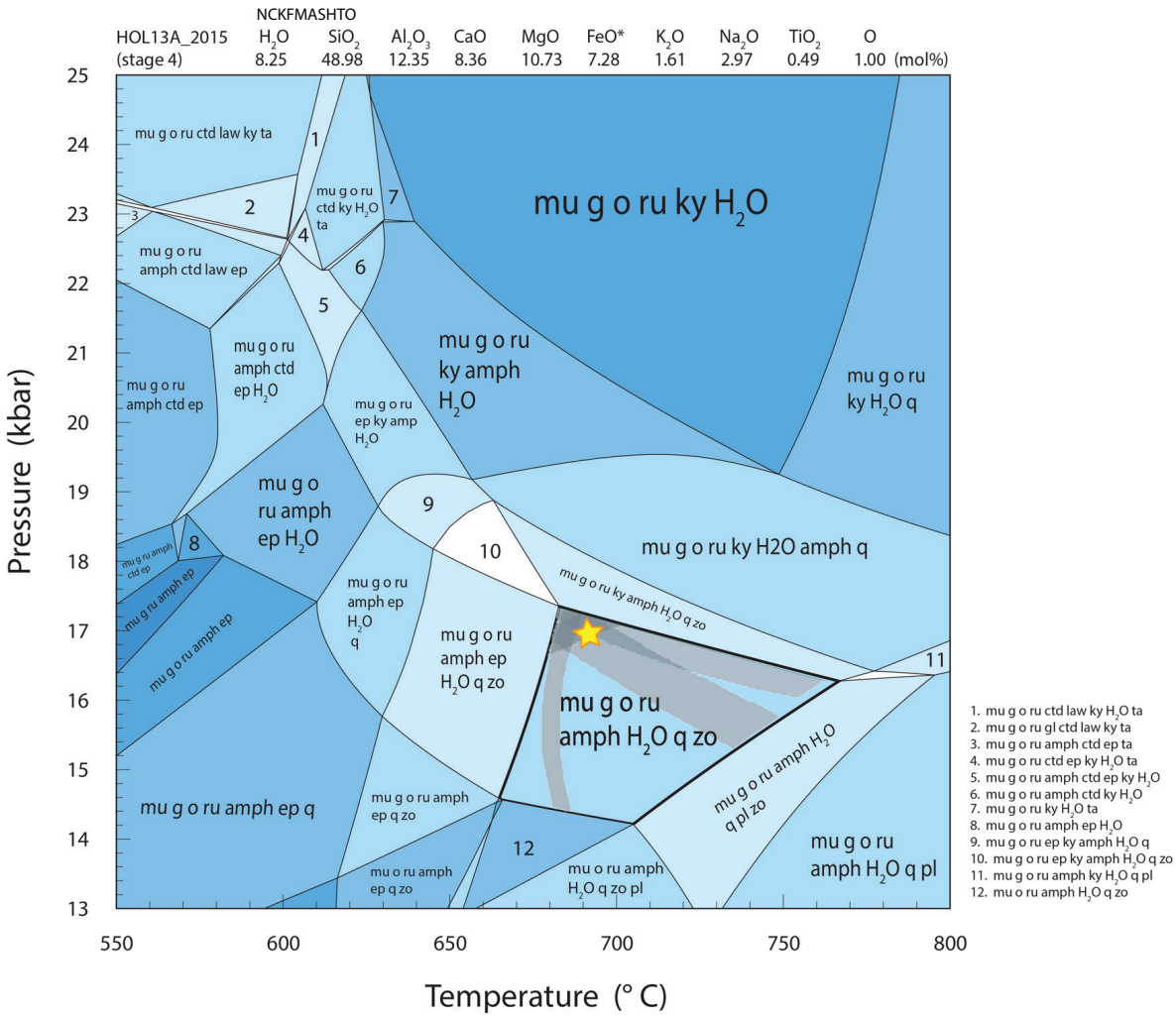

Figure 11. (a) Calculated *P–T* pseudosection for retrogressed eclogite, sample HOL13A_2015. The bulk composition at the top of the model is expressed as mol %. The white fields have a variance of two while the fields with darkest shade of blue have variance of seven. Mineral abbreviations used from Holland and Powell (1998). Note: very were small fields were not labelled. The bold outline indicates peak mineral assemblage and yellow star designates approximate *P–T* conditions. Abundances for omphacite, quartz, zoisite are overlain as grey regions. The peak conditions are more tightly constrained at 16–17 kbar and 680–700 °C where the isopleth ranges overlap in the peak field, indicated by the yellow star.

P–T conditions of around 15.2 –15.7 kbar at ~ 680 °C (Figure 9; individual contour plots provided in Figure S1.7).

4.3.2 HOL7C_2014 (peak eclogite; stage 3)

The phase equilibria model for HOL7C_2014 shown in Figure 10 was calculated using a modified (i.e. with the relict granulite garnet removed; Table 2) bulk composition. The stage 3 peak metamorphic assemblage phengite–garnet–omphacite–rutile–zoisite–kyanite–(free H_2O) lies in the range 21 to >30 kbar and 665 to >800°C. Although we cannot demonstrate that H_2O was present in the peak assemblage, the sample contains pervasive, volumetrically minor retrograde symplectites comprising amphibole and plagioclase that formed principally at the expense of omphacite. Tentatively, the presence of this hydrous retrograde assemblage may provide some support for the presence of a pore-scale fluid within the peak assemblage.

The modelled peak assemblage *P–T* field is large, and as such provides only limited constraints. However, the peak *P–T* estimates can be improved using contours of mineral abundance, in concert with measured mineral chemistry. The measured compositional isopleths corresponding to z(g) of 0.26–0.29, x(o) of 0.10–0.13 and j(o) =of 0.48–0.50 are overlain as faded grey areas on Figure 10 (individual contours are provided in Figure S1.8). Although these compositions cover a large portion of the *P–T* model, they do intersect within the peak assemblage field, which constrains the peak *P–T* conditions for this sample more tightly to approximately 21–22 kbar and 670–690 °C.

4.3.3 HOL13A_2015 (retrogressed eclogite; stage 4)

The peak metamorphic assemblage phengite–garnet–omphacite–rutile–amphibole–zoisite–quartz–(free H_2O) occurs in the range 14.0–17.5 kbar and 650–760 °C (Figure 11). To further constrain the peak conditions, the modal proportions of phengite, omphacite, quartz and zoisite (isopleths presented in Figure S1.9) within the peak assemblage were plotted as grey shaded regions on Figure 11, where they coincide in the top left corner of the peak mineral assemblage field. The more tightly constrained *P–T* conditions occur in the range of 16–17 kbar and 680–700 °C.

5. DISCUSSION

The aim of this study is to provide a *P–T* framework (i.e. burial and exhumation) for the fluid assisted conversion of granulite to eclogite recorded on Holsnøy Island in the northern Bergen Arcs. The *P–T* conditions presented here are linked to the different stages of the deformational evolution that have been described in detail by Austrheim (2013). However, before linking the different *P–T*

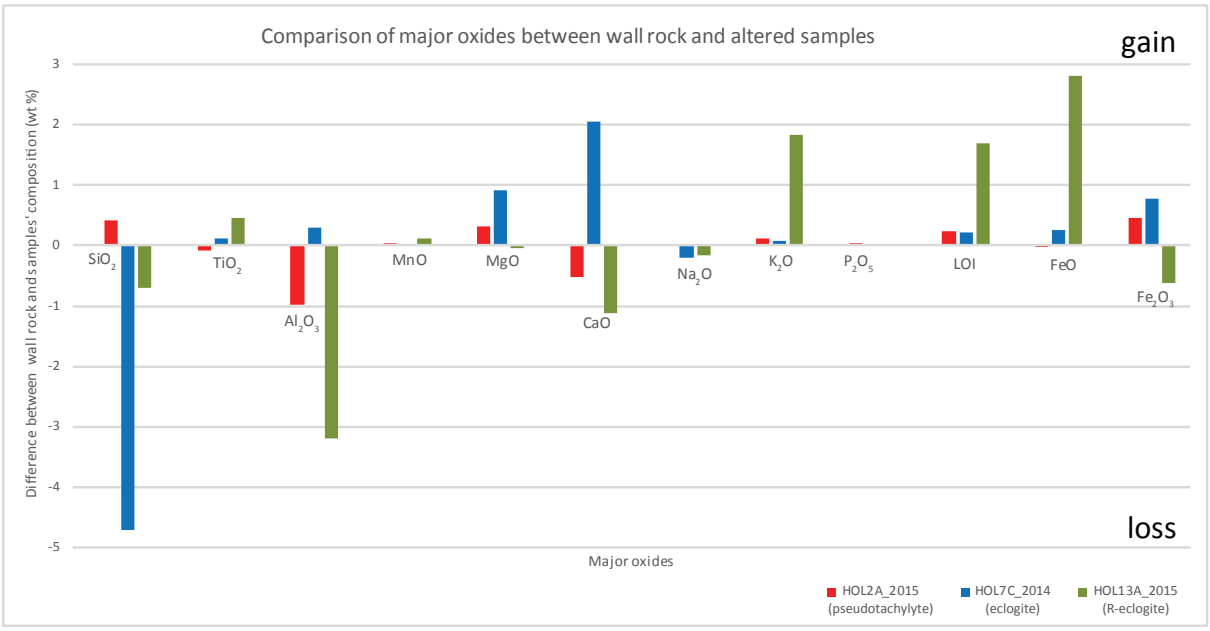

Figure 12. Figure comparing different elements in altered domains and their wall rocks. The chart represents the difference in major elements between the recrystallised pseudotachylite, peak eclogite and retrogressive eclogite and the adjacent granulite. Positive figures represent element 'gains' and negative values represent element 'loss' with respect to the wall rock. Original compositions for the wall-rock and altered rocks are provided in the supplementary data, Table S1.2.

conditions that were calculated in this study, it is essential to assess the validity of phase equilibria modelling for the rocks on Holsnøy Island.

5.1 Application of phase equilibria modelling on Holsnøy Island

The underlying assumption of the mineral equilibria modelling shown in the previous sections is that mineral growth occurs via equilibrium processes within a constant bulk rock composition. Indeed, it is this notion of a closed system requirement that underlies a duality in thinking when applying mineral equilibria modelling to mineral assemblages. For example, the application of melt reintegration modelling to investigate the petrological evolution of granulite (Anderson *et al.*, 2012; Brown, 2007; Korhonen, Brown, Clark, & Bhattacharya, 2013) seeks to adjust the bulk composition of a rock via sequential addition of melt to explain the development of minerals that may have formed before the currently preserved bulk composition of the rock was created. In this way open system behaviour is addressed in a mechanical and user-defined manner.

For the rocks exposed on Holsnøy, it is evident that open system behaviour has played an essential role in the transformation of anorthositic granulite to eclogite (Austrheim, 2013). At the outcrop scale, the manifestation of this open system behaviour is dramatic, with the formation of hydrous high-*P* amphibolite and eclogite domains at the expense of nominally anhydrous garnet–clinopyroxene–orthopyroxene-bearing anorthosite. However, despite clear petrological differences between the protolith and the fluid affected rocks, there is surprisingly little difference in the major element chemistry between the eclogite domains and their wall rocks (Figure 12; Kühn, 2002; Schneider, Bosch, Monié, & Bruguier, 2007). For the samples used in this study, major element comparisons between the protolith granulite and the immediately adjacent sampled recrystallised rock are shown in Figure 12. For the recrystallised pseudotachylite sample HOL2A_2015, it is evident that there is little compositional change compared to the granulite protolith, suggesting an invariant bulk composition during rock recrystallization. However, for the peak metamorphic eclogite sample HOL7C_2014 and interpreted retrograde sample HOL13A_2015, it is evident that compositional changes have occurred. For HOL7C_2015, the eclogite is less silicious and more calcic than its protolith, although based on the loss of ignition (LOI; Table 1; Figure 12), is not significantly more hydrated. In HOL13A_2015, based on LOI, the sample is much more hydrous than its protolith, as well as significantly more Fe-rich and potassic.

It is beyond the scope of this paper to undertake an detailed analysis of the chemical changes associated with the conversion of granulite to eclogite. However, the critical question is to what extent the rock composition changed while the petrologically observed mineral assemblage formed. Schneider *et al.* (2007) undertook an evaluation of scales of chemical equilibrium within

samples that correspond to our stage 2 and stage 3 recrystallisation, concluding that samples at thin section scale did not operate as an equilibrium system. This was most evident in the sample that corresponds to stage 2, which displays complex symplectitic coronas around garnet that reflect microscale chemical domains. Because of these textural complexities and their associated microchemical domains, we chose not to model the stage 2 assemblages. However, for a sample of omphacite-rich eclogite which, corresponds to our stage 3 assemblage Schneider *et al.* (2007) determined that mineral compositions showed comparatively little variation. Notably, compositional variation in minerals like phengite was associated with the formation of volumetrically minor secondary retrograde phengite, rather than the formation of prograde micro-chemical domains. In our stage 3 sample, aside from garnet, we also find comparatively little compositional variation in mineral chemistry.

In the case of recrystallised pseudotachylite sample HOL2A_2015, it appears that little chemical change occurred between the protolith and the recrystallised rock (Figure 12). In eclogite sample HOL7C_2014, there is a strong foliation with a mineral assemblage distribution that shows no textural evidence for sequential or spatially heterogeneous mineral growth, veining, or other textural criteria that would suggest a progressive change in bulk composition occurred during the formation of the currently preserved mineral assemblage. Aside from compositional zoning in the garnet overgrowths surrounding relict protolith garnet, which could reflect the evolving *P–T* conditions, minerals such as omphacite, zoisite and phengite show little compositional variation. We suggest that the lack of obvious sequential mineral growth and compositional zonation reflects a comparatively established bulk composition during the growth of the preserved mineral assemblage. Similarly in HOL13A_2015, there are no systematic mineral textures that point to preservation of fluid-infiltration driven reaction fronts, and the mineral grains (aside from the relict granulite garnet cores) show little zoning. Again we suggest this could be interpreted to reflect a comparatively established bulk composition during the formation of the mineral assemblage in the sample.

Therefore, while we acknowledge that open system behaviour clearly drove the transition of granulite to eclogite, the evidence points to open system processes either establishing an altered bulk composition prior to the growth of the mineral assemblages, or to primarily modifying the hydrous content of the rock (e.g. Bjørnerud, Austrheim, & Lund, 2002; Boundy *et al.*, 1997; Kühn, 2002; Schneider *et al.*, 2007). In this context, Austrheim (1990), Boundy *et al.* (1992), Austrheim *et al.* (1997) and Bjørnerud *et al.* (2002) suggested that the conversion of anhydrous granulite into eclogite was rapid in terms of rate process (see also Camacho, Lee, Hensen, & Braun, 2005). We take the axiom that while some bulk rock compositional change may have occurred subsequent to the mineral growth in the samples we have selected,

insufficient bulk rock compositional change occurred to modify the mineral assemblages. Indeed, the character of the Holsnøy granulite to eclogite transition points to a fluid triggered, but then typically fluid abandoned system, preserving metastable compositional domains that are effectively snapshots of open system modification (see below). Therefore, for the purposes of *P–T* forward modelling, the samples as preserved are effectively quasi-closed systems, and the application of phase equilibria modelling is a valid approach to evaluate the *P–T* conditions of the system, via the careful selection of samples constrained by field relationships that indicate the assemblages formed at different times in the thermobarometric evolution.

A second issue that must be addressed in applying mineral equilibria modelling is the selection of an appropriate bulk composition. Where a rock is texturally homogeneous, and contains unzoned minerals, the choice of an appropriate bulk composition is comparatively straightforward (e.g. Kelsey & Hand, 2015). However, in rocks that are texturally complex, or contain relicts of unreacted protolith minerals, the selection of an appropriate bulk composition is less straightforward (Guevara & Caddick, 2016; Kelsey & Hand, 2015; Stüwe, 1997).

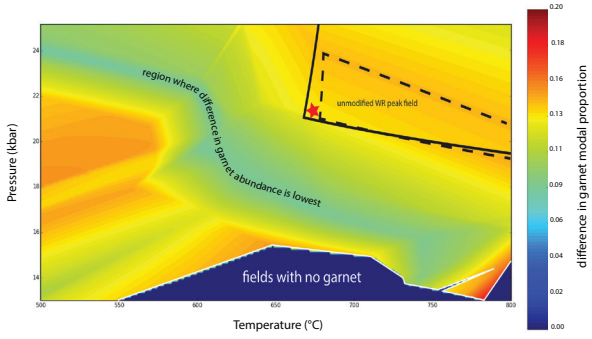

Figure 13. Contour plot showing the difference in garnet abundance across *P–T* space for HOL7C*_2014 and HOL7C_2014 (Table 2). The field outlined by the dashed line represents the peak field in the model using the original, unmodified whole-rock composition. The solid line outlines the peak in the modified composition model and the star indicates the peak conditions modelled using the modified compositions. Red shades represent high differences in garnet abundance between the two models whereas blue shades represent lower differences in abundance. Garnet abundance is presented as a fraction on the scale bar.

For the rocks on Holsnøy Island, while stage 3 mineral assemblages are mesoscopically and microscopically homogeneous, compositional imaging (e.g. Figures 7a, b) shows that the garnet grains contain a compositionally distinct core and rim. This has also been described in numerous previous studies (e.g. Austrheim & Griffin, 1985; Pollok *et al.*, 2008; Russell *et al.*, 2012). Petrographically, some of the garnet cores in the recrystallised samples contain inclusions of coarse-grained spinel (Figure S1.6). Spinel inclusions within garnet are sparse, but widespread within the granulitic protolith. Therefore, we interpret the compositionally distinct garnet cores in eclogite to be relict domains inherited from the granulite protolith. The distinct compositional contrast between the garnet cores and overgrowths suggests the garnets did not contribute significantly to the effective reactive bulk composition comprising the stage 3 eclogite assemblages.

In an attempt to investigate if incorporation of the relict garnet cores exerts a significant influence on the modelled phase relations, the unmodified whole-rock composition for HOL7C_2014 (Table 2; HOL7C*) was modelled and compared with a modified

composition in which the garnet cores have been removed (also Table 2). The comparison between the two bulk compositions is shown in Figure 13. It shows the difference in the abundances of garnet throughout the modelled *P–T* window for the two bulk compositions. It is evident there is only a narrow domain in *P–T* space where the difference in abundance is low (pale blue strip extending across the model from top left corner to bottom right). The peak fields for the two modelled compositions are also plotted on Figure 13 and show a significant difference, which supports the notion that modelling a simple overall bulk rock composition, when it is evident there are compositionally refractory domains, may give rise to biased *P–T* estimations (Marmo, Clarke, & Powell, 2002; Palin, Weller, Waters, & Dyck, 2015; Ren *et al.*, 2016). This highlights a general principle in *P–T* modelling that bulk compositions should be defined only by the minerals that formed from the effective chemical system (Kelsey & Hand, 2015; Stüwe, 1997). In the case of stage 3 mineral assemblages on Holsnøy Island, we suggest that the bulk composition defined by the homogeneously distributed assemblage, including the garnet overgrowths is a defensible bulk composition for modelling.

It is evident from Figure 7c, d that the retrogressed phengite-rich sample, HOL13A_2015, contains relict domains within garnet that are probably also inherited from the granulite protolith. However, in contrast to HOL7C_2014, the garnet in HOL13A_2015 is much smaller (typically 0.2–0.9 mm in diameter), the compositional difference between core and rim is more diffuse, and the rim domains are correspondingly a much greater proportion of the overall garnet volume and composition compared with HOL7C_2014. Additionally, garnet only comprises ~ 11% of the assemblage, making the relict cores a small proportion of the overall bulk composition. For this reason we have taken the bulk thin-section rock block geochemistry as a reasonable approximation of the effective bulk composition of the sample.

Last, a potential limitation of the mineral equilibria modelling is that the predicted presence of fluid in the peak and post-peak metamorphic assemblages relates to a pure H_2O fluid. In particular for the post peak assemblage in HOL13A_2015, the clear increase in bulk rock K_2O content with respect to the protolith granulite attests to a non-pure-H_2O fluid. To what extent such brine-like fluids change the modelled *P–T* conditions is not clear.

5.2 *P–T* evolution

It is important to note when looking at the *P–T* models depicted in Figures 10 and 11, that the modelled samples did not undergo a petrologically recorded prograde path. This is because the metastable protolith granulite did not undergo any reaction unless fluid was available. Therefore, although the Lindas Nappe almost certainly underwent burial through a *P–T* evolution that would have stabilised prograde garnet-bearing assemblages, those assemblages in reality never formed be-

cause they were kinematically unfavourable in fluid-absent rocks. The absence of any obvious prograde mineral textures or prograde mineral zoning in the samples means that the vast bulk of the mineral assemblage fields depicted in Figure 10 are unlikely to have ever formed on the prograde path. Instead, we can only infer with certainty the current mineral assemblage of each sample existed. Given the apparent importance of fluid availability to create a reactive bulk composition, the generally well-preserved nature of the high-*P* assemblages used in this study points to little or no on-going fluid availability after the preserved assemblages formed. In this case, deriving a *P–T* evolution for the Lindas Nappe is effectively provided through a series of *P–T* snapshots, rather than the continuously recorded petrological evolution in one sample. The inferred *P–T* conditions for the recrystallised pseudotachylite, eclogite and retrogressed eclogite are summarised in Figure 14.

Our peak *P–T* conditions are broadly similar to those derived from conventional thermobarometry and average *P–T* approaches (Jamtveit *et al.*, 1990; Raimbourg *et al.*, 2007). However, we note that in several of these earlier studies (e.g. Austrheim & Griffin, 1985; Mattey *et al.*, 1994), plagioclase-bearing equilibria were used even though the peak eclogite assemblage does not contain plagioclase.

The oldest structures that overprint the Neoproterozoic granulite are a series of small scale pseudotachylites and associated brittle structures. The pseudotachylites have recrystallised to fine-grained metamorphic assemblages (Figure 4b). These recrystallised pseudotachylites were the focus of previous studies (Austrheim & Boundy, 1994; Austrheim *et al.*, 1996; Austrheim *et al.*, 2017), and were interpreted to be the record of seismic events that occurred at eclogite facies at *P–T* conditions of 18–19 kbar and ~800 °C during the Caledonian Orogeny. These conditions were calculated using conventional thermobarometry on omphacite–garnet pairs. The formation of the pseudotachylites was interpreted to be the result of fast relaxation of stresses owing to fluid induced eclogitisation of the granulite (Austrheim & Boundy, 1994) as the volume of the domains converted to eclogite decreased. However, based on field relationships and mineral assemblages within the *recrystallised* pseudotachylites, and the fact that the age of the brittle deformation is unknown, it is difficult to unambiguously deduce whether they were formed during the later stage of the Grenvillian Orogeny, the early stages of the Caledonian Orogeny or in the interval between the two. The critical *P–T* information provided by the mineral assemblage within the recrystallised pseudotachylite is that it places upper constraints on the depth of the brittle deformation, which is not necessarily a close constraint for the depth of the deformation itself. The modelling of the assemblage garnet–K-feldspar–plagioclase–kyanite–quartz–omphacite–zoisite–rutile in the recrystallised pseudotachylite does not provide precise *P–T* constraints. However, based on the relative

timing of the pseudotachylite formation (described previously) and the *P–T* conditions of the complete conversion of the granulite to eclogite (see below), we conservatively suggest that the *P–T* conditions at which the pseudotachylite recrystallised was no greater than that modelled for the peak metamorphic eclogites. In this case, the maximum *P–T* for the formation of pseudotachylites would be less than 22 kbar and 700 °C, which are our peak eclogite conditions. This is reflected in the model (Figure 9) where a *P–T* range of 15.2–15.7 kbar and 675–685 °C was calculated for the recrystallisation of the pseudotachylite. This estimate contrasts with previous ones which suggested *P–T* conditions of 18–19 kbar and 800 °C for pseudotachylite (Austrheim & Boundy, 1994; e.g. Lund, Austrheim, & Erambert, 2004). Additionally, the presence of abundant sodic plagioclase in the recrystallised pseudotachylite (Table 4) suggests that it recrystallised at high-pressure amphibolite or granulite grade conditions (De Paoli, Clarke, Klepeis, Allibone, & Turnbull, 2009; Ringwood & Green, 1966; Zhang, Liou, Zheng, & Fu, 2003), rather than eclogite facies conditions as previously suggested (Austrheim & Boundy, 1994). Irrespective, aside from a maximum possible pressure, there are no constraints on the pressure (depth) of the pseudotachylite formation, and no structural evidence they formed at eclogite facies conditions.

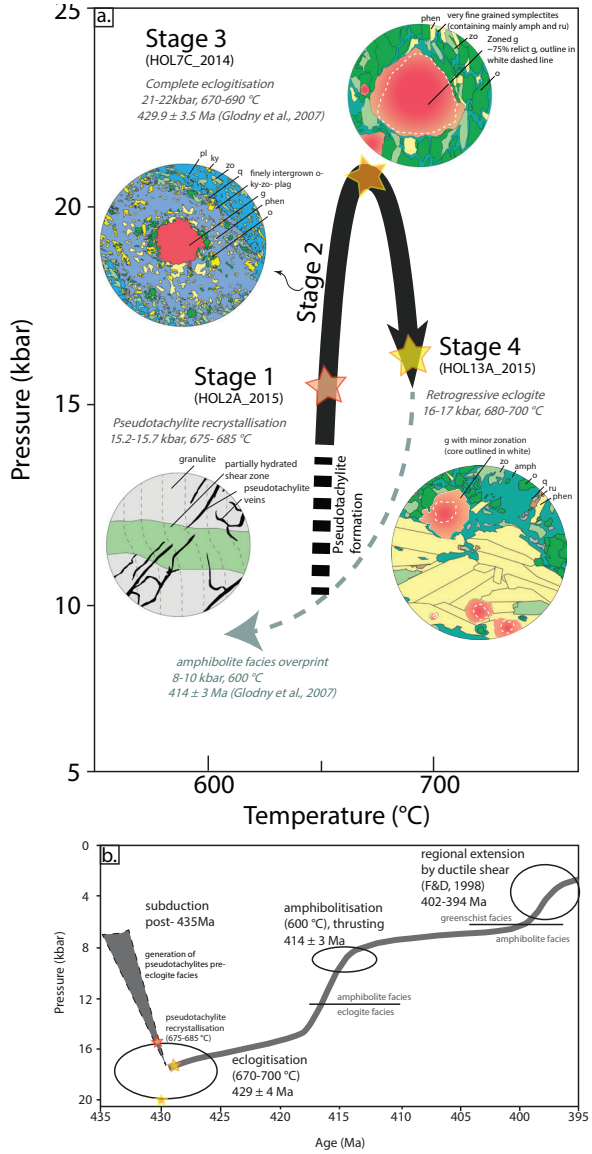

Figure 14. (a) *P–T* path recorded by Holsnøy Island lithological domains based on the calculated *P–T* pseudosections derived from sample HOL2A_2015 (Figure 9), sample HOL7C_2014 (Figure 10), and sample HOL13A_2015 (Figure 11). The stars represent the approximate inferred peak metamorphic conditions for each of the 3 modelled stages. The figure also depicts different metamorphic textures occurring in the different stages of deformation. (b) Figure modified from Glodny *et al.* (2008) depicting the metamorphic evolution of the Holsnøy system. Circles represent extent of their calculated ages.

Based on the maximum pressure constraint, the notion that pseudotachylite recrystallisation occurred under comparatively low-*P* conditions is consistent with the overprinting structural relationships and metamorphic assemblages. The recrystallised pseudotachylites are overprinted by small-scale shear zones (stage 2) associated with hydrous alteration that defines the classic metasomatic alteration on Holsnøy (Figure 3b) that has been described by numerous authors (e.g.

Austrheim, 2013; Jamtveit *et al.*, 1990; Van Wyck *et al.*, 1996). Although this metasomatism is associated with the growth of sodic clinopyroxene, a notable feature in these altered domains is the modal decrease of garnet compared to the granulite protolith. These alteration zones also commonly contain abundant plagioclase that forms part of the recrystallised assemblage, and so stage 2 shear zones do not define eclogite assemblages (Figure 6). Therefore, it is unlikely that the pseudotachylites formed at eclogite facies conditions. A notable feature of stage 1 and stage 2 (Figure 4b) deformation is the extensive fracturing of garnet grains in the granulitic wall rock and in the shear fabric of the altered domain, respectively. These fractured garnets and their compositional response to the high-*P* reworking have been the focus of several studies (Erambert & Austrheim, 1993; Jamtveit *et al.*, 1990; Raimbourg *et al.*, 2007; see below).

Overprinting the stage 2 plagioclase-bearing alteration zones are domains of pervasively recrystallised plagioclase-free rock (stage 3) with the metamorphic assemblage phengite–garnet–omphacite–rutile–kyanite–zoisite, which defines a true eclogite assemblage. These domains form kilometre-scale zones in which an anastomosing foliation envelops relict granulite blocks, creating a structural domain previously referred to as the eclogite "breccia" (Austrheim, 2013). These "breccia" domains are marginal to a system of high-strain zones that were interpreted to have been formed during NW–SE tectonic transport (Raimbourg *et al.*, 2005). Peak metamorphic conditions modelled for eclogite (HOL7C_2014) in these high-strain zones are constrained to around 21–22 kbar and 670–690°C (Figure 10). These new estimates are in general agreement with the higher-*P* and lower-*T* estimates made from conventional thermobarometry (18–21 kbar and 650–800 °C; (Austrheim, 2013; Austrheim & Griffin, 1985; Jamtveit *et al.*, 1990; Pollok *et al.*, 2008). However, there are numerous pitfalls associated with using conventional thermobarometry. Most notably; (1) re-equilibration of mineral compositions with cooling; (2) only using a small subset of the total mineral assemblage for thermobarometry and (3) not knowing whether the derived *P–T* conditions actually occur within the stability field of the assemblage itself. However, the general agreement between conventional *P–T* calculations, which use small-scale mineral pairs (effectively microdomains) and our more general bulk compositionally based forward *P–T* modelling suggests the rock system is compositionally and mineralogically amenable to *P–T* modelling.

The high-strained stage 3 domains are locally overprinted by smaller scale domains that contain coarse-grained phengite-rich mineral assemblages. Forward modelling of sample HOL13A_2015 (Figure 11) which was selected from one of these zones suggests that this post-peak, fluid-rich assemblage recrystallised at around 16–17 kbar and 680–700 °C. The calculated conditions are close to the estimates of peak *P–T* conditions from earlier studies (Austrheim & Griffin, 1985) for high-*P* retrogression of the eclogites.

While it cannot be unequivocally established, the precedent of existing studies (Austrheim, 2013; Austrheim & Boundy, 1994; Jamtveit *et al.*, 1990) suggests that the modelled mineral assemblages all formed during the Caledonian Orogeny between c. 460–430 Ma. Assuming this interpretation is valid, the *P–T* conditions recorded by each of the three samples are linked in sequence by a simple *P–T* evolution path. The interpreted *P–T* path for the Holsnøy eclogites and the associated metasomatic process is shown in Figure 14 and defines a clockwise evolution. If the retrograde path continued along a trajectory of decreasing pressure with further cooling, the rocks would track into the amphibolite facies. Amphibolite facies reworking of eclogites is documented elsewhere in the Bergen arcs and on Holsnøy Island (Andersen, Austrheim, & Burke, 1991a; Andersen *et al.*, 1991b; Bingen *et al.*, 2001; Boundy *et al.*, 1992; Engvik *et al.*, 2000; Glodny *et al.*, 2008; Raimbourg *et al.*, 2005). Despite the record of amphibolite facies reworking, the excellent preservation of the granulite to eclogite transition on northern Holsnøy likely reflects a domain that saw fluid flow in the early to mid-stage of the Caledonian Orogeny. However, the system was then starved of fluids, allowing for the excellent preservation of the high-*P* mineral assemblages.

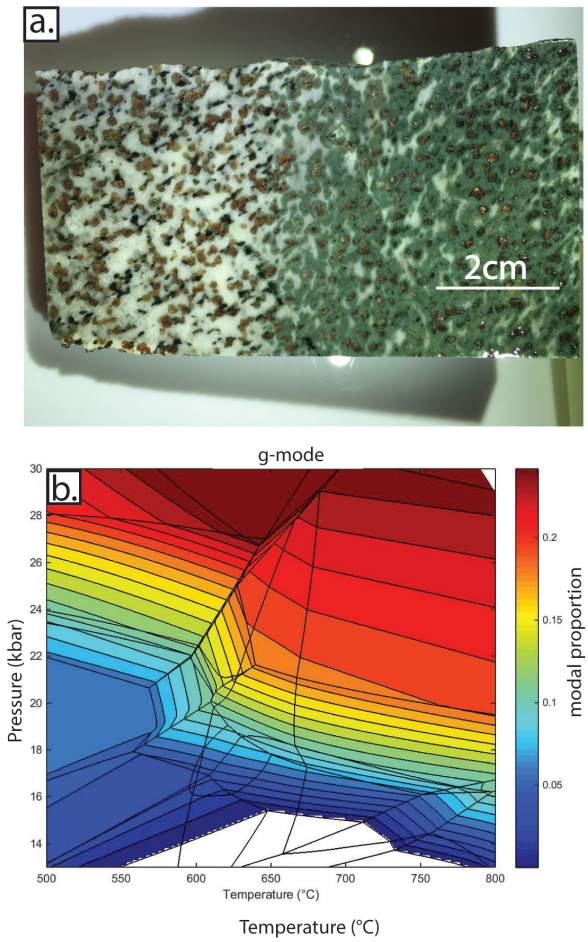

Figure 15. Figure showing (a) decrease in garnet abundance from granulite (white domain) to eclogite (green domain); (b) Plot constructed using TCInvestigator showing the variation of garnet abundance throughout *P–T* space for sample HOL7C_2014. Garnet abundance is presented as a fraction on the scale bar.

5.3 *P–T* constraints and fluid infiltration

A large number of studies have focussed on the role of fluids in facilitating the transition of granulite to eclogite in the Bergen Arcs, and on Holsnøy in particular (e.g. Austrheim, 1987, 1998, 2013; Boundy *et al.*, 1997; Glodny *et al.*, 2008; Jamtveit *et al.*, 1990; Kühn, 2002; Van Wyck *et al.*, 1996). However, the majority of these studies have not evaluated the fluid ingress in a progressive context. Instead fluid, ingress has generally been considered to have occurred at around peak conditions and continued during the retrograde evolution, leading to the development of extensively developed retrograde amphibolite facies assemblages (Bingen *et al.*, 2004; Glodny *et al.*, 2008; Raimbourg *et al.*, 2005) in many places. Fluid ingress appears to have been channelized along zones of fracture- and

shear zone- hosted permeability leading to a volume of at least several cubic kilometres of infiltrated rocks (Austrheim, 2013; Jamtveit *et al.*, 1990). However, the generally low variance of the fluid associated mineral assemblages, and the limited geochemical changes between the protoliths and the recrystallised rocks (Kühn, 2002) suggests that fluid–rock ratios were generally low.

This study does not focus on the fluid–rock interaction specifically or the source of the fluids, but, implicit in the descriptions of the metamorphic assemblages that characterise structural stages 1–4 is that fluid was present during burial before the peak metamorphic eclogitic facies assemblages formed. This is evident from mineral assemblages developed within the recrystallised pseudotachylite that formed during structural stage 1. These assemblages are characterised by the development of phengite and zoisite. While the *P–T* constraints on the development of the mineral assemblages within the recrystallised pseudotachylite are not as precise as would be ideal, within the probable range of temperature constraints, fluid was apparently available in the comparatively early stages of the prograde path to create hydrated mineral assemblages. The low abundance of hydrous minerals in the recrystallised pseudotachylite assemblage, combined with the fact that its chemistry is similar to the host granulite, suggest the fluid came from the granulite instead of an external source reservoir. The fluid may have been derived from pore spaces in the granulite, or in the lattice of nominally anhydrous minerals such as garnet, clinopyroxene and plagioclase (Chen *et al.*, 2007; Müller & Koch-Müller, 2009; Sheng, Xia, Dallai, Yang, & Hao, 2007).

Structurally, stage 2 is characterised by the formation of narrow domains of altered granulite. These may flank thin quartz veins, or occupy the cores of meso-scale low strain kink bands and minor ductile shear zones (Austrheim, 2013). In this study we have not focussed on this stage of recrystallization. However, petrologically stage 2 is characterised by the breakdown of garnet inherited from the granulite protolith to fine-grained symplectic assemblages consisting of omphacite–zoisite–phengite–kyanite (Figure 6); that occur within a matrix of foliated zoisite and recrystallised plagioclase. Modally within these reaction textures, hydrous minerals comprise around 20 % of the replacement minerals, and the surrounding matrix may contain up to 25 % zoisite. The modal abundance of garnet typically undergoes ~30–40 % reduction relative to the protolith granulite (Figure 15a). As with the recrystallised stage 1 pseudotachylite assemblages, petrologically the stage 2 assemblages are not eclogitic because they contain abundant recrystallised plagioclase.

Although the bulk compositions of fluid-affected rocks of stage 2 and stage 3 (peak eclogite stage; sample HOL7C_2014) are different, the difference is not significant (Table 1; Figure 12). This means that the general mineralogical relationships and associated trends in garnet modal abundance proportions, from HOL7C_2014 shown in Figure

15b could act as a general guide to the metamorphic character of stage 2. For example, in most metamorphic systems, the modal abundance of garnet is strongly positively correlated with pressure (Caddick, Konopásek, & Thompson, 2010; Spear, Selverstone, Hickmott, Crowley, & Hodges, 1984; Tracy & Robinson, 1976) as shown in Figure 15b. Figure 15 and the structural history of the different stages of deformation can be used as proxies to estimate where stage 2 occurred in *P–T* space. Figure 15a is a section across the granulite to the stage 2 high-*P* amphibolite transition, which shows that the abundance of garnet significantly decreases in the zone of alteration (i.e. in the presence of fluids). Garnet is partially replaced by fine-grained symplectites composed of omphacite, kyanite, zoisite and plagioclase (Figure 6). Based on Figure 15b, lower abundance of garnet is present at pressures between 16–20 kbar, unless at temperatures below 650 °C. However, since the temperature reached by the recrystallised pseudotachylite assemblage is ~ 685 °C, the colder parts of *P–T* space are not applicable for stage 2. Therefore, it can be inferred that the fluid–rock interaction in stage 2 of deformation occurred at pressures below the inferred peak pressure of ~22 kbar derived from stage 3 mineral assemblages. Moreover, based on the presence of abundant recrystallised plagioclase, fluid ingress occurred before the rock entered the petrological eclogite facies as the maximum pressure at which plagioclase is stable is at ~16.5 kbar (Figure 10).

Stage 3 assemblages form the peak metamorphic (eclogite) assemblages preserved on Holsnøy. They are characterised by true eclogite assemblages that lack plagioclase, but still contain abundant phengite and zoisite. Unlike the preceding stage 2 assemblages, stage 3 assemblages show clear evidence for the growth of new garnet which forms rims on the relict protolith garnets (Figure 7b), thus reversing the reduction in garnet modes evident at stage 2. The progressive structural and mineralogical development culminating in the development of hydrated plagioclase-free stage 3 mineral assemblages implies that fluid infiltration occurred either continuously or sporadically during prograde burial, once the granulitic slab had approximately reached mantle depths. It is difficult to unambiguously demonstrate that progressively more channelised fluid flow culminated in the development of the peak stage 3 assemblages (as opposed to a new and comparatively high flux fluid ingress). However, even within domains dominated by stage 3 assemblages, relict granulite blocks have gradational margins with the enclosing eclogite, and internally contain stage 2 structural features and assemblages (Figure 2c). This suggests that stage 3 assemblages may have progressively developed as fluid flow either increased, or became more structurally focused. The preservation of stage 2 assemblages in close proximity to stage 3 assemblages also implies that fluid infiltration was not pervasive. Rather it suggests that fluid ingress was channelized and/or approximately balanced by consumption

to form the hydrous mineral assemblages, leaving little fluid to catalyse stalled stage 2 reaction assemblages.

The excellent preservation of the granulitic protolith away from areas of obvious fluid mediated recrystallisation highlights the importance of the catalysing effects of fluids. This is further underscored by the comparatively minor bulk rock compositional changes associated with fluid ingress (Schneider *et al.*, 2007; Table 1 and Figure 12). The preservation of the protoliths in areas of comparatively minor (or essentially non-existent) fluid ingress, illuminates an important facet of the Holsnøy system, that is, if fluid ingress ceased into a specific volume, the affected volume essentially froze in its mineralogical state, thereby preserving a snap shot of the system at a point in time. This means that judicious sampling, could effectively discretise the prograde and conceivably the retrograde evolution.

The source(s) of the fluid are beyond the scope of this study. However, based on an assumed mantle reservoir of around $d^{13}C$ -5 ‰ and a shift from comparatively heavy to lighter carbon isotopes accompanying eclogitising of the granulites, Mattey *et al.* (1994) suggested the source of fluid was the dehydration of sedimentary rocks below the granulites. A number of studies (see review by Deines, 2002) have also shown that mantle carbon isotopes are essentially bimodal in composition with peaks at around $d^{13}C$ -5 ‰ and $d^{13}C$ -25 ‰, indicating that the recorded carbon isotope shift associated with the eclogitising fluids on Holsnøy do not preclude a mantle source for the fluids. However, the evidence points to a system that underwent protracted fluid–rock interaction as expressed by the record of fluid–rock interaction that began during prograde burial. This suggests that fluids were, potentially, derived from a source that underwent progressive dehydration, and therefore a source that accompanied the granulites during subduction.

5.4 Duration of fluid-rock interaction

Erambert and Austrheim (1993) and Raimbourg *et al.* (2007) used the diffusional response of garnet in the Lindås Nappe to explore the potential timescales associated with the conversion of the anorthositic granulite to eclogite. They identified two different modes of garnet response; (1) protolith garnets that underwent fracturing and diffusional modification and (2) garnet that grew during high-*P* metamorphism. Fracturing of garnet was associated with the development of stage 1 and stage 2 structures that formed during the prograde evolution, whereas new garnet growth occurred during stage 3, and overprinted fractured garnets that had already been diffusionally modified (Raimbourg *et al.*, 2007). Using a range of different estimates for garnet diffusion coefficients and an assumed temperature of 700°C, calculated timescales for diffusion range between 0.7–12 Ma (Erambert & Austrheim, 1993; Raimbourg *et al.*, 2007), which provides a guide to the potential duration between the time garnet grains fractured and the time that new garnet grew during the metamorphic

peak. Based on the diffusional response of garnet, the bulk of the fluid rock interaction appears to have occurred on time scales of no more than several million years, and potentially significantly less.

6. CONCLUSIONS

Holsnøy Island in the Bergen Arcs, Norway, contains a well-documented record of fluid catalysed conversion of early Neoproterozoic nominally anhydrous anorthositic granulite to hydrous eclogite associated with Caledonian-aged (c. 450 Ma) subduction of continental crust. Prograde burial is recorded by a sequence of mineral assemblages that record the progressive loss of plagioclase as burial and hydration proceeded. The earliest recorded prograde mineral assemblages formed during the recrystallization of structurally early pseudotachylite. *P–T* modelling shows the assemblage is not particularly *P–T* sensitive, but is likely to have recrystallised at conditions between 15.2–15.7 kbar at 675–685 °C, suggesting that the pseudotachylite must have formed below these conditions. The recrystallised pseudotachylite was overprinted by low-strain deformation zones associated with prominent hydrous recrystallisation. The peak eclogite assemblages (i.e. stage 3) are recorded by kilometre-scale domains of foliated eclogite that formed around 22 kbar and 680 °C. The peak assemblages are overprinted by localised phengite-rich assemblages that formed during high-*T* retrogression at around 16–17 kbar and 680–700 °C. The sequentially developed mineral assemblages and *P–T* constraints show that the granulite experienced long-lived (prograde, peak and retrograde) fluid driven recrystallisation during the subduction of anorthositic crust. The availability of fluid during burial and exhumation implies a fluid source that was able to progressively dehydrate during subduction of the granulites. Potentially this fluid source was derived from sedimentary sequences elsewhere in the subducting slab.

ACKNOWLEDGMENTS

Luke Hersey, Curtin University, is thanked for his help with the mapping part of the project. Ben Wade, Angus Netting and Aoife McFadden, Adelaide Microscopy, are also thanked for their assistance with the electron microprobe and SEM. Lastly, many thanks to Stephanie Wikan Tyiasning and Nigel Rees, University of Adelaide, for their invaluable help with Matlab and Python, respectively.

REFERENCES

Andersen, T., Austrheim, H., & Burke, E. A. J. (1990). Fluid inclusions in granulites and eclogites from the Bergen Arcs, Caledonides of W. Norway. Mineralogical Magazine, 54(375), 145-158.

Andersen, T., Austrheim, H., & Burke, E. A. J. (1991a). Fluid-induced retrogression of granulites in the Bergen Arcs, Caledonides of W. Norway: Fluid inclusion evidence from amphibolite-facies shear zones. Lithos, 27(1), 29-42.

Andersen, T., Austrheim, H., & Burke, E. A. J. (1991b). Mineral-fluid-melt interactions in high-pressure shear zones in the Bergen Arcs nappe complex, Caledonides of W. Norway: Implications for the fluid regime in Caledonian eclogite-facies metamorphism. Lithos, 27(3), 187-204. doi: http://dx.doi.org/10.1016/0024-4937(91)90012-A

Anderson, J. R., Payne, J. L., Kelsey, Da. E., Hand, M., Collins, A. S., & Santosh, M. (2012). High-pressure granulites at the dawn of the Proterozoic. Geology, 40(5), 431-434.

Austrheim, H. (1987). Eclogitization of lower crustal granulites by fluid migration through shear zones. Earth and Planetary Science Letters, 81(2), 221-232.

Austrheim, H. (1990). The granulite-eclogite facies transition: A comparison of experimental work and a natural occurrence in the Bergen Arcs, western Norway. Lithos, 25(1), 163-169.

Austrheim, H. (1998). Influence of fluid and deformation on metamorphism of the deep crust and consequences for the geodynamics of collision zones. When continents collide: Geodynamics and Geochemistry of Ultrahigh-Pressure Rocks (pp. 297-323): Springer.

Austrheim, H. (2013). Fluid and deformation induced metamorphic processes around Moho beneath continent collision zones: Examples from the exposed root zone of the Caledonian mountain belt, W-Norway. Tectonophysics, 609, 620-635. doi: 10.1016/j.tecto.2013.08.030

Austrheim, H., & Boundy, T. M. (1994). *Pseudotachylite*s generated during seismic faulting and eclogitization of the deep crust. Science, 265(5168), 82-83.

Austrheim, H., Erambert, M., & Boundy, T. M. (1996). Garnets recording deep crustal earthquakes. Earth and Planetary Science Letters, 139(1), 223-238.

Austrheim, H., Erambert, M., & Engvik, A. K. (1997). Processing of crust in the root of the Caledonian continental collision zone: the role of eclogitization. Tectonophysics, 273(1), 129-153.

Austrheim, H., & Griffin, W. L. (1985). Shear deformation and eclogite formation within granulite-facies anorthosites of the Bergen Arcs, western Norway. Chemical Geology, 50(1), 267-281.

Austrheim, H.., Dunkel, K. G., Plümper, O., Ildefonse, B., Liu, Y., & Jamtveit, B. (2017). Fragmentation of wall rock garnets during deep crustal earthquakes. Science Advances, 3(2), e1602067.

Baxter, E. F., & Caddick, M. J. (2013). Garnet growth as a proxy for progressive subduction zone dehydration. Geolo-

gy, 41(6), 643-646.

Bingen, B., Austrheim, H., Whitehouse, M. J., & Davis, W. J. (2004). Trace element signature and U–Pb geochronology of eclogite-facies zircon, Bergen Arcs, Caledonides of W Norway. Contributions to Mineralogy and Petrology, 147(6), 671-683.

Bingen, B., Davis, W. J., & Austrheim, H. (2001). Zircon U-Pb geochronology in the Bergen arc eclogites and their Proterozoic protoliths, and implications for the pre-Scandian evolution of the Caledonides in western Norway. Geological Society of America Bulletin, 113(5), 640-649.

Bjørnerud, M. G., Austrheim, H., & Lund, M. G. (2002). Processes leading to eclogitization (densification) of subducted and tectonically buried crust. Journal of Geophysical Research: Solid Earth (1978–2012), 107(B10), ETG 14-11-ETG 14-18.

Boundy, T. M., Essene, E. J., Hall, C. M., Austrheim, H., & Halliday, A. N. (1996). Rapid exhumation of lower crust during continent-continent collision and late extension: Evidence from $^{40}Ar/^{39}Ar$ incremental heating of hornblendes and muscovites, Caledonian orogen, western Norway. Geological Society of America Bulletin, 108(11), 1425-1437.

Boundy, T. M., Fountain, D. M., & Austrheim, H. (1992). Structural development and petrofabrics of eclogite facies shear zones, Bergen Arcs, western Norway: implications for deep crustal deformational processes. Journal of Metamorphic Geology, 10(2), 127-146.

Boundy, T. M., Mezger, K., & Essene, E. J. (1997). Temporal and tectonic evolution of the granulite-eclogite association from the Bergen Arcs, western Norway. Lithos, 39(3), 159-178.

Brown, M. (2007). Crustal melting and melt extraction, ascent and emplacement in orogens: mechanisms and consequences. Journal of the Geological Society, 164(4), 709-730.

Caddick, M. J., Konopásek, J., & Thompson, A. B. (2010). Preservation of garnet growth zoning and the duration of prograde metamorphism. Journal of Petrology, 51(11), 2327-2347.

Camacho, A., Lee, J. K. W., Hensen, B. J., & Braun, J. (2005). Short-lived orogenic cycles and the eclogitization of cold crust by spasmodic hot fluids. Nature, 435(7046), 1191-1196.

Centrella, S., Austrheim, H., & Putnis, A. (2015). Coupled mass transfer through a fluid phase and volume preservation during the hydration of granulite: An example from the Bergen Arcs, Norway. Lithos, 236, 245-255.

Chen, R., Zheng, Y., Gong, B., Zhao, Z., Gao, T., Chen, B., & Wu, Y. (2007). Origin of retrograde fluid in ultrahigh-pressure metamorphic rocks: Constraints from mineral hydrogen isotope and water content changes in eclogite–gneiss transitions in the Sulu orogen. Geochimica et Cosmochimica Acta, 71(9), 2299-2325. doi: http://dx.doi.org/10.1016/j.gca.2007.02.012

Coggon, R., & Holland, T. J. B. (2002). Mixing properties of phengitic micas and revised garnet-phengite thermobarometers. Journal of metamorphic geology, 20(7), 683-696.

Connolly, J. A. D. (2009). The geodynamic equation of state: what and how. Geochemistry, Geophysics, Geosystems, 10(10).

De Paoli, M. C., Clarke, G. L., Klepeis, K. A., Allibone, A. H., & Turnbull, I. M. (2009). The eclogite–granulite transition: mafic and intermediate assemblages at Breaksea Sound, New Zealand. Journal of Petrology, 50(12), 2307-2343.

Deines, P. (2002). The carbon isotope geochemistry of mantle xenoliths. Earth-Science Reviews, 58(3), 247-278.

Diener, J. F. A., & Powell, R. (2012). Revised activity–composition models for clinopyroxene and amphibole. Journal of Metamorphic Geology, 30(2), 131-142.

Diener, J. F. A., Powell, R., White, R. W., & Holland, T. J. B. (2007). A new thermodynamic model for clino-and orthoamphiboles in the system Na_2O–CaO–FeO–MgO–Al_2O_3–SiO_2–H_2O–O. Journal of Metamorphic Geology, 25(6), 631-656.

Dragovic, B., Samanta, L. M., Baxter, E. F., & Selverstone, J. (2012). Using garnet to constrain the duration and rate of water-releasing metamorphic reactions during subduction: an example from Sifnos, Greece. Chemical Geology, 314, 9-22.

Ellis, D. J., & Maboko, M. A. H. (1992). Precambrian tectonics and the physicochemical evolution of the continental crust. I. The gabbro-eclogite transition revisited. Precambrian Research, 55(1–4), 491-506. doi: http://dx.doi.org/10.1016/0301-9268(92)90041-L

Engvik, A. K., Austrheim, H., & Andersen, T. B. (2000). Structural, mineralogical and petrophysical effects on deep crustal rocks of fluid-limited polymetamorphism, Western Gneiss Region, Norway. Journal of the Geological Society, 157(1), 121-134.

Erambert, M., & Austrheim, H. (1993). The effect of fluid and deformation on zoning and inclusion patterns in poly-metamorphic garnets. Contributions to Mineralogy and Petrology,

115(2), 204-214.

Ghent, E. D., Dipple, G. M., & Russell, J. K. (2004). Thermodynamic models for eclogitic mantle lithosphere. Earth and Planetary Science Letters, 218(3–4), 451-462. doi: http://dx.doi.org/10.1016/S0012-821X(03)00678-2

Glodny, J., Kühn, A., & Austrheim, H. (2008). Geochronology of fluid-induced eclogite and amphibolite facies metamorphic reactions in a subduction–collision system, Bergen Arcs, Norway. Contributions to Mineralogy and Petrology, 156(1), 27-48.

Green, E., Holland, T., & Powell, R. (2007). An order-disorder model for omphacitic pyroxenes in the system jadeite-diopsidehedenbergite-acmite, with applications to eclogitic rocks. American Mineralogist, 92(7), 1181-1189.

Groppo, C., & Castelli, D. (2010). Prograde *P–T* Evolution of a Lawsonite Eclogite from the Monviso Meta-ophiolite (Western Alps): Dehydration and Redox Reactions during Subduction of Oceanic FeTi-oxide Gabbro. Journal of Petrology, 51(12), 2489-2514. doi: 10.1093/petrology/egq065

Guevara, V. E., & Caddick, M. J. (2016). Shooting at a moving target: phase equilibria modelling of high-temperature metamorphism. Journal of Metamorphic Geology, 34(3), 209-235.

Guiraud, M., Powell, R., & Rebay, G. (2001). H_2O in metamorphism and unexpected behaviour in the preservation of metamorphic mineral assemblages. Journal of Metamorphic Geology, 19(4), 445-454.

Hacker, B. R., Abers, G. A., & Peacock, S. M. (2003). Subduction factory 1. Theoretical mineralogy, densities, seismic wave speeds, and H_2O contents. Journal of Geophysical Research: Solid Earth, 108(B1).

Holland, T. J. B., & Powell, R. (1990). An enlarged and updated internally consistent thermodynamic dataset with uncertainties and correlations: the system K_2O–Na_2O–CaO–MgO–MnO–FeO–Fe_2O_3–Al_2O_3–TiO_2–SiO_2–C–H_2–O_2. Journal of Metamorphic Geology, 8(1), 89-124.

Holland, T. J. B., & Powell, R. (1998). An internally consistent thermodynamic data set for phases of petrological interest. Journal of Metamorphic Geology, 16(3), 309-343.

Holland, T. J. B., & Powell, R. (2003). Activity–composition relations for phases in petrological calculations: an asymmetric multicomponent formulation. Contributions to Mineralogy and Petrology, 145(4), 492-501.

Jackson, J. A., Austrheim, H., McKenzie, D., & Priestley, K. (2004). Metastability, mechanical strength, and the support of mountain belts. Geology, 32(7),

625-628.

Jamtveit, B., Bucher-Nurminen, K., & Austrheim, H. (1990). Fluid controlled eclogitization of granulites in deep crustal shear zones, Bergen arcs, Western Norway. Contributions to Mineralogy and Petrology, 104(2), 184-193.

Jolivet, L., Raimbourg, H., Labrousse, L., Avigad, D., Leroy, Y., Austrheim, H., & Andersen, T. B. (2005). Softening trigerred by eclogitization, the first step toward exhumation during continental subduction. Earth and Planetary Science Letters, 237(3), 532-547.

Kelsey, D. E., & Hand, M. (2015). On ultrahigh temperature crustal metamorphism: phase equilibria, trace element thermometry, bulk composition, heat sources, timescales and tectonic settings. Geoscience Frontiers, 6(3), 311-356.

Korhonen, F. J., Brown, M., Clark, C., & Bhattacharya, S. (2013). Osumilite–melt interactions in ultrahigh temperature granulites: phase equilibria modelling and implications for the *P–T*–t evolution of the Eastern Ghats Province, India. Journal of Metamorphic Geology, 31(8), 881-907.

Krogh, Erling J. (1977). Evidence of Precambrian continent-continent collision in Western Norway. Nature, 267, 17-19.

Kühn, A. (2002). The influence of fluid on the granulite to eclogite and amphibolite facies transition: a study in the anorthositic rocks from the Lindås Nappe, Bergen Arcs, West Norway. Unpub. PhD Thesis, University of Oslo.

Kühn, A., Glodny, J., Austrheim, H., & Raheim, A. (2002). The Caledonian tectono-metamorphic evolution of the Lindas Nappe: constraints from U-Pb, Sm-Nd and Rb-Sr ages of granitoid dykes. Norsk Geologisk Tidsskrift, 82(1), 45-58.

Lardeaux, J. M., & Spalla, M. I. (1991). From granulites to eclogites in the Sesia zone (Italian Western Alps): a record of the opening and closure of the Piedmont ocean. Journal of Metamorphic Geology, 9(1), 35-59.

Liu, J., Bohlen, S. R., & Ernst, W. G. (1996). Stability of hydrous phases in subducting oceanic crust. Earth and Planetary Science Letters, 143(1), 161-171. doi: http://dx.doi.org/10.1016/0012-821X(96)00130-6

Lund, M. G., Austrheim, H., & Erambert, M. (2004). Earthquakes in the deep continental crust-insights from studies on exhumed high-pressure rocks. Geophysical Journal International, 158(2), 569-576.

Marmo, B. A., Clarke, G. L., & Powell, R. (2002). Fractionation of bulk rock composition due to porphyroblast growth: effects on eclogite facies min-

eral equilibria, Pam Peninsula, New Caledonia. Journal of Metamorphic Geology, 20(1), 151-165.

Martin, L. A. J., Rubatto, D., Brovarone, A. V., & Hermann, J. (2011). Late Eocene lawsonite-eclogite facies metasomatism of a granulite sliver associated to ophiolites in Alpine Corsica. Lithos, 125(1), 620-640.

Mattey, D., Jackson, D. H., Harris, N. B. W., & Kelley, S. (1994). Isotopic constraints on fluid infiltration from an eclogite facies shear zone, Holsenøy, Norway. Journal of Metamorphic Geology, 12(3), 311-325.

Müller, A., & Koch-Müller, M. (2009). Hydrogen speciation and trace element contents of igneous, hydrothermal and metamorphic quartz from Norway. Mineralogical Magazine, 73(4), 569-583.

Palin, R. M., Weller, O. M., Waters, D. J., & Dyck, B. (2015). Quantifying geological uncertainty in metamorphic phase equilibria modelling; a Monte Carlo assessment and implications for tectonic interpretations. Geoscience Frontiers, 7(4), 591-607.

Peacock, S. M. (1990). Fluid processes in subduction zones. Science, 248 (4953), 329-337.

Peacock, S. M. (1993). The importance of blueschist→ eclogite dehydration reactions in subducting oceanic crust. Geological Society of America Bulletin, 105(5), 684-694.

Pearce, M. A., White, A. J. R., & Gazley, M. F. (2015). TCInvestigator: automated calculation of mineral mode and composition contours for thermocalc pseudosections. Journal of Metamorphic Geology, 33(4), 413-425.

Philippot, P. (1993). Fluid-melt-rock interaction in mafic eclogites and coesite-bearing metasediments: constraints on volatile recycling during subduction. Chemical Geology, 108(1-4), 93-112.

Pollok, K., Lloyd, G. E., Austrheim, H., & Putnis, A. (2008). Complex replacement patterns in garnets from Bergen Arcs eclogites: a combined EBSD and analytical TEM study. Chemie der Erde-Geochemistry, 68(2), 177-191.

Powell, R., & Holland, T. J. B. (1988). An internally consistent dataset with uncertainties and correlations: 3. Applications to geobarometry, worked examples and a computer program. Journal of Metamorphic Geology, 6(2), 173-204.

Raimbourg, H., Goffé, B., & Jolivet, L. (2007). Garnet reequilibration and growth in the eclogite facies and geodynamical evolution near peak metamorphic conditions. Contributions to Mineralogy and Petrology, 153(1), 1-28.

Raimbourg, H., Jolivet, L., Labrousse, L., Leroy, Y., & Avigad, D. (2005). Kinematics of syn-eclogite deformation in the Bergen Arcs, Norway, implications for exhumation mechanisms. Special Publication-Geological Society of London, 243, 175-192.

Ren, Y., Chen, D., Hauzenberger, C., Liu, L., Liu, X., & Zhu, X. (2016). Petrology and geochronology of ultrahigh-pressure granitic gneiss from South Dulan, North Qaidam belt, NW China. International Geology Review, 58(2), 171-195.

Ridley, J. (1984). Evidence of a Temperature-dependent 'Blueschist' to 'Eclogite' Transformation in High-pressure Metamorphism of Metabasic Rocks. Journal of Petrology, 25(4), 852-870. doi: 10.1093/petrology/25.4.852

Ringwood, A. E., & Green, D. H. (1966). An experimental investigation of the gabbro-eclogite transformation and some geophysical implications. Tectonophysics, 3(5), 383-427.

Rockow, K. M., Haskin, L. A., & Fountain, D. M. (1997). Constraints on element mobility associated with the conversion of granulite to eclogite along fractures in an anorthositic complex on Holsnøy, Norway. Journal of Metamorphic Geology, 15(3), 401-418.

Russell, A. K., Kitajima, K., Strickland, A., Medaris, L. G., Schulze, D. J., & Valley, J. W. (2012). Eclogite-facies fluid infiltration: constraints from δ18O zoning in garnet. Contributions to Mineralogy and Petrology, 165(1), 103-116. doi: 10.1007/s00410-012-0794-9

Schmidt, M. W., & Poli, S. (1998). Experimentally based water budgets for dehydrating slabs and consequences for arc magma generation. Earth and Planetary Science Letters, 163(1–4), 361-379. doi: http://dx.doi.org/10.1016/S0012-821X(98)00142-3

Schneider, J., Bosch, D., Monié, P., & Bruguier, O. (2007). Micro-scale element migration during eclogitisation in the Bergen arcs (Norway): a case study on the role of fluids and deformation. Lithos, 96(3), 325-352.

Sheng, Y., Xia, Q., Dallai, L., Yang, X., & Hao, Y. (2007). H_2O contents and D/H ratios of nominally anhydrous minerals from ultrahigh-pressure eclogites of the Dabie orogen, eastern China. Geochimica et Cosmochimica Acta, 71(8), 2079-2103. doi: http://dx.doi.org/10.1016/j.gca.2007.01.018

Spandler, C., Hermann, J., Arculus, R., & Mavrogenes, J. (2003). Redistribution of trace elements during prograde metamorphism from lawsonite blueschist to eclogite facies; implications for deep subduction-zone processes. Contributions to Mineralogy and Petrology, 146(2), 205-222. doi:

10.1007/s00410-003-0495-5

Spear, F. S., Selverstone, J., Hickmott, D., Crowley, P., & Hodges, K. V. (1984). PT paths from garnet zoning: a new technique for deciphering tectonic processes in crystalline terranes. Geology, 12(2), 87-90.

Stüwe, K. (1997). Effective bulk composition changes due to cooling: a model predicting complexities in retrograde reaction textures. Contributions to Mineralogy and Petrology, 129(1), 43-52.

Stüwe, K. (1998). Tectonic constraints on the timing relationships of metamorphism, fluid production and gold-bearing quartz vein emplacement. Ore Geology Reviews, 13(1), 219-228.

Terry, M. P., & Heidelbach, F. (2006). Deformation-enhanced metamorphic reactions and the rheology of high-pressure shear zones, Western Gneiss Region, Norway. Journal of Metamorphic Geology, 24(1), 3-18.

Tracy, R. J., & Robinson, P. (1976). Garnet composition and zoning in the determination of temperature and pressure of metamorphism, central Massachusetts. American Mineralogist, 6 (7-8), 762-775.

Van Wyck, N., Valley, J. W., & Austrheim, H. (1996). Oxygen and carbon isotopic constraints on the development of eclogites, Holsnøy, Norway. Lithos, 38(3–4), 129-145. doi: http://dx.doi.org/10.1016/0024-4937(96)00004-7

Vry, J., Powell, R., Golden, K. M., & Petersen, K. (2010). The role of exhumation in metamorphic dehydration and fluid production. Nature Geoscience, 3(1), 31-35.

White, R. W., Powell, R., & Holland, T. J. B. (2007). Progress relating to calculation of partial melting equilibria for metapelites. Journal of Metamorphic Geology, 25(5), 511-527.

White, RW., Powell, R., Holland, TJB., & Worley, BA. (2000). The effect of TiO_2 and Fe_2O_3 on metapelitic assemblages at greenschist and amphibolite facies conditions: mineral equilibria calculations in the system K_2O-FeO-MgO-Al_2O_3-SiO_2-H_2O-TiO_2-Fe_2O_3. Journal of Metamorphic Geology, 18(5), 497-512.

Zhang, R. Y., Liou, J. G., Zheng, Y. F., & Fu, B. (2003). Transition of UHP eclogites to gneissic rocks of low-amphibolite facies during exhumation: evidence from the Dabie terrane, central China. Lithos, 70(3), 269-291.

CHAPTER 3

$\delta^{18}O$ and δD constraints on the fluid enhanced eclogitisation of granulite in the Bergen Arcs, western Norway.

Statement of Authorship

Title of Paper	δ18O and δD constraints on the fluid enhanced eclogitisation of granulite in the Bergen Arcs, western Norway.
Publication Status	☐ Published ☐ Accepted for Publication ☐ Submitted for Publication ☑ Unpublished and Unsubmitted w ork w ritten in manuscript style
Publication Details	Written for publication in Lithos as: Bhowany, K., Hand, M., Clark, C., Taylor, R., and Kelsey, D.

Principal Author

Name of Principal Author (Candidate)	Kamini Bhowany		
Contribution to the Paper	Project fieldwork, detailed mapping, sample collection and preparation, data acquisition and analysis, figure making and manuscript writing.		
Overall percentage (%)	80		
Certification:	This paper reports on original research I conducted during the period of my Higher Degree by Research candidature and is not subject to any obligations or contractual agreements with a third party that would constrain its inclusion in this thesis. I am the primary author of this paper.		
Signature		Date	29/08/19

Co-Author Contributions

By signing the Statement of Authorship, each author certifies that:

i. the candidate's stated contribution to the publication is accurate (as detailed above);
ii. permission is granted for the candidate in include the publication in the thesis; and
iii. the sum of all co-author contributions is equal to 100% less the candidate's stated contribution.

Name of Co-Author	Prof. Martin Hand		
Contribution to the Paper	Fieldwork guidance, sample collection, guidance in manuscript structure and writing and manuscript review.		
Signature		Date	21/08/19

Name of Co-Author	Prof. Chris Clark		
Contribution to the Paper	Fieldwork guidance, sample collection, guidance in manuscript structure and writing and manuscript review. SIMS sample preparation and data collection.		
Signature		Date	25/06/2019

Name of Co-Author	Dr. Richard Taylor		
Contribution to the Paper	Sample preparation and data acquisition on the SIMS, post data acquisition imaging on the SEM.		
Signature		Date	24/06/2019

Name of Co-Author	Dr. David E. Kelsey		
Contribution to the Paper	Manuscript writing, manuscript reviewing.		
Signature		Date	29/6/19

ABSTRACT

The large-scale enhancement of eclogitisation due to fluid infiltration is a rare occurring event, based on the limited number of documented locations known to scientists. Arguably, one of the best examples of this process is found in the Lindås Nappe, on Holsnøy Island, western Norway. The conversion of granulite to eclogite on Holsnøy Island is progressive and the evolution of the system can be observed in multiple stages of deformation which spans over a wide range of pressure–temperature (*P–T*) conditions of 15.2–15.7 kbar 680°C, to a peak of 21–22 kbar and 660-690 °C and initial amphibolite-facies retrogression at 16 –17 kbar and 680–700 °C. Average whole-rock $\delta^{18}O$ values for the granulite, peak eclogite (stage 3 of deformation) and retrogressed eclogite (R-eclogite; stage 4 of deformation) are + 6.2, + 6.5 and + 7.2 ‰, respectively, and whole-rock δD values are – 68.0, –52.1, – 35.9 ‰, respectively. The lack of shifts in the $\delta^{18}O$ values from granulite to eclogite suggests a rock-buffered system for stage 3 of deformation. The system subsequently evolves to a fluid-buffered system in stage 4 of deformation as indicated by positive shifts in whole-rock $\delta^{18}O$ and δD for R-eclogite samples. Calculated $\delta^{18}O$ fluid signatures based on omphacite in the eclogite and R-eclogite are both +7.9 ‰, while those based on phengite are +8.6 ‰ and + 9.1‰, respectively. The weighted average for $\delta^{18}O$ values for the fluid calculated based on *in-situ* garnet rim analyses range from 6.66 to 7.23 ‰. δD fluid signatures based on phengite are –20.8 ‰ for the eclogite and – 27.8 ‰ for the R-eclogite. A metamorphic fluid is interpreted as the most likely reservoir for catalysing the conversion of granulite to eclogite on Holsnøy Island.

1. INTRODUCTION

High pressure terranes are usually associated with the presence of fluids, evident by the presence of pegmatites in eclogite domains, hydrous eclogite-facies assemblages or fluid inclusions in eclogite-facies minerals. Examples of high pressure terranes associated with the presence of fluid are: the Monviso Massive and Dora-Maira Massif, Western Alps (Philippot, 1993; Rubatto & Hermann, 2003); Tianshan, north-western China (John *et al.*, 2008); Pouébo Eclogite Mélange, Northern Caledonia (Spandler *et al.*, 2003); and Western Gneissic Region, Norway (Andersen *et al.*, 1989; Engvik *et al.*, 2000). However, examples of the step-wise formation of such terranes are sparse, likely due to the infiltration of fluid along fractures and shear zones. The Bergen Arcs, western Norway, is a unique place to study the effects of fluid infiltration and its availability in a nominally anhydrous granulite terrane to enhance hydrous, high pressure metamorphism.

Rocks that outcrop on Holsnøy Island form part of the Lindås Nappe and consist of anhydrous, metastable granulite-facies domains that juxtapose hydrous eclogite-facies domains (Figure 1). The two domains are visually distinct in the field as the boundaries between the two are sharp. Moreover, the stages of evolution of the system can be can be tracked as specific structural stages at different localities on the island. This evolution has been documented in detail by a number of previous authors (Boundy *et al.*, 1992; Jolivet *et al.*, 2005; Austrheim, 2013; Chapter 2), and summarised in Figure 2.

Many different aspects of the conversion of granulite to eclogite on Holsnøy Island have been studied by previous workers (e.g. Austrheim, 1987; Andersen *et al.*, 1991; Bingen *et al.*, 2004; Jolivet *et al.*, 2005; Raimbourg *et al.*, 2007; Glodny *et al.*, 2008; Centrella *et al.*, 2016; Putnis *et al.*, 2017), which include: (a) characterisation of the initiation of the eclogitisation process due

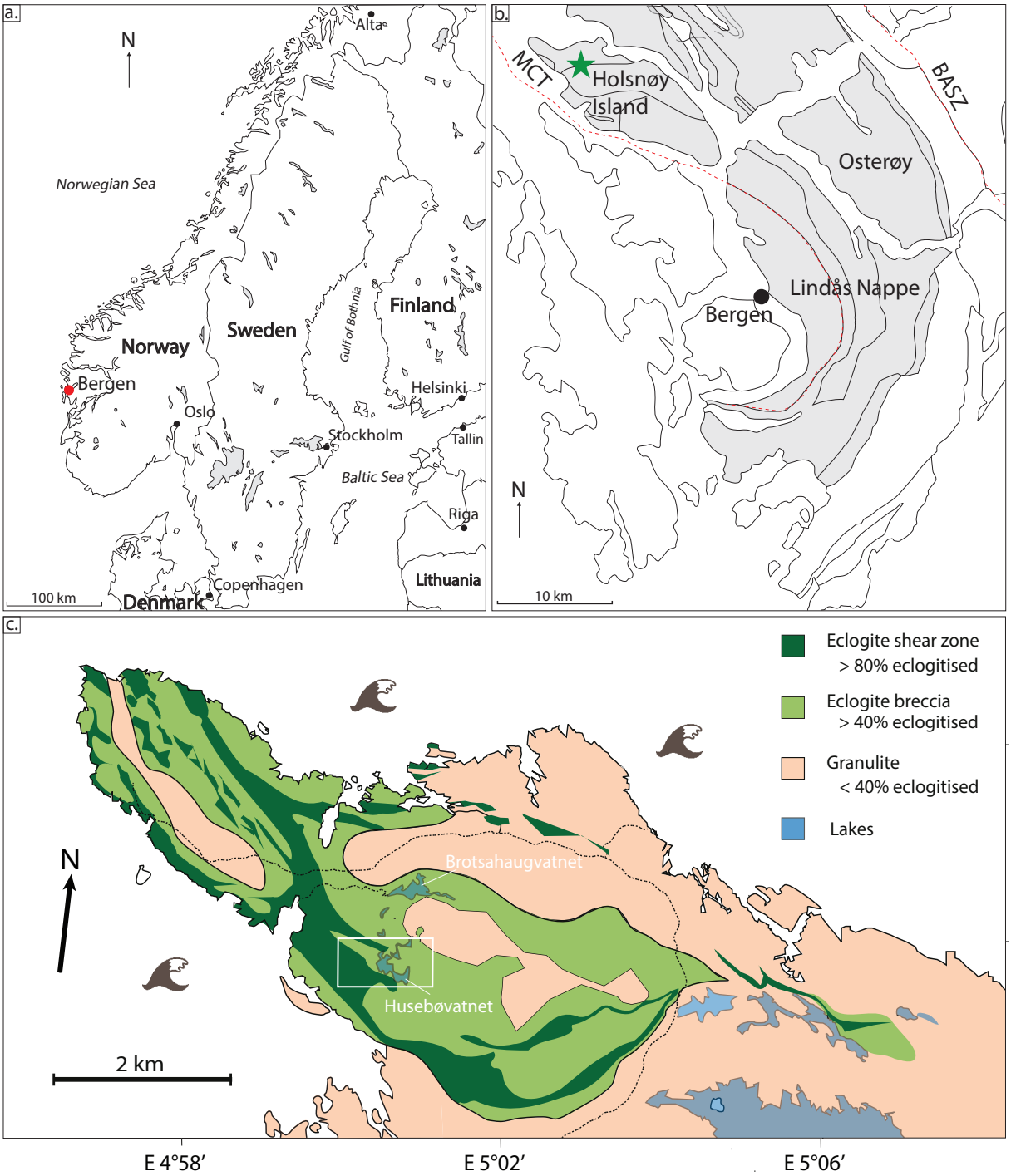

Figure 1. a) Location of Bergen, Norway. b) Location of Holsnøy Island (indicated by green star) relative to Bergen. c) Modified geological map (from Boundy *et al.* 1992 and Austrheim *et al.* 1996) of northern Holsnøy island. White box indicates the approximate location of the field area for this study.

to the formation of pseudotachylite during deep crustal earthquakes; (b) the behaviour of the fluid front during infiltration; (c) mechanisms for the eclogitisation process in subduction; and (d) the pressure and temperature (*P–T*) conditions at which different domains have been metamorphosed. However, despite the numerous studies that have been done on the rocks on Holsnøy, it is still unclear what the source of fluid is to allow for such large scale conversion of granulite to eclogite.

Previous authors have employed different isotopic systems to characterise the fluid that infiltrated the granulites — most identified the presence of a primary fluid generation interacting with the granulite, and a subsequently secondary fluid generation reacting with the eclogite at amphibolite-facies conditions. Through phase equilibria models of granulite and eclogite sample pairs and extensional veins (i.e. pegmatites), Jamtveit *et al.* (1990) suggested that the first fluid available in the system had a high water activity (X_{H2O} > 0.75). Andersen *et al.* (1991) used fluid inclusions within quartz grains from the same extensional veins described by Jamtveit *et al.* (1990) to infer the presence of two generations of fluid inclusions: an initial N_2–H_2O-rich fluid that reacted with the granulite and a secondary N_2–CO_2 fluid that reacted with the eclogite. Mattey *et al.* (1994) showed that from granulite to eclogite the $\delta^{13}C$ and $\delta^{15}N$ signatures obtained from fluid inclusions in garnet grains decreased from – 2 ‰ to – 10 ‰ and + 6 ‰ to + 3 ‰ respectively. Furthermore, Andersen *et al.* (1991) and Kühn (2002) suggested that the infiltrated fluid evolved from an H_2O dominated one, to a 'brine-like' fluid based on Cl^- analyses in fluid inclusions at amphibolite-facies. While these studies provide insightful information on the stable isotopic changes that occurred during the infiltration of fluid during the Caledonian Orogeny, it is not always evident whether the samples are representative of the peak eclogite stage since the eclogite discussed by previous workers contained abundant recrystallised plagioclase (Chapter 2) and are therefore, not eclogite-facies assemblages. For example, the extensional veins described by Jamtveit *et al.* (1990) and used by Andersen *et al.* (1991) are described as crystallised in the middle of the eclogitised shear zones. However, it is unclear whether the timing of this crystallisation is at peak eclogite-facies. Chapter 2 showed these discrete shear zones typically contain plagioclase, and are therefore, pre-peak eclogitic conditions, thereby introducing a degree of uncertainty when utilising their results. Mattey *et al.* (1994) later described the same structures as a retrogressed eclogite, but the presence of plagioclase in that sample indicates that at least some of the sample did not crystallise within the eclogite-facies.

Van Wyck *et al.* (1996) also used whole-rock major and trace element geochemistry to compare isotopic signatures of the granulite to eclogite samples. The study sampled rock in pairs (an eclogite and its closest granulite) to account for the compositional heterogeneity of the anorthosite. Measured whole rock $\delta^{18}O$ values ranged from + 7.3 to + 6.0 ‰ in the granulite, with a mean value of + 6.4 ‰, while that of the eclogite samples ranged from + 7.2 to + 6.1 ‰ with a mean value of + 6.6 ‰. While these values are not significantly different, they noted that, in general, the eclogite samples were slightly enriched in $\delta^{18}O$ compared to their corresponding granulite.

While detailed CO_2 analyses pointed towards the granulite protolith as the most likely source, the provenance of the N_2 is still uncertain and the range of values indicate either a mantle source or any N_2-rich crustal rock (Andersen *et al.*, 1991). Mattey *et al.* (1994) used C, N and Ar isotopes to conclude that devolatilisation of metasediments could be the source of fluid, and ruled out a mantle sourced fluid based on the anomalously high concentrations of radiogenic isotopes. Based on O and N isotopes, Van Wyck *et al.* (1996) also concluded the second generation of fluid was not locally derived, and suggested the dehydration of sediments in proximity to the granulite domains as the most likely source. To date, a robust provenance for the fluid has not been identified. Despite the previous studies in the area using O, N

and C isotopes, in most cases, there is an apparent lack of systematic sampling and analyses to carefully track the isotopic changes that occurred during fluid infiltration within a framework of the structural and pressure–temperature (*P–T*) evolution of Holsnøy Island. Moreover, a crucial missing set of data for the Holsnøy system is the $\delta^{18}O$ and δD of the fluid(s), itself. Van Wyck *et al.* (1996) measured $\delta^{18}O$ for garnet and omphacite, but did not specifically calculate the $\delta^{18}O$ signature for the fluid, which can be achieved through the consideration of fractionation at different temperatures (Taylor, 1974; Bottinga & Javoy, 1975; Zheng, 1993; Valley, 2003).

The aim of this study is to use a combination of oxygen and hydrogen isotopic ratios to systematically compare the isotopic signatures of eclogites and their nearest granulite protolith to determine the potential changes that occurred during fluid infiltration (Austrheim & Griffin, 1985; Jolivet *et al.*, 2005; Putnis *et al.*, 2017). Moreover, this approach allows for the characterisation of the isotopic signatures of the fluid(s), which can be used to determine the type of fluid reservoir that have infiltrated the granulite domains on Holsnøy Island. Isotopic signatures of the fluid(s) were calculated based on measured values of mineral separates of clinopyroxene/omphacite and phengite, as these minerals are present in all stages of eclogite evolution. To further constraint the results of the garnet fraction obtained by Van Wyck *et al.* (1996), this study presents *in–situ* garnet $\delta^{18}O$ analyses to differentiate between garnet cores and garnet rims. Garnet is stable in both the granulite and eclogite mineral assemblages, which indicates that it is able to record potential isotopic changes during fluid infiltration. However, up to 75 vol. % of the garnet grain (cores) is relict from the granulite (Raimbourg *et al.*, 2007; Chapter 2), and could not be differentiated while hand picking mineral separates, necessitating the use of *in–situ* analyses.

Constraining the source of fluid(s) in systems such as preserved on Holsnøy Island would increase the understanding of deep crustal and subduction processes (such as fluid migration and rheology changes), and ultimately, has critical implications for improving geodynamic models of such tectonic settings.

2. GEOLOGICAL SETTING

The samples used in this study were collected on Holsnøy Island, 45 km north-west of Bergen, western Norway (Figure 1a). The domains that make up Holsnøy form part of the Lindås Nappe which, along with the minor and major Bergen Arcs, form part of an arcuate structure around Bergen, collectively known as the Bergen Arcs (Figure 1b). The dominant lithology that outcrops on Holsnøy Island is an anorthositic, plagioclase–clinopyroxene–orthopyroxene–garnet granulite (Figure 1c) that was emplaced and metamorphosed during the Sveconorwegian Orogeny (c. 950 Ma) at estimated *P–T* conditions of 10 kbar and 800–900 °C (Austrheim & Griffin, 1985; Pollok *et al.*, 2008). This nominally anhydrous granulite was subsequently buried during the Caledonian Orogeny (c. 429 Ma) and was progressively converted to eclogite-facies assemblages owing to fluid infiltration (Austrheim & Griffin, 1985; Boundy *et al.*, 1997; Kühn, 2002). Chapter 2 focusses on the structural evolution of the Holsnøy system, and *P–T* conditions were determined for the progressive conversion of the granulite to eclogite. In essence, this process occurred through different stages of deformation as fluid became increasingly available within structures, evolving from a brittle to ductile regime (Jolivet *et al.*, 2005; Austrheim, 2013). Previous studies (Austrheim, 2013 and

Chapter 2) outlined the sequential evolution of the system in four main stages of deformation, based on structural field relationships. Stage 1 is the initiation of brittle deformation resulting in fractures and pseudotachylites, which act as the initial conduit for fluid infiltration in the granulite domains. However, although the pseudotachylites served as a fluid conduit, it is not clear that the age of the pseudotachylites is the same as the age of the early fluid generation. Stage 2 involved an increase in fluid availability to initiate the formation of eclogite-facies mineral assemblages, with the development of discrete shear zones along the initial fractures. Stage 3 is the complete conversion of the granulite to eclogite at *P–T* conditions of 21–22 kbar and 670–690 °C. This occurs at metre to kilometre scales, with granulite blocks sitting in apparent random orientations in an extensively sheared 'matrix' of eclogite. This stage of deformation was previously described as granulite 'breccia' by previous authors (Austrheim & Griffin, 1985; Jolivet *et al.*, 2005; Raimbourg *et al.*, 2005; Austrheim, 2013). Stage 4 is the overprint of the eclogite by a coarse-grained, phengite-rich eclogite. These four stages define the evolution of the Holsnøy system (Figure 2) whereby the domains experienced a near isothermal *P–T* path. The different stages of deformation are perfectly preserved because of the lack of fluid availability at these particular points during the burial and exhumation processes.

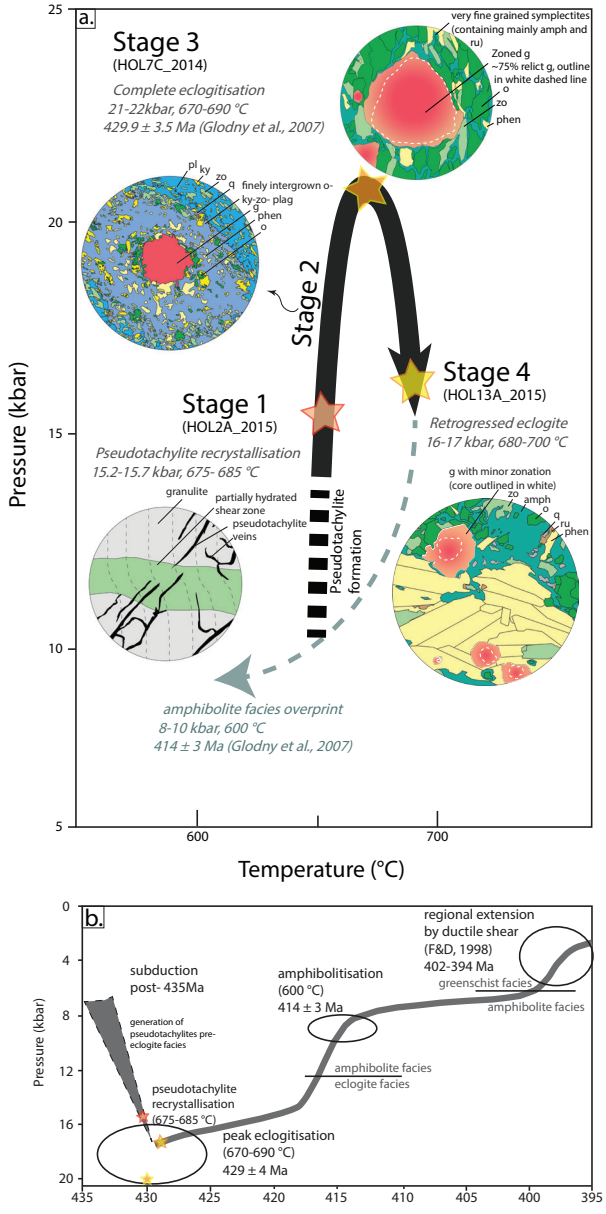

Figure 2. a) *P–T* path (after Bhowany *et al*. 2018) recorded by domains on Holsnøy Island based on different *P–T* pseudosections derived from a *pseudotachylite*, peak eclogite and retrogressed eclogite. b) *P–T-t* evolution of the system.

3. SAMPLING AND METHODS

3.1 Sampling and sample summary

This study focusses on the north-east of Holsnøy Island, around Lake Husebøvatnet, where the granulite was fully converted eclogites, in stages 3 and 4 of deformation (i.e. eclogite and R-eclogite). Sampling was done in pairs; that is, a completely converted eclogite sample and its spatially closest granulite protolith. Eclogite domains in stage 3 of deformation, and their corresponding granulite protoliths were sampled within 3 metres of each other to account for possible fluid fronts in the granulite, while the R-eclogite sample pairs were sampled within 1 metre of each other. This allows for a comparative study, with the assumption that signatures obtained from the granulite reflect pre-fluid conditions and can be used as a baseline for relative isotopic shifts. Granulite

samples were taken from the middle of granulite blocks to avoid any fluid front that may have existed on their margins. A summary of samples is given in Table 1. In general, the granulite samples have eye shaped lenses of garnet coronae around clinopyroxene and orthopyroxene in a plagioclase-garnet matrix, with an interpreted peak mineral assemblage of plagioclase–garnet–clinopyroxene–orthopyroxene ± rutile ± spinel. The eclogites have an interpreted peak assemblage of omphacite–garnet–phengite–zoisite–kyanite ± rutile with relict garnet cores and amphibole-rich symplectite (Chapter 2). R-eclogite samples have an interpreted peak metamorphic assemblage of omphacite–garnet–phengite–zoisite–amphibole ± rutile ± quartz (Chapter 2).

3.2 Methods

3.2.1 Bulk-rock chemistry

Bulk-rock, major elemental geochemistry was completed for all samples at the Department of Earth and Environment, Franklin and Marshall College, Lancaster, Pennsylvania. The volatile content (% LOI) was determined by heating ~1 g of powder of each sample in a muffle furnace at 950 °C for 1.5 hours, removing and cooling to room temperature and re-weighing the dried sample masses. A fraction of the anhydrous sample powders (~ 0.4000 g) was mixed with lithium tertraborate (~ 3.6000 g), placed in a platinum crucible and heated with a meeker burner until molten. The molten materials were then mixed and transferred to a cast for quenching to produce fused disks. X-ray Fluorescence (XRF) was used on the fused disks and major elements were analysed for SiO_2, TiO_2, Al_2O_3, Fe_2O_3, MnO, MgO, CaO, Na_2O, K_2O and P_2O_5. The working curves for each element was determined by analysing geochemical standards (Abbey 1983 and Govindaraju (1994)) prepared in the same way as the samples. The ferric contents of the samples were determined by titration, following a modified method by Reichen and Fahey (1962). Bulk-rock chemistry for each sample is presented in *wt %*, in Table 2.

3.2.2 Major element mineral chemistry

Major element mineral compositions were acquired at Adelaide Microscopy, University of Adelaide, using a Cameca SXFive electron microprobe. Quantitative elemental analyses were undertaken using wavelength dispersive spectrometers (WDS) with a beam current of 20 nA and accelerating voltage of 15 kV. Calibration was performed on certified synthetic and natural mineral standards (andradite crystal) from Astimex Ltd and P&H Associates. Data calibration and reduction were carried out in the software, Probe, for EPMA analyses, distributed by Probe Software Inc.

3.2.3 Whole-rock and single mineral $\delta^{18}O$ and δD

$\delta^{18}O$ and δD analyses were undertaken by the Stable Isotope Laboratory of GNS Science, New Zealand. Whole-rock analyses were acquired on finely ground particles, and single mineral analyses were obtained from hand-picked, crushed and ground mineral grains. $\delta^{18}O$ analysis was undertaken following Sharp (1990). 5 mg of each sample was heated overnight to 150 °C and loaded into a vacuum extraction line. Oxygen was then extracted for analysis using BrF_5 and a CO_2-laser on a Geo20-20 mass spectrometer. The oxygen isotope values were all measured relative to Vienna- Standard Mean Ocean Water (V-SMOW), and reported as $\delta^{18}O$ notation in parts per mille, ‰. All samples were normalised to the international quartz standard (NBS-28) using the value of +9.6 ‰, with internal precision of ± 0.2 ‰.

Hydrogen analyses used 50 mg of powdered samples that were pyrolysed at 1450 °C in silver capsules. δD analysis was conducted using a Hekatech High Temperature Analyser coupled with an Isoprime Mass Spectrometer (GV Instruments). All results are reported with respect to V-SMOW in parts per mille, ‰, and normalised to international standards IAEE-CH-7 (-100 ‰), NBS30 (–66 ‰) and NBS22 (–118 ‰), with internal precision of ± 2.0 ‰

3.2.4 In-situ $\delta^{18}O$ on garnet grains

In-situ garnet $\delta^{18}O$ analyses were performed following a modified version of the method outlined in detail by Raimondo *et al.* (2012). $^{18}O/^{16}O$ ratios were acquired using a multi-collector ion microprobe (Cameca IMS 1280), at the Centre of Microscopy, Characterisation and Analysis (CMCA), University of Western Australia. A static Cs+ beam of 3 nA and an acceleration voltage of 20 kV were used, with a spot size of 20 µm. Secondary O^- ions were accelerated to 10 kV and analysed using dual Faraday Cup detectors set with revolving power of 2400. Analyses were carried out in 20 four second cycles, giving an internal precision of 0.2 ‰.

The instrumental mass fractionation (IMF) correction was performed using UWG-2 (5.80 ‰; Valley *et al.*, 1995; Vielzeuf *et al.*, 2005a; Page *et al.*, 2010). The corrected value obtained for the UWG-2 check standard was 5.80 ± 0.27 ‰ (2σ; n = 54). As discussed by Vielzeuf *et al.* (2005a), Paige *et al.* (2010) and Raimondo *et al.* (2012), the IMF owing to the chemical matrix effect during analysis is correlated with garnet cation compositions. Paige *et al.* 2010 and Raimondo *et al.* 2012 also documented that calibrated IMF is strongly correlated to the grossular and uvarovite contents of garnet grains. Therefore, in this study, matrix correction was performed on all analysis.

Table 1. Sample location and summary

Sample	Location (32V)		Mineralogy	Additional information
	Easting (mE)	*Northing (mN)*		
Granulite				
HOL14-7A	0281226	6723701	pl + g + cpx + opx + ru	Protolith to HOL14-7C
HOL14-8A	0281226	6723701	pl + g + cpx + opx + ru	Protolith to HOL14-8B
HOL15-6	0283310	6724215	pl + g + sp ± ru	Protolith to HOL15-5
HOL15-12	0280999	6723661	pl + g + cpx + opx ± ru ± sp	Protolith to HOL15-10 and HOL15-11
HOL15-15	0282213	6723307	pl + g + cpx + opx	Protolith to HOL15-14, HOL15-13B, HOL15-13F and HOL16-2
Eclogite				
HOL14-7C	0281226	6723701	o + g + phen + zo + ky ± ru ± q	Relict spinel in garnet cores
HOL14-8B	0281226	6723701	o + g + phen + zo + ky ± ru ± q	
HOL15-5	0283310	6724215	o + g + phen + zo ± ru ± q	
HOL15-10	0280999	6723661	o + g + phen + zo ± ru ± q	Relict spinel in garnet cores
HOL15-11	0280999	6723661	o + g + phen + zo ± ru ± q	
R-eclogite				
HOL15-14	0282213	6723307	o + g + phen + zo + amp ± ru ± q	
HOL15-13B	0282213	6723307	o + g + phen + zo + amp ± ru ± q	
HOL15-13F	0282213	6723307	o + g + phen + zo + amp ± ru ± q	
HOL16-2	0282213	6723307	o + g + phen + zo + amp ± ru ± q	

Compared to Raimondo *et al.* 2012, however, the $X_{gross + uvar}$ values were obtained by EPMA analysis next to each spot after secondary ion mass spectrometry (SIMS) analysis. $X_{gross + uvar}$ molar values were calculated using CTcalc (Locock, 2008) and presented in Table 5. The matrix corrected $\delta^{18}O$ values for each analysis are also presented in Table 5, under the heading $\delta^{18}O_{corrected}$. For detailed error propagation scheme, see Appendix 2.1 (after Raimondo *et al.* 2012).

4. RESULTS

$\delta^{18}O$ and δD measurements were acquired on five stage 3 eclogites and four stage 4 retrogressed eclogites (R-eclogite). Specifically, $\delta^{18}O$ was measured on mineral separates of clinopyroxene in granulites, on omphacite in the stage 3 and 4 eclogites, as well as on phengite in both eclogite types. δD was measured on phengites separates only, for all altered samples. The representative whole-rock geochemistry for each lithology and their representative major mineral chemistries are presented in Tables 2 and 3, respectively.

4.1 $\delta^{18}O$ and δD signatures

The measured whole-rock and mineral analyses are presented in Table 4, as well as calculated fluid compositions based on mineral separates.

4.1.1 Whole-rock isotopic signature

Whole-rock $\delta^{18}O$ signatures show no significant shift from granulite to eclogite samples (Figure 3). However, a positive shift is observed in the $\delta^{18}O$ of R-eclogite samples, compared to the granulite and eclogite values. In contrast, δD signatures shift to more positive values from granulite to eclogite and R-eclogite samples (Figure 3). The mean $\delta^{18}O$ values for the granulite, eclogite and R-eclogite are + 6.2, + 6.5 and + 7.2 ‰ (± 0.2‰), respectively, while the mean δD values are – 68.0, – 52.1 and – 35.9 ‰, respectively (± 2 ‰) (Table 4). One $\delta^{18}O$ analysis of the granulites, sample HOL14-8A, is significantly higher (at 7.8 ‰) than the others, which affects the average $\delta^{18}O$ calculation.

Table 2. Representative whole-rock major element composition expressed in wt % (modified from Chapter 2).

	Granulite	Eclogite	R-eclogite
SiO_2	51.22	46.51	48.33
TiO_2	0.49	0.61	0.64
Al_2O_3	18.35	18.65	20.69
MnO	0.19	0.2	0.21
MgO	5.69	6.6	7.1
CaO	8.88	10.93	7.7
Na_2O	3.55	3.34	3.02
K_2O	0.72	0.79	2.49
P_2O_5	0.03	0.03	0.04
LOI	1.14	1.36	2.44
FeO	6.97	7.23	6.22
Fe_2O_3	2.58	3.35	2.63
Total	99.81	99.60	99.76

4.1.2 Clinopyroxene and omphacite

$\delta^{18}O$ signatures for clinopyroxene grain separates from the granulite samples yielded an average signature of + 4.9 ‰ (Figure 4). The $\delta^{18}O$ signatures for omphacite grain separates from the corresponding eclogites and R-eclogites have mean values + 5.8 ‰ and + 5.7 ‰ ± 0.2 ‰, respectively.

4.2.3 Phengite

$\delta^{18}O$ and δD were analysed in phengite grain separates from the eclogite and R-eclogite samples (Figures 4 and 5). The mean $\delta^{18}O$ signature for phengite separates in the eclogites samples is + 7.6 ‰ and that of the R-eclogite is + 8.0 ‰ ± 0.2 ‰. The mean δD value for the eclogite samples is – 26.0 ‰, which lies within error of the average R-eclogite δD value (– 27.8 ‰ ± 2.0 ‰).

4.1.4 In–situ garnet analysis

In–situ $\delta^{18}O$ analyses were performed on four garnet grains from stage 3 peak eclogite (sample

HOL14–7C). The garnet grains were chosen based on their prominent major element zonation and sharp core to rim boundaries (Figure 6). For all samples, the almandine–quartz fractionation coefficient of Valley (2003) and the quartz–water fractionation coefficient of Hu and Clayton (2003) were combined and used to calculate the fluid signature associated with the garnet rims (detailed by Raimondo *et al.* (2012). For the purpose of a core-rim $\delta^{18}O$ comparison, signatures in the garnet cores were assumed to be the measured $\delta^{18}O$ values as there were no fluids involved during the granulite-facies metamorphism.

$\delta^{18}O$ analyses were undertaken as traverses across garnet grains, targeting at least one core–rim boundary (Figure 6). Detailed $\delta^{18}O$ values for each transect is presented in Table 5. The weighted average of $\delta^{18}O$ values for each grain are 5.74 ± 0.42 ‰ for garnet 1; 5.94 ± 0.28 ‰ for garnet 2; 5.53 ± 0.33 ‰ for garnet 3, and ; 5.47 ± 0.24 ‰ for garnet 4. The weighted average $\delta^{18}O$ value for the core is 6.03 ± 0.25 ‰ for garnet 1, 6.00 ± 0.15 ‰ for garnet 2, 5.75 ± 0.21 ‰ for garnet 3, and 5.65 ± 0.15 ‰ for garnet 4. While the weighted average $\delta^{18}O$ value for the rims are 5.11 ± 0.38 ‰ for garnet 1, 5.63 ± 0.33 ‰ for garnet 2, 5.15 ± 0.27 for garnet 2 and 5.08 ± 0.22 for garnet 4. All uncertainties are reported as 2σ, with a 95 % confidence interval. $\delta^{18}O$ garnet analyses show a slight negative shift from core to rim, and $\delta^{18}O$ profiles show possible zonation in the garnet rims, which is highlighted in garnets 1, 3 and 4 (Figure 6).

5. DISCUSSION

In this study, $\delta^{18}O$ and δD are used to evaluate the possible reservoirs for the fluid that infiltrated the Holsnøy system. Isotopic signatures were measured on sample pairs (eclogite with its closest granulite protolith) to account for the possible chemical heterogeneity of the originally emplaced anorthosite. It is assumed here that the isotopic signature of the closest granulite protolith is representative of the domain prior to fluid infiltration, and the observed shifts in the altered samples are purely due to the components that have been brought in by the fluid. In an attempt to increase the resolution of the isotopic shifts resulting from fluid infiltration, mineral separates were also analysed for both $\delta^{18}O$ and δD signatures. This enables a comparison of the isotopic signatures during different stages of deformation within the *P–T* framework set up in Chapter 2 for the Holsnøy system, as well as the estimation of the isotopic signature of the fluid. The following section includes discussions on an assessment of

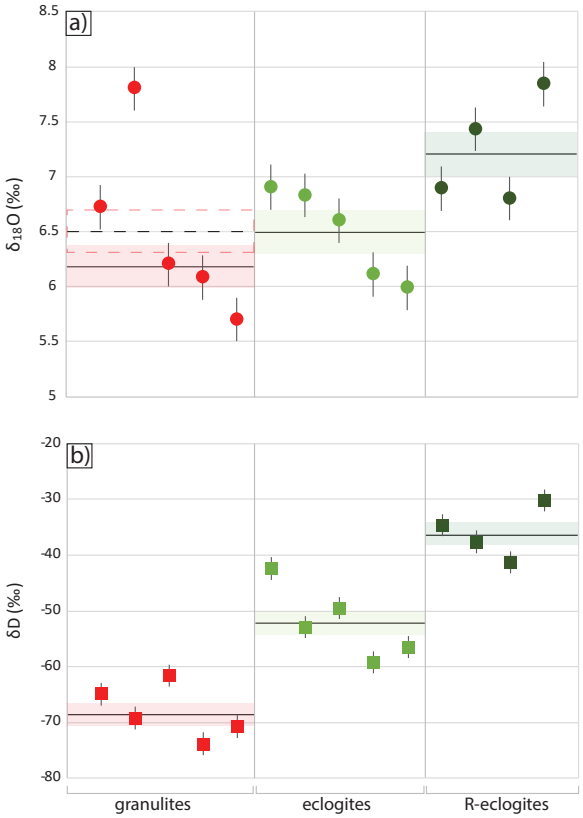

Figure 3. a) Whole-rock $\delta^{18}O$ isotopic signatures in granulite (red), eclogite (light green) and R-eclogite (dark green). b) Whole-rock δD signatures in granulite, eclogite and R-eclogite. The average for each lithology is indicated in shaded horizontal bars. Error bars represent internal precisions of ± 0.2 ‰ for $\delta^{18}O$ analyses and ± 2.0 ‰ for δD analyses.

Table 3. Representative mineral composition expressed in wt % (modified from Chapter 2).

				Stage 3 of deformation					Stage 4 of deformation					
	Granulite			Eclogite					R-eclogite					
	g	pl	px	o	g rim	g core	phen	zo	o	g rim	g core	phen	zo	hb
SiO_2	40.58	64.00	47.10	54.36	37.76	37.93	46.94	38.59	55.23	39.24	40.11	46.79	38.45	43.64
TiO_2	0.09	0.00	0.17	0.24	0.11	0.11	0.52	0.09	0.19	0.06	0.16	0.87	0.04	0.41
Al_2O_3	23.45	22.34	16.76	11.68	21.28	20.75	31.63	31.02	10.85	22.01	22.73	31.85	31.11	15.25
Cr_2O_3	0.02	0.00	0.00	0.01	0	0	0	0.01	0.01	0.03	0.03	0.01	0.02	0
FeO	13.01	0.01	7.25	5.33	22.31	23.3	2.34	3.23	4.63	20.7	17.55	1.87	2.98	11.32
MnO	0.18	0.00	0.04	0.02	0.51	0.76	0	0	0.02	0.68	0.41	0	0	0.2
MgO	15.19	0.00	12.16	8.31	7.79	9.84	2.11	0.04	9.11	8.45	13.56	2.21	0.02	12.26
ZnO	0.00	0.02	0.02	0	0	0.03	0	0.09	0.03	0	0	0	0.09	0.01
CaO	7.60	3.13	11.17	13.21	8.77	5.5	0.01	0	14.19	8.3	5.76	0.01	0.04	9.39
Na_2O	0.01	9.93	2.70	6.68	0.06	0.02	0.91	23.54	6.09	0.03	0.01	1.55	23.86	3.86
K_2O	0.00	0.21	0.78	0	0	0	8.8	0.02	0.01	0	0	8.76	0.02	0.76
Cl	0.00	0.00	0.01	0.02	0	0	0.01	0	0.01	0.01	0.01	0.01	0	0.06
F	0.00	0.00	0.00	0	0.01	0	0	0	0	0	0.01	0	0	0.09
TOTAL	100.14	99.64	98.15	99.89	98.62	98.32	94.28	96.63	100.4	99.52	100.4	94.86	96.63	97.28
No. O	12	8	6	6	12	12	11	13	6	12	12	11	13	23
Si	1.72	2.83	2.95	1.94	2.93	2.94	3.2	2.99	1.96	3	2.96	3.15	2.97	6.85
Ti	0.00	0.00	0.01	0.01	0.01	0.01	0.03	0.01	0.01	0	0.01	0.04	0	0.05
Al	0.72	1.16	2.01	0.49	1.95	1.9	2.54	2.83	0.45	1.98	1.98	2.53	2.84	2.82
Cr	0.00	0.00	0.00	0	0	0	0	0	0	0	0	0	0	0
Fe^{3+}	0.05	0.00	0.09	0.08	0.19	0.21	0	0.18	0.03	0.02	0.09	0.04	0.22	0
Fe^{2+}	0.17	0.00	0.70	0.07	1.25	1.3	0.13	0.03	0.1	1.31	1	0.06	0	1.49
Mn^{2+}	0.00	0.00	0.01	0	0.03	0.05	0	0	0	0.04	0.03	0	0	0.03
Mg	0.66	0.00	1.65	0.44	0.9	1.14	0.21	0	0.48	0.96	1.49	0.22	0	2.87
Zn	0.00	0.00	0.00	0	0	0	0	0.01	0	0	0	0	0.01	0
Ca	0.44	0.15	0.59	0.5	0.73	0.46	0	1.95	0.54	0.68	0.45	0	1.98	1.58
Na	0.19	0.85	0.00	0.46	0.01	0	0.12	0	0.42	0	0	0.2	0.01	1.17
K	0.04	0.01	0.00	0	0	0	0.77	0	0	0	0	0.75	0	0.15
Cl	0.00	0.00	0.00	0	0	0	0	0	0	0	0	0	0	0.02
F	0.00	0.00	0.00	0	0	0	0	0	0	0	0	0	0	0.05
Total cations (S)	8.00	5.00	4.00	3.99	8	8.01	7	8.05	3.99	7.99	8.01	6.99	8.06	17.08

Table 4. Whole-rock and mineral oxygen and hydrogen stable signatures and calculated fluid compositions.
Abbreviations: WR, whole-rock; cpx, clinopyroxene; o, omphacite; phen, phengite.
Fluid $\delta^{18}O$ and δD compositions were calculated by using the following: o[a], Bottinga and Javoy (1975); phen[b], Zheng (1993b) and phen[c], Suzuoki and Esptein (1976).

		$\delta^{18}O$ (‰, V-SMOW)			δD (‰, V-SMOW)		$\delta^{18}O_{fluid}$ (‰)		δD_{fluid} (‰)
Sample	**Lithology**	WR	cpx/o	phen	WR	phen	o[a]	phen[b]	phen[c]
HOL14–7A	Granulite	6.72	4.61		–64.8				
HOL14–8A	Granulite	7.8	4.97		–69.2				
HOL15–6	Granulite	6.2	4.9		–61.6				
HOL15–12	Granulite	6.08	4.76		–73.8				
HOL15–15	Granulite	5.7	5.32		–70.7				
HOL14–7C	Eclogite	6.9	5.76	7.52	–42.4	–21.2	7.86	8.52	–16.0
HOL14–8B	Eclogite	6.83	5.05	8.12	–52.9	–27.1	7.15	9.12	–21.9
HOL15–5	Eclogite	6.6	6.27	7.95	–49.5	–22	8.37	8.95	–16.8
HOL15–10	Eclogite	6.11	5.63	7.32	–59.24	–28.3	7.73	8.32	–23.14
HOL15–11	Eclogite	5.99	6.21	7.06	–56.47	–31.3	8.31	8.06	–26.1
HOL15–14	R-eclogite	6.89	5.34	6.85	–34.6	–31.8	7.54	7.95	–27.1
HOL15–13B	R-eclogite	6.8	5.31	8.59	–41.3	–26.7	7.51	9.69	–22.0
HOL15–13F	R-eclogite	7.43	6.15	8.36	–37.6	–23.4	8.35	9.46	–18.7
HOL16–2	R-eclogite	7.84	5.81	8.13	–30.2	–29.3	8.01	9.23	–24.6

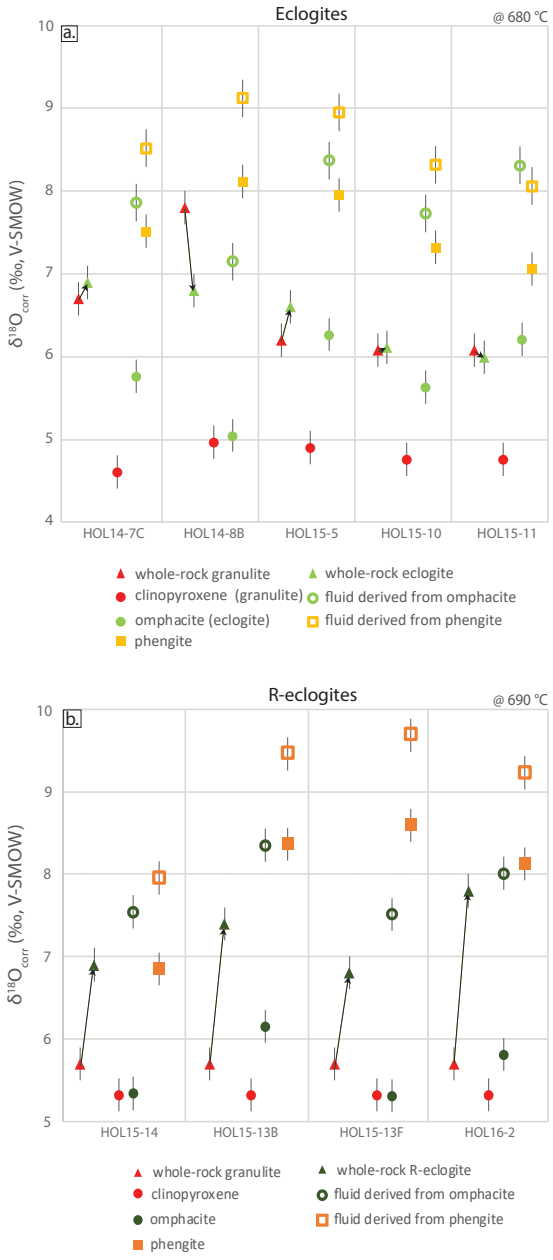

Figure 4. $\delta^{18}O$ signatures for mineral separates (clinopyroxene, omphacite and phengite) and fluids in granulite, eclogite and R-eclogite samples. Error bars only represent internal precisions of ± 0.2 ‰. a) $\delta^{18}O$ isotopic signatures of mineral separates in eclogites (light green and yellow) and their calculated fluid signatures. The arrows indicate the relative shift in $\delta^{18}O$ from protolith (granulite) to eclogite and the whole-rock compositions for both lithologies are plotted for a comparative overview of the different signatures. All calculations for the fluid signatures were done at a temperature of 680 °C. tb) $\delta^{18}O$ isotopic signatures of mineral separates in R-eclogites (dark green and orange) and their calculated fluid signatures. The arrows indicate the relative shift in $\delta^{18}O$ from protolith (granulite) to eclogite and the whole-rock compositions for both lithologies are plotted for a comparative overview of the different signatures. All calculations for the fluid signatures were done at a temperature of 690 °C.

isotopic equilibrium and fractionation temperature for mineral separates, as well as the new data sets and their significance compared to previously published studies. This ultimately provides a more robust understanding of the fluid history with an associated *P–T* evolution for the Holsnøy system.

5.1 Assessing isotopic equilibrium and fractionation temperature

The degree of isotopic equilibrium between minerals in a rock can be assessed by the use of isotherm diagrams (Javoy *et al.,* 1970). This method tests isotopic equilibrium between minerals based on the temperature dependency of fractionation between mineral pairs to assess the extent of their deviation relative to a calculated linear trend of equal temperature. The equilibrium fractionation coefficients (*A*) used in this study are diopside for the omphacite separates (1.38) and garnet (1.78) as presented by Chacko *et al*. (2001) and Valley *et al*. (2003). All calculations are given with respect to muscovite, due to its association with the metasomatic fluid.

An isotherm plot for the eclogite samples based on the bulk mineral compositions provided in Table 4, as well as the *in-situ* garnet rim analyses for the stage 3 samples, is presented in Figure 7. Figure 7a shows a reasonably similar range of $\delta^{18}O$ values for the omphacite grains and garnet rim analyses, relative to an isotherm line of 680 °C based on the lowest phengite $\delta^{18}O$ value (solid line). Two phengite grains have more positive $\delta^{18}O$ values, which suggests that slight isotopic disequilibrium is occurring in phengite $\delta^{18}O$ values. However, if an isotherm is drawn based on the maximum phengite $\delta^{18}O$ (dashed line), the majority of omphacite and garnet rim analyses fall within the two linear arrays, with the maximum of both the omphacite and garnet

values trending towards the dashed isotherm. A similar spread is observed between the phengite and omphacite $\delta^{18}O$ values for R-eclogite based on isotherms calculated at a temperature of 690 °C. A linear array can be drawn based on the minimum $\delta^{18}O$ phengite value (solid line). Two of the omphacite grains plot on this line, while the remaining values lie towards the isotherm calculated from the maximum $\delta^{18}O$ phengite values. The slight disequilibrium between mica grains and other rock forming minerals has been previously observed in other systems (e.g. Peak Hill shear zone, Raimondo *et al*. 2012; Peninsula Granite, Harris and Vogeli, 2010). This is likely due to micas' susceptibly to resetting compared to minerals such as quartz and clinopyroxenes, in the presence of fluids (Chako *et al*., 1996). Moreover, according to observations by Giletti (1986), isotopic equilibrium is not necessarily attained by every mineral in a cooling system, due to the sluggish exchange of oxygen between minerals while passing their blocking temperatures. In addition, Faver (1989) demonstrated that, in general, only the last two minerals to equilibrate are expected to be in isotopic equilibrium, based on diffusion data. The open nature of the Holsnøy system adds complexity to the isotopic equilibration of the eclogite-facies domains. The interaction between minerals and the infiltrated fluid results in varying isotopic signatures in individual grains of the same mineral. Therefore, as shown in Figure 7b, coexisting minerals in the eclogite domains do not record complete isotopic equilibration with each other. However, the degree of disequilibrium is relatively minor considering the majority of omphacite and garnet rim data occur close to or between the isotherms predicted by phengite measurements, particularly for stage 3 eclogites

An important consideration in calculating the

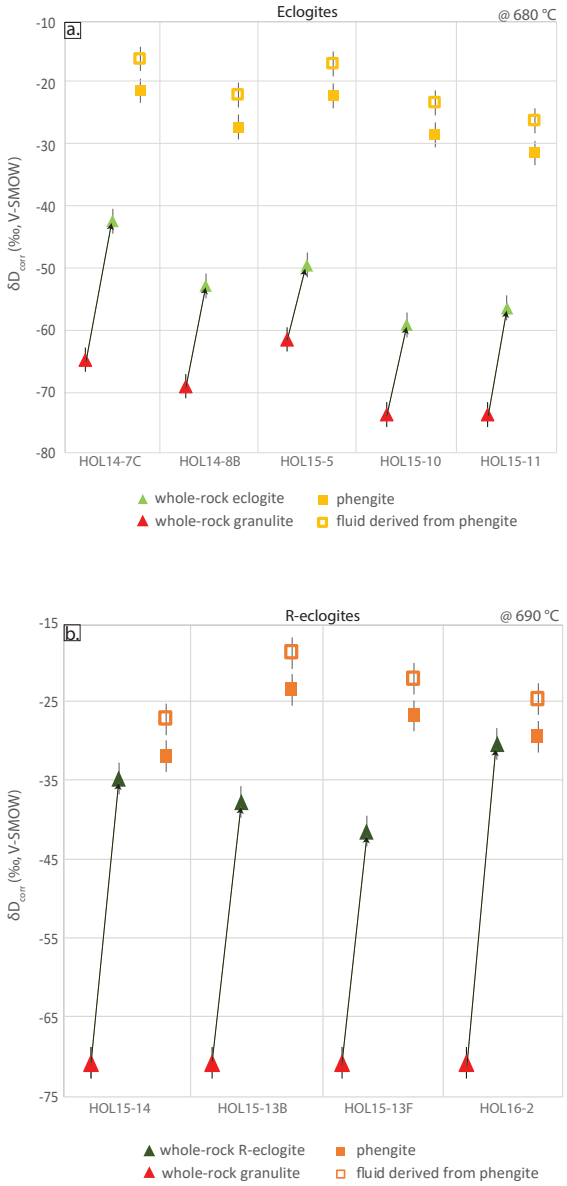

Figure 5. a) δD signatures for mineral separates (phengite) in eclogite and their calculated fluid signatures and respective whole-rock signatures. All calculations were done at a temperature of 680 °C.
b) δD signatures for mineral separates (phengite) in R-eclogite and their calculated fluid signatures and respective whole-rock signature. All calculations were done at a temperature of 690 °C.
Error bars only represent internal precisions of ± 2 ‰.

isotopic signature of fluids is the temperature dependency of isotopic fractionation between the fluid and different minerals. A temperature of 680 °C was used for the fluid calculations in the eclogite samples based on phase equilibria models in Chapter 2, and the stability of garnet, omphacite and kyanite. This estimate falls within

Table 5. Ion mircroprobe *in-situ* garnet analyses.

Spot name	$^{18}O/^{16}O$ (R_{raw})	± 2σ	$^{18}O/^{16}O$ (R_{drift})	± 2σ	$\delta^{18}O$ drift (‰ V-SMOW)	± 2σ	$\delta^{18}O$ sample (‰ V-SMOW)	± 2σ	$X_{gross+uvar}$	$\delta^{18}O$ corrected (‰ V-SMOW)	± 2σ	$\delta^{18}O$ fluid (‰ V-SMOW)	± 2σ
Garnet 1@1	0.0020253	0.0106402	0.002025298	2.155E-07	0.0020253	2.15495E-07	6.16	0.35	0.15	5.75	0.68	5.75	0.68
Garnet 1@2	0.0020260	0.0127694	0.002025981	2.587E-07	0.00202598	2.58706E-07	6.50	0.38	0.13	6.21	0.69	6.21	0.69
Garnet 1@3	0.0020268	0.0093708	0.00202684	1.899E-07	0.00202684	1.89931E-07	6.92	0.33	0.18	6.13	0.67	6.13	0.67
Garnet 1@4	0.0020263	0.0090030	0.002026334	1.824E-07	0.00202633	1.82432E-07	6.67	0.33	0.15	6.24	0.67	6.24	0.67
Garnet 1@5	0.0020258	0.0105854	0.002025824	2.144E-07	0.00202582	2.14442E-07	6.42	0.35	0.14	6.09	0.68	6.09	0.68
Garnet 1@6	0.0020256	0.0092610	0.002025622	1.876E-07	0.00202562	1.87593E-07	6.32	0.33	0.14	5.95	0.67	5.95	0.67
Garnet 1@7	0.0020260	0.0137461	0.002025989	2.785E-07	0.00202599	2.78494E-07	6.50	0.39	0.17	5.81	0.70	5.81	0.70
Garnet 1@8	0.0020259	0.0100612	0.002025932	2.038E-07	0.00202593	2.03833E-07	6.47	0.34	0.28	4.84	0.67	6.44	0.67
Garnet 1@9	0.0020267	0.0062032	0.002026739	1.257E-07	0.00202674	1.25724E-07	6.87	0.30	0.27	5.33	0.66	6.93	0.66
Garnet 1@10	0.0020261	0.0102861	0.002026076	2.084E-07	0.00202608	2.08405E-07	6.54	0.34	0.25	5.14	0.68	6.74	0.68
Weight average	*0.0020261*	*0.0101926*	*0.0020261*	*0.0000002*	*0.0020261*	*0.0000002*	*6.54*	*0.34*	*0.19*	*5.75*	*0.68*	*6.23*	*0.68*
Garnet 2@1	0.002026515	0.0070524	0.002026515	1.429E-07	0.00202652	1.42919E-07	6.76	0.31	0.22	5.64	0.66	7.24	0.66
Garnet 2@2	0.002026671	0.0107403	0.002026671	2.177E-07	0.00202667	2.17671E-07	6.84	0.35	0.22	5.73	0.68	7.33	0.68
Garnet 2@3	0.002026297	0.0111996	0.002026297	2.269E-07	0.0020263	2.26937E-07	6.65	0.35	0.22	5.51	0.68	7.11	0.68
Garnet 2@4	0.002026715	0.0092972	0.002026715	1.884E-07	0.00202672	1.88428E-07	6.86	0.33	0.23	5.65	0.67	7.25	0.67
Garnet 2@5	0.002025931	0.0101869	0.002025931	2.064E-07	0.00202593	2.06379E-07	6.47	0.34	0.15	6.00	0.68	6.00	0.68
Garnet 2@6	0.002025543	0.0106443	0.002025543	2.156E-07	0.00202554	2.15606E-07	6.28	0.35	0.15	5.83	0.68	5.83	0.68
Garnet 2@7	0.002025369	0.007218	0.002025369	1.462E-07	0.00202537	1.46191E-07	6.19	0.31	0.14	5.84	0.66	5.84	0.66
Garnet 2@8	0.002025033	0.0080271	0.002025033	1.626E-07	0.00202503	1.62552E-07	6.02	0.32	0.14	5.72	0.66	5.72	0.66
Garnet 2@9	0.002025492	0.0085145	0.002025492	1.725E-07	0.00202549	1.72461E-07	6.25	0.32	0.14	5.94	0.67	5.94	0.67
Garnet 2@10	0.002025425	0.0089607	0.002025425	1.815E-07	0.00202543	1.81493E-07	6.22	0.33	0.13	5.94	0.67	5.94	0.67
Garnet 2@11	0.002025535	0.0101071	0.002025535	2.047E-07	0.00202554	2.04724E-07	6.27	0.34	0.12	6.09	0.68	6.09	0.68
Garnet 2@12	0.002025285	0.0094163	0.002025285	1.907E-07	0.00202529	1.90706E-07	6.15	0.33	0.13	5.93	0.67	5.93	0.67
Garnet 2@13	0.00202524	0.0087733	0.00202524	1.777E-07	0.00202524	1.7768E-07	6.13	0.33	0.12	5.97	0.67	5.97	0.67
Garnet 2@14	0.002025588	0.0072095	0.002025588	1.46E-07	0.00202559	1.46034E-07	6.30	0.31	0.13	6.09	0.66	6.09	0.66
Garnet 2@15	0.002025277	0.0104307	0.002025277	2.113E-07	0.00202528	2.11251E-07	6.15	0.34	0.12	6.03	0.68	6.03	0.68
Garnet 2@16	0.002025369	0.008692	0.002025369	1.76E-07	0.00202537	1.76045E-07	6.19	0.32	0.13	5.96	0.67	5.96	0.67
Garnet 2@17	0.002025716	0.0070344	0.002025716	1.425E-07	0.00202572	1.42497E-07	6.36	0.31	0.13	6.16	0.66	6.16	0.66
Garnet 2@18	0.002025673	0.0072028	0.002025673	1.459E-07	0.00202567	1.45905E-07	6.34	0.31	0.13	6.08	0.66	6.08	0.66
Garnet 2@19	0.002025701	0.0084181	0.002025701	1.705E-07	0.0020257	1.70525E-07	6.36	0.32	0.12	6.24	0.67	6.24	0.67
Garnet 2@20	0.002025584	0.0100493	0.002025584	2.036E-07	0.00202558	2.03558E-07	6.30	0.34	0.12	6.16	0.67	6.16	0.67
Garnet 2@21	0.002025483	0.011533	0.002025483	2.336E-07	0.00202548	2.33598E-07	6.25	0.36	0.12	6.12	0.68	6.12	0.68
Garnet 2@22	0.002025147	0.0092603	0.002025147	1.875E-07	0.00202515	1.87535E-07	6.08	0.33	0.12	5.98	0.67	5.98	0.67
Weight average	*0.002025663*	*0.009089*	*0.002025663*	*1.841E-07*	*0.00202566*	*1.84122E-07*	*6.34*	*0.33*	*0.15*	*5.94*	*0.67*	*6.23*	*0.67*
Garnet 3@1	0.002025626	0.0104746	0.002025626	2.122E-07	0.00202563	2.12176E-07	6.32	0.35	0.26	4.86	0.68	6.46	0.68
Garnet 3@2	0.002026632	0.0111091	0.002026632	2.251E-07	0.00202663	2.2514E-07	6.82	0.35	0.25	5.40	0.68	7.00	0.68
Garnet 3@3	0.002026325	0.0111808	0.002026325	2.266E-07	0.00202633	2.2656E-07	6.67	0.35	0.24	5.31	0.68	6.91	0.68
Garnet 3@4	0.002026465	0.0090058	0.002026465	1.825E-07	0.00202647	1.825E-07	6.74	0.33	0.18	5.94	0.67	7.54	0.67
Garnet 3@5	0.002025907	0.007946	0.002025907	1.61E-07	0.00202591	1.60978E-07	6.46	0.32	0.16	5.89	0.66	7.49	0.66
Garnet 3@6	0.002025302	0.009364	0.002025302	1.896E-07	0.0020253	1.89649E-07	6.16	0.33	0.16	5.62	0.67	5.62	0.67
Garnet 3@7	0.002024909	0.008415	0.002024909	1.704E-07	0.00202491	1.70396E-07	5.96	0.32	0.14	5.61	0.67	5.61	0.67

Garnet 3@8	0.002025766	0.0119532	0.002025766	2.421E-07	0.00202577	2.42144E-07	6.39	0.36	0.15	5.91	0.69	5.91	0.69
Garnet 3@9	0.002024653	0.0087953	0.002024653	1.781E-07	0.00202465	1.78074E-07	5.84	0.33	0.15	5.41	0.67	5.41	0.67
Garnet 3@10	0.002025143	0.0081944	0.002025143	1.659E-07	0.00202514	1.65948E-07	6.08	0.32	0.14	5.71	0.66	5.71	0.66
Garnet 3@11	0.002025103	0.0108065	0.002025103	2.188E-07	0.0020251	2.18843E-07	6.06	0.35	0.13	5.77	0.68	5.77	0.68
Garnet 3@12	0.002024726	0.0111547	0.002024726	2.259E-07	0.00202473	2.25851E-07	5.87	0.35	0.14	5.57	0.68	5.57	0.68
Garnet 3@13	0.002025797	0.0108989	0.002025797	2.208E-07	0.0020258	2.2079E-07	6.40	0.35	0.14	6.05	0.68	6.05	0.68
Garnet 3@14	0.002025502	0.0089707	0.002025502	1.817E-07	0.0020255	1.81701E-07	6.26	0.33	0.23	5.03	0.67	6.63	0.67
Garnet 3@15	0.002025863	0.0092342	0.002025863	1.871E-07	0.00202586	1.87073E-07	6.44	0.33	0.23	5.22	0.67	6.82	0.67
Garnet 3@16	0.002025683	0.0091519	0.002025683	1.854E-07	0.00202568	1.85389E-07	6.35	0.33	0.23	5.11	0.67	6.71	0.67
Weighted average	*0.002025588*	*0.009791*	*0.002025588*	*1.983E-07*	*0.00202559*	*1.98326E-07*	*6.30*	*0.34*	*0.18*	*5.53*	*0.67*	*6.33*	*0.67*
Garnet 4@1	0.002026144	0.0090594	0.002026319	1.48E-07	0.00202614	1.83557E-07	6.58	0.33	0.22	5.45	0.67	7.05	0.67
Garnet 4@2	0.002026319	0.007305	0.002024405	1.661E-07	0.00202632	1.48022E-07	6.66	0.31	0.24	5.34	0.66	6.94	0.66
Garnet 4@3	0.002024405	0.0082068	0.002024786	1.734E-07	0.00202441	1.66139E-07	5.71	0.32	0.14	5.38	0.66	6.98	0.66
Garnet 4@4	0.002024786	0.0085642	0.002024404	1.991E-07	0.00202479	1.73406E-07	5.90	0.32	0.14	5.57	0.67	5.57	0.67
Garnet 4@5	0.002024404	0.0098366	0.00202485	1.533E-07	0.0020244	1.99133E-07	5.71	0.34	0.12	5.55	0.67	5.55	0.67
Garnet 4@6	0.00202485	0.007573	0.002024606	1.929E-07	0.00202485	1.53342E-07	5.93	0.31	0.14	5.61	0.66	5.61	0.66
Garnet 4@7	0.002024606	0.0095301	0.002024507	2.177E-07	0.00202461	1.92947E-07	5.81	0.33	0.14	5.49	0.67	5.49	0.67
Garnet 4@8	0.002024507	0.0107526	0.002025457	1.979E-07	0.00202451	2.17687E-07	5.76	0.35	0.13	5.52	0.68	5.52	0.68
Garnet 4@9	0.002025457	0.00977	0.002024963	1.891E-07	0.00202546	1.97888E-07	6.24	0.34	0.13	5.95	0.67	5.95	0.67
Garnet 4@10	0.002024963	0.0093377	0.002025219	1.761E-07	0.00202496	1.89086E-07	5.99	0.33	0.13	5.72	0.67	5.72	0.67
Garnet 4@11	0.002025219	0.0086937	0.002024495	2.37E-07	0.00202522	1.76066E-07	6.12	0.32	0.13	5.92	0.67	5.92	0.67
Garnet 4@12	0.002024495	0.0117073	0.002025107	1.666E-07	0.0020245	2.37013E-07	5.76	0.36	0.13	5.51	0.69	5.51	0.69
Garnet 4@13	0.002025107	0.0082255	0.002024546	2.013E-07	0.00202511	1.66576E-07	6.06	0.32	0.13	5.85	0.66	5.85	0.66
Garnet 4@14	0.002024546	0.0099453	0.002025556	2.172E-07	0.00202455	2.01347E-07	5.78	0.34	0.13	5.57	0.67	5.57	0.67
Garnet 4@15	0.002025556	0.0107223	0.002024665	1.861E-07	0.00202556	2.17187E-07	6.28	0.35	0.13	6.08	0.68	6.08	0.68
Garnet 4@16	0.002024665	0.0091938	0.00202534	2.325E-07	0.00202467	1.86143E-07	5.84	0.33	0.13	5.56	0.67	5.56	0.67
Garnet 4@17	0.00202534	0.0114794	0.002024288	1.994E-07	0.00202534	2.32498E-07	6.18	0.36	0.13	5.90	0.68	5.90	0.68
Garnet 4@18	0.002024288	0.0098493	0.002025197	1.935E-07	0.00202429	1.99379E-07	5.65	0.34	0.13	5.39	0.67	5.39	0.67
Garnet 4@19	0.002025197	0.009556	0.00202421	1.763E-07	0.0020252	1.93527E-07	6.11	0.33	0.13	5.86	0.67	5.86	0.67
Garnet 4@20	0.00202421	0.0087117	0.002024803	2.327E-07	0.00202421	1.76342E-07	5.62	0.32	0.12	5.48	0.67	5.48	0.67
Garnet 4@21	0.002024803	0.0114936	0.002024529	1.609E-07	0.0020248	2.32723E-07	5.91	0.36	0.13	5.68	0.68	5.68	0.68
Garnet 4@22	0.002024529	0.0079465	0.002025006	2.242E-07	0.00202453	1.6088E-07	5.77	0.32	0.14	5.46	0.66	5.46	0.66
Garnet 4@23	0.002025006	0.0110716	0.002025366	1.74E-07	0.00202501	2.242E-07	6.01	0.35	0.17	5.34	0.68	5.34	0.68
Garnet 4@24	0.002025366	0.008591	0.002025532	1.741E-07	0.00202537	1.73999E-07	6.19	0.32	0.24	4.84	0.67	6.44	0.67
Garnet 4@25	0.002025532	0.0085947	0.002025483	1.324E-07	0.00202553	1.74089E-07	6.27	0.32	0.22	5.10	0.67	6.70	0.67
Garnet 4@26	0.002025483	0.0065344	0.002025365	2.07E-07	0.00202548	1.32353E-07	6.25	0.30	0.23	5.05	0.66	6.65	0.66
Garnet 4@27	0.002025365	0.010221	0.002025197	1.909E-07	0.00202537	2.07012E-07	6.19	0.34	0.23	4.99	0.68	6.59	0.68
Garnet 4@28	0.002025197	0.0094244	0.002024766	1.602E-07	0.0020252	1.90863E-07	6.11	0.33	0.23	4.87	0.67	6.47	0.67
Garnet 4@29	0.002024766	0.0079125	0.002024788	1.633E-07	0.00202477	1.60209E-07	5.89	0.32	0.22	4.72	0.66	6.32	0.66
Weighted average	*0.002025004*	*0.009304*	*0.002024957*	*1.877E-07*	*0.002025*	*1.884E-07*	*6.01*	*0.33*	*0.16*	*5.47*	*0.67*	*5.97*	*0.67*

Molar proportion of garnet end-members grossular + uvarovite ($X_{gross + uvar}$) values were calculated following Locock (2008).

the range of temperatures of 650–800 °C previously calculated based on the Fe–Mg exchange between garnet and omphacite and garnet and amphibole mineral pairs (Austrheim & Griffin, 1985; Boundy *et al*., 1997; Jamtveit *et* al., 1990), as well as the use of Gibbs energy minimisation methods in combination with average *P–T* calculations by Raimbourg *et al*. (2007). Calculations of fluid composition based on mineral separates from the R-eclogite samples were performed at a temperature of 690 °C based on the stability of coexisting omphacite, quartz and zoisite (Chapter 2). To date, this is the only temperature estimate for the equilibration of the R-eclogites.

As evident in the range of temperatures (i.e. 650 °C to 800 °C; Austrheim and Griffins, 1985; Boundy *et al*., 1996; Raimbourg *et al.*, 2007) obtained for the equilibration of eclogites on Holsnøy Island, there is the potential for an over or under-estimation for the calculated fluid values. The following equations are used to determine the isotopic composition of a fluid in equilibrium with an analysed mineral:

$$\delta^{18}O_{fluid} = \delta^{18}O_i - \Delta\, i\text{–fluid} \quad , \quad (1)$$

$$\delta D_{fluid} = \delta D_i - \Delta\, i\text{–fluid} \quad , \quad (2)$$

where, $\delta^{18}O_i$ and δD_i are the measured isotopic values, and $\Delta\, i$–fluid is the fractionation factor between the mineral phase *i* and the fluid. Therefore, the fractionation factors can be used to assess the degree of bias in $\delta^{18}O$ and δD values calculated for the fluid. Thus, fractionation factors for the pyroxene–H_2O (for $\delta^{18}O$) and muscovite–H_2O (for $\delta^{18}O$ and δD) mineral pairs at 650 °C and 800 °C were determined and compared with those calculated at 680 °C, for stage 3 eclogite samples. For oxygen data, the pyroxene–H_2O fractionation factor at 680 °C is – 2.1 ‰, while those at 650 °C and 800 °C are – 2.0 ‰ and – 2.5 ‰, respectively. The muscovite–H_2O pair results in fractionation factors of – 1.0 ‰ at 680 °C, – 0.9 ‰ at 650 °C and – 1.5 ‰ at 800 °C for $\delta^{18}O$, while those for δD result in factors of – 5.2 at 680 °C, – 6.8 at 650 °C and – 0.1 at 800 °C.

For both mineral–H_2O pairs, the fractionation factors calculated for the $\delta^{18}O_{fluid}$ at 650 °C are within the ± 0.2 ‰ error to that calculated at a temperature of 680 °C. Fractionation factors calculated at a temperature of 800 °C, however, result in $\delta^{18}O_{fluid}$ values 0.5 ‰ more negative than those at 680 °C. Although the higher temperature fractionation factors have a noticeable effect on the calculated $\delta^{18}O_{fluid}$ values, an assumption of calculations to determine $\delta^{18}O_{fluid}$ is that the outputs are minimum values rather than absolute $\delta^{18}O_{fluid}$ values (Rollinson, 1993). With respect to equation (1), a more negative fractionation factor input will result in an increased $\delta^{18}O_{fluid}$ value. Therefore, to calculate minimum values for the $\delta^{18}O_{fluid}$ that infiltrated the Holsnøy system, calculations at lower temperatures of 650 and 680 °C are more suitable. For the calculation of δD_{fluid} values based on the muscovite–H_2O fractionation, however, the effect of temperature on fractionation factors is arguably more significant. While fractionation factors calculated at 650 and 680 °C (– 6.8 and –5.2, respectively) still within the ± 2.0 ‰ error, a fractionation factor of only 0.1 is obtained at 800 °C. Applying this fractionation factor to calculate δD of fluid would result in the minimum possible value for δD_{fluid} in the Holnøy system. However, based on the isotherm presented in Figure 7a, phengite grains only show a slight isotopic disequilibrium at 680 °C, and some grains are arguably in equilibrium with omphacite and garnet grains. Therefore, the isotopic values for δD would be closer to that calculated at 680 °C than 800 °C. Temperatures estimates by Chapter 2 are, hence, reasonable to calculate

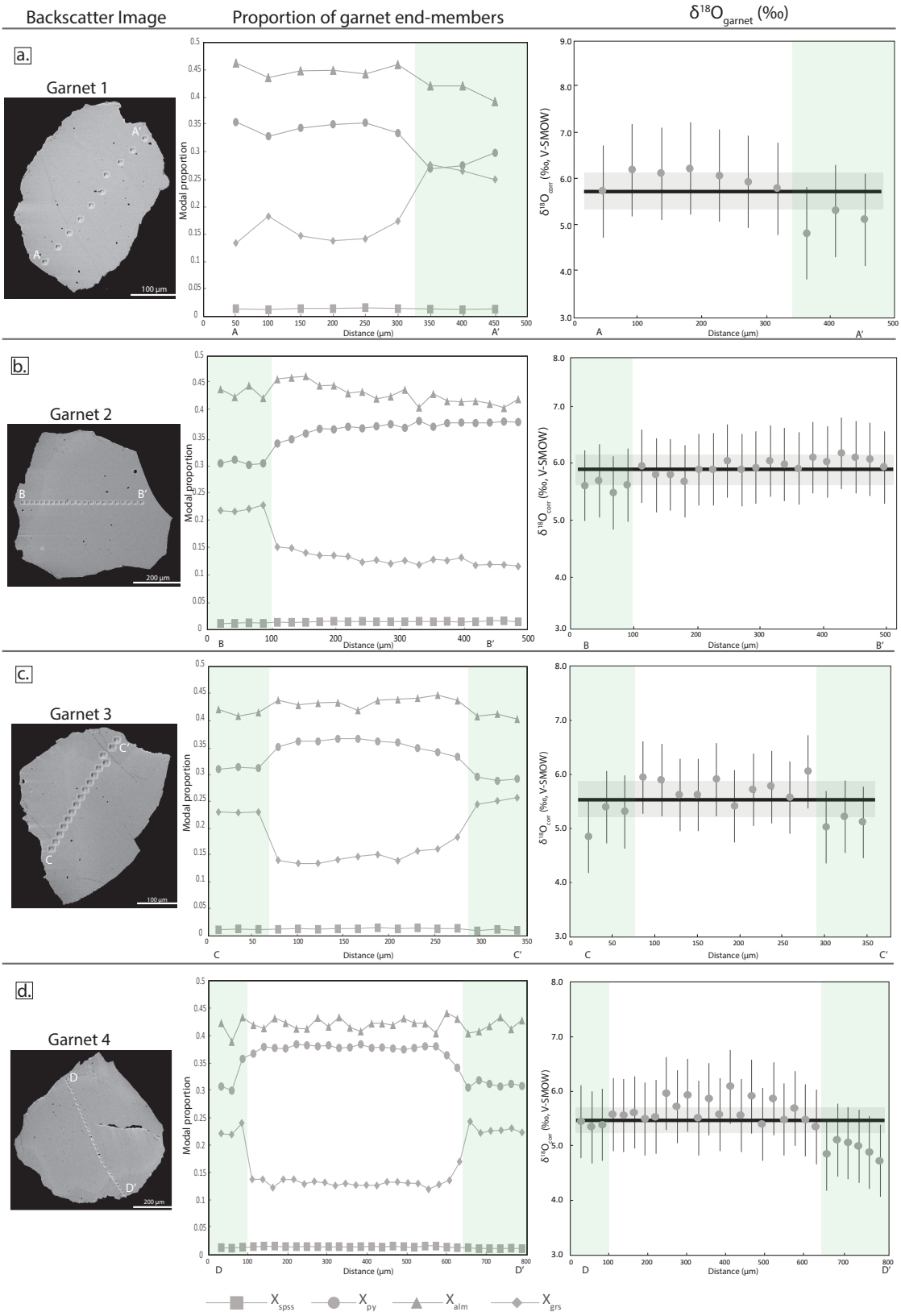

Figure 6. Integrated garnet major element profiles and matrix corrected $\delta^{18}O$ isotopic signatures along the profiles. a) Garnet 1 and corresponding elemental profiles from A to A'; b) Garnet 2 and corresponding elemental profiles from B to B'; c) Garnet 3 and corresponding elemental profiles from C to C' and d) Garnet 4 and corresponding elemental profiles from D to D'. Rim analyses are shaded in green while core analyses remain unshaded.

the isotopic values of the fluid responsible for the conversion of granulite to eclogite on Holsnøy Island.

5.2 $\delta^{18}O$ and δD isotopic signatures

5.2.1 Whole-rock data

Whole-rock analyses of the granulite, eclogite and R-eclogite show the system on Holsnøy Island shifted towards heavier isotopic signatures with increasing degree of conversion to eclogite-facies mineral assemblages, temperature increase and fluid infiltration. However, comparing the whole-rock shifts in eclogite samples (Figure 4a) and R-eclogite samples (Figure 4b) to the granulite protolith, the shifts are less significant at stage 3 than stage 4 of deformation.

The presence of relict garnet cores can explain the slight discrepancies in whole-rock $\delta^{18}O$ shifts (all within error of each other). However, it cannot be used to explain the large negative shift from granulite to eclogite values observed in sample pair HOL14–8A/8B. There is no obvious petrological explanation for the comparatively high $\delta^{18}O$ value in the granulite sample HOL14–8A, and including its signature renders the average granulite value more positive, as shown in Figure 3a (dashed-red box). If its $\delta^{18}O$ value (+ 7.8 ‰) is not considered for calculating the average granulite $\delta^{18}O$ value, then the new average for the granulite is + 6.2 ± 0.2 ‰, as illustrated by the solid red box in Figure 3a. It can be argued that this reflects the positive shift from granulite to eclogite observed in δD. However, this slightly more negative average is within error of that of the eclogite samples (+ 6.5 ± 0.2 ‰), and relies on the $\delta^{18}O$ values of only four samples. Therefore, it is interpreted that no significant shift is recorded in the $\delta^{18}O$ whole-rock values during stage 3 of deformation compared to the δD values (Figure 3b).

The whole-rock dataset, however, highlights the ability for deuterium to record isotopic changes in rock systems, mostly in stage 3 of deformation. Figure 3a shows no significant change in the whole-rock $\delta^{18}O$ from granulite to eclogite, whereas a significant positive shift occurs in the δD (Figure 3b). The lack of shift in $\delta^{18}O$ from granulite to eclogite samples attests for a rock-buffered system in stage 3 of deformation, i.e. the volume of fluid available was not significant enough to shift the $\delta^{18}O$ of the rock as silicate mineral contain abundant oxygen in their lattices. However, due to anhydrous nature of the granulite protolith compared to the hydrous eclogite, the δD of the system shifts readily, even with low fluid volumes. The inverse (i.e. a fluid-buffered system) can be interpreted for stage 4 of deformation as a significant shift in both $\delta^{18}O$ and δD is observed from the granulite, to the eclogite, to the R-eclogite samples.

To test the relative volume of fluid present between stages 3 and 4 of deformation, water–rock ratios were calculated using the following equations, derived by Taylor (1974, 1977):

$$W/R_{closed} = \frac{\delta^{18}O_{final\ rock} - \delta^{18}O_{initial\ rock}}{\delta^{18}O_{initial\ fluid} - \delta^{18}O_{final\ fluid}} \quad , \qquad (3)$$

$$W/R_{open} = \ln(W/R_{closed} + 1) \quad , \qquad (4)$$

where W/R_{closed} represents ratios for a closed system and W/R_{open} for an open system. Lower water–rock ratios indicate that the $\delta^{18}O$ of a system is rock dominated while high water–rock ratios indicate that the system was fluid dominated, hence changing the $\delta^{18}O$ of a rock (Roll-

inson, 1993). The $\delta^{18}O_{final\ rock}$ used are the average whole-rock values for the eclogite (+ 6.5 ‰) and R-eclogite samples (+ 7.2 ‰), and $\delta^{18}O_{initial\ rock}$ used is the average whole-rock $\delta^{18}O$ value for the granulite domains (+ 6.2 ‰). Assuming that the phengite signatures are the closest vectors for the fluid present in both the eclogite and R-eclogite domains, due to phengite's hydrous nature, the $\delta^{18}O_{final\ fluid}$ values used the signatures in both rock types (i.e. + 8.5 and + 9.1, respectively). To determine water–rock ratios, the $\delta^{18}O_{initial\ fluid}$ are usually assumed to be of locally derived fluid signatures. Given the Holsnøy Island eclogites are currently interpreted to have been formed in a deep subduction setting (Austrheim, 2013; Jolivet *et al.,* 2005; Raimbourg *et al.,* 2005; Jamtveit *et al.,* 2018), an initial $\delta^{18}O$ value for altered MORB signatures (+ 10 ‰, Arthur *et al.,* 1983; Muehlenbachs, 1986) was applied as the $\delta^{18}O_{initial\ fluid}$. The resulting W/R_{open} values for stages 3 and 4 of deformation are 0.18 and 0.75, respectively, attesting to a significant increase in fluid volume from stage 3 to stage 4 of deformation.

5.2.2 In-situ garnet analysis

Garnet is stable in both the granulite and eclogite mineral assemblages, which indicates its potential to record isotopic changes, due to its fractionation with the infiltrated fluid. Moreover, the slow diffusion of oxygen in garnet at crustal conditions (Coghlan, 1990; Cole and Charkraborty, 2001; Vielzeuf *et al.* 2005b) make it a valuable isotopic tracer during the evolution of a system. While the $\delta^{18}O$ analyses from garnet cores and rims fall within error of each other, a slight negative shift can be observed from garnet cores to rims as shown in the $\delta^{18}O$ profiles in Figure 6. The weighted average for $\delta^{18}O$ values for all four garnet cores range from 5.65–6.03 ‰, whereas $\delta^{18}O$ values in garnet rims range from 5.08–5.63 ‰. By contrast Van Wyck *et al.* (1996) obtained bulk $\delta^{18}O$ values for granulitic garnets ranging from 5.24 to 5.87 ‰, and bulk $\delta^{18}O$ values for eclogitic garnet ranging from 5.31 to 5.93 ‰, and thus found no conclusive systematic shift in $\delta^{18}O$ in garnet between the two rock types. However, the values of Van Wyck *et al.* (1996) are in agreement with those obtained for the weighted average of each garnet grain (core and rim included) presented Table 5, highlighting the ability for garnet cores to buffer the $\delta^{18}O$ values for the bulk eclogitic garnet analysed by Van Wyck *et al.* (1996).

The negative shift in $\delta^{18}O$ values from garnet core to rim is not consistent with the expected observations for an influx of H_2O-rich fluid, as indicated by the δD whole-rock shift (i.e. positive shifts from core to rim). While at face value this might reflect of a depletion in oxygen-18 by a hydrothermal fluid (Taylor, 1974), this is inconsistent with increases in LOI documented by multiple authors (Chapter 2; Centrella *et al.,* 2016; Jamtveit *et al.,* 1990). It is therefore suggested that the apparent negative shift is more reflective of a metamorphic fractionation effect at eclogite-facies conditions. Indeed, Kohn and Valley (1998) demonstrated that Ca-poor garnet has comparatively higher $\delta^{18}O$ values at eclogite-facies, therefore, establishing an inverse relationship between the grossular content (X_{grs}) of garnet grains and their corresponding $\delta^{18}O$ values. This can observed in each garnet grain, whereby the cores have comparatively lower X_{grs} contents (Figure 6), and hence higher $\delta^{18}O$ values compared to the rim values. This supports the interpretation of stage 3 of deformation being a rock-buffered system.

While the garnet rims equilibrated in a rock-buffered system, the reactions through which they crystallised were catalysed by the availability of the infiltrated fluid (Raimbourg, 2007; Chapter

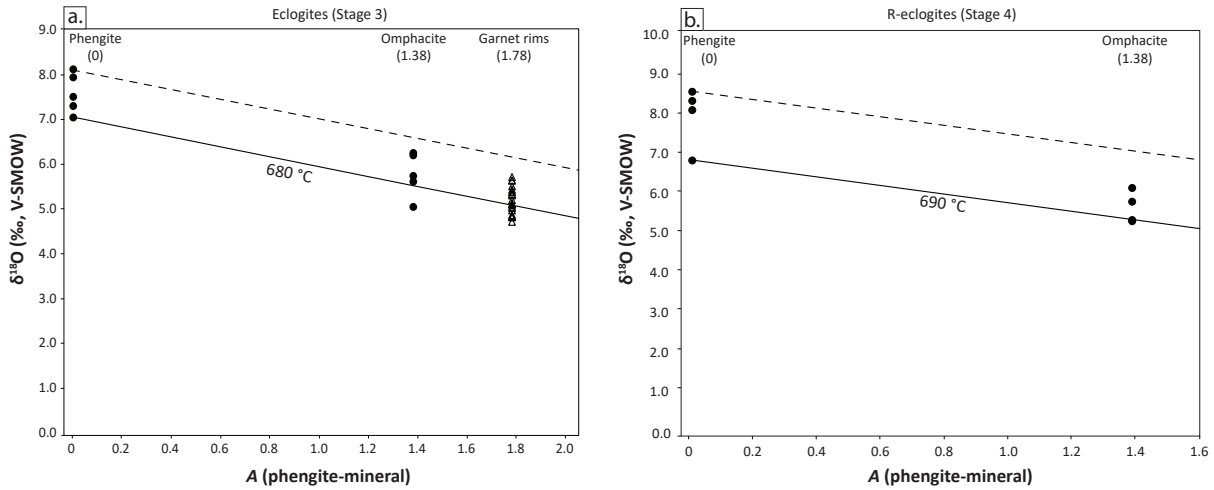

Figure 7. Isotherm plots indicating the extent of isotopic equilibrium in, (a) eclogite samples for coexisting phengite, omphacite and garnet grains, and (b) R-eclogite samples for coexisting phengite and omphacite grains. Filled circles represent bulk mineral analyses while triangle represent in-situ data analyses.

2). Putnis (2010) argued that the observed sharp contact between garnet cores and garnet rims (Figure 7; Chapter 2) are likely to reflect dissolution–re-precipitation reactions, owing to the presence of fluid. Assuming a close-system and equilibrium between the garnet rims and the fluid, fractionation of oxygen between the two can provide further information on the possible $\delta^{18}O$ values of the fluid as discussed below.

5.2.3 Mineral and fluid signatures

Equations 1 and 2 were used to determine the possible $\delta^{18}O$ and δD values for the Holsnøy sytem. To calculate the $\delta^{18}O$ fluid signatures, the pyroxene–fluid fractionation coefficient by Bottinga and Javoy (1975) was used for the omphacite separates, while the phengite–fluid fractionation coefficient from Zheng (1993b) was used for phengite separates in eclogite samples. δD fluid signatures were calculated using phengite mineral separates and the Suzuoki and Epstein (1976) muscovite–fluid fractionation coefficient.

The average $\delta^{18}O$ signature for the fluid, based on omphacite for the eclogite and R-eclogite is + 7.9 ‰. These values are within error of the value calculated based on garnet rims, with weighted average of fluid $\delta^{18}O$ values of 6.71 ± 0.38 ‰ for garnet 1; 7.23 ± 0.33 ‰ for garnet 2; 6.96 ± 0.29 ‰ for garnet 3; and 6.66 ± 0.20 ‰ for garnet 4. A plausible interpretation for the consistency between the isotopic values for the garnet and omphacite analyses is that the fluid maintained the same $\delta^{18}O$ signature during exhumation of the slab. However, this could also be due to the slow diffusivity of clinopyrexenes at lower temperatures (Farver, 1989), which would lead to non-effective fractionation during the isothermal evolution of the Holsnøy eclogites. Moreover, the fluid signatures calculated based on phengite separates show a slight positive increase in average $\delta^{18}O$ values from + 8.5 ‰ to + 9.1 ‰ from the eclogite to R-eclogite, which could potentially reflect the fluid evolution. If it is assumed that phengite, like other micas, acts as an appropriate proxy for the fluid signatures due to its hydrous nature (Dehnari *et al.,* 2019; Warren *et al.,* 2011), this relative positive shift in $\delta^{18}O$ implies the addition of oxygen-18 to the system during the retrogression. This is consistent with an open system behaviour previously documented on Holsnøy Island (Mattey *et al.*, 1994; Van Wyck *et al.*,

1996; Kühn, 2002; Centrella *et al.*, 2016).

In contrast, the mean δD values of phengite separates from eclogite and R-eclogite samples show a negative shift from – 20.6 ‰ to – 23.1 ‰ respectively (Table 4). While this shift is small, the two weighted means are distinct, and are not consistent with the whole-rock dataset, which shows a positive increase in δD values from eclogite to R-eclogite samples (Figure 3b). The major shift in δD observed in the whole-rock isotopic compositions from eclogite to R-eclogite is mainly due to the increase in abundance of phengite itself, rather than a change in isotopic composition of the fluid. The significantly higher abundance of phengite in the R-eclogite (~ 36%), compared to the eclogite (~ 7 %), obscures the relatively negative shift in δD detected by phengite separates. Two possible scenarios can account for a possible negative shift in the δD value of fluids during stage 4 of the metamorphic evolution: 1) the fluid in the Holsnøy system internally evolved to be isotopically lighter in deuterium composition as crystallisation occurred, or; 2) the fluid's composition changed prior to infiltration. At this stage, it is not possible to distinguish between the two possibilities. However, a number of previous studies by Jamtveit *et al.* (1990), Andersen *et al.* (1993) and Mattey *et al.* (1994) suggested the presence of two fluid generations in the Holsnøy system: a D-dominant fluid that interacted with the granulite to form eclogite-facies mineral assemblages; and a relatively D-depleted fluid that later interacted with the eclogite during the amphibolite-facies metamorphism. Based on the fluid signatures of the R-eclogite, it is plausible that the initiation of the second D-depleted fluid infiltration occurred before stage 4 of deformation at *P–T* conditions of 16–17 kbar and 680–700 kbar (Chapter 2; Figure 2).

At such depths, sources of free fluids are considered to be limited as the lower crust is typically fluid poor, and hydrous phases are more likely to be stable within the crystal lattice rather than as a free phase (Yardley, 1981; Connolly & Thompson, 1989). To be able to understand the potential source of fluids, it is crucial to determine the type of fluid that infiltrated the Holsnøy system. Figure 8 shows a plot of all $\delta^{18}O$ and δD values obtained in this study, as well as the isotopic ranges for different fluid reservoirs given by Epstein (1970), Sheppard (1981), and Taylor (1970). While the spread in $\delta^{18}O$ is comparatively large, the majority of the calculated fluid isotopic ratios fall within the range of metamorphic signatures, which usually range from + 2 .0 to + 25.6 ‰ and magmatic signatures which range from + 5.7 and + 9.4 ‰ (Sheppard; Onuma *et al.*, 1972; Taylor, 1974; Graham & Harmon, 1983; Hoefs, 2009). However, the spread of δD based on phengite separates fall within the range of metamorphic signatures, only. This suggests that the fluid that infiltrated the Holsnøy system would have likely been formed by a metamorphic process.

5.2.4 Additional considerations

The isotopic characterisation of the Holsnøy system has been the focus of numerous previous studies and it is generally agreed that the open behaviour for the conversion of granulite to eclogite- facies assemblages renders any isotopic interpretation complex (Van Wyck et al., 1996; Jamtveit *et al.,* 1990; Kühn, 2002; Putnis and Austrheim, 2017). This section discusses some considerations taken during this study, and their possible implications for the $\delta^{18}O$ and δD datasets.

Firstly, for a full and comprehensive check of mineral isotopic values, all major rock forming minerals should be analysed for $\delta^{18}O$ and δD so

that a mass balance calculation can be performed and compared to the whole-rock values. However, finer- grained (< 0.5 mm) minerals—specifically zoisite and amphibole—were not analysed in this study as it was not possible to obtain clean mineral separates by hand-picking. The acquisition of $\delta^{18}O$ and δD data from these two hydrous minerals would have enhanced discussions and interpretations about the composition and source of metamorphic fluid infiltrating the Holsnøy system.

Secondly, for more conclusive identification of fluid types that infiltrate a system, the analysis of both $\delta^{18}O$ and δD on all minerals is advisable (Epstein *et al*., 1965; Epstein 1970; Taylor, 1970; Sheppard, 1977). However, due to analytical limitations in the methods at GNS Science, δD analyses were not obtained on garnet and omphacite grains, but only on phengite separates. The $\delta^{18}O$ and δD values calculated for the fluid based on phengite grains in both eclogite and R-eclogite samples, however, all fall within an unambiguously constricted range (7.95 to 9.69 ‰ for $\delta^{18}O$ and –16.0 to –27.1 ‰ for δD). Combined with the $\delta^{18}O$ data obtained on garnet, omphacite and phengite grains, the dataset herein is the most extensive deuterium and oxygen isotopic dataset obtained for the eclogite on Holnøy Island.

Lastly, the calculations of fluid signatures based on omphacite separates were performed using the pyroxene–H_2O fractionation coefficient by Bottinga and Javoy (1975). This coefficient was chosen as it accounts for oxygen fractionation between temperatures of 500–800 °C, resulting in fractionation factor of –2.1 at 680 °C. Kohn and Valley (1998) suggested that fractionation between garnet and pyroxene is affected by the Ca^{2+} and Fe^{3+} contents of the two minerals, and observed enrichments of ^{18}O in Ca-poor, Fe-rich garnets, compared to omphacite and grossular in eclogite-facies rocks that equilibrated at $\leq$ 650 °C. However, to date, there is lack of experimental calibration for an omphacite–H_2O fractionation coefficient. The comparison of multiple fractionation factors, determined based on different studies and clinopyroxene end-members at a temperature of 680 °C, allowed an exploration into the effects of differing fractionation coefficients on the resultant $\delta^{18}O$ values for fluid. Fractionation factors calculated based on diopside–H_2O and hedenbergite–H_2O pairs by Zheng (1993a) were both –2.1 ‰. Fractionation factors can also be calculated (at 680 °C) based on a combination of multiple mineral pairs and the results are as follows: The diopside –quartz (Valley 2003) and quartz –H_2O (Hu 1979) pairs give a fractionation factor of – 2.6; and the diopside–grossular (Valley 2003) and grossular–H_2O (Zheng 1993a) pairs give a fractionation factor of – 2.9. As demonstrated by equation (1), the more negative the fractionation factor, the higher the $\delta^{18}O$ of the fluid. Therefore, the use of a fractionation factor of – 2.1 results in the minimum possible signature of the fluid based on omphacite separates and is the best estimate available with the lack of experimental fractionation values for omphacite–H_2O. To overcome this lack of experimental data, Matthew *et al.* (1983) previously used a combination of the quartz –diopside and quartz –grossular to determine the fractionation of $\delta^{18}O$ for omphacite and garnet at eclogite-facies conditions, while Kohn and Valley (1998) extrapolated theoretical omphacite fractionation based on empirical data from diopside.

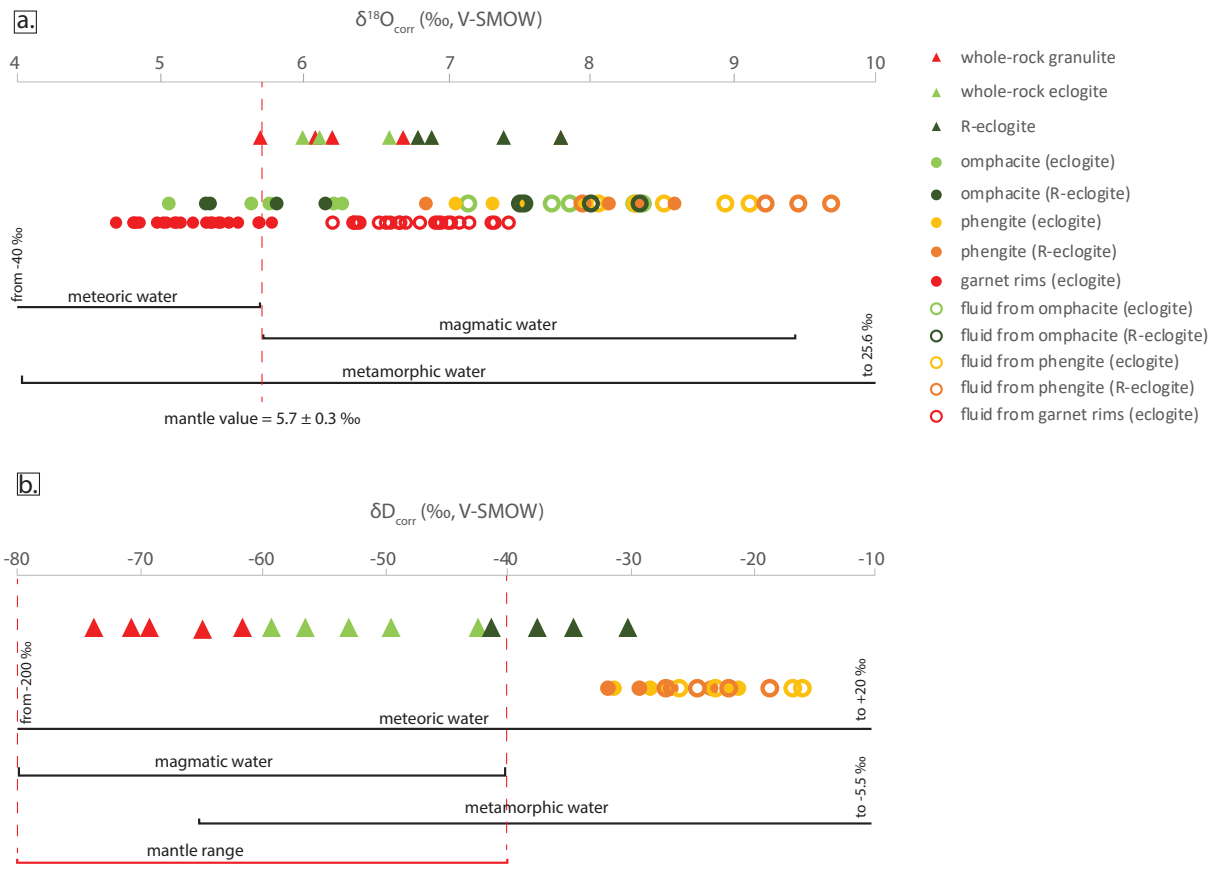

Figure 8. Evolution of $\delta^{18}O$ and δD signatures on Holsnøy Island vs fluid reservoirs. a) Plot of $\delta^{18}O$ data set. b) Plot of δD data set.

6. CONCLUSIONS

In–situ $\delta^{18}O$ garnet analysis provides a powerful tool to investigate possible isotopic changes during fluid influx as garnet grains have the ability to record oxygen zonation at the sub-grain scale. This method is crucial in instances where significant relict garnet cores are present in a metamorphic rock. However, careful consideration should be taken when interpreting *in-situ* $\delta^{18}O$ garnet values, based on the dependency of oxygen-18 on the grossular content of garnet grains.

$\delta^{18}O$ and δD analyses on different minerals suggest metamorphic processes as the most likely source of fluids for the conversion of granulite to eclogite on Holsnøy Island. The presence of a comparatively D-rich fluid is initiated between 15 kbar and 21 kbar on the burial path, with the potential for a subsequent second, comparatively D-poor fluid, between 22kbar to 16 kbar during regression.

REFERENCES

Abbey, S., 1983, Studies in "Standard Samples" of silicate rocks and minerals 1969-1982: *Geological Survey of Canada Paper*, **83-15**, 1-114.

Andersen, T., Austrheim, H. & Burke, E. A. J., 1990. Fluid inclusions in granulites and eclogites from the Bergen Arcs, Caledonides of W. Norway. *Mineralogical Magazine*, **54**, 145-158.

Andersen, T., Austrheim, H. & Burke, E. A. J., 1991. Fluid-induced retrogression of granulites in the

Bergen Arcs, Caledonides of W. Norway: Fluid inclusion evidence from amphibolite-facies shear zones. *Lithos*, **27**, 29-42.

Andersen, T., Austrheim, H., Burke, E. A. J. & Elvevold, S., 1993. N 2 and CO 2 in deep crustal fluids: evidence from the Caledonides of Norway. *Chemical Geology*, **108**, 113-132.

Andersen, T., Burke, E. & Austrheim, H., 1989. Nitrogen-bearing, aqueous fluid inclusions in some eclogites from the Western Gneiss Region of the Norwegian Caledonides. *Contributions to Mineralogy and Petrology*, **103**, 153-165.

Austrheim, H., 1987. Eclogitization of lower crustal granulites by fluid migration through shear zones. *Earth and Planetary Science Letters*, **81**, 221-232.

Austrheim, H., 2013. Fluid and deformation induced metamorphic processes around Moho beneath continent collision zones: Examples from the exposed root zone of the Caledonian mountain belt, W-Norway. *Tectonophysics*, **609**, 620-635.

Austrheim, H. & Boundy, T. M., 1994. Pseudotachylytes generated during seismic faulting and eclogitization of the deep crust. *Science*, **265**, 82-83.

Austrheim, H. & Griffin, W. L., 1985. Shear deformation and eclogite formation within granulite-facies anorthosites of the Bergen Arcs, western Norway. *Chemical Geology*, **50**, 267-281.

Bhowany, K., Hand, M., Clark, C., Kelsey, D., Reddy, S., Pearce, M., Tucker, N. & Morrissey, L., 2018. Phase equilibria modelling constraints on P–T conditions during fluid catalysed conversion of granulite to eclogite in the Bergen Arcs, Norway. *Journal of Metamorphic Geology*, **36**, 315-342.

Bingen, B., Austrheim, H., Whitehouse, M. J. & Davis, W. J., 2004. Trace element signature and U–Pb geochronology of eclogite-facies zircon, Bergen Arcs, Caledonides of W Norway. *Contributions to Mineralogy and Petrology*, **147**, 671-683.

Bottinga, Y. & Javoy, M., 1975. Oxygen isotope partitioning among the minerals in igneous and metamorphic rocks. *Reviews of Geophysics*, **13**, 401-418.

Boundy, T. M., Fountain, D. M. & Austrheim, H., 1992. Structural development and petrofabrics of eclogite facies shear zones, Bergen Arcs, western Norway: implications for deep crustal deformational processes. *Journal of metamorphic geology*, **10**, 127-146.

Boundy, T. M., Mezger, K. & Essene, E. J., 1997. Temporal and tectonic evolution of the granulite-eclogite associ-

ation from the Bergen Arcs, western Norway. *Lithos*, **39**, 159-178.

Centrella, S., Austrheim, H. & Putnis, A., 2016. Mass transfer and trace element redistribution during hydration of granulites in the Bergen Arcs, Norway. *Lithos*, **262**, 1-10.

Chacko, Thomas, et al. "Oxygen isotope fractionations in muscovite, phlogopite, and rutile. " *Geochimica et Cosmochimica Acta* **60.14** (1996): 2595-2608.

Coghlan, R.A.N., 1990. Studies in Diffusional Transport: Grain Boundary Transport of Oxygen in Feldspars, Strontium and REEs in Garnet, and Thermal Histories of Granitic Intrusions in

South-Central Maine Using Oxygen Isotopes. *PhD thesis, Brown University, Providence, RI, USA.*

Cole, D.R. & Chakraborty, S., 2001. Rates and Mechanisms of Isotopic Exchange. Reviews in *Mineralogy and Geochemistry*, **43**, 83–223.

Connolly, J. A. & Thompson, A. B., 1989. Fluid and enthalpy production during regional metamorphism. *Contributions to Mineralogy and Petrology*, **102**, 347-366.

Engvik, A. K., Austrheim, H. & Andersen, T. B., 2000. Structural, mineralogical and petrophysical effects on deep crustal rocks of fluid-limited polymetamorphism, Western Gneiss Region, Norway. *Journal of the Geological Society*, **157**, 121-134.

Erambert, M. & Austrheim, H., 1993. The effect of fluid and deformation on zoning and inclusion patterns in poly-metamorphic garnets. *Contributions to mineralogy and petrology*, **115**, 204-214.

Glodny, J., Kühn, A. & Austrheim, H., 2008. Geochronology of fluid-induced eclogite and amphibolite facies metamorphic reactions in a subduction–collision system, Bergen Arcs, Norway. *Contributions to mineralogy and petrology*, **156**, 27-48.

Govindaraju, K. 1994: Compilation of Working Values and Sample Description for 383 Geochemical standards: Geostandards Newsletter, Vol. 18, Special Issue, 1-58.

Graham, C. & Harmon, R., 1983. Stable isotope evidence on the nature of crust-mantle interactions. In: *Continental basalts and mantle xenoliths*, pp. 20-45, Shiva Nantwich.

Harris, Christopher, and Jacques Vogeli. "Oxygen isotope composition of garnet in the Peninsula Granite, Cape Granite Suite, South Africa: constraints on melting and emplacement mechanisms." *South African Journal of Geology* **113.4** (2010): 401-412.

Hoefs, J., 2009. Variations of Stable Isotope Ratios in Nature. *Stable Isotope Geochemistry*, 93-227.

Hu, G. & Clayton, R. N., 2003. Oxygen isotope salt effects at high pressure and high temperature and the calibration of oxygen isotope geothermometers. *Geochimica et Cosmochimica Acta*, **67**, 3227-3246.

Jamtveit, B., Bucher-Nurminen, K. & Austrheim, H., 1990. Fluid controlled eclogitization of granulites in deep crustal shear zones, Bergen arcs, Western Norway. *Contributions to mineralogy and petrology*, **104**, 184-193.

Jamtveit, B., Moulas, E., Andersen, T. B., Austrheim, H., Corfu, F., Petley-Ragan, A. & Schmalholz, S. M., 2018. High Pressure Metamorphism Caused by Fluid Induced Weakening of Deep Continental Crust. *Scientific reports*, **8**, 17011.

John, T., Klemd, R., Gao, J. & Garbe-Schönberg, C.-D., 2008. Trace-element mobilization in slabs due to non steady-state fluid–rock interaction: constraints from an eclogite-facies transport vein in blueschist (Tianshan, China). *Lithos*, **103**, 1-24.

Jolivet, L., Raimbourg, H., Labrousse, L., Avigad, D., Leroy, Y., Austrheim, H. & Andersen, T. B., 2005. Softening trigerred by eclogitization, the first step toward exhumation during continental subduction. *Earth and Planetary Science Letters*, **237**, 532-547.

Kühn, A., 2002. The influence of fluid on the granulite to eclogite and amphibolite facies transition: a study in the anorthositic rocks from the Lindås Nappe, Bergen Arcs, West Norway. *Unpub. PhD Thesis, University of Oslo*.

Locock, A. J., 2008. An Excel spreadsheet to recast analyses of garnet into end-member components, and a synopsis of the crystal chemistry of natural silicate garnets. *Computers & Geosciences*, **34**, 1769-1780.

Mattey, D., Jackson, D. H., Harris, N. B. W. & Kelley, S., 1994. Isotopic constraints on fluid infiltration from an eclogite facies shear zone, Holsenøy, Norway. *Journal of metamorphic geology*, **12**, 311-325

Muehlenbachs, K. in Stable Isotopes in High Temperature Geological Processes (eds Valley, J.W.,Taylor, H. P. & O'Neil, J. R.) Reviews in Mineralogy Vol. 16, 425±444*, Mineralogical Society of America*, Washington, DC, 1986.

Onuma, N., Clayton, R. N. & Mayeda, T. K., 1972. Oxygen isotope cosmothermometer. *Geochimica et Cosmochimica Acta*, **36**, 169-188.

Petley-Ragan, A., Dunkel, K. G., Austrheim, H., Ildefonse, B. & Jamtveit,

B., 2018. Microstructural records of earthquakes in the lower crust and associated fluid-driven metamorphism in plagioclase-rich granulites. *Journal of Geophysical Research: Solid Earth*.

Philippot, P., 1993. Fluid-melt-rock interaction in mafic eclogites and coesite-bearing metasediments: constraints on volatile recycling during subduction. *Chemical Geology*, **108**, 93-112.

Pollok, K., Lloyd, G. E., Austrheim, H. & Putnis, A., 2008. Complex replacement patterns in garnets from Bergen Arcs eclogites: a combined EBSD and analytical TEM study. *Chemie der Erde-Geochemistry*, **68**, 177-191.

Putnis, A., Jamtveit, B. & Austrheim, H., 2017. Metamorphic Processes and Seismicity: the Bergen Arcs as a Natural Laboratory. *Journal of Petrology*, **58**, 1871-1898.

Raimbourg, H., Goffé, B. & Jolivet, L., 2007. Garnet reequilibration and growth in the eclogite facies and geodynamical evolution near peak metamorphic conditions. *Contributions to Mineralogy and Petrology*, **153**, 1-28.

Raimbourg, H., Jolivet, L., Labrousse, L., Leroy, Y. & Avigad, D., 2005. Kinematics of syn-eclogite deformation in the Bergen Arcs, Norway, implications for exhumation mechanisms. *Special Publication-Geological Society of London*, **243**, 175-192.

Raimondo, T., Clark, C., Hand, M., Cliff, J. & Harris, C., 2012. High-resolution geochemical record of fluid–rock interaction in a mid-crustal shear zone: a comparative study of major element and oxygen isotope transport in garnet. *Journal of Metamorphic Geology*, **30**, 255-280.

Reichen, L.E. and Fahey, J.J, 1962, An Improved Method for the Determination of FeO in Rocks and Minerals Including Garnet. U.S. *Geological Survey Bulletin* **1144B**. 1-5.

Rubatto, D. & Hermann, J., 2003. Zircon formation during fluid circulation in eclogites (Monviso, Western Alps): implications for Zr and Hf budget in subduction zones. *Geochimica et Cosmochimica Acta*, **67**, 2173-2187.

Sharp, Z. D., 1990. A laser-based microanalytical method for the in situ determination of oxygen isotope ratios of silicates and oxides. *Geochimica et Cosmochimica Acta*, **54**, 1353-1357.

Sheppard, S., M. F. 1977. The Cornubian batholith, SW England: DiH and 1sO/160 studies of kaolinite and other alteration minerals. *J. geol. Soc. London*, **133**, 573-91.

Spandler, C., Hermann, J., Arculus, R. & Mavrogenes, J., 2003. Redistribution of trace elements during prograde metamorphism from lawsonite

blueschist to eclogite facies; implications for deep subduction-zone processes. *Contributions to Mineralogy and Petrology*, **146**, 205-222.

Suzuoki, T. & Epstein, S., 1976. Hydrogen isotope fractionation between OH-bearing minerals and water. *Geochimica et Cosmochimica Acta*, **40**, 1229-1240.

Taylor, H., 1974. The application of oxygen and hydrogen isotope studies to problems of hydrothermal alteration and ore deposition. *Economic geology*, **69**, 843-883.

Valley, J. W., 2003. Oxygen isotopes in zircon. *Reviews in mineralogy and geochemistry*, **53**, 343-385.

Van Wyck, N., Valley, J. W. & Austrheim, H., 1996. Oxygen and carbon isotopic constraints on the development of eclogites, Holsnøy, Norway. *Lithos*, **38**, 129-145.

Yardley, B. W., 1981. Effect of cooling on the water content and mechanical behavior of metamorphosed rocks. *Geology*, **9**, 405-408.

Zheng, Y.-F., 1993. Calculation of oxygen isotope fractionation in hydroxyl-bearing silicates. *Earth and Planetary Science Letters*, **120**, 247-263.

CHAPTER 4

Trace element and Sm–Nd constraints on the fluid enhanced eclogitisaion of granulite in the Bergen Arcs, western Norway.

Statement of Authorship

Title of Paper	Sm-Nd and REE constraints on the fluid enhanced eclogitisation of granulite in the Bergen Arcs, western Norway.
Publication Status	☐ Published ☐ Accepted for Publication ☐ Submitted for Publication ☑ Unpublished and Unsubmitted w ork w ritten in manuscript style
Publication Details	Written for publication in Lithos as: Bhowany, K., Hand, M., Clark, C., and Kelsey, D.

Principal Author

Name of Principal Author (Candidate)	Kamini Bhowany		
Contribution to the Paper	Project fieldwork, detailed mapping, sample collection and preparation, data acquisition and analysis, figure making and manuscript writing.		
Overall percentage (%)	80		
Certification:	This paper reports on original research I conducted during the period of my Higher Degree by Research candidature and is not subject to any obligations or contractual agreements with a third party that would constrain its inclusion in this thesis. I am the primary author of this paper.		
Signature		Date	29/08/19

Co-Author Contributions

By signing the Statement of Authorship, each author certifies that:

i. the candidate's stated contribution to the publication is accurate (as detailed above);

ii. permission is granted for the candidate in include the publication in the thesis; and

iii. the sum of all co-author contributions is equal to 100% less the candidate's stated contribution.

Name of Co-Author	Prof. Martin Hand		
Contribution to the Paper	Guidance in the field, assistance during sample and data collection, guidance during manuscript writing, drafting and editing		
Signature		Date	21/08/19

Name of Co-Author	Prof. Chris Clark		
Contribution to the Paper	Guidance in the field, assistance during sample collection, guidance during manuscript drafting and editing		
Signature		Date	4/07/19

Name of Co-Author	Dr. David E. Kelsey
Contribution to the Paper	Guidance in data acquisition, guidance in manuscript writing, manuscript reviewing.
Signature	Date 29/6/19

ABSTRACT

The Lindås Nappe in the Bergen Arcs, western Norway, is one of the best examples of large-scale formation of eclogites due to fluid infiltration within a crustal domain. On Holsnøy Island, the conversion of an anorthositic granulite to eclogite-facies mineral assemblages is progressive, and the evolution of the system can be observed via multiple stages of deformation. These stages span over a range of pressure–temperature (*P–T*) conditions with initial pseudotachylyte recrystallisation at 15.2–15.7 kbar 680°C (stage 1 of deformation), to peak eclogite-facies conditions of 21–22 kbar and 660–690 °C (stage 3 of deformation) and the initial amphibolite-facies retrogression at 16–17 kbar and 680–700 °C (stage 4 of deformation). The systematic sampling of altered domains and their spatially closest granulite protolith allows for a comparative study for the isotopic shifts caused by the influx of fluids. Whole-rock trace elements and Sm–Nd systematics for the eclogite show no significant shifts from granulite to eclogite samples, attesting for a rock-buffered system at stage 3 of deformation. Whole-rock trace elements and Sm–Nd systematics for stage 4 of deformation, however, record significant shifts supporting a fluid-buffered system. Comparatively higher Cu and MnO, and lower Ni and Co contents suggest a sediment-derived fluid for metasomatism, while higher Cr and Y contents, whole-rock REE data and radiogenic εNd signatures suggest a MORB-like-derived fluid. These data support the dehydration of a sedimentary rock with mafic components as the likely source of fluid. However, more trace element data are required to fully characterise the fluid source.

1. INTRODUCTION

The availability and infiltration of fluids in the Earth's crust are important geological processes as drastic changes occur on short timescales (e.g. rock density, regional rheology and geochemical shifts Cooper & Ireland; Austrheim, 1998; Guiraud *et al.*, 2001; Connolly & Kerrick, 2002; Massonne *et al.*, 2007; Faccenda *et al.*, 2012). Fluid infiltration in the crust is often associated with deformation and the formation of high-pressure (HP) and ultra-high pressure (UHP) terranes (Philippot, 1993; Spandler *et al.*, 2003; Tumiati *et al.*, 2007; John *et al.*, 2008) at great depths (> 60 km). However, one aspect of this process that is not always well understood, is the potential source for large volumes of free fluid(s) at HP/UHP conditions (Andersen *et al.*, 1993; Giaramita & Sorensen, 1994; Hacker *et al.*, 2010; Guo *et al.*, 2015). This lack of knowledge limits the understanding of plausible tectonic settings for certain HP/UHP terranes, and more significantly, the geodynamic processes of such terranes.

The HP eclogite domains in the Bergen Arcs, western Norway (Figure 1), are an ideal location to study the process of fluid infiltration in anhydrous crustal rocks as an unaltered granulite protolith and a resulting eclogite domain are perfectly preserved next to each other. This process on Hoslnøy Island is progressive and the evolution of the system can be followed via different stages of deformation over a few kilometres and has been documented by a number of previous authors (Boundy *et al.*, 1992; Austrheim, 2013; Chapter 2). Moreover, the two domains are easily distinguished in the field (Figure 2).

Previous authors have investigated different aspects of the fluid–rock interaction that occurred on Holsnøy Island, such as: the initiation of fluid infiltration through pseudotachylyte formation and its association with deep-seated earthquakes (Austrheim & Boundy, 1994); the density and rheology changes occurring during the conversion of granulite to eclogite (Jolivet *et al.*, 2005); the mechanisms by which fluid infiltrated the

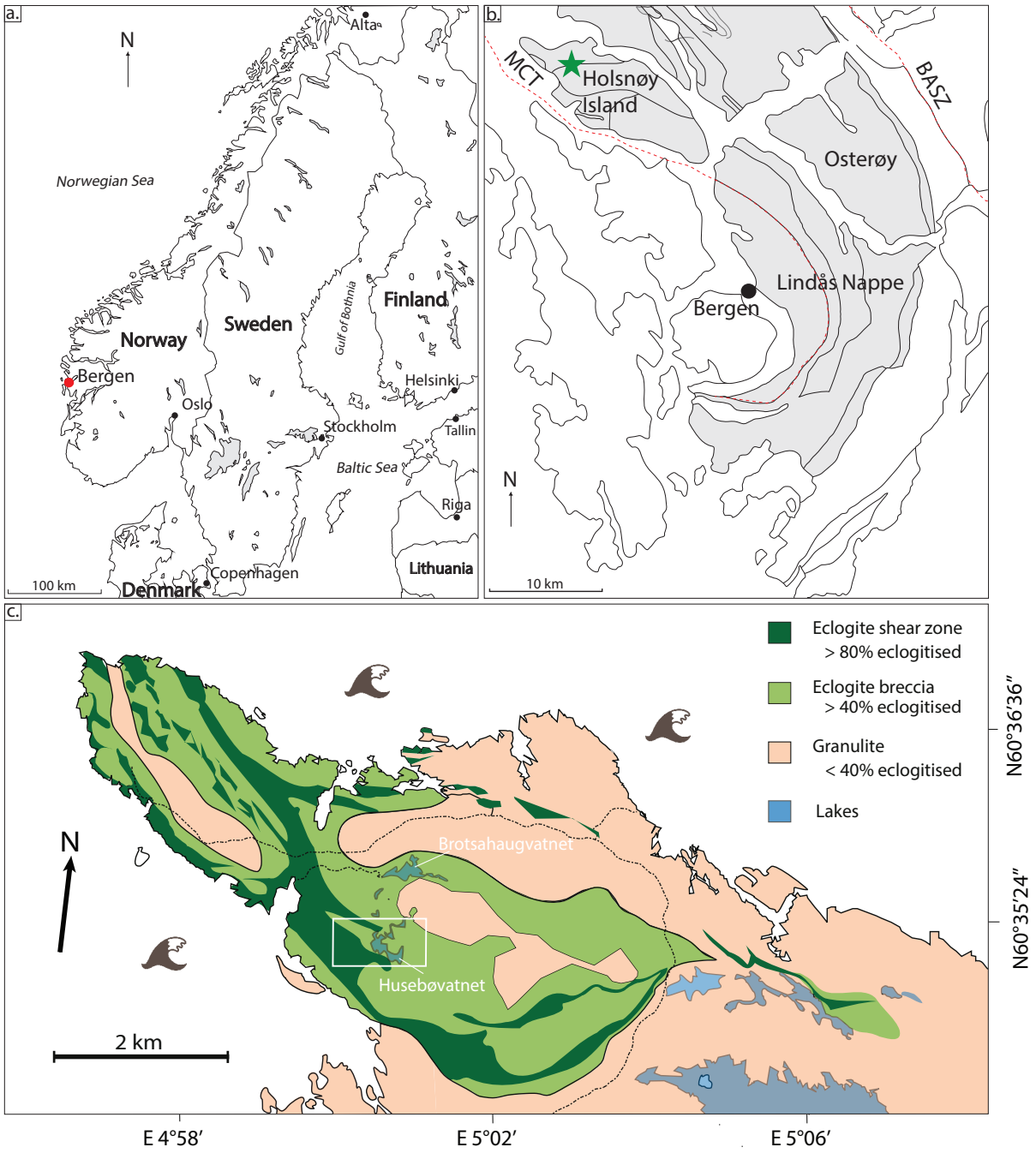

Figure 1. a) Location of Bergen, Norway. b) Location of Holsnøy Island relative to Bergen. c) Modified geological map (from and Boundy *et al.* 1992 and Austrheim *et al.* 1996) of northern Holsnøy island. White box indicates the approximate location of the field area for this thesis.

system (Austrheim, 1987; Jamtveit *et al.*, 1990; Schneider *et al.*, 2007); the potential geophysical response of the resulting hydrous eclogite (Putnis *et al.*, 2017; Jamtveit *et al.*, 2018a); the ages and *P–T* conditions at which different events occurred (Austrheim & Griffin, 1985; Boundy *et al.*, 1997; Chapter 2); and the geochemical fingerprint of the infiltrating fluids (Jamtveit *et al.*, 1990; Andersen *et al.*, 1991a; Andersen *et al.*, 1991b; Mattey *et al.*, 1994; Kühn, 2002) as a means to identify the source of the fluid(s).

To characterise the geochemical signature of the fluid that infiltrated the Holsnøy system, a num-

ber of studies used different stable isotopes (such as O, D, N, C, Cl and Ar) on multiple minerals/ phases (e.g. fluid inclusions in garnet, eclogite and amphibolite-facies pegmatites and veins, and mineral separates in both granulite and eclogite ; Andersen *et al.*, 1990; Jamtveit *et al.*, 1990; Andersen *et al.*, 1991b; Andersen *et al.*, 1993; Van Wyck *et al.*, 1996; Kühn, 2002). The use of stable isotope chemistry revealed two generations of fluids (Andersen *et al.*, 1993; Mattey *et al.*, 1994), with significantly different isotopic signatures, hence two distinct sources. Based on C, N and O isotopic analyses in fluid inclusions in garnet grains the granulite protolith and pegmatites, Andersen *et al.* (1990) and Andersen *et al.* (1993) concluded that the first generation of fluid was likely derived from the granulite protolith.

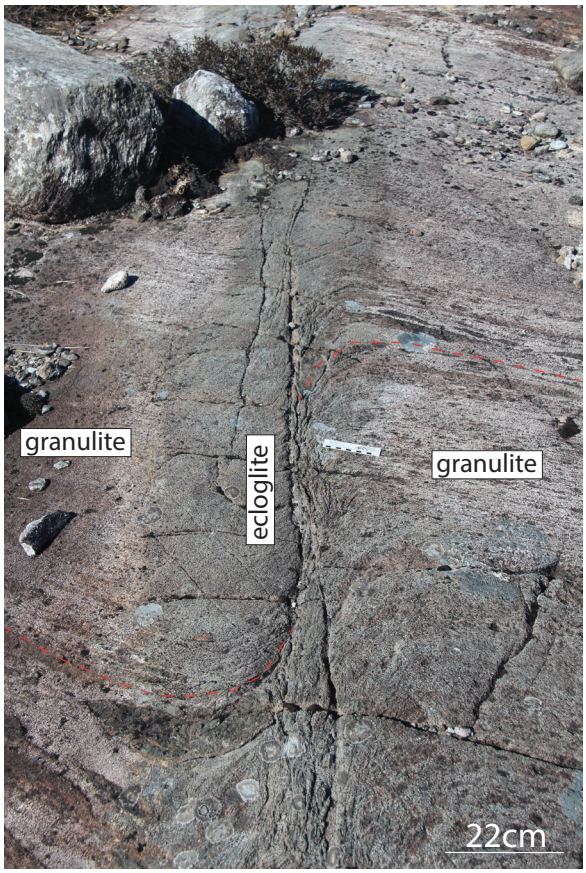

Figure 2. Field photograph of a small scale shear zone. The greyish-green colour of the eclogite domain is distinct in colour the pink granulite. The dotted red line represent displacement of garnet-pyroxene bands due to shear zone. *scale in photograph is 11cm long.

The second generation of fluid is, generally, considered to be from an external source (Andersen *et al.*, 1990; Andersen *et al.*, 1993; Mattey *et al.*, 1994; Van Wyck *et al.*, 1996), most likely the dehydration of either N_2-rich metasediments or other crustal rocks, as proposed by Andersen *et al.* (1993) and Mattey *et al.* (1994), based on N, Ar and C analyses. However, besides the potentially N-rich nature of the units that dehydrated to provide N-rich fluids for the rehydration of the granulite domains on Holsnøy Island, no other isotopic characteristics are known for these potential source units. To be able to constrain which underlying units dehydrated to produce the fluid responsible for the formation of the eclogites, more information is needed about the geochemical signature (e.g. radiogenic and trace element chemistry) of the external fluid. Constraining the provenance of the externally derived fluid is crucial as this can help improve tectonic models of the Bergen Arcs, and ultimate, the geodynamic processed that drives the formation of HP terranes during fluid-rock interaction.

This study is complementary to the $\delta^{18}O$ and δD constraints determined on both whole-rock chemistry and fluid chemistry based on the isotopic signature of mineral separates and *in-situ* $\delta^{18}O$ garnet analyses previously presented in Chapter 3. The work presented here, however, uses the combination Sm–Nd isotopic data, trace element chemistry in whole-rock and mineral grains and trace element distribution in garnet grains to determine chemical shifts occurring during fluid infiltration. While radiogenic isotopes and trace elements have previously been used for dating the fluid–rock interaction (Bingen *et al.*, 2001; Kühn *et al.*, 2002; Glodny *et al.*, 2003) and to investigate the role of fluid and deformation on elemental migration (Schneider *et al.*, 2007; Centrella *et al.*, 2016), no other studies have used them as

a mean to investigate the signature of the fluids that permeated through the granulite domains on Holsnøy Island. The systematic sampling of altered domains and their nearest granulite protolith undertaken herein, allows for any chemical shift observed from the protolith to the eclogite to be assumed to be due to the composition of the fluid. Additionally, the samples used allow for the radiogenic and trace elemental characterisation of the infiltrated fluid within the *P–T* framework developed in Chapter 2. Together, these place constraints on the most likely lithology type that dehydrated to produce the external source of fluid responsible for the formation of the eclogite and R-eclogite.

2. GEOLOGICAL SETTING AND BACKGROUND

Holsnøy Island is situated approximately 45 km north west of Bergen, western Norway (Figure 1b). The rocks on Holsnøy Island form part of the Lindås Nappe, which is part of an arcuate structure around Bergen, called the Bergen Arcs. The eclogite domains mainly outcrop on the north western part of Holsnøy Island and (Figure 1c) and the progressive structural evolution of the system can be observed within a few kilometres of each other (Boundy *et al.*, 1992; Austrheim, 2013).

The originally emplaced anorthosite was metamorphosed at granulite-facies during the Grenvillian Orogeny (c. 950 Ma; Austrheim & Griffin, 1985) at estimated *P–T* conditions 8 kbar and 800–900 °C, and characterised by an anhydrous peak mineral assemblage of garnet, orthopyroxene, clinopyroxene and plagioclase. The granulite cooled down and was subsequently buried during the Caledonian Orogeny (c. 450 Ma; Boundy *et al.*, 1992; Bingen *et al.*, 2001; Kühn *et al.*, 2002; Glodny *et al.*, 2008) during the collision of Laurentia and Baltica. The progressive conversion of the anhydrous granulite to eclogite was enhanced by the availability of fluid, and has been documented in detail by previous authors (Austrheim & Griffin, 1985; Austrheim, 1987; Van Wyck *et al.*, 1996; Austrheim, 1998; Pollok *et al.*, 2008; Jamtveit *et al.*, 2018b). This study is founded on the *P–T* framework set in place in Chapter 2 (Figure 3), based on different stages of

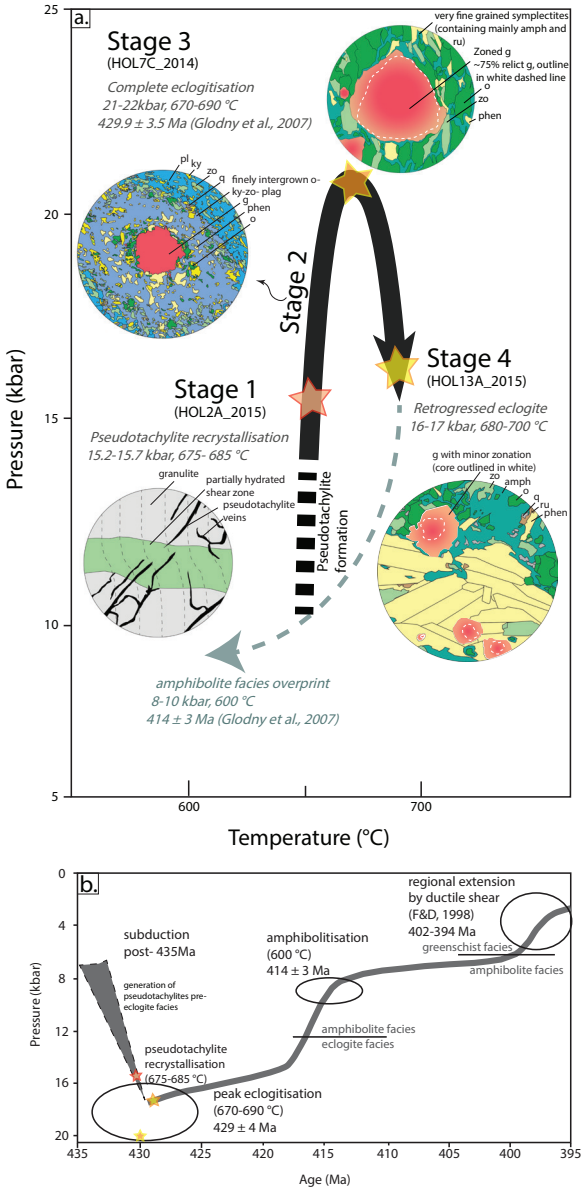

Figure 3. a) *P–T* path undergone by the Holsnøy domains, after Bhowany *et al.* (2018). b) *P–T–t* evolution of the Holsnøy system after Boundy *et al.* (1997).

deformation in the structural evolution of the Holsnøy system. In summary, the eclogite domains were formed in four main stages of deformation, depicted in Figure 3. Stage 1 of deformation involves the formation of pseudotachylyte at *P–T* conditions 15.2–15.7 kbar and 675–685 °C, as well as fractures, which both provided the initial conduit for fluid infiltration. Stage 2 involved the formation of small-scale discrete shear zones along the initial fractures, as fluid availability increased. This stage of deformation is indicated by the breakdown of garnet grains to form hydrous assemblage (Figure 3). Stage 3 of deformation is the complete, large scale conversion of granulite to eclogite, indicated by the complete disappearance of plagioclase. This stage occurred at peak metamorphic conditions 21–22 kbar and 670–690 °C, based on phased equilibria modelling done on eclogite sample, HOL14–7C. (Figure 3; Chapter 2), and has interpreted peak mineral assemblage, garnet rims–omphacite–zoisite–phengite–kyanite ± rutile. Stage 4 of deformation is the formation of a phengite-rich retrogressed eclogite (R–eclogite) at *P–T* conditions 16–17 kbar and 680–700 °C, with interpreted peak mineral assemblage garnet–omphacite–phengite–zoisite–quartz ± rutile (Figure 3). This study focuses on the two most fluid affected stages, 4 (eclogite) and 5 (R–eclogite), to obtain potential information on the fluid that infiltrated the Holsnøy system.

The use of stable and radiogenic isotopes revealed the potential infiltration of two distinct generations of fluids, each with their unique signatures, measured on fluid inclusions in quartz and garnet grains: a relatively N_2–H_2O-rich fluid reacting with the granulite pre-eclogite facies (i.e. stage 1 and 2 of deformation), followed by N_2–CO_2-fluid reacting with the eclogite during retrogression (i.e. stage 3 of deformation; Chapter 3). The initial fluid that infiltrated the Holsnøy system (i.e. first generation of fluid), pre-peak eclogite metamorphic conditions, has been interpreted to be internally derived, based on N_2 analyses done on fluid inclusions, yielding $\delta^{15}N$ values of +6 ‰ in the granulite and +3 ‰ in the eclogite (Andersen *et al.*, 1991b; Andersen *et al.*, 1993; Mattey *et al.*, 1994). Moreover, Jamtveit *et al.* (1990) used phase-equilibria constraints to estimate high water activity ($X_{H_2O} > 0.75$) on granulite, eclogite and eclogite-facies extension veins, for the fluid that first reacted with the granulite domains. This is also consistent with the minor positive shifts described by Van Wyck *et al.* (1996) from whole-rock granulite to fluid-affected domains (+ 6.4 ‰ to + 6.6 ‰) as well as the positive shifts in δD observed in Chapter 3 (– 68.0 ‰ to – 52.1 ‰). This increase in $\delta^{18}O$ is also reflected in mineral separates such as clinopyroxene, and *in-situ* garnet analyses from core to rim in the eclogite facies samples (Chapter 3). Therefore, it was interpreted by those authors that an internally derived N_2–H_2O-rich fluid reacted with the granulite at conditions prior peak eclogite-facies. The second generation of fluid infiltrated the system at post-peak eclogite-facies conditions, during retrogression (Chapter 3; Andersen *et al.*, 1993; Mattey *et al.*, 1994), and was proposed to be externally derived based $\delta^{13}C$ and $\delta^{15}N$ data. An increase in $\delta^{13}C$ in fluid inclusions in garnet grains, from –10 ‰ in the eclogite to –5 ‰ in a retrogressed-eclogite was interpreted as the infiltration of a CO_2-rich fluid. While $\delta^{15}N$ decreased from +6 ‰ to +3 ‰, from granulite to eclogite samples, Mattey *et al.* (1994) suggested an N_2-rich fluid based on $\delta^{15}N$ values of +14.7 ‰ in pegmatites. This is supported by Andersen *et al.* (1990) who detected a second, post-peak eclogite, pulse of pure N_2 and CO_2 fluids inclusions, using Raman microanalysis. Moreover, Andersen *et al.* (1991b) suggested the introduction of a 'brine-like' fluid based on Cl^- fluid

Table 1. Sample location and summary

Sample	Location (32V)		Mineralogy	Additional information
	Easting (mE)	*Northing (mN)*		
Granulite				
HOL14-7A	0281226	6723701	pl + g + cpx + opx + ru	Protolith to HOL14-7C
HOL14-8A	0281226	6723701	pl + g + cpx + opx + ru	Protolith to HOL14-8B
HOL15-6	0283310	6724215	pl + g + sp ± ru	Protolith to HOL15-5
HOL15-12	0280999	6723661	pl + g + cpx + opx ± ru ± sp	Protolith to HOL15-10 and HOL15-11
HOL15-15	0282213	6723307	pl + g + cpx + opx	Protolith to HOL15-14, HOL15-13B, HOL15-13E and HOL16-2
Eclogite				
HOL14-7C	0281226	6723701	o + g + phen + zo + ky ± ru ± q	Relict spinel in garnet cores
HOL14-8B	0281226	6723701	o + g + phen + zo + ky ± ru ± q	
HOL15-5	0283310	6724215	o + g + phen + zo ± ru ± q	
HOL15-10	0280999	6723661	o + g + phen + zo ± ru ± q	Relict spinel in garnet cores
HOL15-11	0280999	6723661	o + g + phen + zo ± ru ± q	
R-eclogite				
HOL15-14	0282213	6723307	o + g + phen + zo + amp ± ru ± q	
HOL15-13B	0282213	6723307	o + g + phen + zo + amp ± ru ± q	
HOL15-13E	0282213	6723307	o + g + phen + zo + amp ± ru ± q	
HOL16-2	0282213	6723307	o + g + phen + zo + amp ± ru ± q	

inclusion in eclogite shear zones, Kühn (2002) suggested the same fluid type of fluids throughout the amphibolite-facies based the detection of Cl^- in amphibolite grains.

While the first fluid pulse is generally agreed to be internally derived, the origin of the secondary post-peak eclogite sourced H_2O–CO_2–N_2–Na-Cl-rich fluid is not very clear (Andersen *et al.*, 1991b). Van Wyck *et al.* (1996) used a combination of O and C isotopes to suggest the devolatilisation of an underlying sediment in close proximity of the Lindås Nappe as the potential source for the external fluid, whereas Andersen (1991) previously suggested the devolatilisation of either a mantle-like or N_2-rich crustal rock as the source of fluid. However, Mattey *et al.* (1994) argued that the eclogite domains are too radiogenic—based on Ar data—to be a mantle-like source, and instead leaned towards the dehydration or N_2-rich crustal rocks being the source of the fluid. This is in line with observations from Chapter 3, whereby $\delta^{18}O$ and δD isotopic values are consistent with that of metamorphic fluids. Moreover, Mattey *et al.* (1994) suggested a potentially K-rich unit-rich crustal source based on high $^{40}Ar/^{36}Ar$ ratio in the sheared eclogite domains. However, they also concluded that the C, N and Ar compositions obtained for the fluid do not necessarily point to any particular sources, but is likely associated with the devolatilisation of sediments.

To address this uncertainty around the diagnosis of a particular source for the external fluid that infiltrated Holsnøy Island, this study uses radiogenic Sm–Nd and trace element chemistry to determine the chemical shifts that occurred due to fluid influx. This is done in sample pairs (i.e. an altered domain and its spatially closest granulite protolith) to account for the heterogeneity of the granulite domains. The Sm–Nd system has previously been used to date the ages of fluid–rock

interaction of the eclogitisation process (425–440 Ma; Boundy *et al.*, 1997; Kühn *et al.*, 2002) and REE chemistry has previously been employed to investigate the role of fluid and deformation in elemental migration (Schneider *et al.*, 2007). However, no other studies have used these two systems as a means to characterise the infiltrated fluid, and potentially, to obtain more information on the source of the fluid.

3. SAMPLES

A summary of the samples used in this chapter is presented in Table 1. Like in Chapter 3, the samples were systematically collected in pairs; i.e. the sampling of altered domains and their spatially nearest granulite protolith. This is important as the characterisation of the closest granulite protolith for each sample needs to account for the potential heterogeneity of the originally emplaced anorthosite. Moreover, it is ideal for a comparative study whereby the geochemical signatures of the granulite protoliths are assumed to be that of the host rocks pre-fluid infiltration during the Caledonian Orogeny, thus providing a baseline for relative shifts observed in the altered domains. Sample pairs for stage 3 of deformation (i.e. eclogites) were collected no more than 3 m apart, and sample pairs for stage 4 of deformation (i.e. R-eclogites), were within 1 m of each other. The interpreted peak mineral assemblages for each sample is presented in Table 1. However, the general mineral assemblage for each lithology is as follows; granulite, garnet–clinopyroxene–plagioclase ± rutile; eclogite, garnet–omphacite–zoisite–phengite–kyanite ± rutile ± quartz and R-eclogite, garnet–omphacite–zoisite–phengite–amphibole ± rutile ± quartz. The type of analysis performed on each sample is summarised in Table 2.

4. METHODS

4.1 Whole-rock geochemistry and mineral major elemental analysis

Whole-rock analyses for major and trace elements were performed at the Department of Earth and Environment, Franklin and Marshall College, Lancaster, Pennsylvania. Elements were analysed

Table 2. Summary of analyses performed on each sample

Samples	Analyses					
	WR major and trace elements	***Mineral major elements***	***WR REE***	***Mineral REE***	***LA-ICP-MS mapping***	***Sm/Nd***
Granulite						
HOL14-7A	✓	✓	✓	✓		✓
HOL14-8A	✓					✓
HOL15-6						✓
HOL15-12						✓
HOL15-15	✓	✓	✓	✓	✓	✓
Eclogite						
HOL14-7C	✓	✓	✓	✓	✓	✓
HOL14-8B	✓					✓
HOL15-5						✓
HOL15-10						✓
HOL15-11						✓
R-eclogite						
HOL15-14	✓					✓
HOL15-13B			✓	✓	✓	✓
HOL15-13E	✓	✓				✓
HOL16-2						✓

by Wavelength Dispersive X-ray Fluorescence (WD-XRF) spectrometry, on fused disks prepared using a lithium tetraborate flux. The amount of ferric and ferrous iron was determined by wet chemistry.

Quantitative analyses of major elements in the major rock forming minerals were acquired using a CAMECA SXFive electron microprobe at the Adelaide Microscopy, University of Adelaide. A beam current of 20nA was used, with an accelerating voltage of 15 kV. The calibration of the instrument was done prior to analyses on an andradite standard. Wavelength dispersive spectrometers (WDS) were used to analyse for SiO_2, TiO_2, Al_2O_3, Cr_2O_3, FeO, MnO, MgO, ZnO, CaO, Na_2O, K_2O, Cl and F.

4.2 Whole-rock REE and mineral trace elemental analysis

Whole-rock REE (La, Ce, Pr, Nd, Sm, Eu, Gd, Tb, Dy, Ho, Er, Tm, Yb and Lu) analysis was conducted at Bureau Veritas Minerals (Perth) using Fused Bead Ablation ICP–MS, a method developed by Bureau Veritas. Approximately 0.3 g of each sample was fused with Lithium Borate flux to form a homogeneous fused bead and elements of interest were analysed using Inductively Coupled Plasma–Optical Emission Spectrometry (ICP–OES) and Inductively Coupled Plasma–Mass Spectrometry (ICP–MS) on a 5300V Perkin Elmer and Nexin Perkin Elmer, respectively.

Quantitative REE analyses on major rock forming minerals were obtained using Laser Ablation–Inductively Coupled Plasma–Mass Spectrometry (LA–ICP–MS) at the Adelaide Microscopy, University of Adelaide. Mineral grains were analysed with a Resonetics M-50-LR 193 nm excimer laser, coupled with an Agilent 7700x Quadropole ICP–MS. A suite of 33 elements, including trace elements Y, La, Ce, Pr, Nd, Sm, Eu, Gd, Tb, Dy, Ho, Er, Tm, Yb, Lu and Hf, were measured with a total acquisition time 70.7 s, including a 30 s background measurement. Spot sizes differed based on the grain sizes of specific minerals; 19 µm for smallest grains and 43 µm for the larger grains. Samples were ablated with a fluence of ~3.5 J/cm^2 and repetition rate of 10 Hz. The NIST612 standard was used as the primary standard for calibration and drift correction, and GSD-1G was analysed as a secondary standard (values reported in Table S3.1).

Post-acquisition data reduction was performed using the open source software *Iolite* (Woodhead et al., 2007; Hellstrom et al., 2008; Paton et al., 2011), developed by the Melbourne Isotope Research Group (University of Melbourne). NIST612 was used as the analysed standard and Ca, Al and Fe as internal standards using different oxide values based on minerals and samples.

4.3 Trace elements maps

Qualitative REE maps were acquired on three samples (HOL14–7A, HOL15–15 and HOL15–13B) using a Resonetics M-50-LR excimer laser, coupled with an Agilent 7700x Quadropole ICP-MS at Adelaide Microscopy, The University of Adelaide. Instrument conditions for mapping were done based on acquisition techniques outlined by Raimondo *et al.* (2017) for silicates (Ismail *et al.*, 2014; Kontonikas-Charos *et al.*, 2014; Sharrad *et al.*, 2014; Xu *et al.*, 2016). Garnet maps were acquired from a standard 30 µm thin section, placed into the analysis chamber with a mounted spring-loaded holder designed for 25 mm glass slides. Images were acquired by the ablation of a series of parallel rasters across the garnet grain's surface to produce a rectangular

Table 3. Representative whole-rock chemistry. Element oxides are in wt % and trace elements in ppm

				Stage 3 of deformation		*Stage 4 of deformation*	
	Granulite			**Eclogite**		**R-eclogite**	
	HOL14-7A	HOL14-8A	HOL15-15	HOL14-7C	HOL14-8B	HOL15-13E	HOL15-14
SiO_2	51.22	50.77	49.03	46.51	47.45	48.33	49.87
TiO_2	0.49	0.57	0.18	0.61	0.64	0.64	0.94
Al_2O_3	18.35	19.19	23.88	18.65	19.40	20.69	22.96
MnO	0.19	0.19	0.10	0.20	0.20	0.21	0.10
MgO	5.69	5.45	7.14	6.60	6.17	7.10	6.34
CaO	8.88	8.52	8.81	10.93	9.67	7.70	6.80
Na_2O	3.55	3.63	3.19	3.34	3.58	3.02	2.63
K_2O	0.72	0.71	0.65	0.79	0.50	2.49	4.36
P_2O_5	0.03	0.04	0.04	0.03	0.04	0.04	0.02
LOI	1.14	0.91	0.74	1.36	1.40	2.44	2.99
FeO	6.97	6.40	3.41	7.23	7.07	6.22	2.88
Fe_2O_3	2.58	3.50	3.24	3.35	3.59	2.63	2.37
Total	100.59	100.59	100.05	100.41	100.50	99.76	99.59
Rb	2.1	1.1	4.0	2.0	1.1	25.0	39.0
Sr	1002.0	1212.0	993.0	948.0	1248.0	424.0	599.0
Y	10.8	11.1	0.8	13.4	13.1	14.4	6.2
Zr	19.0	26.0	27.0	19.0	21.0	19.0	26.0
V	185.0	175.0	24.0	262.0	225.0	154.0	157.0
Ni	32.0	29.0	125.0	39.0	46.0	124.0	105.0
Cr	48.0	48.0	41.0	60.0	160.0	162.0	170.0
Nb	<1	<1	<0.5	<1	<1	<0.5	<0.5
Ga	18.8	19.6	16.7	18.9	19.7	15.8	20.7
Cu	9.0	11.0	7.0	34.0	21.0	61.0	12.0
Zn	95.0	83.0	43.0	90.0	96.0	48.0	43.0
Co	39.0	37.0	37.0	42.0	41.0	31.0	17.0
Ba	567.0	840.0	560.0	847.0	639.0	2912.0	4813.0
Ce	14.0	15.0	19.0	14.0	18.0	4.0	10.0
U	<0.5	1.3	<0.5	<0.5	<0.5	<0.5	1.0
Th	<0.5	<0.5	<0.5	<0.5	<0.5	<0.5	<0.5
Sc	25.0	20.0	5.0	33.0	27.0	22.0	17.0
Pb	<1	2.0	<1	<1	<1	8.0	41.0

grid. Each raster was pre-ablated to limit the effect of redeposition, and a background measurement of 30 s was performed before each scan. The Resonetics M-50 uses a two-volume laser ablation cell (designed by Laurin Technic Pty), to facilitate the fast wash out of ablated material. Ablation was carried out in an atmosphere of UHP He (0.70 L min^{-1}), mixed Ar (0.93 L min^{-1}) after each ablation cell. Different beam diameters were required for different samples for optimum resolution, as follows: 16 µm for HOL15–13B, and 23 µm for HOL14–7C and HOL15–15. A laser repetition rate of 10 Hz was used to produce an energy density of ~ 3.5 J cm^{-2}, and scan speeds of 16 µm s^{-1} (HOL15–13B) and 23 µms^{-1} (HOL14–7C and HOL15–15). Line spacing differed from sample to sample, depending on the beam diameter used (i.e. spacing of 16 µm for beam diameter 16 µm and spacing of 23 µm for beam diameter of 23 µm). Data acquisition time differed from sample, depending on the dimensions of the areas mapped. However, acquisition was done in time-resolved analysis mode as a single continuous experiment. Each analysis comprised a suite of 32 elements (Table S3.2), with a total sweep time of 0.285 s. The primary standard, GSD-1D and secondary standard NIST610, were analysed before and after each

mapping run and are reported in Table S3.3, with a total acquisition time of 70.4 s, including 30.8 s background.

Post-acquisition data reduction was performed using the open source software. The MatLab based software, XMapTools (Lanari *et al.*, 2014) was used for image processing and analysis.

4.4 Whole-rock Sm–Nd chemistry

Whole-rock Sm–Nd analyses were performed at the University of Adelaide. Approximately 0.2 g of rock power was digested with a $^{150}Nd/^{147}Sm$ mixed spike solution and evaporated to dryness in 2 ml of HNO_3 (7 M) and 4 mL of HF (28 M) at 140 °C in sealed Teflon vials. Samples were then digested in a 7M HNO_3 and 4 mL of 28 M HF at 190 °C for over 96 hr. After complete digestion, the samples were redissolved in 6 mL of 6 M HCl, and heated for two days at 160 °C for conversion to chlorides, then evaporated to dryness. Sm and Nd samples were then separated out by ion chromatography, in Teflon-powder columns, and their isotopic abundance ratios were determined by Thermal Ionisation Spectrometry (TIMS) on an Isotopx Phoenix. Throughout data acquisition, Nd concentrations were corrected to 100 pg blank whereas Sm concentrations to 50 pg blank, and the USGS-G2 standard was used with measured value of 0.512280 ± 0.000002.

5. RESULTS

5.1 Whole-rock geochemistry and mineral major elemental chemistry

Major and trace element whole-rock geochemistry was performed on three granulite samples (HOL14–7A, HOL14–8A and HOL15–15), two eclogite samples (i.e. stage three of deformation; HOL14–7C, HOL14–8B) and two R-eclogite

Table 4. Representative mineral chemistry, in wt %.

				Stage 3 of deformation					*Stage 4 of deformation*					
	Granulite			Eclogite					R-eclogite					
	g	pl	cpx	o	g rim	g core	phen	zo	o	g rim	g core	phen	zo	amp
SiO_2	40.58	64.00	47.10	54.36	37.76	37.93	46.94	38.59	55.23	39.24	40.11	46.79	38.45	43.64
TiO_2	0.09	0.00	0.17	0.24	0.11	0.11	0.52	0.09	0.19	0.06	0.16	0.87	0.04	0.41
Al_2O_3	23.45	22.34	16.76	11.68	21.28	20.75	31.63	31.02	10.85	22.01	22.73	31.85	31.11	15.25
Cr_2O_3	0.02	0.00	0.00	0.01	0	0	0	0.01	0.01	0.03	0.03	0.01	0.02	0
FeO	13.01	0.01	7.25	5.33	22.31	23.3	2.34	3.23	4.63	20.7	17.55	1.87	2.98	11.32
MnO	0.18	0.00	0.04	0.02	0.51	0.76	0	0	0.02	0.68	0.41	0	0	0.2
MgO	15.19	0.00	12.16	8.31	7.79	9.84	2.11	0.04	9.11	8.45	13.56	2.21	0.02	12.26
ZnO	0.00	0.02	0.02	0	0	0.03	0	0.09	0.03	0	0	0	0.09	0.01
CaO	7.60	3.13	11.17	13.21	8.77	5.5	0.01	0	14.19	8.3	5.76	0.01	0.04	9.39
Na_2O	0.01	9.93	2.70	6.68	0.06	0.02	0.91	23.54	6.09	0.03	0.01	1.55	23.86	3.86
K_2O	0.00	0.21	0.78	0	0	0	8.8	0.02	0.01	0	0	8.76	0.02	0.76
Cl	0.00	0.00	0.01	0.02	0	0	0.01	0	0.01	0.01	0.01	0.01	0	0.06
F	0.00	0.00	0.00	0	0.01	0	0	0	0	0	0.01	0	0	0.09
TOTAL	100.14	99.64	98.15	99.89	98.62	98.32	94.28	96.63	100.4	99.52	100.4	94.86	96.63	97.28
No. O	12	8	6	6	12	12	11	13	6	12	12	11	13	23
Si	1.72	2.83	2.95	1.94	2.93	2.94	3.2	2.99	1.96	3	2.96	3.15	2.97	6.85
Ti	0.00	0.00	0.01	0.01	0.01	0.01	0.03	0.01	0.01	0	0.01	0.04	0	0.05
Al	0.72	1.16	2.01	0.49	1.95	1.9	2.54	2.83	0.45	1.98	1.98	2.53	2.84	2.82
Cr	0.00	0.00	0.00	0	0	0	0	0	0	0	0	0	0	0
Fe^{3+}	0.05	0.00	0.09	0.08	0.19	0.21	0	0.18	0.03	0.02	0.09	0.04	0.22	0
Fe^{2+}	0.17	0.00	0.70	0.07	1.25	1.3	0.13	0.03	0.1	1.31	1	0.06	0	1.49
Mn^{2+}	0.00	0.00	0.01	0	0.03	0.05	0	0	0	0.04	0.03	0	0	0.03
Mg	0.66	0.00	1.65	0.44	0.9	1.14	0.21	0	0.48	0.96	1.49	0.22	0	2.87
Zn	0.00	0.00	0.00	0	0	0	0	0.01	0	0	0	0	0.01	0
Ca	0.44	0.15	0.59	0.5	0.73	0.46	0	1.95	0.54	0.68	0.45	0	1.98	1.58
Na	0.19	0.85	0.00	0.46	0.01	0	0.12	0	0.42	0	0	0.2	0.01	1.17
K	0.04	0.01	0.00	0	0	0	0.77	0	0	0	0	0	0.75	0	0.15
Cl	0.00	0.00	0.00	0	0	0	0	0	0	0	0	0	0	0	0.02
F	0.00	0.00	0.00	0	0	0	0	0	0	0	0	0	0	0	0.05
Total cations (S)	8.00	5.00	4.00	3.99	8	8.01	7	8.05	3.99	7.99	8.01	6.99	8.06	17.08

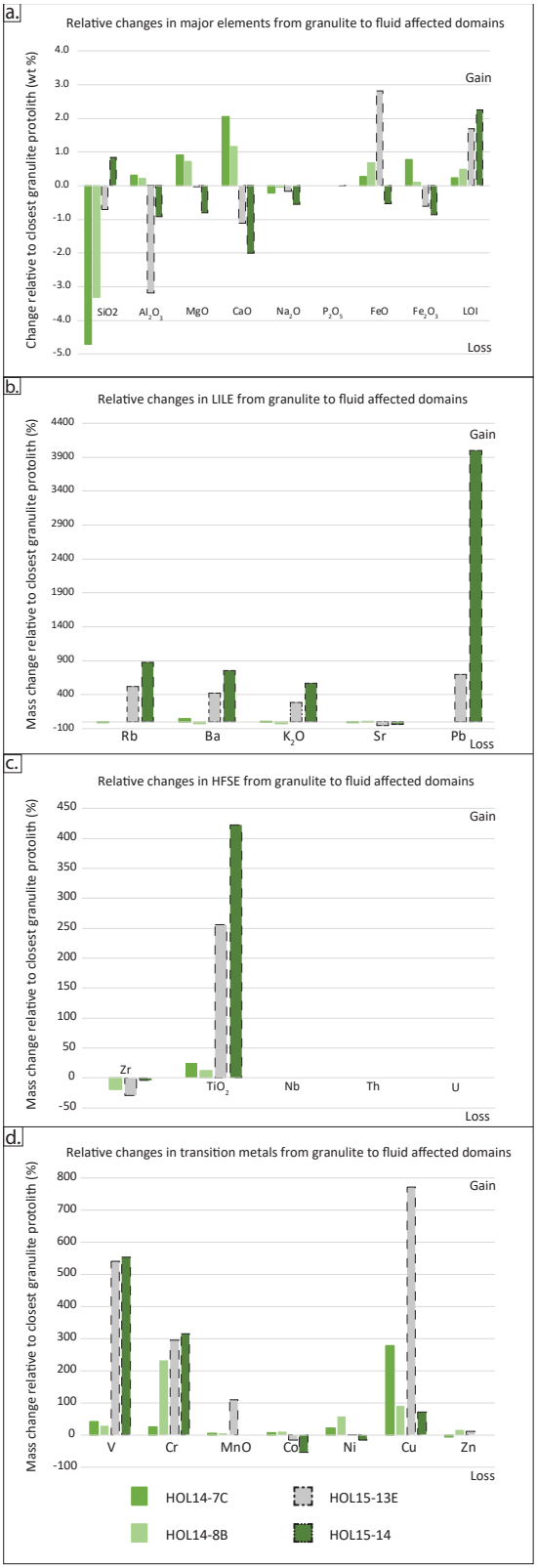

Figure 4. Relative enrichment and depletion plots for altered domains compared to their spatially closest granulite protoliths. a) Relative changes in major oxide in wt %. b) Relative changes in LILE, presented as %. c) Relative changes in HFSE, presented as %. d) Relative changes in transition metals, presented as %.

samples (HOL15–13E and HOL15–14). Major elements for samples in each lithology are presented in Table 3, in wt %. The major elements results corresponding to each evolutionary stage have been presented and discussed in detail in Chapter 2. However, Figure 4a presents the relative changes in major elements from granulite protolith to altered domains, in wt %. Both eclogite samples show consistent changes compared to the granulite. The most significant change observed is the decrease of SiO_2 in both samples (–4.71 wt % for HOL14–7C and –3.32 wt % for HOL14–8B), accompanied by a minor Na_2O decrease. Relative increases occur in Al_2O_3, MgO (0.91 and 0.72 wt %), CaO (2.05 and 1.15 wt %), FeO, Fe_2O_3 and LOI (Figure 4a). The two R-eclogite samples show consistent decreases in Al_2O_3 (–3.19 wt % and –0.92 wt % for HOL15–13E and HOL15–14, respectively), MgO (–0.80 and –0.04), CaO (–1.11 wt % and –2.01 wt %) and Fe_2O_3 whereas significant increases are observed in LOI (1.70 wt % and 2.25 wt %). However, the two samples record inconsistent relative changes in SiO_2, with HOL15–13E showing a decrease of –0.70 wt % and HOL15–14 showing an increase of 0.84 wt %. The same inconsistency is observed in FeO content, with a relative increase in HOL15–13E (2.81 wt %) and a decrease HOL15–14 (–0.53 wt %).

Trace element chemistries are summarised in Table 3, and presented in ppm. All lithologies record low Nb, U and Th contents (under detection limits). Whereas Pb is under the detection limit for the granulite and eclogite samples, the R-eclogites samples HOL15–13E and HOL15–14 have Pb contents of 8 ppm and 41 ppm, respectively. Cr contents in granulite samples is up to 48 ppm, and up to 60 and 160 ppm in eclogites samples HOL14–7C and HOL14–8B, respectively. High Cr contents of up to 170 ppm occur

Table 5. Whole-rock REE analyses in each lithology and representative in-situ REE analyses in major rock forming mineral analyses, presented in ppm.

Stage 3 of deformation

	Granulite protoliths to eclogites					**Eclogite**							
	Whole-rock		*Major minerals*			*Whole-rock*		*Major minerals*					
	HOL14 -7A	HOL14 -8A	g	cpx	pl	HOL14 -7C	HOL14 -8B	g core	g rim	o	zo	phen	amp
La	3.67	4.38	0.019	3.57	3.42	4.82	5.64	0.003	0.001	0.0007	22.5	0.011	0.001
Ce	7.14	8.56	0.148	15.1	3.33	8.78	12.4	0.139	0.056	0.0078	47.9	0.000	0.004
Pr	1.13	1.46	0.079	3.09	0.23	1.39	2.14	0.075	0.037	0.0013	7.34	0.000	0.001
Nd	5.96	6.94	1.26	18.1	0.68	7.38	10.5	1.26	0.809	0.0146	38.5	0.000	0.014
Sm	1.50	1.84	1.57	4.54	0.03	1.89	2.70	1.60	1.32	0.0101	8.95	0.010	0.064
Eu	1.03	1.00	1.24	1.77	0.31	1.13	1.18	1.12	1.01	0.0252	4.56	0.590	0.103
Gd	1.60	1.96	3.55	2.89	0.01	2.12	2.62	3.62	3.57	0.0528	5.40	0.035	0.367
Tb	0.25	0.25	0.692	0.292	0.00	0.30	0.36	0.695	0.760	0.0100	0.451	0.000	0.088
Dy	1.51	1.56	4.92	1.17	0.00	1.74	2.05	4.94	5.70	0.0649	1.49	0.000	0.573
Ho	0.31	0.32	1.11	0.144	0.00	0.38	0.47	1.09	1.29	0.0109	0.140	0.000	0.110
Er	0.87	0.93	3.27	0.272	0.00	1.09	1.31	3.21	3.80	0.0212	0.208	0.000	0.283
Tm	0.13	0.13	0.462	0.024	0.00	0.13	0.19	0.456	0.528	0.0007	0.014	0.000	0.033
Yb	0.93	0.75	3.29	0.110	0.00	0.92	1.26	3.15	3.67	0.0092	0.055	0.000	0.216
Lu	0.12	0.14	0.500	0.010	0.00	0.13	0.18	0.481	0.542	0.0005	0.007	0.000	0.030
Eu/Eu*	2.03	1.51				1.73	1.61						
(La/Lu)$_N$	3.18	3.97				3.85	3.25						
Ce/Ce*	0.82	0.81				0.79	0.84						

Stage 4 of deformation

	Granulite protolith to R-eclogites				**R-eclogite**							
	Whole-rock	*Major minerals*			*Whole-rock*		*Major minerals*					
	HOL15-15	g	cpx	pl	HOL15 -13B	HOL16 -2	g core	g rim	o	zo	phen	amp
La	2.14	0.003	25.0	3.67	0.69	0.330	0.000	0.000	0.010	7.63	0.008	0.002
Ce	4.20	0.076	51.6	5.19	2.02	0.920	0.023	0.007	0.081	17.8	0.002	0.009
Pr	0.55	0.048	5.39	0.372	0.36	0.170	0.022	0.010	0.026	2.87	0.000	0.001
Nd	2.26	0.819	17.7	1.11	2.07	1.13	0.582	0.361	0.236	15.8	0.000	0.013
Sm	0.43	0.572	1.28	0.020	0.61	0.410	0.998	0.908	0.153	4.35	0.007	0.053
Eu	0.43	0.622	0.876	0.232	0.17	0.000	0.750	0.773	0.083	2.36	0.427	0.037
Gd	0.32	0.754	0.545	0.012	0.95	0.580	3.18	3.41	0.252	3.27	0.036	0.248
Tb	0.05	0.091	0.035	0.00	0.20	0.100	0.731	0.843	0.048	0.342	0.000	0.075
Dy	0.23	0.500	0.103	0.00	1.65	0.660	5.93	7.17	0.302	1.23	0.000	0.741
Ho	0.04	0.082	0.010	0.00	0.39	0.140	1.45	1.77	0.050	0.120	0.000	0.191
Er	0.15	0.219	0.022	0.00	1.03	0.480	4.46	5.52	0.122	0.138	0.000	0.582
Tm	0.00	0.027	0.002	0.00	0.15	0.060	0.627	0.781	0.014	0.004	0.000	0.084
Yb	0.09	0.165	0.009	0.00	1.02	0.590	4.32	5.43	0.089	0.025	0.000	0.562
Lu	0.02	0.024	0.000	0.00	0.15	0.060	0.618	0.802	0.010	0.003	0.000	0.083
Eu/Eu*	3.54				0.68	0 .00						
(La/Lu)$_N$	11.11				0.48	0.57						
Ce/Ce*	0.91				0.95	0.91						

in the R-eclogite samples. Cu contents in all granulite samples range between 7.0–9.0 ppm. The eclogite samples have varying amounts of Cu (34.0 ppm in HOL14–7C and 21.0 ppm in HOL14–8A) as well as in the R-eclogite samples (61.0 ppm in HOL15–13E and 12.0 ppm in HOL15–14). The Ni content in the granulite protolith varies, with comparatively lower values in the eclogite protoliths (32.0 ppm for HOL14–7A and 29.0 ppm for HOL14–8A), and higher content in the R-eclogite protolith (125 ppm). Relatively lower Ni contents occur in the eclogite samples, with values of 39.0 ppm and 46.0 ppm, whereas higher values were measured in the R-eclogites (124 and 105 ppm, respectively). Co contents for all granulite samples are similar, with values ranging from 37.0 – 39.0 ppm, as well as for the eclogite samples, with values of 42.0 ppm

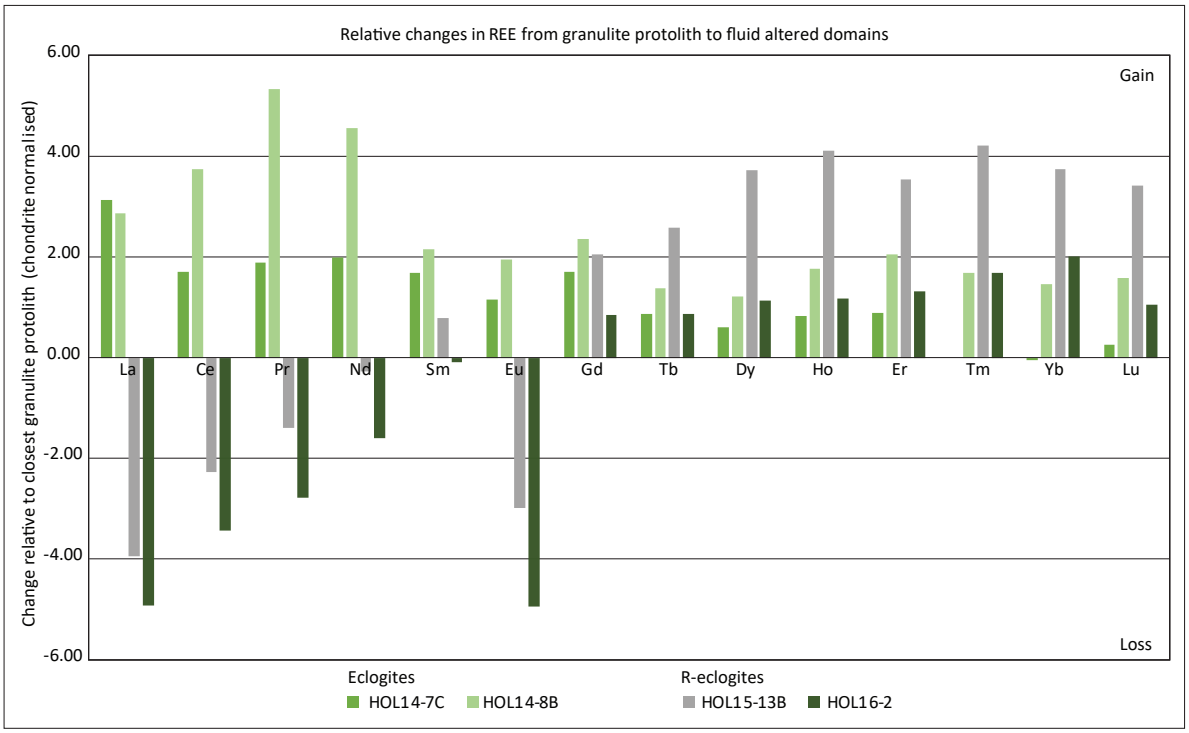

Figure 5. Relative enrichment and depletion plots in REE for altered domains compared to their spatially closest granulite protoliths presented as chondrite normalised values.

for HOL14–7C and 41.0 ppm for HOL14–8B. However, R-eclogite contents vary; 31.0 ppm in HOL15–13B and 17.0 ppm in HOL15–14. Y content is variable in the granulite samples, with eclogite protoliths HOL14–7A and HOL14–8A having measured values of 10.8 ppm and 11.1 ppm, respectively, and the R-eclogite protolith, sample, HOL15–15, has relatively low Y content of 0.8 ppm. Both eclogite samples have comparatively similar Y contents of 13.4 ppm and 13.1 ppm. However, R-eclogite samples have varying Y contents, of 14.4 ppm and 6.2 ppm for sample HOL15–13E and HOL15–14, respectively.

Fluid mobile elements Rb, Sr and Ba were also measured, and their concentrations vary between the three lithologies. Rb contents in the granulite samples vary from 1.1–4.0 ppm. Similar values were measured in the eclogite samples, with 2.0 ppm in HOL14–7C and 1.1 ppm in HOL14–8B. However, relatively high Rb contents of 25.0 ppm and 39.0 ppm were measured in the R-eclogite samples. Granulite and eclogite samples have relatively high Sr contents with values ranging from 993–1212 ppm for the granulites, and 948–1248 ppm for the eclogites. However, lower Sr contents were obtained for R-eclogite samples, with values of 424 ppm and 599 ppm for HOL15–13E and HOL15–14, respectively. Ba contents are also similar in the granulite and eclogite samples, with granulite values ranging between 560–840 ppm, and 639 ppm and 847 ppm for eclogite samples HOL14–7C and HOL14–8B, respectively. However, comparatively higher Ba values were obtained in the R-eclogite samples; 2912 and 4813 ppm of HOL15–13E and HOL15–14, respectively.

The changes in trace element chemistry for all sample pairs were also calculated, and are presented as large ion lithophile elements (LILE) in Figure 4b, high field strength elements (HFSE) in Figure 4c and transition metals in Figure 4d, as percentage differences relative to their closest

granulite protoliths. All eclogite samples show little changes in LILE. Minor changes in Ba, K_2O and Sr are observed in the eclogite pairs, but are inconsistent (Figure 4b). However, R-eclogite samples show significant increases in LILE, with changes of up to 875 % for Rb, 760 % for Ba, 570 % for K_2O, and 4000 % for Pb.

Zr and TiO_2 are the only HFSE that change from protolith to altered domain No changes occur in Nb, Th and U. Sample HOL14–8B shows a slight decrease in Zr, while both HOL14–7B and HOL14–8B samples show an increase in TiO_2 contents (Figure 4c.). Eclogite samples HOL14–8A show a decrease of –19.2 % in Zr, as well as R-eclogite samples HOL14–13E and HOL15–14, with –29.6 % and –3.7 % decrease, respectively. Eclogite sample, HOL14–7C, has a 24.5 % increase in TiO_2 and there is a 12.3 % gain in HOL14–8B. The R-eclogite samples pairs show significant TiO_2 increases of 255 % for sample HOL15–3E and 422 % for HOL15–14.

Transition metals V, Cr, MnO and Cu all show enrichments from granulite protoliths to altered samples (Figure 4d). V content in eclogite increases by up to 41.6 % whereas R-eclogite samples increase by up to 554 %. Cr content in eclogite sample HOL14–7C is increased by 25 %, whereas in HOL14–8B by 233 %. Cr content in R-eclogite samples differ by similar amounts (+ 295 and 314 %). Eclogite samples has a slight increase in MnO content with a percentage increase of up to 5.3 %, whereas R-eclogite samples are comparatively enriched by 110 %. Cu content increase by 277 % in HOL14–7C, 9 % in HOL15-8B, 771 % in HOL15–13E and 71 % in HOL15–14. Eclogite sample pairs show only slight increases in Co (7.7 % in HOL14–7C and 5.3 % in HOL14–8B). However, Co contents in R-eclogite samples HOL15–13E and HOL15–14

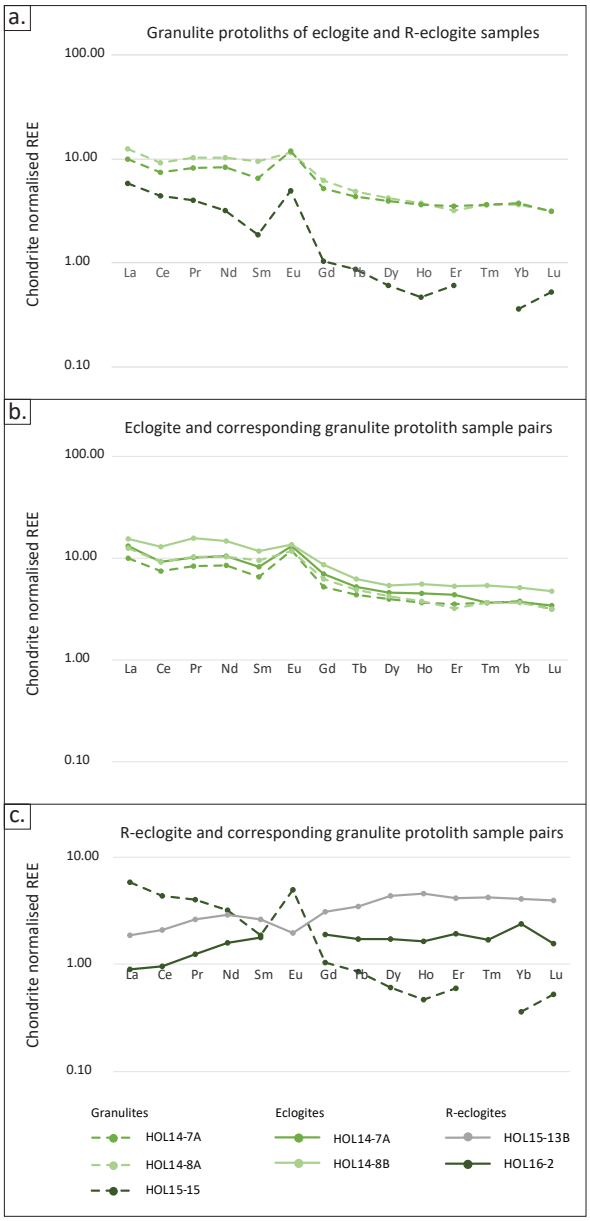

Figure 6. Spider diagrams presenting whole-rock REE patterns as chondrite normalised values, using chondrite values by Taylor and McLennan (1995). a) Comparison between all granulite protoliths. b) Eclogite-granulite sample pairs. c) R-eclogite-granulite sample pairs.

decreases by –16 % and –54%, respectively. Ni contents in both eclogite samples are higher by 21 % and 59 %, whereas in R-eclogite sample (HOL15–13E) it lower by – 16 %. Lastly, Zn content is relatively depleted by –5.3 % in eclogite sample HOL14–7C, whereas relatively enriched by 16 % in HOL14–8B and by 12 % in the R-eclogite (HOL15–13E).

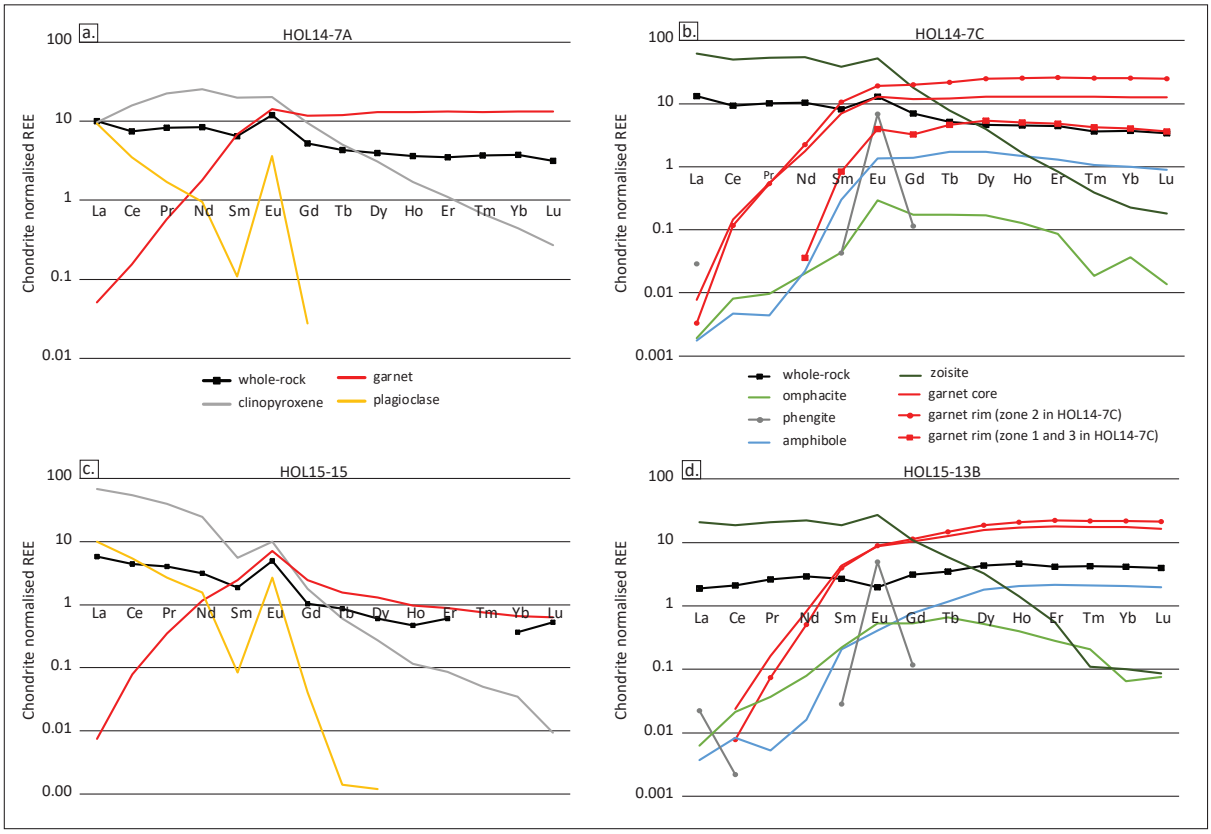

Figure 7. *In-situ* chondrite normalised REE patterns for major rock forming minerals in; a) granulite sample HOL14–7A; b) eclogite sample HOL14–7C; c) granulite sample HOL15–15; and d) R-eclogite sample HOL15–13B.
Chondrite values used for normalisation are by Taylor and McLennan (1995).

The major element chemistry for major rock forming minerals have been presented in detail in Chapter 2. However, representative analyses for minerals in each of the lithology are summarised in Table 4.

2 Whole-rock and mineral chemistry

The REE whole-rock analyses (Table 5) were performed on two eclogite samples (HOL14–7C and HOL14–8B), and their corresponding granulite protoliths (HOL14–7A and HOL14–8A), and two R-eclogites (HOL15–13B and HOL16–2) and their corresponding granulite protolith (HOL15–15), as presented in Table 5. The Eu/Eu* and Ce/Ce* ratios were calculated following McLennan (1989), as well as the $(La/Lu)_N$ ratio (where *N* represents the normalised values; Table 5), which represents the slope of REE spider diagrams. As for major and trace elements, the relative enrichment and depletion for each altered domain relative to their closest granulite protolith have been calculated for REE. These are presented in Figure 5, as chondrite normalised relative changes. Moreover, whole-rock REE spider diagrams are presented in Figure 6 to illustrate the relative distribution of REE in each sample pair.

The Stage 3 eclogite samples show a relative enrichment in all REE compared to their granulite pairs, except for sample HOL14–7C, which shows a negligible decrease in Yb content, of –0.04. La content increases by similar amounts for both samples, with changes up to 3.13. Both samples are enriched in light REE (LREE) compared to heavy REE (HREE). However, HOL14–8B is more enriched in all REE than HOL14–7C (Figure 5). Stage 4 R-eclogites samples are com-

paratively depleted in LREE compared to their granulite pairs, except for sample HOL15–13B, which shows an increase in Sm by 0.78. Sample HOL16–2 records larger changes in LREE, with decreases in La of up to –4.93 and Eu of –4.94. HOL16–2, however, records larger changes in HREE, with Ho and Tm having similar increases of 4.11 and 4.21, respectively, whereas Dy, Er, Yb and Lu record similar enrichments (Figure 5).

The whole rock REE chemistry of the granulite protoliths is presented in Figure 6a. All granulite samples have positive Eu anomalies, with Eu/Eu* ratios of 2.03, 1.51 and 3.54 for HOL14–7A, HOL14–8A and HOL15–15, respectively. The $(La/Lu)_N$ ratios for samples HOL14–7A, HOL14–8A and HOL15–15 are 3.18, 3.97 and 11.11, respectively. The REE spider diagrams for the Stage 3 eclogites samples, HOL14–7C and HOL14–8B are presented in Figure 6b, as well as their corresponding granulite protoliths (dashed lines). Both eclogite samples have similar patterns to that of their granulite protoliths, with positive Eu anomalies. However, a slight decrease in the Eu anomalies is observed in both eclogite samples, with Eu/Eu* values of 1.73 and 1.36 for samples HOL14–7C and HOL14–8B, respectively. The $(La/Lu)_N$ ratio for HOL14–7C is 3.85 whereas that of HOL14–8B is 3.25, which are relatively similar to that of the paired granulite protoliths. The Ce/Ce* ratios for the granulite and eclogite samples from stage 3 of deformation are similar, with values ranging from 0.79–0.84 (Table 5). The REE spider diagrams for the R-eclogite samples, HOL15–13B and HOL16–2, are presented in Figure 6c, along with their granulite protolith, HOL15–15 (dashed line). Sample HOL15–13B show a negative Eu anomaly (Eu/Eu*= 0.68), whereas the Eu value for HOL16–2 was below detection limit. This indicates a shift from positive to negative Eu anomaly from granulite to R-eclogite. Moreover, a shift in the slopes occurs from granulite to R-eclogite samples (Figure 6b), with $(La/Lu)_N$ ratios of 0.48 and 0.57

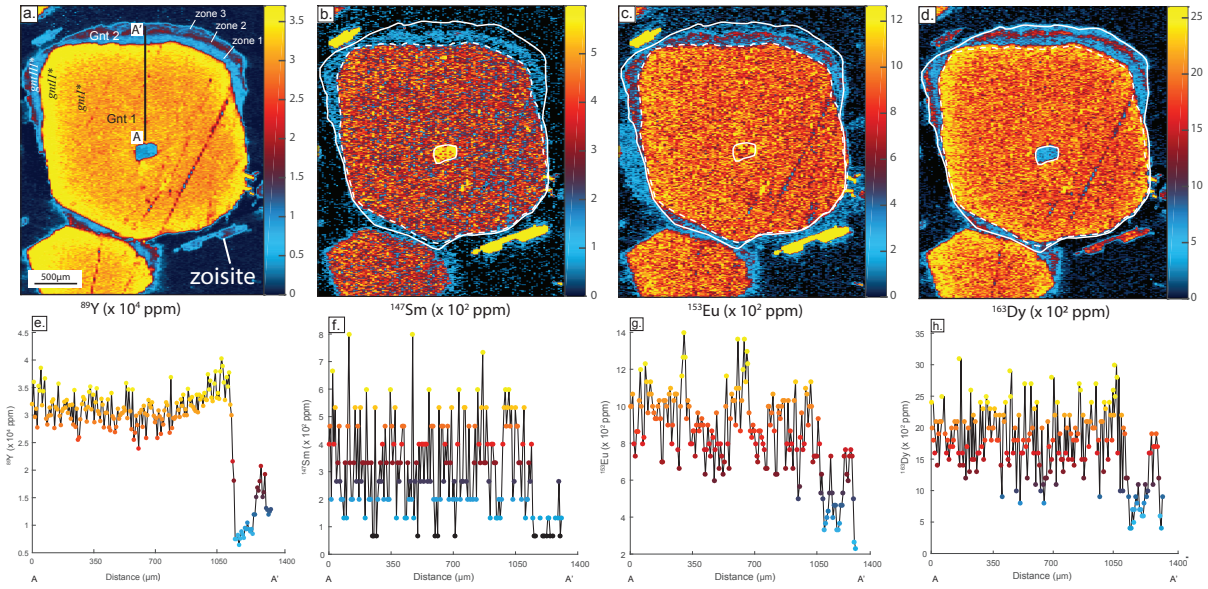

Figure 8. Quantified LA-ICP-MS trace element maps for garnet grains in eclogite sample, HOL14–7C. Warmer colours represent higher concentrations. Dashed lines represent the core/rim boundary in the garnet grains. a) Y distribution map; b) Sm distribution map; c) Eu distribution map and d) Dy distribution map.
The positions A and A' represent the transect used for data extraction, using the line mode sampling function in *XmapTools* (values in ppm). e) Y concentration profile; f) Sm concentration profile; g) Eu concentration profile and h) Dy concentration profile.

for samples HOL15–13B and HOL16–2, respectively. The granulite and R-eclogite samples in stage 4 of deformation have similar Ce/Ce* ratios ranging from 0.91–0.95 (Table 5).

In-situ REE chemistry for the major rock forming minerals in samples HOL14–7A, HOL14–7C, HOL15–15 and HOL15–13B are presented in Table 5 (in ppm), and their corresponding chondrite normalised values are displayed as spider diagrams in Figure 7, along with each whole-rock analysis. Garnet grains in granulite sample HOL14–7A are depleted in LREE (La to Nd) and enriched in HREE relative to the whole-rock composition (Figure 7a). The inverse is observed for clinopyroxene grains, which are comparatively enriched in LREE (La to Tb) and depleted in HREE. Plagioclase grains contain no HREE (Tb to Lu), and have lower LREE contents compared to the whole-rock composition. Garnet analyses in the eclogite sample HOL14–7C show three distinct signatures of garnet REE compositions. This is supported by the zoning observed in LA-ICP-MS maps produced for this sample, presented in Figure 8. The maps are those of elements showing the most prominent zonation (i.e. Y, Sm, Eu and Dy; Figure S3.1 for more elemental maps) along with core to rim transects from A to A'. The garnet core for the eclogite sample (Figure 7b) has REE patterns and concentrations consistent with that of garnet grains in the granulite sample. Garnet maps for the eclogite samples show three zones in the garnet rims, labelled zone 1, 2 and 3. Zones 1 and 3 (indicated by squares in Figure 7b) are relatively depleted in REE compared to zone 2 (indicated by circles) and garnet core. All garnet analyses, however, are relatively enriched in HREE. Zoisite grains in HOL14–7C are comparatively enriched in LREE and depleted in HREE (Dy to Lu), and shows a slight Eu anomaly. Omphacite and amphibole analyses are depleted in REE compared to the whole-rock, and are both comparatively depleted in LREE and enriched in HREE. Phengite grains contain no REE, except for low amounts of La, Sm, Eu and Gd, which result in an Eu anomaly. The REE spider diagrams for R-eclogite protolith, granulite

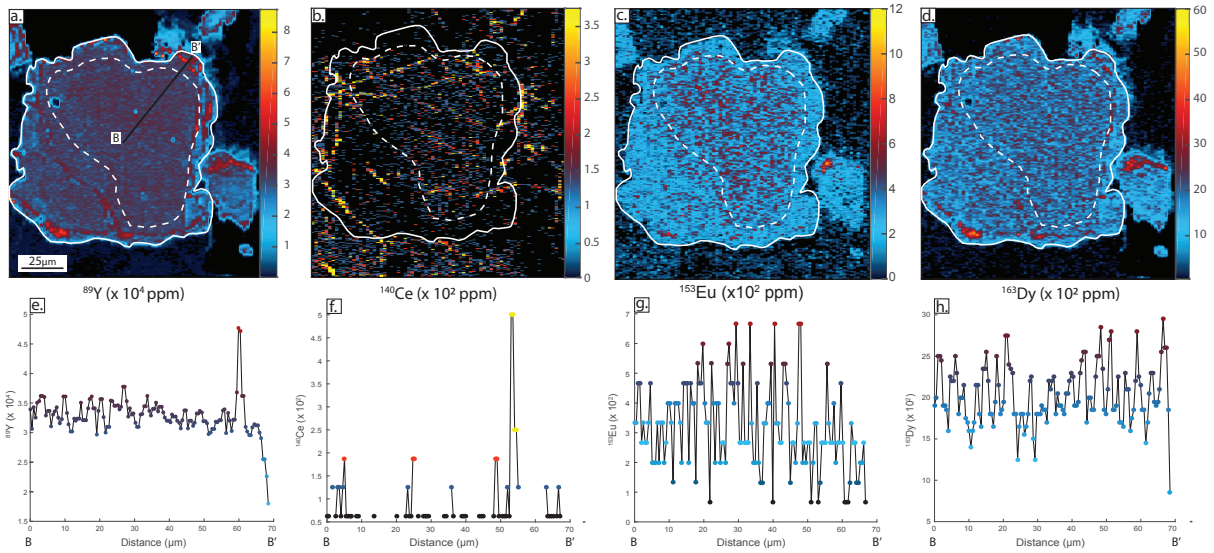

Figure 9. Quantified LA-ICP-MS trace element maps for garnet grains in R-eclogite sample, HOL15–13B. Warmer colours represent higher concentrations. Dashed lines represent the core/rim boundary in the garnet grains. a) Y distribution map; b) Ce distribution map; c) Eu distribution map and d) Dy distribution map.
The positions A and A' represent the transect used for data extraction, using the line mode sampling function in *XmapTools* (values in ppm). e) Y concentration profile; f) Ce concentration profile; g) Eu concentration profile and h) Dy concentration profile.

Table 6. Sm–Nd systematics for samples within stages 3 (eclogite) and 4 (R-eclogite) of deformation. CHUR and DM at t=0 values used to calculated εNd are after Goldstein *et al.* (1984).

Sample	Domain	Sm (ppm)	Nd (ppm)	$^{147}Sm/^{144}Nd$	$^{143}Nd/^{144}Nd$	2 S.E.	εNd (t=0)*	εNd (t=429)
HOL14-7A	Granulite	1.7	6.4	0.1621	0.512255	2.0E-06	–7.68	–5.80
HOL14-8A	Granulite	1.8	6.6	0.1617	0.512250	2.0E-06	–7.81	–5.90
HOL15-6	Granulite	0.2	1.4	0.1055	0.512022	3.0E-06	–13.15	–8.16
HOL15- 12	Granulite	0.3	1.2	0.1299	0.512393	3.0E-06	–11.22	–7.38
HOL15-15	Granulite	0.4	2.1	0.1204	0.512248	2.0E-06	–11.55	–7.38
HOL14-7C	Eclogite	2.2	7.8	0.1675	0.512279	2.0E-06	–7.16	–5.57
HOL14-8B	Eclogite	2.7	10.3	0.1608	0.512222	2.0E-06	–8.27	–6.31
HOL15-5	Eclogite	0.6	3.5	0.1109	0.512074	3.0E-06	–11.42	–6.73
HOL15-10	Eclogite	0.6	3.7	0.0900	0.511841	3.0E-06	–15.87	–10.04
HOL15-11	Eclogite	0.5	3.4	0.0978	0.512016	2.0E-06	–13.60	–8.20
HOL15-13B	R-eclogite	0.4	0.4	0.6075	0.514368	1.1E-06	30.40	7.89
HOL15-13E	R-eclogite	1.0	3.1	0.1913	0.512752	2.0E-06	1.72	2.01
HOL16-2	R-eclogite	0.3	0.7	0.2535	0.512982	8.0E-06	4.70	1.58
HOL15- 14	R-eclogite	1.0	2.5	0.2314	0.512988	2.0E-06	4.04	2.14

sample HOL15–15, are presented in Figure 7c. REE patterns for each mineral are similar to that of eclogite HOL14–7C, but have lower concentrations and with a more prominent Eu anomaly in the clinopyroxene grains. In HOL15–15, plagioclase grains contain no HREE (Ho to Lu). R-eclogite sample, HOL15–13B, has similar REE partitioning and patterns compared to HOL14–7C (Figure 7). However, garnet analyses show no notable difference between the garnet cores and garnet rims. This is also observed in REE distribution maps in garnet, displayed in Figure 9 (see more elemental maps in Figure S3.2), where the garnet core, established on the basis of major element chemistry, is outlined by the white dashed line. Mass balance calculations comparing measured whole-rock REE analyses and calculated whole-rock values based on mineral chemistries for all four samples are presented in Appendix S3.1 (Tables S3.4 – S3.7; Figure S3.3).

5.4 Sm–Nd isotope systematics

Sm–Nd isotopic analyses were obtained on all samples in this study; i.e. five granulite, four eclogite four R-eclogite samples (see summary in Table 2). The measured Sm and Nd values are reported as ppm values in Table 6, as well as the $^{147}Sm/^{144}Nd$ and $^{143}Nd/^{144}Nd$ ratios. Measured $^{147}Sm/^{144}Nd$ ratios range from 0.1055 to 0.1617 in the granulite samples, 0.0900 to 0.1675 in the eclogite samples and 0.1913 to 0.6075 in the R-eclogite samples. The $^{143}Nd/^{144}Nd$ ratio range between 0.512022 to 0.512393 for the granulites, 0.511841 to 0.512279 for the eclogites and 0.512752 to 0.514368 for the R-eclogites. Figure 10a displays the variation of $^{143}Nd/^{144}Nd$ to $^{147}Sm/^{144}Nd$ ratios from each lithology. There are two distinct groupings in the ratios, with the R-eclogite having distinctly higher $^{143}Nd/^{144}Nd$ values than the granulite and eclogite samples. The Nd growth curves are also presented in Figure 10b. Growth curves were drawn based metamorphic ages of 950 Ma for the granulite (Table 6 and indicated by unfilled shapes in Figure 10b; Austrheim and Griffins, 1985; Bingen *et al.*, 1997) whereas 429 Ma was used for the eclogite and R-eclogite samples (Table 6) as the documented peak metamorphic age for the complete eclogitisation process during the Caledonian Orogeny (Boundy *et al.*, 1997; Bingen *et al.*, 2004). εNd(t) values for the granulite samples range from –2.07 to –3.57 at 950 Ma, whereas

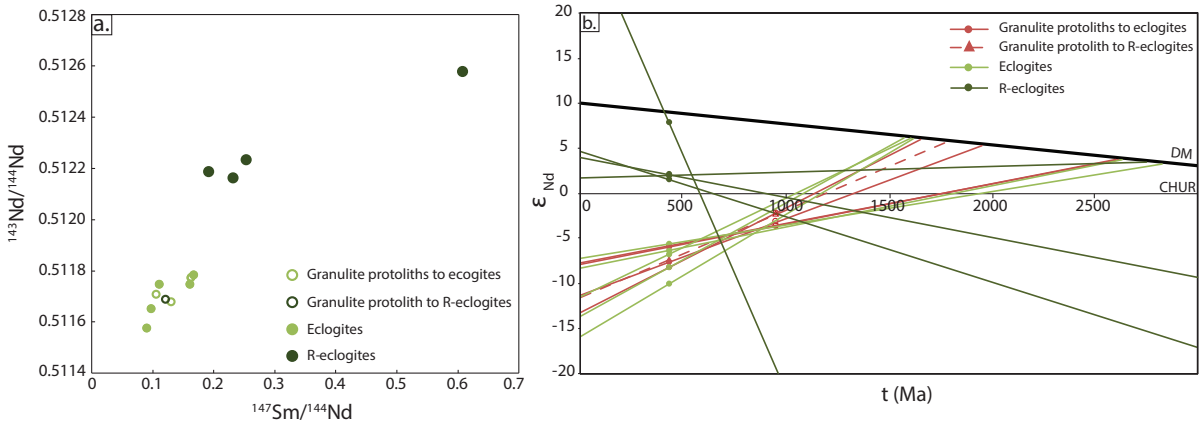

Figure 10. Sm–Nd systematics for the granulite and altered domains on Holsnøy Island.
a) $^{143}Nd/^{144}Nd$ vs $^{147}Sm/^{144}Nd$ distribution plot for eclogite and R-eclogite samples, along with their protolith domains. Pale green circles represent samples within stage 3 of deformation and dark green circles represent samples within stage 4 of deformation. Unfilled circles are granulite samples and filled samples are the fluid affected samples.
b) εNd(t) plot for whole-rock analyses for the granulite, eclogite and R-eclogite samples, depicting isotopic shifts as the Holsnøy system evolved with increasing fluid availability. Growth curves were performed at t=950 Ma for the granulite samples (unfilled red shapes) and t=429 Ma for all fluid affected samples. However, for an appropriate comparison of εNd(t) during the Caledonian Orogeny (filled circles), all granulite samples were recalculated at 429 Ma.
CHUR and DM at t=0 values used are after Goldstein *et al.* (1984).

those of the eclogites and R-eclogites ranged from –5.57 to –10.04 and +1.58 to +7.89, respectively, at 429 Ma.

6. DISCUSSION

The changes in REE, other trace elements and Sm–Nd chemistry from granulite to eclogite domains are discussed below. This is also done within the *P–T* framework illustrated in Figure 3, with main focus on the most fluid affected domains, stages 3 and 4 of deformation. This discussion commences with a consideration of the granulite protolith. The heterogeneity of the protolith is evident in Figure 6a. The granulite sample HOL15–15 has lower REE contents than granulite samples HOL14–7A and HOL14–8A. For example, La content in HOL14–7A and HOL14–8A are 3.67 ppm and 4.38 ppm, respectively, whereas that of HOL15–15 is 2.14 and the Lu contents are 0.12 ppm and 0.14 ppm for HOL14–7A and HOL14–8A, respectively, and 0.02 for HOL15–15. Moreover, the Eu anomaly for HOL14–7A and HOL14–8A are 2.03 and 1.51, respectively, whereas that of HOL15–15 is 11.11 (Table 5). Positive Eu anomalies are generally associated with plagioclase in crustal rocks owing to its preferential partitioning in feldspars, compared to other REE (Weill and Drake, 1973). Therefore, the higher Eu anomaly in HOL15–15 potentially indicates a greater abundance of plagioclase relative to clinopyroxene and garnet compared to HOL14–7A and HOL14–8A. This highlights the importance of sampling in pairs for this study, to minimise errors in apparent chemical shifts caused by the heterogeneity of the granulite protolith.

6.1 Elemental and isotopic shifts and distribution

The geochemical evolution of the Holsnøy system has been discussed in detail by previous authors (Austrheim & Griffin, 1985; Austrheim, 1987; Boundy *et al.*, 1992; Boundy *et al.*, 1997; Schneider *et al.*, 2007; Centrella *et al.*, 2015;

Putnis *et al.*, 2017). Mass transfer calculations by a number of previous authors (e.g. Van Wyck *et al.*, 1996; Centrella *et al.*, 2016) demonstrated that, while there are no significant changes in most major elemental content from granulite to eclogite, there is a systematic increase in LOI and K content (Figure 4a) that cannot be explained by the composition of minerals in the protolith granulite and supports the interpretation of Holsnøy Island being open system. Therefore, any chemical shift that occurs from the granulite protolith to the altered domains can potentially reflect changes caused by the fluid that infiltrated the system.

1.1.1 STAGE 3 OF DEFORMATION

Comparing individual granulite-eclogite pairs (i.e. HOL14–7A vs HOL14–7C and HOL14–8A vs HOL14–8B) in stage 3 of deformation (i.e. eclogite samples), slight increases in REE are observed (Figure 5). This increase in REE content in the eclogite samples can be explained by one of the following: either 1) the addition of REE to the system by the infiltrated fluid, or; 2) stripping away of REE from the rocks, accompanied by mass loss. The conversion of the granulite to eclogite has resulted in a net density increase from 3.10 g/cm^3 to up to 3.58 g/cm^3 accompanied by volume preservation (Austrheim, 1987; Austrheim, 2013; Centrella *et al.*, 2015). This, therefore, rules out the stripping away of REE elements from the system as a likely scenario to account for the enrichment observed in whole-rock REE for stage 3 of deformation. However, the similarity in the whole-rock REE patterns for the granulite and eclogite samples (Figure 6), as well as the negligible changes in Eu values (2.03 and 1.51 for granulite samples and 1.51 and 1.73 and 1.61 for eclogite samples) attest to a rock-buffered system during stage 3 of deformation. This is also reflected in the measured Sm–Nd chemistry for the eclogite samples, as presented in Figure 10. Measured $^{143}Nd/^{144}Nd$ and $^{147}Sm/^{144}Nd$ ratios (Figure 10) for the granulite samples (light green unfilled circles) and eclogite samples (light green filled circles), are within uncertainty of each each other. The evolution of the granulite Sm–Nd system to c.429 Ma (filled red dots, Figure 10b) results in a mean εNd(t) value – 7.0, while that of the eclogites is – 7.4 at the same age. The interpretation of a rock buffered system at stage 3 of deformation supports results obtained in Chapter 3, whereby no whole-rock $\delta^{18}O$ shift was recorded from granulite to eclogite domains.

The REE analyses in mineral grains for the eclogite sample pair HOL14–7A and 7C show the potential redistribution of elements during fluid infiltration. The LREE in clinopyroxene grains in the granulite likely partitioned in zoisite grains in the eclogite sample, as they are both the main LREE reservoir in their respective samples. The LREE preferentially partitioning in zoisite at HP/UHP conditions is consistent with previous studies such as Brunsmann *et al.* (2001) and Spandler *et al*. (2003). The breakdown of granulite-facies minerals, such as garnet and plagioclase likely resulted in the redistribution of REE within the garnet rims, omphacite and amphibolite grains. Whereas the complete breakdown of plagioclase occurs at eclogite-facies (Chapter 2), the Eu anomaly in the whole-rock eclogite samples is determined by the partitioning of Sm, Eu and Gd in phengite grains. To check the mineral data, mass balance calculations were performed and compared to the whole-rock data (Figure S3.3). Both samples have small discrepancies between the calculated whole-rock compositions compared to the measured values. Sample HOL14–7A has consistently lower calculated whole-rock values from La to Nd (up to 3.48 ppm) and higher cal-

culated values from Sm to Lu (up to 1.56 ppm). However, HOL14–7C has consistently lower calculated whole-rock values based on calculations from mineral compositions (Figure S3.3b). Such minor discrepancies can be explained by either the difference in analytical techniques used to measure the mineral compositions and the whole-rock compositions or the lack of analysis of accessory phases such as rutile, as well as the symplectites in the eclogite sample.

Of particular interest in stage 3 of deformation are the garnet analyses. Eclogite sample, HOL14–7C, has three distinct garnet REE signatures as highlighted in Figure 7b. Garnet core analyses show similar patterns to garnet grain analyses in the corresponding granulite protolith, HOL14–7A (compare Figure 7a with 7b). This supports the interpretation that garnet cores in the eclogite are relict from the granulite protolith, based on major element chemistry, made previously in Chapter 2 and supported by a number of authors (Austrheim, 1987; Erambert & Austrheim, 1993; Raimbourg *et al.*, 2007). Garnet rim analyses in sample HOL14–7C show two distinct signatures: a relatively depleted population, with slight positive Eu anomaly and flat HREE patterns and a relatively enriched population with no Eu anomaly and flat HREE patterns. Similar patterns were documented in zircon cores and rims by Bingen *et al.* (2004), and support the reported interpretation of the co-precipitation of garnet and zircon rims during fluid-infiltration. Additionally, Raimbourg *et al.* (2007) suggested the existence of three generations of garnet growth based on composition: 1) gnt I is the relict granulite core; gnt II, a re-equilibrated zone of the relict garnet and; 3) gnt III, garnet overgrowth during the eclogite-facies (Figure 8a, 8b). However, this classification was not identifiable in the major elemental maps (Figure S2.1), it can arguably be observed in the Y map (Figure 8a): gnt I, the core of the grain; gnt II the relatively enriched outer core and; gnt III, the rim. However, for consistency with work done in Chapter 2, this study uses the interpretation of two generations of garnet growth: Gnt 1, relict garnet core from granulite protolith and Gnt 2, the eclogite-facies growth.

The most noticeable feature in the HREE maps in Figure 8 is the distinct zonation present in the garnet rims (i.e. in Gnt 2). The zonation in Gnt 2 can be observed in the Y map and in MREE such as Eu and Dy (Figure 8b, c and d) and to a lesser extent in the Ca and Mn maps (Figure S3.1). The presence of different zones in Gnt 2 explains the two signatures of REE analyses presented in Figure 6a. Inner zone 1 and outermost zone 3 of Gnt 2 (Figure 8a) are relatively depleted in HREE compared to zone 2. However, REE analyses for zones 1 and 3 could not be distinguished from each other.

The REE maps presented in this chapter are the first acquired on the eclogite domains in the Bergen Arcs. Whereas analyses on zones 1 and 3 have been documented by Schneider *et al.* (2007), the presence of zone 2 in garnet rims has not been documented in previous studies. The oscillatory zonation in Eu, Gd, Tb, Dy and Ho, observed in Gnt 2, are similar to zonation patterns in garnet grains previously documented by a number of studies, which are generally associated with fluid influx (Jamtveit, 1991; Jamtveit *et al.*, 1993; Clechenko & Valley, 2003; Baxter & Caddick, 2013). However, there are other potential explanations for the observed oscillatory zonation in the eclogite garnet. Moore *et al.* (2013) characterised a number of plausible explanations for the interpretation of Y+REE distribution in garnet grains, including diffusion-limited uptake during mineral growth, overprint zoning, equilibration

with an unchanging matrix, equilibration with reaction-modulated major- and accessory- phase assemblages and equilibration with externally sourced fluid. Two possible scenarios can explain the zonation patterns observed in Figure 8. First, equilibrium changes to the mineral assemblage, due to continuous reaction amongst major minerals, can have a significant role to play in the chemistry of eclogite-facies Gnt 2. Although garnet grows as Gnt 2 during stage 3 of deformation, the total mode of garnet is significantly less (by 18%) in the eclogite than in the protolith granulite and 75 % of total garnet consists of relict granulite cores. This results in a net percentage mode of only 8 volume % of eclogite garnet (Chapter 2). This is in large part because Stage 2 involves garnet consumption rather than growth. This has as consequence the reduced mode of Gnt 1 in the eclogite, but results in higher REE abundance in Gnt 2 during re-precipitation. Second, there is the possibility of re-equilibration with a fluid as a plausible reason for the observed patterns. The presence of zonation in Y+REE, Ca and Mn (Chapter 2) aligns with the expected patterns observed due to fluid induced oscillatory zonation (Jamtveit, 1991; Moore *et al.*, 2013). Moreover, the MREE peaks in Gnt 2 (i.e. zone 2; Figures 8e, g and h) correspond to peaks in $\delta^{18}O$ signatures in garnet rims detected by *in-situ* analysis in Chapter 3.

It is likely that the growth of part of Gnt 2 in stage 3 of deformation was due to the re-equilibration of minerals in response to changes in *P–T* conditions (zone 1), in a rock-buffered scenario. However, the slight increase in whole-rock REE from granulite protolith to eclogite sample, suggests to some degree, the addition of REE in the system contributed to the oscillatory zoning observed (zone 2). Therefore, the zonation observed in the garnet grains in HOL14–7C is likely due to both.

6.1.2 STAGE 4 OF DEFORMATION

This stage of deformation shows the most significant elemental shifts from granulite protolith to altered samples. Firstly, REE $(La/Lu)_N$ ratios shift from 11.11 for the granulite HOL15–15, to 0.48 and 0.57 for R-eclogites samples HOL15–13B and HOL16–2, respectively (Figure 6c). This is because the R-eclogite samples are relatively depleted in LREE, and enriched in HREE. The negative Eu anomaly recorded by R-eclogite samples, compared to the positive anomaly of the granulite, can likely be explained by the disappearance of plagioclase (and thus Eu) from the rock. However, mass balance calculations on REE performed using the mineral analyses of HOL15–13B highlight the potential for no representative XRF-based whole-rock REE analyses. For both HOL15–15 and HOL13–13B the variations in REE elements are small and consistent with those observed in stage 3 of deformation. For example the Eu concentration, calculated based on mineral analyses in HOL15–13B (Figure S3.2), varies by almost 4 ppm, compared to that of the measured whole-rock. One possible reason for this discrepancy is the heterogeneity of R-eclogites samples, due to the coarse-grained nature of phengite grains (up to 1.5 cm). The aliquot of sample used for whole-rock analysis may have not been representative possibly containing higher modal abundances of omphacite and amphibole, compared to the thin-section on which mineral abundances were estimated. From an analytical point, a potential explanation for this discrepancy is the interference of BaO during the phengite-grain analysis, as well as the lack of identification of accessory mineral phases such as rutile and apatite (possible LREE reservoir)

in the R-eclogite samples. While there is only a slight discrepancy between the whole-rock versus mineral-based mass balance REE analyses in HOL15–13B, more significant isotopic shifts in the whole-rock Sm–Nd systematics in all R-eclogite samples occur. The $^{143}Nd/^{144}Nd$ and $^{147}Sm/^{144}Nd$ ratios for the granulite protolith to the R-eclogite (HOL15–15) is consistent with the granulite protoliths to the eclogites in stage 3 of deformation (Figure 10a). The R-eclogite samples, however, have considerably higher $^{143}Nd/^{144}Nd$ ratios, which result in more positive εNd(t) values (mean of +3.4), with lower Sm and Nd concentrations. Figure 10b presents the Nd growth curves, based on a depleted mantle age model. The evolution line slopes of the R-eclogite samples are not consistent with that of the eclogite and granulite samples, and opposite to the evolution slope of DM models. This is due to the very low concentrations of Sm and Nd in the rocks, and therefore, the quality of the results is highly dependent on the precision of the instrument used. Nevertheless, Figure 10a shows the R-eclogites are comparatively more radiogenic, with a decrease in the concentration of Sm and Nd (Table 6), but an increase in radiogenic ratios. A possible explanation for these apparent shifts, however, is the heterogeneity of the protolith for the R-eclogite. While sample HOL15–15 is the closest anorthositic granulite to the R-eclogite samples, their protolith might have been of different composition to that of HOL15–15, and closer to the R-eclogite composition. However, there is a lack of evidence for other domains with compositions consistent with that of the R-eclogite samples in the area (e.g. dykes and sills of mafic composition). Moreover, the diffuse boundaries between the R-eclogite outcrop and that of their nearest granulite indicates that the fluid reacted with the anorthositic granulite during the Caledonian Orogeny, post peak metamorphic conditions. It is, therefore, assumed in this study that HOL15–15 is the precursor to the R-eclogite samples.

Mineral analyses in both granulite HOL15–15 and R-eclogite HOL15–13B show similar elemental partitioning between minerals to samples from stage 3 of deformation (Figure 7). Interestingly, there is no differentiation between the core and rim analyses in garnet grains in R-eclogite sample, HOL15–13B. Moreover, there is a lack of similarity in REE patterns in garnet grains in the granulite protolith and garnet cores in the R-eclogite. This points towards the re-equilibration of garnet grains during retrogression, which is contradictory to the major element maps presented in Chapter 2, which showed the presence of a small volume of relict cores in garnet grains in stage 4 of deformation, with diffuse core to rim boundary.

REE maps for garnet in R-eclogite sample, HOL15–13B, are presented in Figure 9 (see more detailed maps in Figure S2.2), along with corresponding core-to-rim element transects. Garnet maps reveal major element zonation, mainly in Mg and Mn, supporting EPMA data by Chapter 2. Whereas a slight zonation in LREE is evident in the garnet grains with a comparatively LREE-enriched core, zonation is less visible in the Y and HREE maps. However, Y and HREE maps show relatively enriched and discontinuous zones in the garnet rim. This is most evident in the Y, Tb, Dy and Ho maps (Figure S2.2). In this case, however, the discontinuity of the Y and HREE zones cannot be interpreted as oscillatory zonation but rather patterns dictated by fractures in the garnet grains, that can be observed in Y and Ce maps (Figure 9 a and b).

Based on REE distribution characterisation of Moore *et al.* (2013) the most likely equilibration

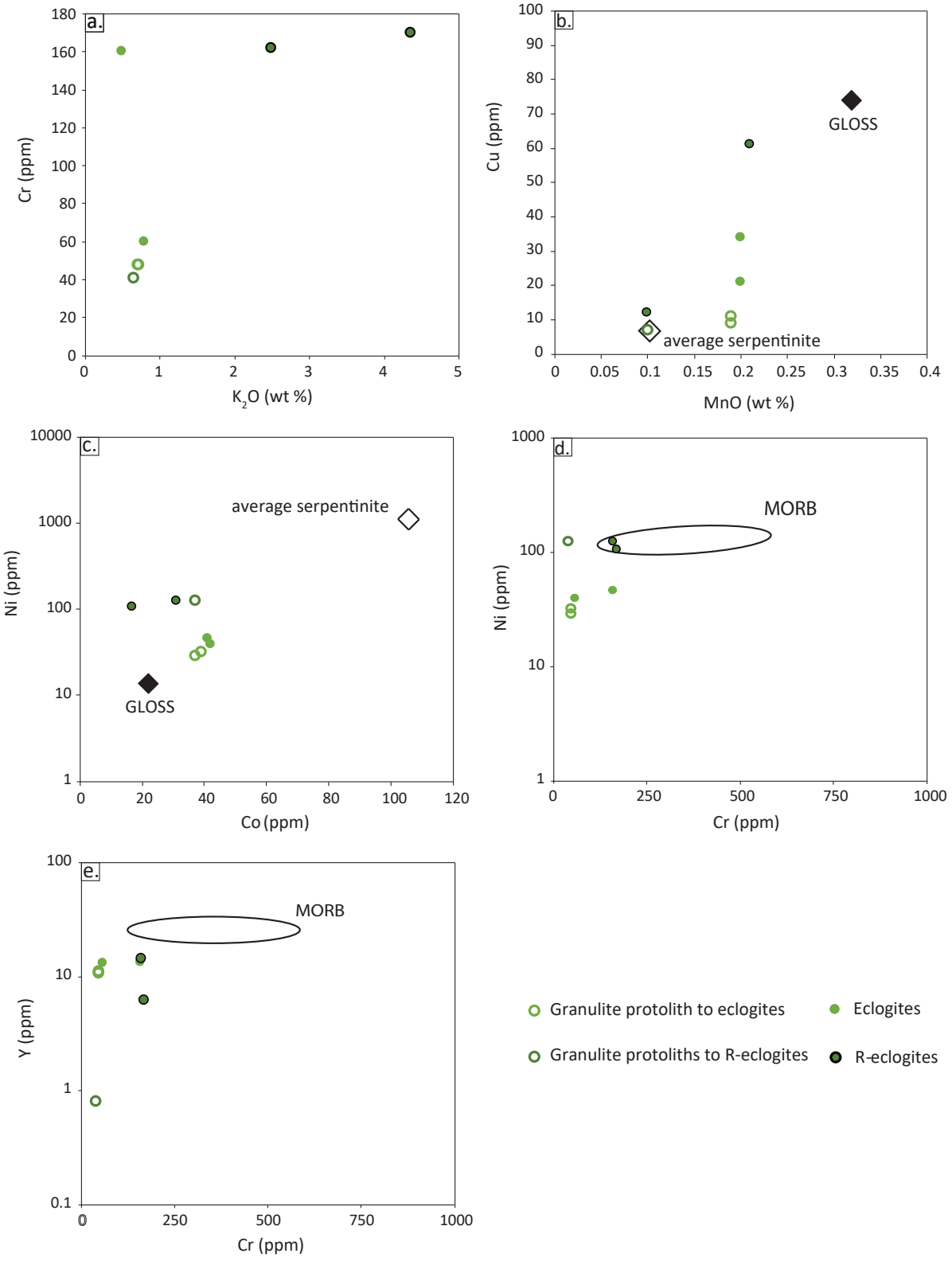

Figure 11. Variations in bulk-rock in a) Cr vs K_2O; b) Cu vs MnO; c) Ni vs Co; Ni vs Cr; and Y vs Cr, for all samples. Average serpentinite values are after Hattori and Guillot (2003); Savov *et al.* (2005) and Paulick *et al*. (2006). GLOSS values are after Plank and Langmuir (1993) and MORB values after Kelemen et al. (2003) and Klein (2003).

scenario for stage 4 of deformation is the equilibration with external fluids. In this case, the lack of zonation in HREE compared to LREE and major elements in garnet grains, the absence of relict granulitic garnet, and the zoning patterns dictated mainly by fractures suggest equilibration resulting from an external fluid as the most likely scenario. Moreover, the consistent comparative depletion in LREE and enrichment of HREE as well as in whole-rock REE concentrations and the increase in radiogenic signatures support the potential for changes occurring due to an external fluid, in an open system. This interpretation is further supported by $\delta^{18}O$ and δD isotopic results from Chapter 3.

6.2 Trace element mobility and fluid provenance

To explain the elemental shifts, especially in stage 4 of deformation, it is important to address elemental mobility in fluids. REE and certain trace elements (e.g. HFSE, Cr and Ni) are typically considered immobile during hydrothermal alteration. However, studies by Rubatto and Hermann (2003), Spandler and Hermann (2003), John *et al.* (2005), van der Straaten *et al.* (2008) and Spandler *et al.* (2011) documented the mobility of multiple HFSE and typically immobile trace elements at HP and UHP conditions. Moreover, studies done by Taylor *et al.* (1981), Yongliang and Yusheng (1991), Gieré and Williams (1992) and Tsay *et al.* (2017), demonstrated the increase in REE mobility due to interaction with fluids rich in ligands such as F^-, Cl^-, CO_3^{2-}, HCO_3^- and PO_4^{3-}. The presence of both Cl^- and CO_3^{2-} in the Holsnøy Island eclogites has previously been documented. For example, Kühn (2002) reported an increase in Cl content in the rocks, from granulite to eclogite to amphibolite-facies, concluding that the fluid that infiltrated the Holnøy system likely evolved to a 'brine-like' fluid, which is also supported by fluid-inclusion studies by Jamtveit *et al.* (1990) and Andersen *et al.* (1991). Boundy *et al*. (2002) documented high pressure carbonate rocks on Holsnøy Island, and argued that CO_3^{2-} likely originated from scapolite grains within granulite-facies domains on the island and was incorporated in the fluids to enhance eclogitisation. The presence of the Cl^- and CO_3^{2-} ligands interacting with the granulite-facies rocks points towards their presence throughout the evolution of the Holsnøy system. Klein-Ben David *et al.* (2011) previously showed that Cr, a typically immobile trace element in the crust, increases in solubility in KCl solutions with increasing salinity at high pressures. Figure 11a presents the variability of both Cr (in ppm) and K_2O (in wt %) in each domain, and shows a noticeable increase of both Cr and K from granulite to R-eclogite domains. It is, therefore, probable that the salinity of the fluid at stage 4 of deformation was high enough to remobilise Cr. This Cr enrichment is consistent with that of fluid mobile trace elements such as Rb, Ba and Pb as well as Cr enrichment in other HP and UHP terranes, such as the Monviso Ophiolite (Spandler *et al.* 2011). It is probable that the elemental shifts from granulite protoliths to altered domains observed in this study were due to the presence of ligands that enhanced REE and HFSE mobility in the fluid. Thus, the fluid that infiltrated the Holsnøy system also likely stripped away Sr (Figure 4a), Zr (Figure 4c) and LREE (Figure 6c), but added Sc, Rb, Ba, K, Pb, Ti, V, Cr, Cu and HREE to the system. The strongest evidence for the source of external fluid is from stage 4 of deformation domains, the R-eclogites. Mattey *et al.* (1994), and (Van Wyck *et al.*, 1996) previously proposed the dehydration of a N-rich sediment or crustal rock, underlying the Holsnøy system, as the potential source of the second fluid type. The $\delta^{18}O$ and δD isotopic signatures presented in Chapter 3 support the

notion of a metamorphic fluid. To further constrain the type of rock that likely dehydrated to provide the fluid responsible for the eclogitisation of the granulite protolith, whole-rock analyses of some trace elements (e.g. Cr, Cu, Ni, Co and Y) are used and compared to reservoirs previously published (i.e. serpentinite, GLOSS and MORB; Plank and Langmuir, 1993; Hattori and Guillot, 2003; Kelemen *et al.*, 2003; Klein, 2003; Savov *et al*., 2005; Paulick *et al.,* 2006). The higher Cu and MnO content of the fluid affected domains (eclogites and R-eclogites) compared to the granulite suggest a subducted sediment-derived fluid (GLOSS; Figure 11b), which is arguably supported by relatively lower Ni and Co contents (Figure 11c). Relatively higher Cr and Y contents (Figure 11d and c), suggest MORB-like derived fluids for stage 4 of deformation, which is supported by the relatively flat REE trends for the R-eclogite (Figure 6c; White, 2013) and apparent high radiogenic Sm–Nd signatures (Figure 10). While the dataset in this study is too small to be conclusive, a preliminary scenario to obtain a metamorphic, sedimentary and MORB-like derived fluid is the dehydration of a sedimentary rock consisting of mafic components. However, the chemical complexity associated with the stage 4 of deformation samples, highlights the need for more isotopic work, particularly of potential source rocks within the Bergen Arcs, to fully understand and characterise the source of the fluid.

7. CONCLUSIONS

Whole-rock REE analyses in the granulite protoliths, eclogite and R-eclogite samples on Holsnøy Island demonstrated the importance of sampling in pairs to characterise potential shifts observed in an open system, as the heterogeneity of host rocks add uncertainties to the chemical changes observed. The remobilisation of typically immobile elements (e.g. REE and HFSE, Cr, Ti and Ni) particularly during stage 4 of deformation has significant implications for our understanding of elemental distribution in the Earth's crust, and elemental recycling during HP/UHP metamorphism. While the dataset presented in this chapter is not extensive enough to confidently constrain the source of the fluid, the combination of REE data and patterns, Sm–Nd isotopic data and other trace elements suggest that a possible source involves dehydration of a sedimentary rock, with mafic components. The potential remobilisation of typically immobile elements (e.g. REE and HFSE, Cr, Ti and Ni) has significant implications for our understanding of elemental distribution in the Earth's crust, and elemental recycling during HP/UHP metamorphism. However, more data (e.g. mineral trace elements) are required to fully characterise the fluid that infiltrated the Holsnøy system.

REFERENCES

Adam, J. & Green, T., 1994. The effects of pressure and temperature on the partitioning of Ti, Sr and REE between amphibole, clinopyroxene and basanitic melts. *Chemical Geology*, **117**, 219-233.

Andersen, T., Austrheim, H. & Burke, E. A. J., 1990. Fluid inclusions in granulites and eclogites from the Bergen Arcs, Caledonides of W. Norway. *Mineralogical Magazine*, **54**, 145-158.

Andersen, T., Austrheim, H. & Burke, E. A. J., 1991a. Fluid-induced retrogression of granulites in the Bergen Arcs, Cale-

donides of W. Norway: Fluid inclusion evidence from amphibolite-facies shear zones. *Lithos*, **27**, 29-42.

Andersen, T., Austrheim, H. & Burke, E. A. J., 1991b. Mineral-fluid-melt interactions in high-pressure shear zones in the Bergen Arcs nappe complex, Caledonides of W. Norway: Implications for the fluid regime in Caledonian eclogite-facies metamorphism. *Lithos*, **27**, 187-204.

Andersen, T., Austrheim, H., Burke, E. A. J. & Elvevold, S., 1993. N 2 and CO 2 in deep crustal fluids: evidence from the Caledonides of Norway. *Chemical Geology*, **108**, 113-132.

Austrheim, H., 1987. Eclogitization of lower crustal granulites by fluid migration through shear zones. *Earth and Planetary Science Letters*, **81**, 221-232.

Austrheim, H., 1998. Influence of fluid and deformation on metamorphism of the deep crust and consequences for the geodynamics of collision zones. In: *When continents collide: Geodynamics and geochemistry of Ultrahigh-Pressure Rocks*, pp. 297-323, Springer.

Austrheim, H., 2013. Fluid and deformation induced metamorphic processes around Moho beneath continent collision zones: Examples from the exposed root zone of the Caledonian mountain belt, W-Norway. *Tectonophysics*, **609**, 620-635.

Austrheim, H. & Boundy, T. M., 1994. Pseudotachylytes generated during seismic faulting and eclogitization of the deep crust. *Science*, **265**, 82-83.

Austrheim, H. & Griffin, W. L., 1985. Shear deformation and eclogite formation within granulite-facies anorthosites of the Bergen Arcs, western Norway. *Chemical Geology*, **50**, 267-281.

Banner, J. L., Hanson, G. & Meyers, W., 1988. Rare earth element and Nd isotopic variations in regionally extensive dolomites from the Burlington-Keokuk Formation (Mississippian); implications for REE mobility during carbonate diagenesis. *Journal of Sedimentary Research*, **58**, 415-432.

Baxter, E. F. & Caddick, M. J., 2013. Garnet growth as a proxy for progressive subduction zone dehydration. *Geology*, **41**, 643-646.

Bea, F., 1996. Residence of REE, Y, Th and U in granites and crustal protoliths; implications for the chemistry of crustal melts. *Journal of petrology*, **37**, 521-552.

Bingen, B., Austrheim, H., Whitehouse, M. J. & Davis, W. J., 2004. Trace element signature and U–Pb geochronology of eclogite-facies zircon, Bergen Arcs, Caledonides of W Norway. *Contributions to mineralogy and petrology*,

147, 671-683.

Bingen, B., Davis, W. J. & Austrheim, H., 2001. Zircon U-Pb geochronology in the Bergen arc eclogites and their Proterozoic protoliths, and implications for the pre-Scandian evolution of the Caledonides in western Norway. *Geological Society of America Bulletin*, **113**, 640-649.

Boundy, T. M., Fountain, D. M. & Austrheim, H., 1992. Structural development and petrofabrics of eclogite facies shear zones, Bergen Arcs, western Norway: implications for deep crustal deformational processes. *Journal of metamorphic geology*, **10**, 127-146.

Boundy, T. M., Mezger, K. & Essene, E. J., 1997. Temporal and tectonic evolution of the granulite-eclogite association from the Bergen Arcs, western Norway. *Lithos*, **39**, 159-178.

Centrella, S., Austrheim, H. & Putnis, A., 2015. Coupled mass transfer through a fluid phase and volume preservation during the hydration of granulite: An example from the Bergen Arcs, Norway. *Lithos*.

Centrella, S., Austrheim, H. & Putnis, A., 2016. Mass transfer and trace element redistribution during hydration of granulites in the Bergen Arcs, Norway. *Lithos*, **262**, 1-10.

Clechenko, C. & Valley, J., 2003. Oscillatory zoning in garnet from the Willsboro Wollastonite Skarn, Adirondack Mts, New York: a record of shallow hydrothermal processes preserved in a granulite facies terrane. *Journal of Metamorphic Geology*, **21**, 771-784.

Connolly, J. A. D. & Kerrick, D. M., 2002. Metamorphic controls on seismic velocity of subducted oceanic crust at 100-250 km depth. *Earth and Planetary Science Letters*, **204**, 61-74.

Cooper, A. F. & Ireland, T. R., The Pounamu terrane, a new Cretaceous exotic terrane within the Alpine Schist, New Zealand; tectonically emplaced, deformed and metamorphosed during collision of the LIP Hikurangi Plateau with Zealandia. *Gondwana Research*.

Ducea, M. N., Ganguly, J., Rosenberg, E. J., Patchett, P. J., Cheng, W. & Isachsen, C., 2003. Sm–Nd dating of spatially controlled domains of garnet single crystals: a new method of high-temperature thermochronology. *Earth and Planetary Science Letters*, **213**, 31-42.

Erambert, M. & Austrheim, H., 1993. The effect of fluid and deformation on zoning and inclusion patterns in poly-metamorphic garnets. *Contributions to mineralogy and petrology*, **115**, 204-214.

Exley, R., 1980. Microprobe studies of REE-rich accessory minerals: implications for Skye granite petrogenesis and REE mobility in hydrothermal sys-

tems. *Earth and Planetary Science Letters*, **48**, 97-110.

Faccenda, M., Gerya, T. V., Mancktelow, N. S. & Moresi, L., 2012. Fluid flow during slab unbending and dehydration: Implications for intermediate-depth seismicity, slab weakening and deep water recycling. *Geochemistry, Geophysics, Geosystems*, **13**.

Faure, G. & Mensing, T. M., 2005. *Isotopes: principles and applications*. John Wiley & Sons.

García-Casco, A., Torres-Roldán, R., Millán, G., Monié, P. & Schneider, J., 2002. Oscillatory zoning in eclogitic garnet and amphibole, Northern Serpentinite Melange, Cuba: a record of tectonic instability during subduction? *Journal of Metamorphic Geology*, **20**, 581-598.

Giaramita, M. & Sorensen, S., 1994. Primary fluids in low-temperature eclogites: evidence from two subduction complexes (Dominican Republic, and California, USA). *Contributions to Mineralogy and Petrology*, **117**, 279-292.

Glodny, J., Austrheim, H., Molina, J. F., Rusin, A. I. & Seward, D., 2003. Rb/Sr record of fluid-rock interaction in eclogites: The Marun-Keu complex, Polar Urals, Russia. *Geochimica et Cosmochimica Acta*, **67**, 4353-4371.

Glodny, J., Kühn, A. & Austrheim, H., 2008. Geochronology of fluid-induced eclogite and amphibolite facies metamorphic reactions in a subduction–collision system, Bergen Arcs, Norway. *Contributions to mineralogy and petrology*, **156**, 27-48.

Guiraud, M., Powell, R. & Rebay, G., 2001. H2O in metamorphism and unexpected behaviour in the preservation of metamorphic mineral assemblages. *Journal of Metamorphic Geology*, **19**, 445-454.

Guo, S., Chen, Y., Ye, K., Su, B., Yang, Y., Zhang, L., Liu, J. & Mao, Q., 2015. Formation of multiple high-pressure veins in ultrahigh-pressure eclogite (Hualiangting, Dabie terrane, China): Fluid source, element transfer, and closed-system metamorphic veining. *Chemical Geology*, **417**, 238-260.

Hacker, B. R., Andersen, T. B., Johnston, S., Kylander-Clark, A. R. C., Peterman, E. M., Walsh, E. O. & Young, D., 2010. High-temperature deformation during continental-margin subduction & exhumation: The ultrahigh-pressure Western Gneiss Region of Norway. *Tectonophysics*, **480**, 149-171.

Hellstrom, J., Paton, C., Woodhead, J. & Hergt, J., 2008. Iolite: software for spatially resolved LA-(quad and MC) ICPMS analysis. *Mineralogical Association of Canada short course series*, **40**, 343-348.

Ismail, R., Ciobanu, C. L., Cook, N. J., Teale, G. S., Giles, D., Mumm, A. S. & Wade, B., 2014. Rare earths and other trace elements in minerals from skarn assemblages, Hillside iron oxide–copper–gold deposit, Yorke Peninsula, South Australia. *Lithos*, **184**, 456-477.

James, R. H. & Elderfield, H., 1996. Chemistry of ore-forming fluids and mineral formation rates in an active hydrothermal sulfide deposit on the Mid-Atlantic Ridge. *Geology*, **24**, 1147-1150.

Jamtveit, B., 1991. Oscillatory zonation patterns in hydrothermal grossular-andradite garnet: Nonlinear dynamics in regions of immiscibility. *American Mineralogist*, **76**, 1319-1327.

Jamtveit, B., Ben-Zion, Y., Renard, F. & Austrheim, H., 2018a. Earthquake-induced transformation of the lower crust. *Nature*, **556**, 487-491.

Jamtveit, B., Bucher-Nurminen, K. & Austrheim, H., 1990. Fluid controlled eclogitization of granulites in deep crustal shear zones, Bergen arcs, Western Norway. *Contributions to mineralogy and petrology*, **104**, 184-193.

Jamtveit, B., Moulas, E., Andersen, T. B., Austrheim, H., Corfu, F., Petley-Ragan, A. & Schmalholz, S. M., 2018b. High Pressure Metamorphism Caused by Fluid Induced Weakening of Deep Continental Crust. *Scientific reports*, **8**, 17011.

Jamtveit, B., Wogelius, R. A. & Fraser, D. G., 1993. Zonation patterns of skarn garnets: Records of hydrothermal system evolution. *Geology*, **21**, 113-116.

John, T., Klemd, R., Gao, J. & Garbe-Schönberg, C.-D., 2008. Trace-element mobilization in slabs due to non steady-state fluid–rock interaction: constraints from an eclogite-facies transport vein in blueschist (Tianshan, China). *Lithos*, **103**, 1-24.

John, T., Scherer, E. E., Haase, K. & Schenk, V., 2004. Trace element fractionation during fluid-induced eclogitization in a subducting slab: trace element and Lu–Hf–Sm–Nd isotope systematics. *Earth and Planetary Science Letters*, **227**, 441-456.

Jolivet, L., Raimbourg, H., Labrousse, L., Avigad, D., Leroy, Y., Austrheim, H. & Andersen, T. B., 2005. Softening trigerred by eclogitization, the first step toward exhumation during continental subduction. *Earth and Planetary Science Letters*, **237**, 532-547.

Kontonikas-Charos, A., Ciobanu, C. L. & Cook, N. J., 2014. Albitization and redistribution of REE and Y in IOCG systems: insights from Moonta-Wallaroo, Yorke Peninsula, South Australia. *Lithos*, **208**, 178-201.

Kühn, A., 2002. The influence of fluid on the granulite to eclogite and amphibolite

facies transition: a study in the anorthositic rocks from the Lindås Nappe, Bergen Arcs, West Norway. *Unpub. PhD Thesis, University of Oslo*.

Kühn, A., Glodny, J., Austrheim, H. & Raheim, A., 2002. The Caledonian tectono-metamorphic evolution of the Lindas Nappe: constraints from U-Pb, Sm-Nd and Rb-Sr ages of granitoid dykes. *Norsk Geologisk Tidsskrift*, **82**, 45-58.

Lanari, P., Vidal, O., De Andrade, V., Dubacq, B., Lewin, E., Grosch, E. G. & Schwartz, S., 2014. XMapTools: A MATLAB©-based program for electron microprobe X-ray image processing and geothermobarometry. *Computers & Geosciences*, **62**, 227-240.

Massonne, H., Willner, A. P. & Gerya, T., 2007. Densities of metapelitic rocks at high to ultrahigh pressure conditions: What are the geodynamic consequences? *Earth and Planetary Science Letters*, **256**, 12-27.

Mattey, D., Jackson, D. H., Harris, N. B. W. & Kelley, S., 1994. Isotopic constraints on fluid infiltration from an eclogite facies shear zone, Holsenøy, Norway. *Journal of metamorphic geology*, **12**, 311-325.

Mezger, K., Essene, E. J. & Halliday, A., 1992. Closure temperatures of the Sm—Nd system in metamorphic garnets. *Earth and Planetary Science Letters*, **113**, 397-409.

Moore, S., Carlson, W. D. & Hesse, M. A., 2013. Origins of yttrium and rare earth element distributions in metamorphic garnet. *Journal of Metamorphic Geology*, **31**, 663-689.

Mørk, M. B. E. & Mearns, E. W., 1986. Sm-Nd isotopic systematics of a gabbro-eclogite transition. *Lithos*, **19**, 255-267.

Paton, C., Hellstrom, J., Paul, B., Woodhead, J. & Hergt, J., 2011. Iolite: Freeware for the visualisation and processing of mass spectrometric data. *Journal of Analytical Atomic Spectrometry*, **26**, 2508-2518.

Philippot, P., 1993. Fluid-melt-rock interaction in mafic eclogites and coesite-bearing metasediments: constraints on volatile recycling during subduction. *Chemical Geology*, **108**, 93-112.

Pollok, K., Lloyd, G. E., Austrheim, H. & Putnis, A., 2008. Complex replacement patterns in garnets from Bergen Arcs eclogites: a combined EBSD and analytical TEM study. *Chemie der Erde-Geochemistry*, **68**, 177-191.

Putnis, A., Jamtveit, B. & Austrheim, H., 2017. Metamorphic Processes and Seismicity: the Bergen Arcs as a Natural Laboratory. *Journal of Petrology*, **58**, 1871-1898.

Raimbourg, H., Goffé, B. & Jolivet, L., 2007. Garnet reequilibration and growth in the eclogite facies and geodynamical evolution near peak metamorphic conditions. *Contributions to Mineralogy and Petrology*, **153**, 1-28.

Raimondo, T., Payne, J., Wade, B., Lanari, P., Clark, C. & Hand, M., 2017. Trace element mapping by LA-ICP-MS: assessing geochemical mobility in garnet. *Contributions to Mineralogy and Petrology*, **172**, 17.

Roberts, S., Palmer, M. R., Cooper, M. J., Buchaus, P. & Sargent, D., 2009. REE and Sr isotope characteristics of carbonate within the Cu–Co mineralized sedimentary sequence of the Nchanga Mine, Zambian Copperbelt. *Mineralium Deposita*, **44**, 881.

Schneider, J., Bosch, D., Monié, P. & Bruguier, O., 2007. Micro-scale element migration during eclogitisation in the Bergen arcs (Norway): a case study on the role of fluids and deformation. *Lithos*, **96**, 325-352.

Sharrad, K. A., McKinnon-Matthews, J., Cook, N. J., Ciobanu, C. L. & Hand, M., 2014. The Basil Cu–Co deposit, Eastern Arunta Region, Northern Territory, Australia: A metamorphosed volcanic-hosted massive sulphide deposit. *Ore Geology Reviews*, **56**, 141-158.

Smith, M., 2007. Metasomatic silicate chemistry at the Bayan Obo Fe–REE–Nb deposit, Inner Mongolia, China: contrasting chemistry and evolution of fenitising and mineralising fluids. *Lithos*, **93**, 126-148.

Spandler, C., Hermann, J., Arculus, R. & Mavrogenes, J., 2003. Redistribution of trace elements during prograde metamorphism from lawsonite blueschist to eclogite facies; implications for deep subduction-zone processes. *Contributions to Mineralogy and Petrology*, **146**, 205-222.

Taylor, S. R. & McLennan, S. M., 1995. The geochemical evolution of the continental crust. *Reviews of Geophysics*, **33**, 241-265.

Tumiati, S., Godard, G., Martin, S., Klötzli, U. & Monticelli, D., 2007. Fluid-controlled crustal metasomatism within a high-pressure subducted mélange (Mt. Hochwart, Eastern Italian Alps). *Lithos*, **94**, 148-167.

Van Wyck, N., Valley, J. W. & Austrheim, H., 1996. Oxygen and carbon isotopic constraints on the development of eclogites, Holsnøy, Norway. *Lithos*, **38**, 129-145.

White, W. M., 2013. *Geochemistry*. John Wiley & Sons.

Woodhead, J. D., Hellstrom, J., Hergt, J. M., Greig, A. & Maas, R., 2007. Isotopic and elemental imaging of geological materials by laser ablation inductive-

ly coupled plasma-mass spectrometry. *Geostandards and Geoanalytical Research*, **31**, 331-343.

Xu, J., Ciobanu, C. L., Cook, N. J., Zheng, Y., Sun, X. & Wade, B. P., 2016. Skarn formation and trace elements in garnet and associated minerals from Zhibula copper deposit, Gangdese Belt, southern Tibet. *Lithos*, **262**, 213-231.

Zertani, S., Labrousse, L., John, T., Andersen, T. B. & Tilmann, F., 2019. The Interplay of Eclogitization and Deformation During Deep Burial of the Lower Continental Crust—A Case Study From the Bergen Arcs (Western Norway). *Tectonics*, **38**, 898-915.

CHAPTER 5

This chapter is written as a short format article, intended for submission as: Bhowany, K., Hand, M., Clark, C., Kelsey, D. Records of extreme exhumation rates of high-pressure terrane on Holsnøy Island, western Norway: evidence for large-scale overpressure?

Statement of Authorship

Title of Paper	Records of extreme exhumation rates of high-pressure terrane on Holsnøy Island, western Norway: evidence for large-scale overpressure?
Publication Status	☐ Published ☐ Accepted for Publication ☐ Submitted for Publication ☑ Unpublished and Unsubmitted w ork w ritten in manuscript style
Publication Details	Written for submission in short-format

Principal Author

Name of Principal Author (Candidate)	Kamini Bhowany		
Contribution to the Paper	Project fieldwork and sample collection, sample preparation, data collection and analysis, manuscript structure, writing and editing and figure making.		
Overall percentage (%)	80		
Certification:	This paper reports on original research I conducted during the period of my Higher Degree by Research candidature and is not subject to any obligations or contractual agreements with a third party that would constrain its inclusion in this thesis. I am the primary author of this paper.		
Signature		Date	29/08/19

Co-Author Contributions

By signing the Statement of Authorship, each author certifies that:

i. the candidate's stated contribution to the publication is accurate (as detailed above);

ii. permission is granted for the candidate in include the publication in the thesis; and

iii. the sum of all co-author contributions is equal to 100% less the candidate's stated contribution.

Name of Co-Author	Prof. Chris Clark		
Contribution to the Paper	Guidance in the field, sample collection, guidance in manuscript writing, structure and review.		
Signature		Date	4/07/19

Name of Co-Author	Dr. David E. Kelsey		
Contribution to the Paper	Guidance in manuscript writing, structure and review.		
Signature		Date	29/6/19

Name of Co-Author	Ass. Prof. Mark Caddick		
Contribution to the Paper	Coding of scripts for the forward modelling of diffusion durations in garnet grains, assistance in running the program and troubleshooting, manuscript review.		
Signature		Date	1st July, 2019

Name of Co-Author	Prof. Martin Hand		
Contribution to the Paper	Guidance in the field, guidance in manuscript writing, structure and review.		
Signature		Date	21/08/19

ABSTRACT

The presence of high-pressure (HP) and ultra-high-pressure (UHP) terranes on the Earth's surface is generally considered to be the consequence of rapid exhumation from great depths— such interpretations are based on metamorphic pressures being correlated to depth. However, in some cases, the exhumation rates are too fast and cannot easily be explained by typical exhumation mechanisms such as erosion, tectonic extension, and accretion prism dynamics. The eclogite-facies domains on Holsnøy Island, Bergen Arcs, are an example of an exotic terrane surrounded by relatively low-pressure domains, namely the Blåmanen Nappe and the Minor and Major Bergen Arcs. The minimum estimated exhumation rate for the eclogite on the island is 161 mm/yr, based on diffusion durations in zoned garnet grains and pressure drop constraints from eclogite to amphibolite-facies assemblages. While the scientific consensus is that pressure is correlated to depth in the Earth's crust, the discrepancy between extremely fast exhumation rates for the Holsnøy eclogites, and the lack of plausible known exhumation mechanisms highlight the importance of reassessing the systematic use of pressure as depth constraints. In this study, it is concluded that HP/UHP terranes can, not only be products of deep-seated HP metamorphism, but could likely be the results of tectonic overpressure in rheologically weaker units at shallower depths in the Earth's crust.

1. INTRODUCTION

High-pressure (HP) and ultra-high-pressure (UHP) terranes are known to form within orogenic belts and their presence on the Earth's surface helps geologists understand the processes occurring in the lower crust during subduction and exhumation. The general geological interpretation is that HP metamorphic assemblages (e.g. eclogites) are formed at great depths, with the assumption that pressure is near-lithostatic (Spear, 1993). However, geodynamic models by Li *et al.* (2010), Schmalholz and Podladchikov (2013) and Gerya (2015) suggest that tectonic overpressure is another plausible mechanism for the emplacement of HP/UHP terranes at shallower depths; i.e. the formation of HP/UHP terranes due to high differential stress in the crust during deformation, instead of lithospheric pressure. While there are currently no known natural examples for large-scale tectonic overpressure, Chu *et al.* (2017) documented fast forming eclogites due to melting-induced overpressure at local-scale during the Taconic Orogeny in New England.

A study by Yamato and Brun (2016) investigated the correlation between peak metamorphic pressure and their near isothermal pressure decrease in subduction zones. The authors concluded that peak metamorphic pressures do not necessarily correlate to maximum burial depths, but instead reflect a change in tectonic regime (the relaxation from compressional to extensional setting) prior to exhumation. Moreover, the subsequent near isothermal pressure decrease experienced by HP/UHP terranes likely also reflects this change in regime, as opposed to the 'first stage of exhumation' that is usually interpreted by multiple for the ascension of such terranes within the Earth's crust studies (e.g. Palmeri *et al*., 2007; Guillot *et al*., 2008; Gabudianu Radulescu *et al*., 2009; Angiboust *et al*., 2012; McClelland and Lapen, 2013). Moulas *et al.* (2013) argued that geodynamically, the major challenge of using pressure as a proxy for depth, is to propose plausible mechanisms to account for the extremely fast exhumation rates obtained for some HP/UHP terranes.

A summary of typical exhumation rates of well-known HP/UHP terranes is presented in Figure 1. It is generally accepted that exhumation due to erosion and uplift occur at a rate of c. 5–10 mm/yr, based on modern day rates (Figure 1; Anczkiewicz *et al.*, 2004; Glodny *et al.*, 2005), while faster rates (up to 40 mm/yr) are credited

to a of combination slab breakoff and buoyancy of continental crust (Ernst *et al.*, 1997; Rubatto & Hermann, 2001; Jolivet *et al.*, 2005). However, exhumation rates exceeding those illustrated in Figure 1 are yet to be explained by conventional geological processes and highlight the importance of exploring other geodynamic scenarios such as the overpressure hypothesis.

This study focuses on the HP terrane on Holsnøy Island, western Norway (Figure 2a). The eclogite-facies domains on the island are exotic to the area, as they are surrounded by relatively low-pressure terranes (i.e. the Blåmanen Nappe and Minor and Major Bergen Arcs; Figure 2b). The current tectonic models suggest the formation of the eclogite-facies rocks on Holsnøy Island at a depths ≃ 70 km in a subduction zone during the collision of Baltica and Laurentia, during the Caledonian Orogeny (Austrheim, 2013; Jolivet *et al.,* 2005), followed by exhumation. However, there is increasing evidence that the area experienced an extreme pressure decrease on short time-scales (Boundy *et al.*, 1996; Raimbourg *et al.*, 2007; Jamtveit *et al.*, 2018). If this were indeed the case, then extremely fast rates should be obtained for the exhumation of the eclogites, which cannot be explained by current mechanisms. Compared to Chu *et al.* (2017) who used the unrealistically fast rates of compression (exceeding that of plate tectonic burial, > 150 mm/yr) as a test for overpressure, this study uses the rate of decompression/exhumation greater than geodynamically feasible as a test for overpressure, assuming pressure is correlated to depth. This is achieved by using a combination of phase equilibria forward modelling and multi-component diffusion modelling in zoned garnets to constrain the exhumation rates of the eclogite-facies domains to amphibolite-facies conditions.

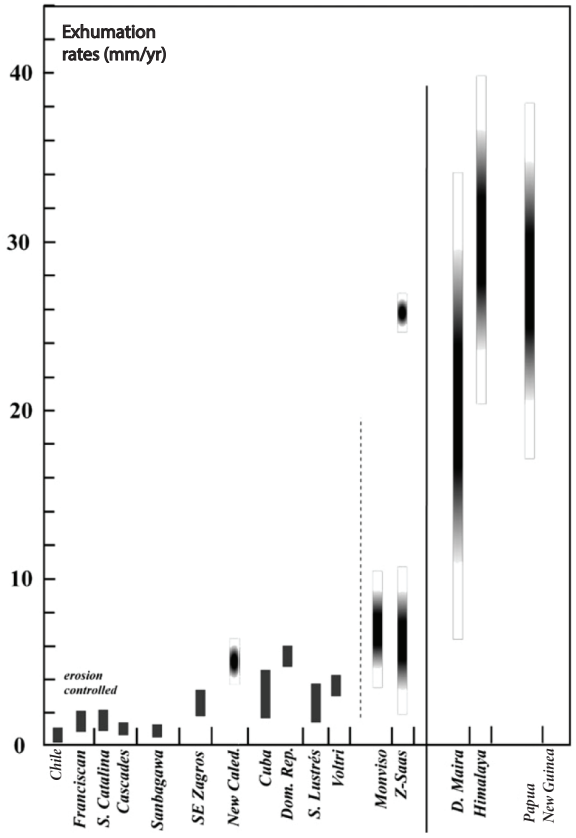

Figure 1. Summary of well-known HP and UHP terranes, after Agard *et al*. (2009)

2. GEOLOGICAL SETTING AND BACKGROUND

Holsnøy Island is located approximately 45 km north-west of Bergen (Figure 2a). The rocks present on the island form part of the main formation of the Bergen Arcs, the Lindås Nappe (Kolderup, 1934), which is bounded by the Blåmanen Nappe and major and minor Bergen Arcs (Figure 2b). This location is an excellent natural laboratory to study deep crustal processes as the progressive conversion of an anhydrous granulite domains to hydrous eclogites, owing to fluid infiltration, are perfectly preserved. Moreover, these progressive stages (Austrheim, 2013; Chapter 2) are preserved within kilometres of each other due to the limiting volumes of fluids available during each stage.

The protolith anorthositic granulite is composed

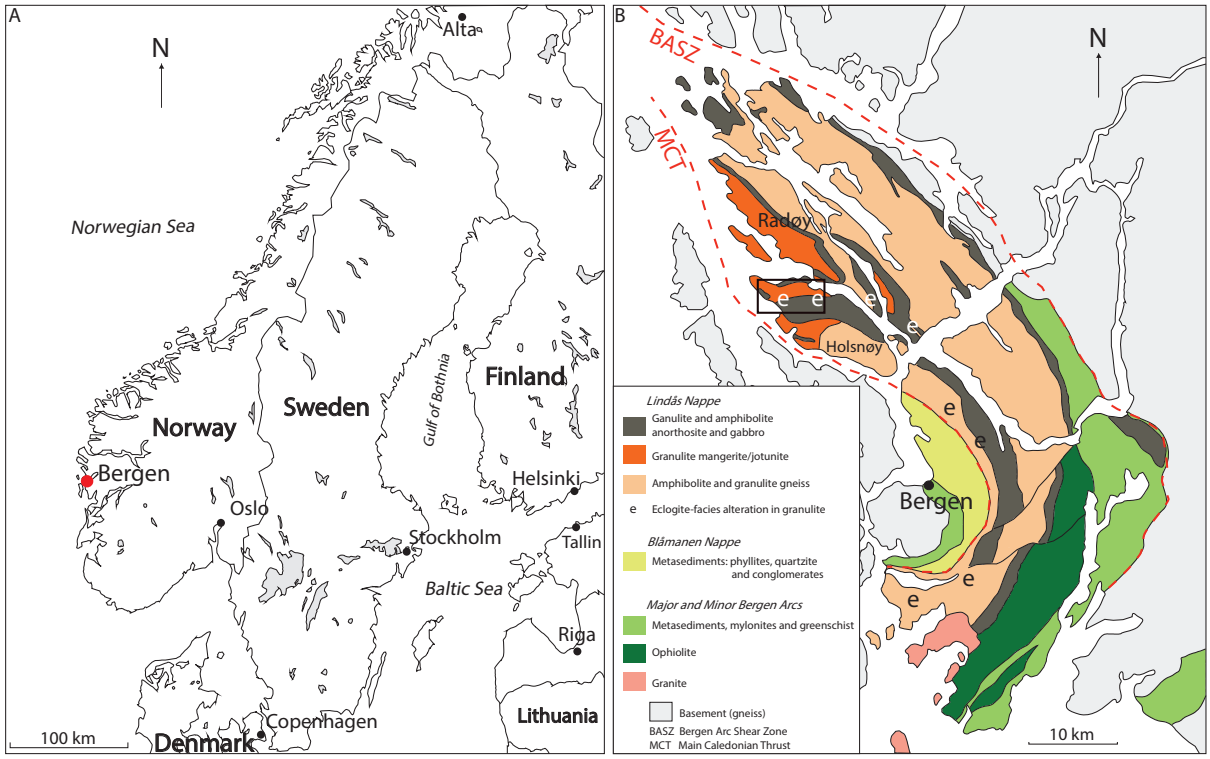

Figure 2. a) Location of Bergen in Norway. b) Geological map of the Bergen Arcs. The study area is indicated by the black box in northern Holsnøy Island.

of plagioclase, clinopyroxene, garnet and orthopyroxene and was metamorphosed during the Grenvillian Orogeny (Krogh, 1977; Austrheim & Griffin, 1985) at approximately c. 950 Ma. Its peak metamorphic conditions were 10 kbar and 800–900 °C (Austrheim, 1987; Boundy *et al.*, 1996). The granulite domain was subsequently buried during the Caledonian Orogeny (c. 429–450 Ma; Austrheim & Griffin, 1985; Glodny *et al.*, 2008), and reacted with fluids that infiltrated the system to form the peak eclogite-facies assemblages: garnet, omphacite, zoisite, phengite ± kyanite ± rutile ± quartz.

The conversion of the granulite to eclogite was triggered by a combination of fluid availability and deformation during the subduction of the Lindås Nappe in the Caledonian Orogeny (Austrheim, 1987; Jamtveit *et al.*, 1990; Austrheim *et al.*, 1997). This study follows the initial *P–T* framework depicted in Chapter 2. The study conducted in Chapter 2 was based on rocks that crystallised at different stages of deformation. Stage 1 involved the formation of pseudotachylites in the granulite, providing the initial conduits for fluid infiltration and their metamorphic recrystallisation at *P–T* conditions 15.2–15.7 kbar and 675–685 °C. Stage 2 involved the formation of discrete shear zones at centimetre to metre scales and the formation of a hydrous metamorphic assemblage due to the breakdown of garnet. Stage 3 is the complete conversion of granulite to an omphacite-rich eclogite, indicated by the disappearance of plagioclase and peak metamorphic assemblage of omphacite–zoisite–phengite–garnet–kyanite ± quartz ± rutile, at *P–T* conditions 21–22 kbar and 670–690 °C. Stage 4 is the over-print of the peak omphacite-rich eclogite by a later, retrogressed phengite-rich one at *P–T* conditions 16–17 kbar and 680–700 °C.

3. APPROACH

This study focuses on the exhumation of the peak eclogite-facies rocks (Stage 3 sample HOL14–7C, Chapter 2) to the amphibolite-facies (sample HOL17–4A; 32V 280906E, 280906 N), as it represents the extremely fast ascension described by previous authors (e.g. Raimbourg *et al.* 2007, Jamtveit *et al.,* 2018; 2020). In some localities, eclogite-facies domains sit as relict blocks within the sheared amphibolite-facies assemblages (highlighted by red outlines in Figure 3). Muscovite and zoisite grains define the foliation of the sheared amphibolite, which strikes E/W and wraps around the relict eclogite blocks. Work conducted by Glodny et *al.* (2007), estimated a Rb/Sr age of 414 ± 2.8 Ma for the amphibolite-facies shear zones. As a result of the geochronological and field observations, the amphibolite-facies domain sampled in this study has been interpreted to have been metamorphosed during the retrogression of the Holsnøy system.

Figure 3. Relict eclogite blocks present in amphibolite-facies shear zones, outlined in red. Hammer in the middle of the photograph for scale. This outcrop was sampled and field observation used to interpret the formation of the amphibolite-facies shear zone post peak eclogite-facies metamorphism.

The calculation of exhumation rates is performed by first estimating a pressure decrease from eclogite-facies to amphibolite-facies. Pressure estimates of 21– 22 kbar for the eclogite-facies rocks were obtained in Chapter 2 and this study uses phase equilibria forward modelling, in the same chemical system as in Chapter 2, to estimate *P–T* conditions for the amphibolite-facies metamorphism. The pressure decrease between the two metamorphic facies is then converted to the change of depth of the domain in the Earth's crust, assuming pressure is lithostatic only. Secondly, the duration for this ascension is estimated based on forward diffusion modelling on zoned garnet grains in the eclogite sample HOL14–7C. The methods for each step are outlined below.

3.1 Phase equilibria modelling: amphibolite sample, HOL17–4A

The *P–T* pseudosection was calculated for amphibolite-facies sample, HOL17–4A using THERMOCALC v.3.33 and the internally consistent dataset, ds55 by Holland and Powell (1998; updated in November 2003). It is acknowledged here that internally consistent dataset ds62 could be used, however, ds55 was used to keep this study consistent to previously published *P–T* framework in Chapter 2. The bulk-rock compositions were modelled in a geologically realistic system NCKFMASHTO, with the following activity–composition (*a–x*) models: amphibole (Diener *et al.*, 2007; Diener & Powell, 2012); clinopyroxenes (Holland & Powell, 2003; Diener & Powell, 2012); chlorite, talc and epidote–clinozoisite (Holland & Powell, 1998); garnet

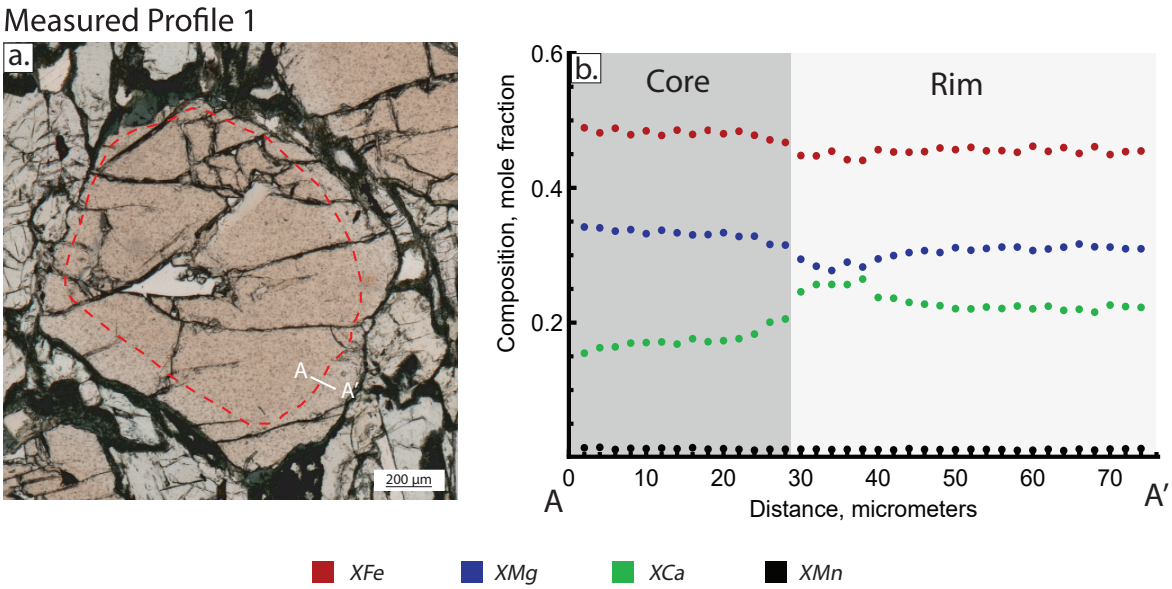

Figure 4. Example of measured core-rim traverse used for forwared diffusion modelling, in sample HOL14–7C. a) Location of traverse in first garnet grain from A to A'. b) The measured composition of Profile 1, from A to A'.
* The core of the garnet grains are outlined with a red-dashed line.

and biotite (White *et al.*, 2007); plagioclase and K-feldspar (Holland & Powell, 2003); ilmenite and chloritoid (White *et al.*, 2000); muscovite and paragonite (Coggon & Holland, 2002).

The amphibolite-facies sample, HOL17–4A, has interpreted peak metamorphic mineral assemblage, garnet rim–plagioclase–hornblende–muscovite–zoisite ± quartz ± rutile. The foliation is defined by coarse-grained muscovite (0.2–0.7 mm), finer-grained zoisite (< 0.3 mm) and hornblende (< 0.2 mm). Porphyroblastic garnet grains (0.5–2 mm) are zoned and the cores are interpreted to be inherited from the protolith, as was the case for garnet grains in the eclogite-facies rocks in Chapter 2. The abundances of the major rock forming minerals were determined using pixel counting in the Adobe Photoshop software, and are as follows: plagioclase, 32.0 %; hornblende, 26.2 %; muscovite, 27.2 %; garnet rims, 0.3 %; zoisite, 12.4 %; and quartz, 3.3 %. The peak *P–T* conditions were determined by plotting the isopleths for the modal abundances of garnet, quartz and hornblende.

3.2 Multi-component forward diffusion modelling on garnet grains: eclogite sample HOL14–7C

Garnet compositions for diffusion modelling were acquired on eight transects (example in Figure 4) using a CAMECA SXFive electron probe micro-analyser (EPMA) at Adelaide Microscopy, University of Adelaide. Calibration of the apparatus was conducted prior to analysis on an andradite standard. A beam current of 20 nA and acceleration voltage of 15 kV were used for elemental analyses at 2 µm intervals along the core to rim boundary (see below). Elemental oxides were acquired in wt %, and recast as end-member modal proportion of garnet using excel spreadsheet by Locock (2008).

Diffusion modelling was performed following methods outlined by Caddick *et al.* (2010) and Caddick and Thompson (2008), using the software Wolfram Mathematica. Composition-dependent Fe, Mg, Ca and Mn diffusivities of Chakraborty and Ganguly (1991), Carlson (2006), Vielzeuf *et al.* (2007) and Chu and Ague (2015)

were used, with formulation for multi-component diffusion in ionic lattices by Lasaga (1979). The initial profiles for the transects were assumed to be ramped, based on the sharp compositional changes in yttrium in the garnet grains in sample HOL14–7C, as presented in Chapter 4. Moreover, a ramped initial compositional profile results in maximum diffusion durations, hence minimum exhumation rates. To ensure that this assumption is valid, profiles 4 and 8 were also performed with initial 'stepped' profiles (Figure S4.1), and the results were compared to those with initial ramped initial profiles.

Three sets of fixed *P–T* parameters were used for the diffusion models. Firstly, peak metamorphic conditions of 22 kbar and 680 °C for eclogite-facies sample, HOL14–7C (Chapter 2), were used to estimate the duration of exhumation from the eclogite-facies to the amphibolite-facies. Secondly, the models were performed at conditions of 22 kbar and 600 °C to assess the temperature dependency of diffusion durations in the garnet grains. And lastly, peak *P–T* conditions of 10.5 kbar and 600 °C for the amphibolite-facies metamorphism obtained by Jamtveit *et al.* (2018) were used to maximise the modelled durations for the exhumation of the Holsnøy system. It should be noted that diffusion modelling at fixed *P–T* does not require transects from the centre of the garnet grain (core) to the edge of the grain (rim) as only the diffusional gradient at the core/rim boundaries is considered. Therefore, transects were shortened in the homogeneous parts of the cores and rims to reduce the running times of models.

4. RESULTS

4.1 Pressure decrease from the eclogite-facies to amphibolite-facies

The *P–T* pseudosection for the amphibolite-facies sample, HOL17–4A is presented in Figure 5. The boundaries of the peak mineral assemblage field are shown in bold lines. The *P–T* conditions for the peak assemblage were constrained to 11.8–12.2 kbar and 723–732 °C using the modal abundances of quartz, garnet and hornblende. These estimates are not in agreement with previous studies, which employed conventional thermobarometry (Austrheim & Griffin, 1985; Boundy *et al.*, 1997) to estimate *P–T* conditions of 8–9 kbar and 600 °C. A more recent study by Jamtveit *et al.* (2018) estimated *P–T* conditions of 10.5 kbar and 600 °C for the formation of the amphibolite-facies assemblages, using forward phase equilibria modelling. Despite using the same method, the two estimates are different, especially that of temperature. It is likely that the samples used in the two studies are representative of different stages of retrogression. The amphibolite sample used in this study is from an amphibolite-facies shear zone, while Jamtveit *et al.* (2018) sampled amphibolite assemblages that developed around feldspar-rich pegmatites that cross-cut both eclogite and amphibolite-facies shear zones. With such differing field relationships, it is difficult to ascertain whether the *P–T* conditions calculated in this study and those of Jamtveit *et al.* (2018) are comparable. Since samples modelled in Jamtveit *et al.* (2018) cross-cut an amphibolite shear zone it is plausible that the peak *P–T* conditions reported represent a later stage in the evolution of the Holsnøy system.

Nevertheless, in this study the *P* estimates of 11.8–12.2 kbar were used for the pressure change of the Holsnøy system to remain consistent with

Table 1. Calculated diffusion durations and exhumation rates for Profiles 1–8 (see Figure S4.2). The exhumation rates were calculated on a minimum ascension of 30 km in the Earth's crust. Results under Stepped profiles indicate the two profiles performed with initial stepped profile (Figure S4.1).
Values in italics represent minimum and maximum values for exhumation durations and rates.

***P–T* conditions**	**22 kbar, 680 °C**		**22 kbar, 600 °C**		**10.5 kbar, 600 °C**	
	Duration (Ma)	Exhumation rates (mm/yr)	Duration (Ma)	Exhumation rates (mm/yr)	Duration (Ma)	Exhumation rates (mm/yr)
Profile 1						
Carlson (2006)	*0.0049* – 0.0055	5455 – *6122*	*0.092*–0.104	289–*326*	*0.016*–0.032	938–*1880*
Chakraborty and Ganguly (1991)	0.038 – 0.041	732 – 790	1.03–1.18	25.4–29.1	0.420–0.500	60.0–71.4
Vielzeuf *et al*. (2007)	0.094 – 0.106	283 – 319	1.00–1.30	23.1–30.0	0.400–0.500	60.0–75.0
Chu and Ague (2015)	0.038 – 0.041	732 – 790	1.00–1.21	24.8–30.0	0.420–0.500	60.0–71.4
Profile 2						
Carlson (2006)	0.0118 – 0.0132	2272 – 2542	0.150–0.170	176–200	0.035–0.045	667–857
Chakraborty and Ganguly (1991)	0.065 – 0.075	400 – 462	1.90–2.05	14.6–15.8	0.70–0.90	33.3–42.9
Vielzeuf *et al*. (2007)	0.172 – 0.186	161 – 174	1.95–2.10	14.3–15.4	0.75–0.90	33.3–40.0
Chu and Ague (2015)	0.065 – 0.075	400 – 462	1.90–2.05	14.6–15.8	0.80–0.90	33.3–37.5
Profile 3						
Carlson (2006)	0.068–0.076	395–441	1.20–1.40	24.4–25.0	0.280–0.320	93.8–107
Chakraborty and Ganguly (1991)	0.310–0.350	86.0–97.0	9.00–9.60	3.33–3.13	3.70–*4.10*	*7.32*–8.11
Vielzeuf *et al.* (2007)	0.690–*0.730*	*41.0*–43.0	9.40–*10.0*	*3.00*–3.19	3.50–4.00	7.50–8.57
Chu and Ague (2015)	0.320–0.350	86.0–94.0	9.20–9.60	3.13–3.26	3.70–*4.10*	*7.32*–8.11
Profile 4						
Carlson (2006)	0.042–0.050	600–714	0.820–0.900	33.65.23–36.6	0.190–0.220	136–158
Chakraborty and Ganguly (1991)	0.205–0.225	133–146	5.60–6.30	4.76–5.36	2.30–2.60	11.5–13.0
Vielzeuf *et al.* (2007)	0.490–0.540	55.6–61.2	5.80–6.40	4.69–5.17	2.30–2.60	11.5–13.0
Chu and Ague (2015)	0.190–0.240	125–158	5.60–6.30	4.76–5.36	2.30–2.60	11.5–13.0
Profile 5						
Carlson (2006)	0.004–0.007	4290–7500	0.100–0.120	250–300	0.018–0.026	1150–1670
Chakraborty and Ganguly (1991)	0.050–0.060	500–600	1.40–1.80	16.7–21.4	0.600–0.800	37.5–50.0
Vielzeuf *et al.* (2007)	0.100–0.140	214–300	1.40–1.80	16.7–21.4	0.500–0.700	42.9–60.0
Chu and Ague (2015)	0.050–0.060	500–600	1.40–1.80	16.7–21.4	0.600–0.800	37.5–50.0
Profile 6						
Carlson (2006)	0.020–0.023	1300–1500	0.370–0.440	68.2–81.1	0.080–0.095	316–375
Chakraborty and Ganguly (1991)	0.150–0.180	166–200	4.50–5.00	6.00–6.67	1.80–2.10	14.3–16.7
Vielzeuf *et al.* (2007)	0.430–0.490	61.2–69.8	4.70–5.10	5.88–6.38	1.80–2.10	14.3–16.7
Chu and Ague (2015)	0.150–0.190	158–200	4.50–4.90	6.12–6.67	1.80–2.10	14.3–16.7
Profile 7						
Carlson (2006)	0.020–0.022	1360–1500	0.400–0.460	65.2–75.0	0.08–0.095	316–375
Chakraborty and Ganguly (1991)	0.170–0.200	150–176	5.00–5.60	5.36–6.00	1.80–2.60	11.5–16.7
Vielzeuf *et al.* (2007)	0.460–0.540	55.6–65.2	5.20–5.80	5.17–5.77	2.00–2.50	12.0–15.0
Chu and Ague (2015)	0.170–0.210	143–176	5–5.60	5.36–6.00	2.00–2.60	11.5–15

***P–T* conditions**	**22 kbar, 680 °C**		**22 kbar, 600 °C**		**10.5 kbar, 600 °C**	
	Duration (Ma)	Exhumation rates (mm/yr)	Duration (Ma)	Exhumation rates (mm/yr)	Duration (Ma)	Exhumation rates (mm/yr)
Profile 8						
Carlson (2006)	0.021–0.024	1250–1430	0.400–0.460	65.2–75.0	0.08–0.095	316–375
Chakraborty and Ganguly (1991)	0.080–0.120	250–375	5.00–5.40	5.56–6.00	2.00–2.40	12.5–15.0
Vielzeuf *et al.* (2007)	0.260–0.280	107–115	5.20–5.80	5.17–5.77	2.00–2.40	12.5–15.0
Chu and Ague (2015)	0.090–0.120	250–333	5.00–5.60	5.36–6.00	2.00–2.40	12.5–15.0
Stepped profiles						
Profile 4						
Carlson (2006)	0.018–0.024	1250–1670				
Chakraborty and Ganguly (1991)	0.120–0.140	214–250				
Vielzeuf *et al.* (2007)	0.180–0.200	150–167				
Chu and Ague (2015)	0.120–0.150	200–250				
Profile 8						
Carlson (2006)	0.0065–0.0085	3530–4620				
Chakraborty and Ganguly (1991)	0.024–0.040	750–1200				
Vielzeuf *et al.* (2007)	0.060–0.080	375–500				
Chu and Ague (2015)	0.025–0.030	1000–1200				

the software, dataset and chemical system used for phase equilibria modelling in Chapter 2. More importantly, they result in the minimum pressure decrease compared to estimates by Jamtveit *et al*. (2018), which results in minimum possible exhumation rates. To complete the *P–T* framework established in Chapter 2, the constraints for the amphibolite-facies was added as illustrated in Figure 6, as Stage 5 of deformation. Combining these constraints with that previously obtained for the peak eclogite conditions (21–22 kbar and 670– 690 °C), the minimum pressure change experienced by the eclogites on Holsnøy Island is approximately – 8.8 kbar (Figure 6).

4.2 Diffusion models on zoned garnet grains and exhumation rates

Diffusion modelling (e.g. Figure 7) was performed on eight garnet grains in the peak-eclogite sample, HOL14–7C, described in Chapter 2 and used to calculate the peak metamorphic conditions for *P–T* framework presented in Figure 6. This sample is ideal for diffusion modelling as it is prominently zoned in major elements from core to rim (Chapter 2 and see Figure S4.2). It is assumed here that, as sample HOL14–7C is interpreted to represent the peak metamorphic stage in the evolution of the Holnøy sytem, the zonation patterns in its garnet grains are a response to changes in the *P–T* conditions during retrogression.

Multiple diffusion coefficients were used for the modelling of diffusion durations (Table 1) and the exhumation rates were calculated on the assumption that a pressure change of – 8.8 kbar equates to a minimum ascension of 30 km. For all three sets of *P–T* conditions used for the diffusion models, Profile 1 yielded minimum durations (i.e. maximum exhumation rates) while Profile 3 yielded the longest durations (i.e. minimum exhumation rates). In general, models performed

using the diffusion coefficient by Carlson (2006) yielded the shortest durations. Models performed using coefficients by Chakraborty and Ganguly (1991), Vielzeuf *et al.* (2007) and Chu and Ague (2015) are generally in agreement with each other, except at 680 °C, and models using coefficient by Vielzeuf (2007) yielded the longest duration (Table 1).

Diffusion models using *P–T* conditions of 22 kbar and 680 °C resulted in the shortest durations, ranging from 0.0049–0.730 Ma, with corresponding exhumation rates of 41.0–6122 mm/yr. The slower exhumation rates (< 85 mm/yr) were obtained on Profiles 3, 4, 6 and 7, using the diffusion coefficient by Vielzeuf *et al.* (2007). Models on all other profiles and coefficients yielded exhumation rates greater than 85 mm/yr. Diffusion models performed at 22 kbar and 600 °C yielded the longest durations of all three parameter sets, with durations ranging from 0.092–10.0 Ma, and corresponding slowest exhumation rates ranging from 3–326 mm/yr. Lastly, duration estimations range from 0.016–4.10 Ma, with corresponding exhumation rates of 7–1880 mm/yr for models run at 10.5 kbar and 600 °C.

5. DISCUSSION AND CONCLUSIONS

It has previously been suggested that the eclogite domains on Holsnøy Island were enhanced by the availability of fluids during formation at depths of 70 km in the Earth's crust during the continental collision of Baltica and Laurentia, during the Caledonian Orogeny (Austrheim and Griffin, 1985; Austrheim, 2013, Jamtveit *et al*., 1990). The domains were exhumed to amphibolite-facies conditions (Glodny *et al.*, 2007), and then to the Earth's surface. Jolivet *et al.* (2005) suggested the décollement of the subduction slab, when buoyancy forces (due to the lower density of granulite slab) overcame that of the descending lithosphere, as the most likely mechanism to account for the seemingly fast exhumation rates, although no quantitative data were reported in the study. While this model is plausible, there is increasing evidence in the Bergen Arcs that the rocks on Holsnøy Island might not have been formed in a typical subduction setting, as previously suggested. For example, field relationships suggest that amphibolite metamorphism occurred after the peak eclogite conditions, as relict eclogite blocks are enclosed by sheared amphibolite domains in places (Figure 3). However, Centrella *et al.* (2018) suggested that in some localities, the formation of the amphibolite and eclogite-facies domains occur at the same structural level (based on their continuous foliations into the shear zones and mass transfer calculations), in the evolution of the system as the fluid front migrates from amphibolite-facies shear zones, to eclogite and granulite domains. The authors also concluded that the traditional scenario, whereby eclogites form at great depths, followed by the formation of amphibolites during uplift, cannot be explained by these spatial relationships. Geochronology undertaken in previous studies indicates that the age for the eclogite metamorphism is often within uncertainty of the amphibolite metamorphsim. Jamtveit *et al.* (2018) reported $^{206}Pb/^{238}U$ ages of 423.6 ± 1.0 Ma on zircons in an amphibolite-facies pegmatite, while mineral Sm–Nd analyses by Glodny *et al.* (2003) yielded amphibolite-facies ages of 422 ± 10 Ma, which are in agreement with reported zircon $^{206}Pb/^{238}U$ ages of 423 ± 4 Ma by Bingen *et al.* (2004) and Rb-Sr ages of 425 ± 4 Ma by Glodny *et al.* (2003) for eclogite-facies metamorphism. The quasi-isothermal burial and exhumation indicated by the *P–T* framework in Chapter 2 and updated herein (Figure 6), is further evidence that these rocks were not formed

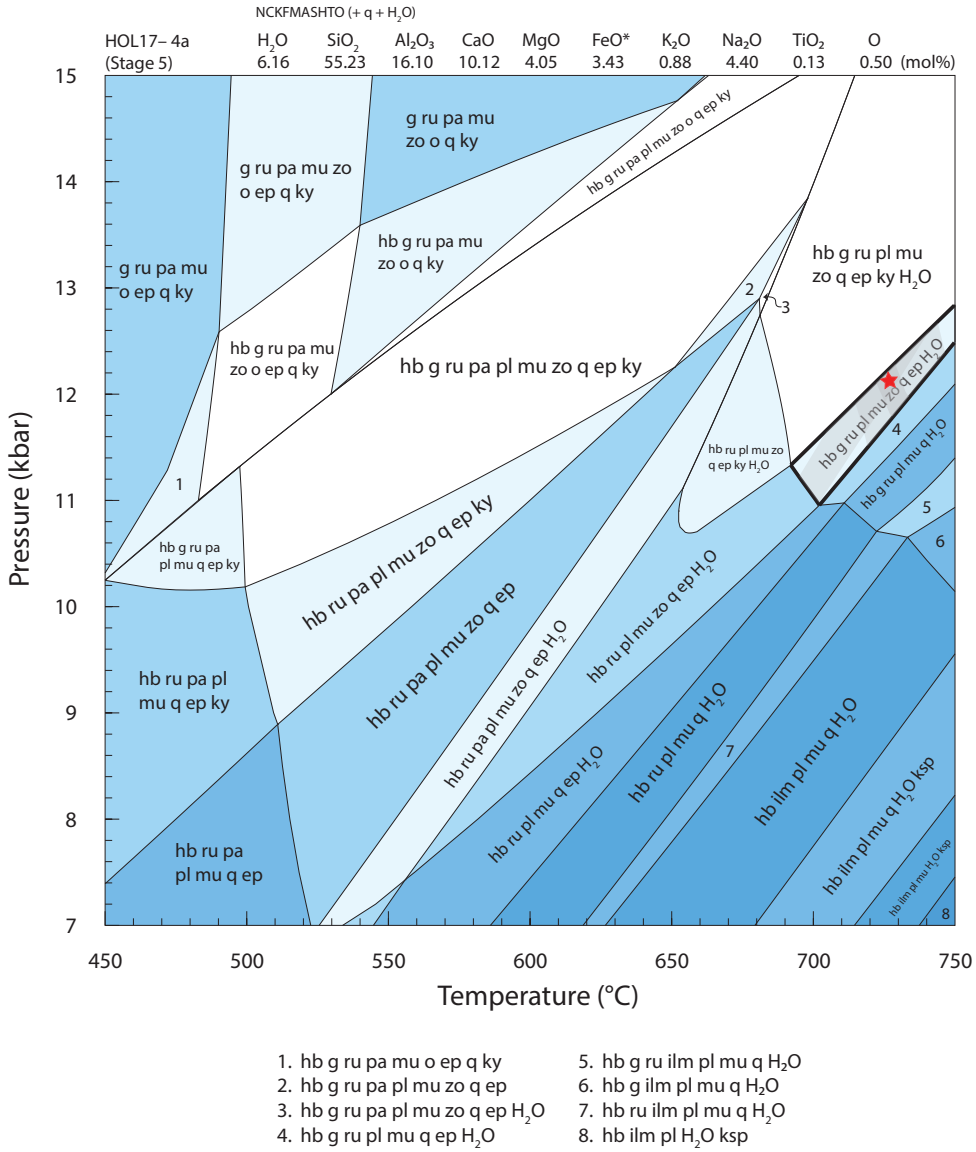

1. hb g ru pa mu o ep q ky
2. hb g ru pa pl mu zo q ep
3. hb g ru pa pl mu zo q ep H_2O
4. hb g ru pl mu q ep H_2O
5. hb g ru ilm pl mu q H_2O
6. hb g ilm pl mu q H_2O
7. hb ru ilm pl mu q H_2O
8. hb ilm pl H_2O ksp

Figure 5. Calculated *P–T* pseudosection for stage 5 of deformation, amphibolite-facies sample, HOL17–4A. The interpreted peak metamorphic field is indicated in bold. The red star indicates the peak metamorphic conditions constrained by the modal abundances of garnet, quartz and hornblende (grey shaded regions). The mineral abbreviations used after Holland and Powell (1998).

in typical subduction related settings. Jamtveit *et al.* (2018) stated that, based on a reasonable thermal gradient for subductions (e.g. ~ 5 °C/km), subduction of 5 kbar should result in a temperature increase of over 90 °C. Hence, isothermal subduction is not a likely burial mechanism for the eclogite domains. Lastly, it is intriguing that the only HP domains that exist in the Bergen Arcs are the eclogite-facies assemblages, which are localised in only a minor fraction of the Lindås Nappe, especially within shear zones. The highest metamorphic grade experienced by domains in the Major and Minor Bergen Arcs, Blåmanen Nappe, and the majority of the Lindås Nappe, occur in the amphibolite-facies (Figure 2b). This study adds to recent lines of evidence that potentially extreme rates of exhumation may exist for the ascension of eclogite-facies domains to the amphibolite-facies in the Bergen Arcs.

The *P–T* parameters chosen for the diffusion models on eclogite sample, HOL14–7C, were

22 kbar and 680 °C. These are the calculated peak *P–T* conditions experienced by the eclogite domains on Holsnøy Island (Chapter 2). The highest pressure recorded by the eclogite samples (i.e. 22 kbar) was used for modelling this would result in slower diffusion durations. A temperature of 680 °C also results in slower durations as it is on the lower end of temperature estimates for the eclogites compared to previous studies (650 – 800 °C; Austrheim and Griffins, 1985; Boundy *et al.*, 1996; Jamtveit *et al.*, 1990; Raimbourg, 2007). This set of parameters, therefore, arguably yield the slowest possible exhumation rates for the ascension of the eclogite domains, to the amphibolite-facies on Holsnøy Island. In a tectonic scenario where pressure is correlated to depth, a pressure change of – 8.8 kbar corresponds to a minimum ascension of 30 km within the Earth's crust. Most minimum exhumation rates calculated using these three parameters result in values above that of typical exhumation values when compared to other terranes (Figure 1), and range between 125–6122 mm/yr. While profiles 3, 4, 6 and 7 yielded comparatively slower exhumation rates based on the diffusion coefficient of Vielzeuf *et al.* (2007), their values vary from 41.0–69.8 mm/year, which are on the faster end of typical exhumation rates for HP/UHP terranes.

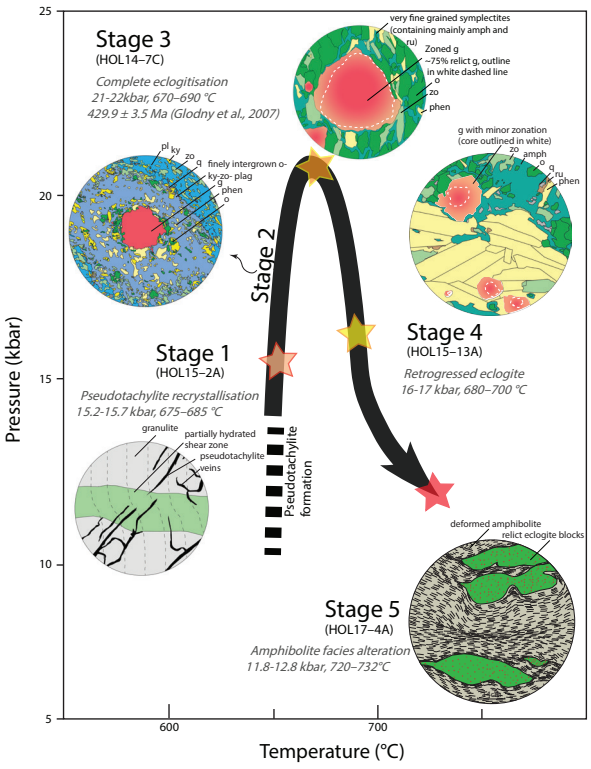

Figure 6. Updated *P–T* path for the Holsnøy system, from Chapter 2. *P–T* conditions for stage 5 of deformation, calculated herein and complete the evolution of the system.

To test the extent of temperature dependency of the models and its corresponding effect on these extreme exhumation rates, the comparatively lower temperature recorded by the amphibolite-facies domains (600 °C after Jamveit *et al.* (2018)) was adopted. The models performed at *P–T* conditions of 22 kbar and 600 °C yielded durations approximately 27 times longer than those performed at 22 kbar and 680 °C (Table 1). This resulted in rates consistent with those previously reported for other HP/UHP terranes (Figure 1), for most profiles, with values ranging from 3.0 to 36.6 mm/yr. However, Profiles 1, 2, 5, 6, 7 and 8 resulted in comparatively faster, exhumation rates, ranging from 65–326 mm/yr, using the Carlson (2006) coefficient. While most of these values agree with previously recorded exhumation rates for other HP/UHP terranes, the parameters at which these models were performed are not recorded by the rocks on Holsnøy Island. Indeed, at a temperature of 600 °C, the Hoslnøy system is reported to be within the amphibolite-facies, and hence significantly lower pressures than 22 kbar. Previous authors estimated pressures ranging from 8–14 kbar and temperatures of 525 to 675 °C for the amphibolite-facies metamorphism (Austrheim, 1978; Austrheim and Griffins, 1985; Khün, 2002; Glodny, 2007). To complement the lower temperature of 600 °C used, models were also performed at 10.5 kbar (after Jamtveit *et al.* 2019) to reflect more realistic conditions, recorded by the rocks within the system. Models run at 10.5 kbar and 600 °C resulted in variable exhumation rates.

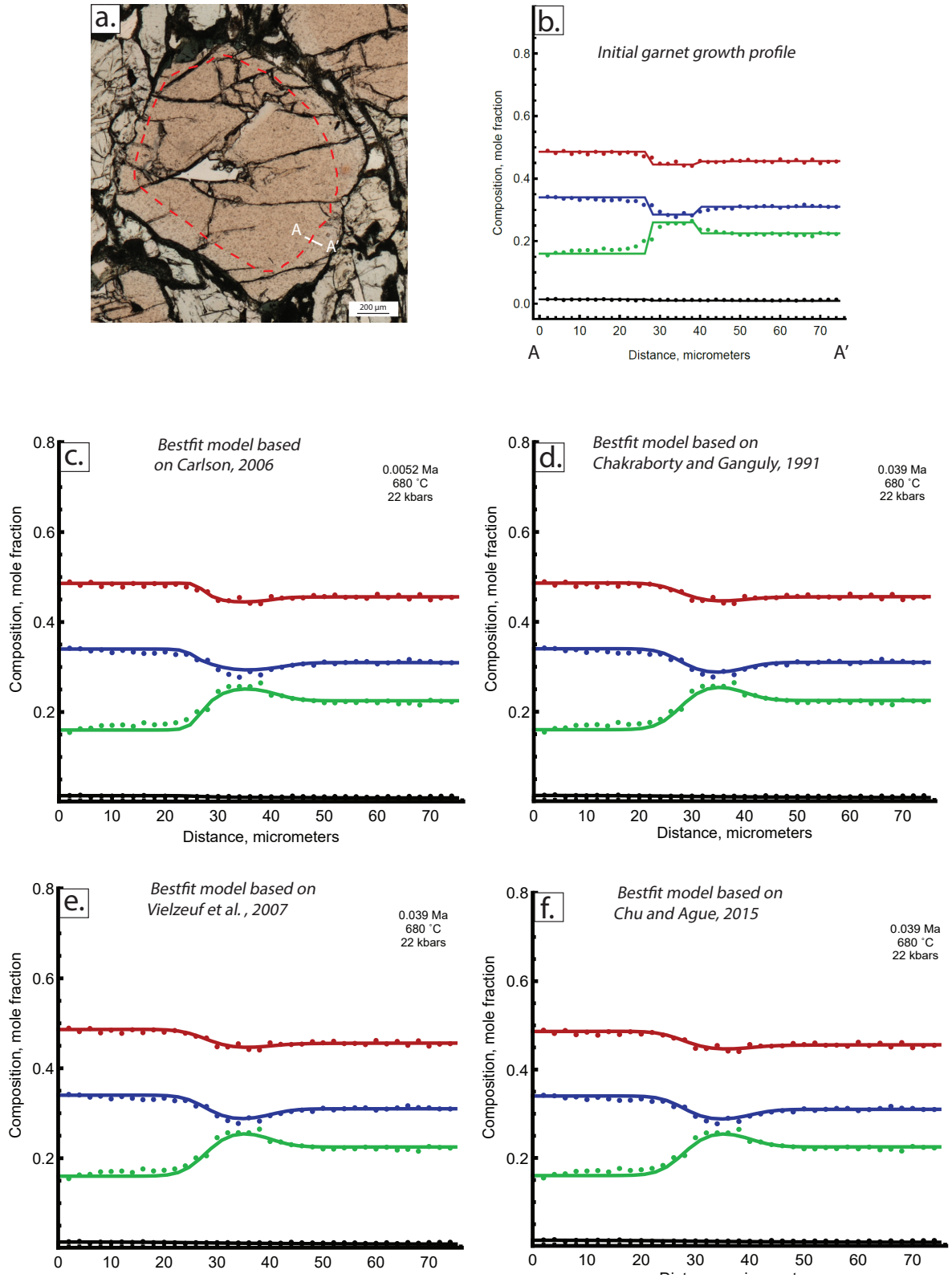

Figure 7. Examples of best fit modelled durations for Profile 1. a) Location of traverse on garnet grain for Profile 1. b) Initial profile set for modelling: i.e. compositional profile pre-diffusion . Bestfit modelled durations based on diffusion coefficient by: c) Carlson (2006); d) Charkraborty and Ganguly (1991); e) Vielzeuf et al. (2007); f) Chu and Ague (2005).

All values based on the diffusion coefficient by Carlson (2006) are reflective of significantly faster exhumation rates (93.8–1880 mm/yr). Those based on coefficients by Chakraborty and Ganguly (1991), Vielzeuf *et al.* (2007) and Chu and Ague (2015) yielded variable values. Profiles 3, 4, 6, 7 and 8 record comparatively slower exhumation rates, ranging from 7.32–16.7 mm/yr, which are well within the typical values expected for HP/UHP terranes. Profiles 1, 2 and 5, however, record faster rates ranging between 33.3–60.0 mm/yr, which are on the faster end of exhumation rates recorded by HP/UHP (Figure 1). While there is a significant difference between the rates obtained at 22 kbar and 680 °C and 10.5 kbar and 600 °C, those calculated using the eclogite-facies conditions (i.e. 22 kbar, 680 °C) are arguably more representative of the ascension of the altered domains on Holsnøy Island. This is because the amphibolite *P–T* conditions represent what the system retrogressed to after ascension from the eclogite-facies and therefore, postdates the exhumation history that this study focuses on. Moreover according to Chakraborty and Ganguly (1991) and Baxter *et al.* (2017), most elemental diffusion in garnet occurs at or close to peak temperature of a system, which provides an ideal avenue to estimate diffusion rates of complex *P–T* histories. It should be noted that based on Chapter 2, the maximum temperature reached by the Holsnøy system is 700 °C, which was not taken into consideration when performing the diffusion models in this study.

While the diffusion models presented in this study provide an indication for the minimum exhumation rates for the eclogites on Holsnøy Island, there are limitations to be considered with the approach taken. Firstly, the acquisition of the zonation profiles is assumed to be perpendicular to the compositional zonation of garnet grains. It is difficult to distinguish between different inclinations of zonation in thin section, which leads to the smearing out of signals during data acquisition on the EPMA. This, therefore, results in variable diffusion durations between profiles, as observed in Table 1. To increase the confidence in the data presented, more profiles are required, possibly acquired on different eclogite-facies samples. Secondly, the initial compositional profiles for modelling are not easily constrained. This study uses the sharp compositional changes in Y in garnet grains as an indication for the initial profile for the major elemental compositions (Chapter 4). However, it is not possible to confidently constrain the initial profile of each garnet grain. A ramped profile is therefore, assumed for all profiles, as this should theoretically yield maximum durations, hence minimum exhumation rates. Two profiles (4 and 8) were run with an initial stepped compositional profiles (see Figure S4.1) to test this assumption. In both cases, the resulting exhumation rates were considerably faster than those modelled with initial ramped profiles (Table 1). Lastly, it is difficult to differentiate between the diffusion in response to the eclogite to amphibolite-facies ascension, and that beyond the amphibolite-facies retrogression conditions (i.e. to closure temperature of garnet). In the calculations undertaken for the exhumation rates, it was assumed that the diffusion durations obtained were only due to the eclogite to amphibolite-facies retrogression. However, the eclogite-facies domains should also record elemental diffusion until the closure temperature of garnet, as diffusion would still occur at a slower rates, as demonstrated by models performed at 600 °C. Therefore, it can be argued that the exhumation rates are potentially faster than those estimates in Table 1, due to the lack of differentiation between the two exhumation stages. A potential avenue to test

the contribution of the second stage ascension to those calculated in this study is by modelling the diffusion duration on amphibolite-facies garnet grains. However, the diffusion relaxation beyond the amphibolite-facies might not be significant as volume diffusion in garnet grains decreases with temperatures below ~ 600 °C, as the rocks cool to the closure temperature of garnet (Charkraborty and Ganguly, 1991; Baxter *et al*., 2017).

If the 22 kbar and 680 °C parameters are indeed, more representative of the exhumation of the eclogite domains to the amphibolite-facies, these estimates are in agreement with a previous study by Raimbourg *et al.* (2007), who suggested considerably faster diffusion durations between two generations of garnet growths (140 – 2900 yrs) for the peak eclogite. These durations result in an extremely fast and unrealistic minimum exhumation rate of 10344 mm/yr, for an ascension of 30 km. Such extreme rates are tectonically not feasible and cannot be explained by known mechanisms for the exhumation of deeply buried terranes (e.g. erosion and tectonic uplift). This highlights the potential need for alternative mechanisms/models that can lead to these rapid exhumation rates, or/and begs the question of whether the pressure change recorded by the Holsnøy eclogites correlates to exhumation. One significant assumption in most exhumation models and calculations is that pressure is correlated to depth in the Earth's crust. HP terranes are hypothesised to form at depths of > 55 km due to the amount of pressure required to stabilise their assemblages.

It is proposed here that the formation of the eclogites on Holsnøy Island occurred at shallower depths than what has previously been proposed and the mineralogy observed is a result of tectonic overpressure, instead of lithospheric pressure. Schmalholz and Podladchikov (2013) modelled the response of pressure in the lower and upper crust when subjected to shear deformation due to viscous heating during crustal shortening. These models demonstrated that within a weakened crustal shear zone, pressure can be significantly larger than lithostatic pressure; i.e. tectonic overpressure can be significantly greater than the deviatoric stress in the same location. Moreover, tectonic models by Li *et al.* (2010) and Gerya (2015) concluded that, at depth of ~ 42km in rheologically stronger and dry crust, overpressure (in weaker zones) can be up to 22 kbar when subjected to deviatoric stresses of ~ 15 kbar. These pressures are consistent with the pressure history experienced by the Holsnøy system, summarised in Figure 6. Jamtveit *et al.* (2018) demonstrated that, in the case of the Bergen Arcs, pressure perturbations exceeding 5 kbar can be produced if the strong granulite were to be subjected to high differential stress. These models can potentially explain why: (1) there is no evidence of HP/UHP domains in the Bergen Arcs besides the sheared eclogites on Holsnøy Island; (2) the effectively synchronous formation of eclogite and amphibolite-facies domains based on geochronology and mass transfer calculations, and (3) the seemingly extreme exhumation rates of the eclogite domains. Therefore, it is likely that the eclogites on Holsnøy Island were never buried to depths > 70 km. If considered all together, the Bergen Arcs potentially only reached depths equivalent to that of amphibolite-facies pressures (~ 12.2 kbar), as indicated by most of the domains present in the Lindås Nappe. This interpretation is consistent with more recent studies by Reuber *et al.* (2016), Marques and Mandal (2018), and Jaquet and Schmalholz (2018) who modelled the formation of HP/UHP terranes at much lower crustal depths based on varying factors such as rheology and deformation during subduction. This points

towards the Holnøy eclogites being a potential example of mineralogical responses and records of overpressure at on a significant scale. The *P–T* path calculated in Chapter 2 suggests records of an isothermal pressure increase and decrease, consistent with an extreme pressure variation, which is to be expected with an overpressure development and release. Therefore, the *P–T* records on Holsnøy Island likely reflects a change is stress regime instead of ascension in the crust, as suggested previously by Yamato and Braun (2016).

REFERENCES

Agard, P., Yamato, P., Jolivet, L. & Burov, E., 2009. Exhumation of oceanic blueschists and eclogites in subduction zones: timing and mechanisms. *Earth-Science Reviews*, **92**, 53-79.

Anczkiewicz, R., Platt, J. P., Thirlwall, M. F. & Wakabayashi, J., 2004. Franciscan subduction off to a slow start: evidence from high-precision Lu–Hf garnet ages on high grade-blocks. *Earth and Planetary Science Letters*, **225**, 147-161.

Andersen, T., Austrheim, H. & Burke, E. A. J., 1991. Fluid-induced retrogression of granulites in the Bergen Arcs, Caledonides of W. Norway: Fluid inclusion evidence from amphibolite-facies shear zones. *Lithos*, **27**, 29-42.

Austrheim, H., 1987. Eclogitization of lower crustal granulites by fluid migration through shear zones. *Earth and Planetary Science Letters*, **81**, 221-232.

Austrheim, H., 2013. Fluid and deformation induced metamorphic processes around Moho beneath continent collision zones: Examples from the exposed root zone of the Caledonian mountain belt, W-Norway. *Tectonophysics*, **609**, 620-635.

Austrheim, H., Erambert, M. & Engvik, A. K., 1997. Processing of crust in the root of the Caledonian continental collision zone: the role of eclogitization. *Tectonophysics*, **273**, 129-153.

Austrheim, H. & Griffin, W. L., 1985. Shear deformation and eclogite formation within granulite-facies anorthosites of the Bergen Arcs, western Norway. *Chemical Geology*, **50**, 267-281.

Bhowany, K., Hand, M., Clark, C., Kelsey, D., Reddy, S., Pearce, M., Tucker, N. & Morrissey, L., 2018. Phase equilibria modelling constraints on P–T conditions during fluid catalysed conversion of granulite to eclogite in the Bergen Arcs, Norway. *Journal of Metamorphic Geology*, **36**, 315-342.

Bingen, B., Austrheim, H., Whitehouse, M. J. & Davis, W. J., 2004. Trace element signature and U–Pb geochronology of eclogite-facies zircon, Bergen Arcs, Caledonides of W Norway. *Contributions to mineralogy and petrology*, **147**, 671-683.

Boundy, T. M., Essene, E. J., Hall, C. M.,

Austrheim, H. & Halliday, A. N., 1996. Rapid exhumation of lower crust during continent-continent collision and late extension: Evidence from 40Ar/39Ar incremental heating of hornblendes and muscovites, Caledonian orogen, western Norway. *Geological Society of America Bulletin*, **108**, 1425-1437.

Boundy, T. M., Mezger, K. & Essene, E. J., 1997. Temporal and tectonic evolution of the granulite-eclogite association from the Bergen Arcs, western Norway. *Lithos*, **39**, 159-178.

Caddick, M. J., Konopásek, J. & Thompson, A. B., 2010. Preservation of Garnet Growth Zoning and the Duration of Prograde Metamorphism. *Journal of Petrology*, **51**, 2327-2347.

Caddick, M. J. & Thompson, A. B., 2008. Quantifying the tectono-metamorphic evolution of pelitic rocks from a wide range of tectonic settings: mineral compositions in equilibrium. *Contributions to Mineralogy and Petrology*, **156**, 177-195.

Carlson, W. D., 2006. Rates of Fe, Mg, Mn, and Ca diffusion in garnet. *American Mineralogist*, **91**, 1-11.

Chakraborty, S. & Ganguly, J., 1991. Compositional zoning and cation diffusion in garnets. In: *Diffusion, Atomic Ordering, and Mass Transport*, pp. 120-175, Springer.

Chu, X. & Ague, J. J., 2015. Analysis of experimental data on divalent cation diffusion kinetics in aluminosilicate garnets with application to timescales of peak Barrovian metamorphism, Scotland. *Contributions to Mineralogy and Petrology*, **170**, 25.

Chu, X., Ague, J. J., Podladchikov, Y. Y. & Tian, M., 2017. Ultrafast eclogite formation via melting-induced overpressure. *Earth and Planetary Science Letters*, **479**, 1-17.

Coggon, R. & Holland, T. J. B., 2002. Mixing properties of phengitic micas and revised garnet-phengite thermobarometers. *Journal of metamorphic geology*, **20**, 683-696.

Diener, J. F. A. & Powell, R., 2012. Revised activity–composition models for clinopyroxene and amphibole. *Journal of metamorphic geology*, **30**, 131-142.

Diener, J. F. A., Powell, R., White, R. W. & Holland, T. J. B., 2007. A new thermodynamic model for clino-and orthoamphiboles in the system Na2O–CaO–FeO–MgO–Al2O3–SiO2–H2O–O. *Journal of metamorphic geology*, **25**, 631-656.

Ernst, W., Maruyama, S. & Wallis, S., 1997. Buoyancy-driven, rapid exhumation of ultrahigh-pressure metamorphosed continental crust. *Proceedings of the National Academy of Sciences*, **94**, 9532-9537.

Ganguly, J., Cheng, W. & Chakraborty, S., 1998. Cation diffusion in aluminosilicate garnets: experimental determination in pyrope-almandine diffusion couples. *Contributions to Mineralogy and Petrology*, **131**, 171-180.

Gerya, T., 2015. Tectonic overpressure and underpressure in lithospheric tectonics and metamorphism. *Journal of Metamorphic Geology*, **33**, 785-800.

Glodny, J., Austrheim, H., Molina, J. F., Rusin, A. I. & Seward, D., 2003. Rb/Sr record of fluid-rock interaction in eclogites: The Marun-Keu complex, Polar Urals, Russia. *Geochimica et Cosmochimica Acta*, **67**, 4353-4371.

Glodny, J., Kühn, A. & Austrheim, H., 2008. Geochronology of fluid-induced eclogite and amphibolite facies metamorphic reactions in a subduction–collision system, Bergen Arcs, Norway. *Contributions to mineralogy and petrology*, **156**, 27-48.

Glodny, J., Lohrmann, J., Echtler, H., Gräfe, K., Seifert, W., Collao, S. & Figueroa, O., 2005. Internal dynamics of a paleoaccretionary wedge: insights from combined isotope tectonochronology and sandbox modelling of the South-Central Chilean forearc. *Earth and Planetary Science Letters*, **231**, 23-39.

Holland, T. J. B. & Powell, R., 1998. An internally consistent thermodynamic data set for phases of petrological interest. *Journal of metamorphic Geology*, **16**, 309-343.

Holland, T. J. B. & Powell, R., 2003. Activity–composition relations for phases in petrological calculations: an asymmetric multicomponent formulation. *Contributions to mineralogy and petrology*, **145**, 492-501.

Jamtveit, B., Bucher-Nurminen, K. & Austrheim, H., 1990. Fluid controlled eclogitization of granulites in deep crustal shear zones, Bergen arcs, Western Norway. *Contributions to mineralogy and petrology*, **104**, 184-193.

Jamtveit, B., Moulas, E., Andersen, T. B., Austrheim, H., Corfu, F., Petley-Ragan, A. & Schmalholz, S. M., 2018. High Pressure Metamorphism Caused by Fluid Induced Weakening of Deep Continental Crust. *Scientific reports*, **8**, 17011.

Jolivet, L., Raimbourg, H., Labrousse, L., Avigad, D., Leroy, Y., Austrheim, H. & Andersen, T. B., 2005. Softening trigerred by eclogitization, the first step toward exhumation during continental subduction. *Earth and Planetary Science Letters*, **237**, 532-547.

Kolderup, C. F., 1934. The geology of the Bergen Arcs. *Proceedings of the Geologists' Association*, **45**, 373-IN17.

Krogh, E. J., 1977. Evidence of Precambrian

continent-continent collision in Western Norway. *Nature*, **267**, 17-19.

Kühn, A., 2002. The influence of fluid on the granulite to eclogite and amphibolite facies transition: a study in the anorthositic rocks from the Lindås Nappe, Bergen Arcs, West Norway. *Unpub. PhD Thesis, University of Oslo*.

Lasaga, A. C., 1979. Multicomponent exchange and diffusion in silicates. *Geochimica et Cosmochimica Acta*, **43**, 455-469.

Li, Z. H., Gerya, T. V. & Burg, J.-P., 2010. Influence of tectonic overpressure on P–T paths of HP–UHP rocks in continental collision zones: thermomechanical modelling. *Journal of Metamorphic Geology*, **28**, 227-247.

Mattey, D., Jackson, D. H., Harris, N. B. W. & Kelley, S., 1994. Isotopic constraints on fluid infiltration from an eclogite facies shear zone, Holsenøy, Norway. *Journal of metamorphic geology*, **12**, 311-325.

Moulas, E., Podladchikov, Y. Y., Aranovich, L. Y. & Kostopoulos, D., 2013. The problem of depth in geology: When pressure does not translate into depth. *Petrology*, **21**, 527-538.

Raimbourg, H., Goffé, B. & Jolivet, L., 2007. Garnet reequilibration and growth in the eclogite facies and geodynamical evolution near peak metamorphic conditions. *Contributions to Mineralogy and Petrology*, **153**, 1-28.

Rubatto, D. & Hermann, J. r., 2001. Exhumation as fast as subduction? *Geology*, **29**, 3-6.

Schmalholz, S. M. & Podladchikov, Y. Y., 2013. Tectonic overpressure in weak crustal-scale shear zones and implications for the exhumation of high-pressure rocks. *Geophysical Research Letters*, **40**, 1984-1988.

Vielzeuf, D., Baronnet, A., Perchuk, A., Laporte, D. & Baker, M., 2007. Calcium diffusivity in alumino-silicate garnets: an experimental and ATEM study. *Contributions to Mineralogy and Petrology*, **154**, 153-170.

White, R. W., Powell, R. & Holland, T. J. B., 2007. Progress relating to calculation of partial melting equilibria for metapelites. *Journal of metamorphic geology*, **25**, 511-527.

White, R. W., Powell, R., Holland, T. J. B. & Worley, B. A., 2000. The effect of TiO_2 and Fe_2O_3 on metapelitic assemblages at greenschist and amphibolite facies conditions: mineral equilibria calculations in the system K_2O-FeO-MgO-Al_2O_3-SiO_2-H_2O-TiO_2-Fe_2O_3. *Journal of metamorphic geology*, **18**, 497-512.

Yamato, P. & Brun, J. P., 2016. Metamorphic record of catastrophic pressure drops in subduction zones. *Nature Geoscience*, **10**, 46.

CHAPTER 6

Final comments and Conclusions

FINAL REMARKS AND THESIS CONCLUSIONS

The eclogite domains on Holsnøy Island have been the subject of many significant studies in different fields of geology, such as seismicity in the lower crust (Austrheim & Boundy, 1994; Putnis *et al.*, 2017; Jamtveit *et al.*, 2018a; Petley-Ragan *et al.*, 2018), fluid-rock interaction in the lower crust, the role of fluid-infiltration and deformation (Austrheim & Griffin, 1985; Erambert & Austrheim, 1993; Jolivet *et al.*, 2005; Austrheim, 2013) and processes in HP terranes (Austrheim, 1987; Jamtveit *et al.*, 1990; Austrheim, 2013; Jamtveit *et al.*, 2018b) . This thesis uses a combination of both conventional and innovative methods to understand the evolution of the fluid-rock interaction that occurred on Holsnøy Island. The chapters presented include multiple new datasets for the area, as well as adding to the existing datasets in the literature.

Firstly, a detailed structural relationship analysis was carried out to understand the evolution of the fluid-rock system with increasing fluid availability. Combining Chapters 2 and 5, five significant stages of deformation were identified, based on cross cutting relationships. Phase equilibria modelling performed on samples four of the stages depicts the first robust *P–T* path for the enigmatic rocks on Holsnøy Island (Figure 6; Chapter 5). A near isothermal pressure change is recorded by the different domains, with initial infiltration along fractures and pseudotachylytes at *P–T* conditions 15.2–15.7 kbar and 675–680 °C, peak eclogite conditions at 21–22 kbar and 670–690 °C, and retrogression through 16–17 kbar and 680 –700 kbar to amphibolite-facies conditions 11.8–12.8 kbar and 720–732 °C.

Secondly, the chemical characterisation of the fluid signatures was performed by a systematic sampling approach, whereby any altered domain collected has a corresponding granulite protolith, which acts as the baseline for pre-infiltration signatures (Chapter 3 and 4). Collection of samples was done within the *P–T* framework from Chapter 2, to keep the constraints within a tectonic context. Whole-rock $\delta^{18}O$ isotopic values for the stage 3 peak eclogite show no shifts from granulite protolith (+ 6.5 ‰) to altered domains (+ 6.5 ‰). However, *in-situ* $\delta^{18}O$ in garnet grains in eclogite samples show a slight negative shift from core to rim (5.65–6.03 ‰ for the core values and 5.08–5.63 ‰ for rim values). Stage 4 of deformation shows a positive shift in whole rock $\delta^{18}O$ from granulite protoliths to R-eclogite samples, with average values of + 7.2‰ for the R-eclogites. The δD values show a general positive shift from granulite protoliths to altered domains, with an average values of – 68.0 ‰ for the granulites, – 52.1 ‰ for the eclogites and – 35.9 ‰ for the R-eclogite samples. Calculated $\delta^{18}O$ and δD values for the fluids, based on measured values on mineral separates (omphacite, garnet and phengite) are consistent with that of metamorphic fluids, suggesting the dehydration of hydrous units as a possible source of fluid. Trace element chemistry (i.e. comparatively higher Cu and MnO and lower Ni and Co contents) suggest a sediment-derived fluid. Comparatively higher Cr and Y contents, as well as whole-rock REE patterns and εNd(t) signatures at stage 4 of deformation, suggest MORB-like signatures (i.e. mafic sediment input). Combined, the findings of Chapters 3 and 4 suggest the dehydration of a sedimentary-unit with mafic components as a likely source of the fluids. These two chapters include the first δD constraints for the eclogites on Holsnøy Island and REE garnet maps for the domains on Holsnøy Island. Moreover, combining the datasets from both chapters provide the first detailed and

robust isotopic constraints on this system, allowing for the characterisation of the fluids that infiltrated the granulite domains on Holsnøy Island, within a specific *P–T* framework.

Thirdly, the estimation of exhumation rates for Hoslnøy system from eclogite-facies to amphibolite-facies were calculated using a combination of phase equilibria modelling, to constrain the pressure drop and forward diffusion modelling in zoned garnet, to constrain exhumation durations. Tectonically infeasible minimum rates of exhumation, ranging from 41 to 6122 mm/yr were calculated based on different diffusion coefficients by Chakraborty and Ganguly (1991), Carlson (2006), Vielzeuf *et al.* (2007) and Chu and Ague (2015) . These extreme rates can, however, be explained by the overpressure hypothesis in a sheared crust as illustrated by models published by Li *et al.* (2010) and Gerya (2015); i.e. the hypothesis that a comparatively weaker crust can experience significantly larger deviatoric stress in the same location. This likely makes the Holsnøy eclogite the first documented petrological expression of tectonic overpressure.

Lastly, this thesis highlights the need to reassess the general scientific consensus that pressure equates to depth in the Earth's crust. The tectonic infeasibility of the extreme exhumation rates recorded by the domains on Holsnøy Island attests for the potential misuse of pressure as a proxy for depth in the Earth's crust, therefore, the misinterpretation of *P–T* paths for certain areas. Such misinterpretations can have significant impacts on the reconstruction of tectonic models for these areas. As a whole, this study provides a sound basis for future work done on HP/UHP terranes, and encourages future researchers to reconsider their interpretation of pressure and *P–T* paths, when constructing tectonic models.

An interesting avenue to pursue for future studies is to consider other forces acting on rocks, other than lithostatic pressure, as the major driving force for metamorphic processes. Locations analogous to the Hoslnøy system (i.e. highly sheared domains with mineral assemblages recording higher *P–T* conditions than the wall rock), such as the HP of the Alpine Orogen (Schmalholz & Podladchikov, 2013; Gerya, 2015) or the Isdal Shear Zones (Putnis *et al.*, 2017), where the conventional tectonic models do not fit field and measured observations should be targeted to further investigate the overpressure hypothesis as valid a mechanism for the emplacement of HP and UHP terranes.

REFERENCES

Austrheim, H., 1987. Eclogitization of lower crustal granulites by fluid migration through shear zones. *Earth and Planetary Science Letters*, **81**, 221-232.

Austrheim, H., 2013. Fluid and deformation induced metamorphic processes around Moho beneath continent collision zones: Examples from the exposed root zone of the Caledonian mountain belt, W-Norway. *Tectonophysics*, **609**, 620-635.

Austrheim, H. & Boundy, T. M., 1994. Pseudotachylytes generated during seismic faulting and eclogitization of the deep crust. *Science*, **265**, 82-83.

Austrheim, H. & Griffin, W. L., 1985. Shear deformation and eclogite formation within granulite-facies anorthosites of the Bergen Arcs, western Norway. *Chemical Geology*, **50**, 267-281.

Carlson, W. D., 2006. Rates of Fe, Mg, Mn, and Ca diffusion in garnet. *American Mineralogist*, **91**, 1-11.

Chakraborty, S. & Ganguly, J., 1991. Compositional zoning and cation diffusion in garnets. In: *Diffusion, Atomic Ordering, and Mass Transport*, pp. 120-175, Springer.

Chu, X. & Ague, J. J., 2015. Analysis of experimental data on divalent cation diffusion kinetics in aluminosilicate garnets with application to timescales of peak Barrovian metamorphism, Scotland. *Contributions to Mineralogy and Petrology*, **170**, 25.

Erambert, M. & Austrheim, H., 1993. The effect of fluid and deformation on zoning and inclusion patterns in poly-metamorphic garnets. *Contributions to mineralogy and petrology*, **115**, 204-214.

Gerya, T., 2015. Tectonic overpressure and underpressure in lithospheric tectonics and metamorphism. *Journal of Metamorphic Geology*, **33**, 785-800.

Jamtveit, B., Ben-Zion, Y., Renard, F. & Austrheim, H., 2018a. Earthquake-induced transformation of the lower crust. *Nature*, **556**, 487-491.

Jamtveit, B., Bucher-Nurminen, K. & Austrheim, H., 1990. Fluid controlled eclogitization of granulites in deep crustal shear zones, Bergen arcs, Western Norway. *Contributions to mineralogy and petrology*, **104**, 184-193.

Jamtveit, B., Moulas, E., Andersen, T. B., Austrheim, H., Corfu, F., Petley-Ragan, A. & Schmalholz, S. M., 2018b. High Pressure Metamorphism Caused by Fluid Induced Weakening of Deep Continental Crust. *Scientific reports*, **8**, 17011.

Jolivet, L., Raimbourg, H., Labrousse, L., Avigad, D., Leroy, Y., Austrheim, H. & Andersen, T. B., 2005. Softening trigerred by eclogitization, the first step toward exhumation during continental subduction. *Earth and Planetary Science Letters*, **237**, 532-547.

Li, Z. H., Gerya, T. V. & Burg, J.-P., 2010. Influence of tectonic overpressure on P–T paths of HP–UHP rocks in continental collision zones: thermomechanical modelling. *Journal of Metamorphic Geology*, **28**, 227-247.

Petley-Ragan, A., Dunkel, K. G., Austrheim, H., Ildefonse, B. & Jamtveit, B., 2018. Microstructural records of earthquakes in the lower crust and associated fluid-driven metamorphism in plagioclase-rich granulites. *Journal of Geophysical Research: Solid Earth*.

Putnis, A., Jamtveit, B. & Austrheim, H., 2017. Metamorphic Processes and Seismicity: the Bergen Arcs as a Natural Laboratory. *Journal of Petrology*, **58**, 1871-1898.

Schmalholz, S. M. & Podladchikov, Y. Y., 2013. Tectonic overpressure in weak crustal-scale shear zones and implications for the exhumation of high-pressure rocks. *Geophysical Research Letters*, **40**, 1984-1988.

Vielzeuf, D., Baronnet, A., Perchuk, A., Laporte, D. & Baker, M., 2007. Calcium diffusivity in alumino-silicate garnets: an experimental and ATEM study. *Contributions to Mineralogy and Petrology*, **154**, 153-170.

Appendix 1

Supplementary material for Chapter 2:
Phase equilibria constraints on *P*–*T* conditions during fluid catalysed conversion of granulite to eclogite in the Bergen Arcs, Norway.
Chapter 2

Table S1.1 Sample and map locations.

Samples/maps	Lithology description	Location (UTM 32V)
HOL2A_2015 (stage 1)	Recrystallised pseudotachylite in the granulite facies rocks that get overprinted by mylonite	0283435 E 6724274 N
HOL4B_2014 (stage 2)	Partially hydrated sheared domain. Rock type still contains plagioclase which suggests it wasn't formed at eclogite facies.	0283368 E 6724132 N
HOL7C_2014 (stage 3)	Peak eclogite denoted by the complete disappearance of plagioclase in matrix. Rock sample sits right outside the margin of a granulite 'breccia'	0281226 E 6723701 N
HOL13A_2015 (stage 4)	Phengite-rich domains within peak eclogite. Domain is about 1m around the margins of a granulite 'breccia'.	0282213 E 6723307 N
Fig. 3a (stage 1)	Pseudotachylite overprinted by partially hydrated shear zone (2x2 m)	0283335 E 6724250 N
Fig. 3b (stage 2)	Discrete shear zones and fractures with partially hydrated domains running along their margins (50x15m)	0283370 E 6724131 N
Fig. 3c (stage 3)	Granulite 'breccia' sitting in highly sheared eclogite matrix (18 x 15m)	0281191 E 6723619 N

Table S1.2. Bulk-rock compositions of wall-rocks and samples in wt%.

Major Oxides	Granulite wall-rock to HOL2A_2015 (wt %)	HOL2A_2015 (wt %)	Granulite wall-rock to HOL7C_2014 (wt %)	HOL7C_2014 (wt %)	Granulite wall-rock to HOL13A_2015 (wt %)	HOL13A_2015 (wt %)
SiO2	50.40	50.81	51.22	46.51	49.03	48.33
TiO2	0.17	0.08	0.49	0.61	0.18	0.64
Al2O3	25.69	24.72	18.35	18.65	23.88	20.69
MnO	0.06	0.09	0.19	0.20	0.10	0.21
MgO	4.40	4.72	5.69	6.60	7.14	7.10
CaO	10.54	10.02	8.88	10.93	8.81	7.70
Na2O	4.05	4.06	3.55	3.34	3.19	3.02
K2O	0.45	0.57	0.72	0.79	0.65	2.49
P2O5	0.03	0.07	0.03	0.03	0.04	0.04
LOI	0.68	0.91	1.14	1.36	0.74	2.44
FeO	2.83	2.80	6.97	7.23	3.41	6.22
Fe2O3	-3.15	-3.11	-7.75	-8.04	3.24	2.63

Appendix S1.1

Determination of mineral abundances by pixel counting using Photoshop

- Open photomicrograph in Photoshop
- Go to Window menu → Histogram
- On top-right corner of the Histogram window choose 'Expanded view' and 'Show Statistics'
- Select whole map and record the pixel number given at the bottom of histogram window
- Using the 'Magic Wand' tool (tools panel), select desired grain (e.g. garnet)
- Right click the grain and select 'Similar'. This selects all grains with the same colour
- Adjust the 'Tolerance' on the top toolbar to adjust the selection of mineral grains (if tolerance is too large, other mineral grains with similar colours can be selected)
- When all the grains with same colour has been selected, record the pixel number
- Repeat for other mineral(s)
- Calculate percentage abundances based on different pixel counts

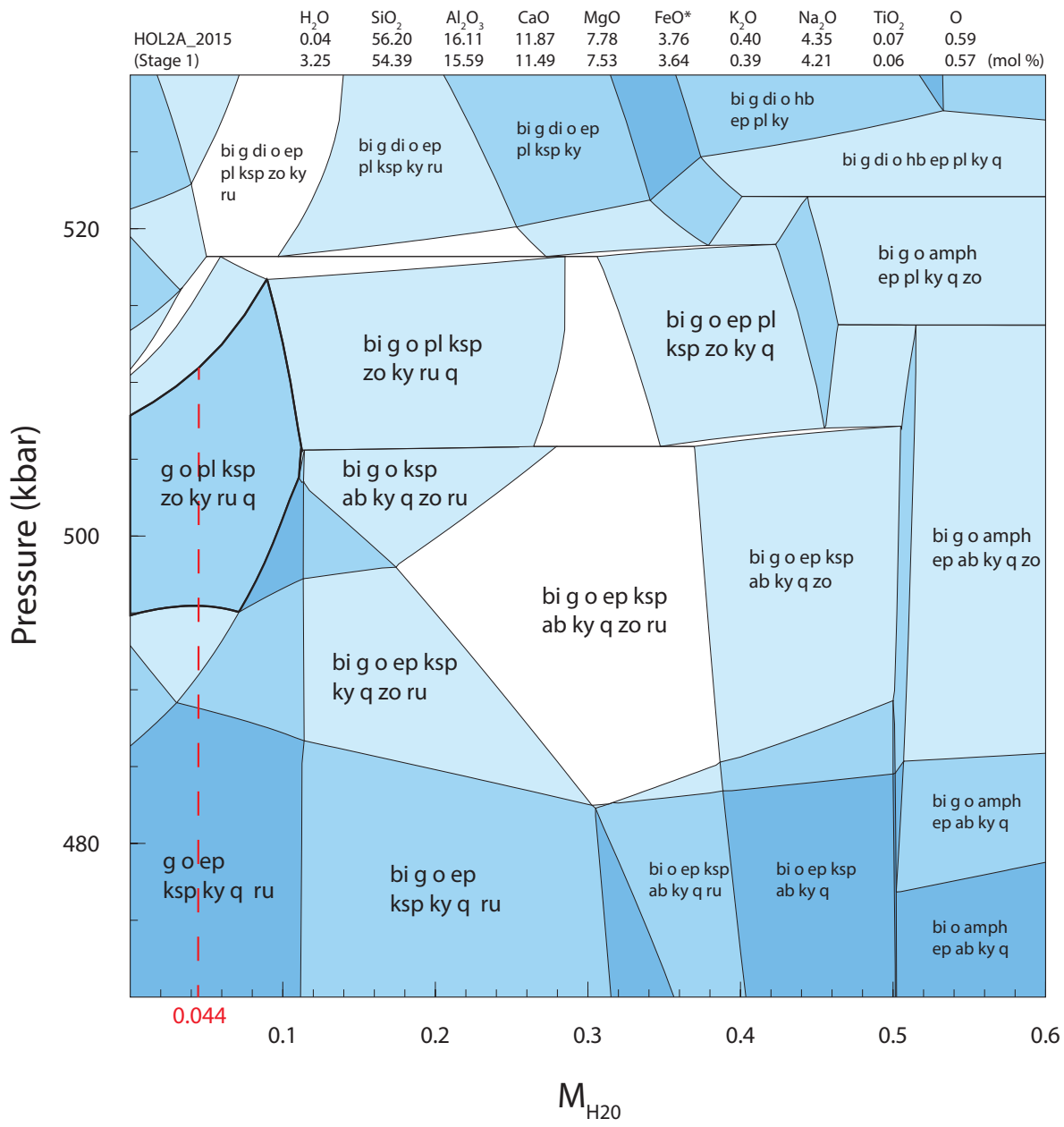

Figure S1.1. Calculated T–M_{H2O} for HOL2A_2015 (stage 1). P–T pseudosection was calculated using bulk-rock composition at 0.044 M_{H2O}.

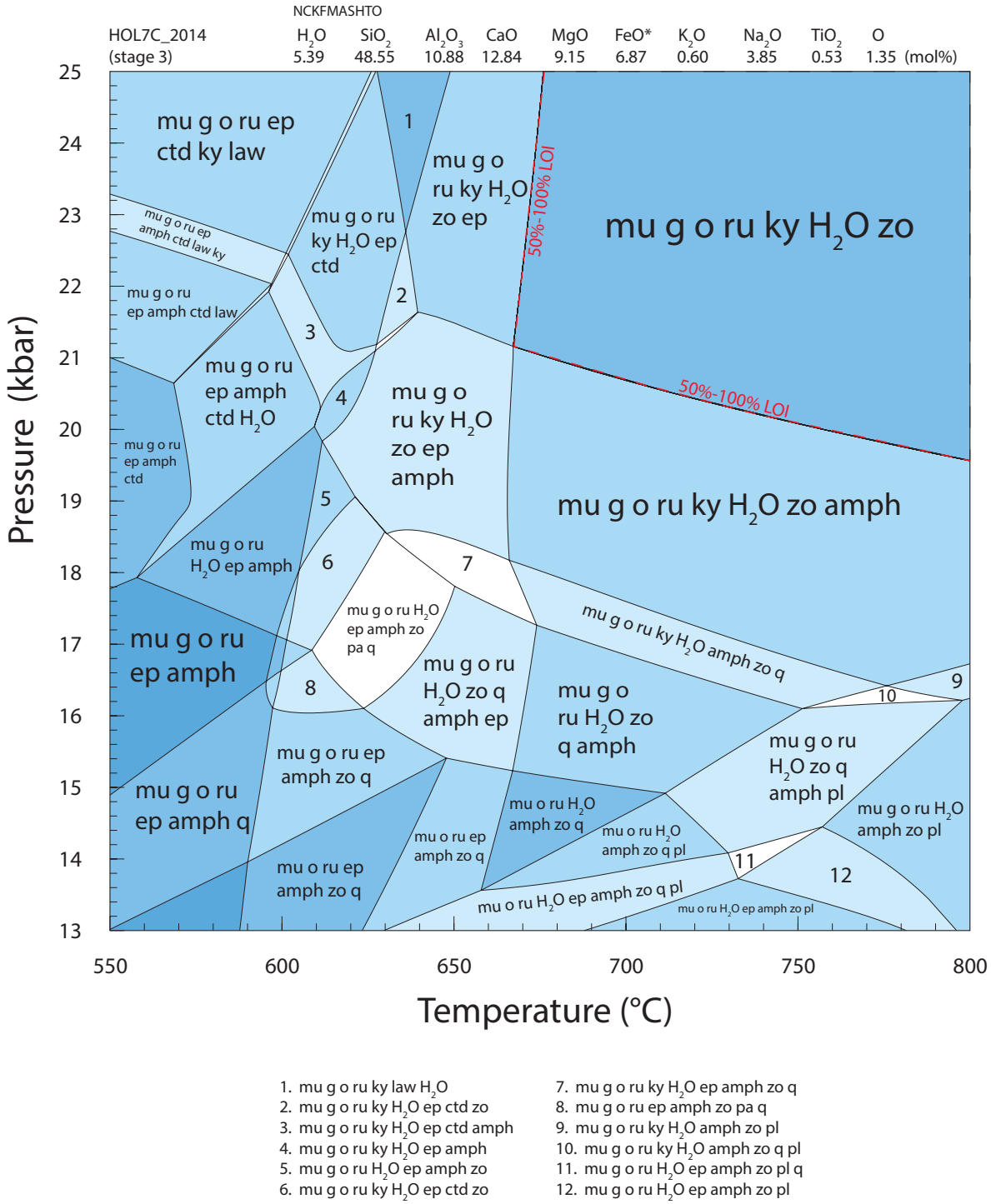

Figure S1.2. Calculated *P–T* pseudosection with peak field boundaries calculated at different percentage of LOI (red dashed line) for sample HOL7C_2014. The peak field boundaries were calculated with 50%, 60%, 70%, 80%, 90% and 100% of LOI. Decreasing water content does not affect the position of the peak field boundaries in *P–T* space.

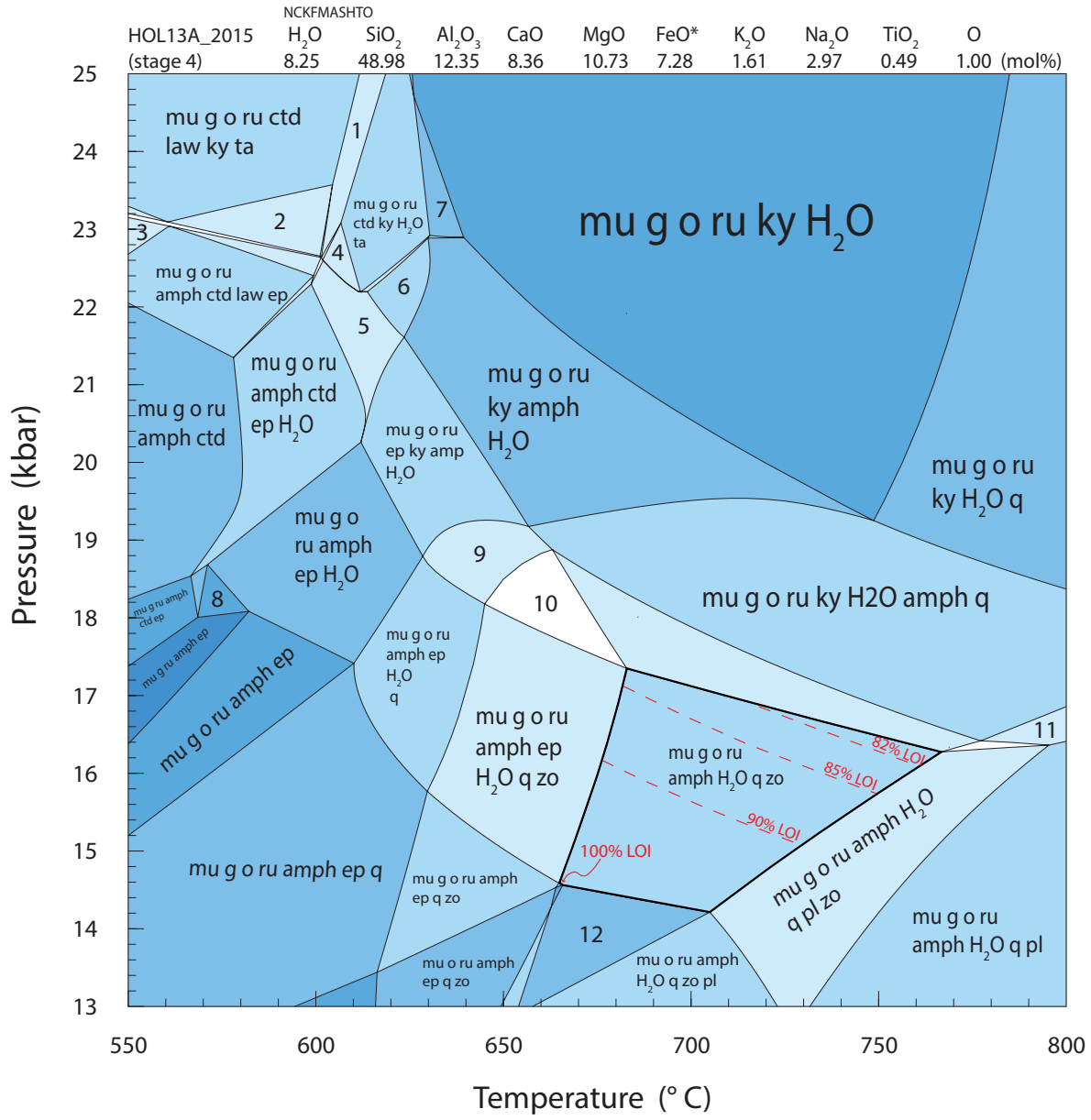

1. mu g o ru ctd law ky H_2O ta
2. mu g o ru gl ctd law ky ta
3. mu g o ru amph ctd ep ta
4. mu g o ru ctd ep ky H_2O ta
5. mu g o ru amph ctd ep ky H_2O
6. mu g o ru amph ctd ky H_2O
7. mu g o ru ky H_2O ta
8. mu g o ru amph ep H_2O
9. mu g o ru ep ky amph H_2O q
10. mu g o ru ep ky amph H_2O q zo
11. mu g o ru amph ky H_2O q pl
12. mu o ru amph H_2O q zo

Figure S1.3. Calculated *P–T* pseudosection with peak field boundaries calculated at different percentage of LOI for sample HOL13A_2015. The red-dashed line represent the H2O line which migrates up pressure and temperature as water content is decreased from 100% of LOI to 82% LOI, making the peak field smaller. At 80% LOI, the peak field boundaries can no longer be calculated.

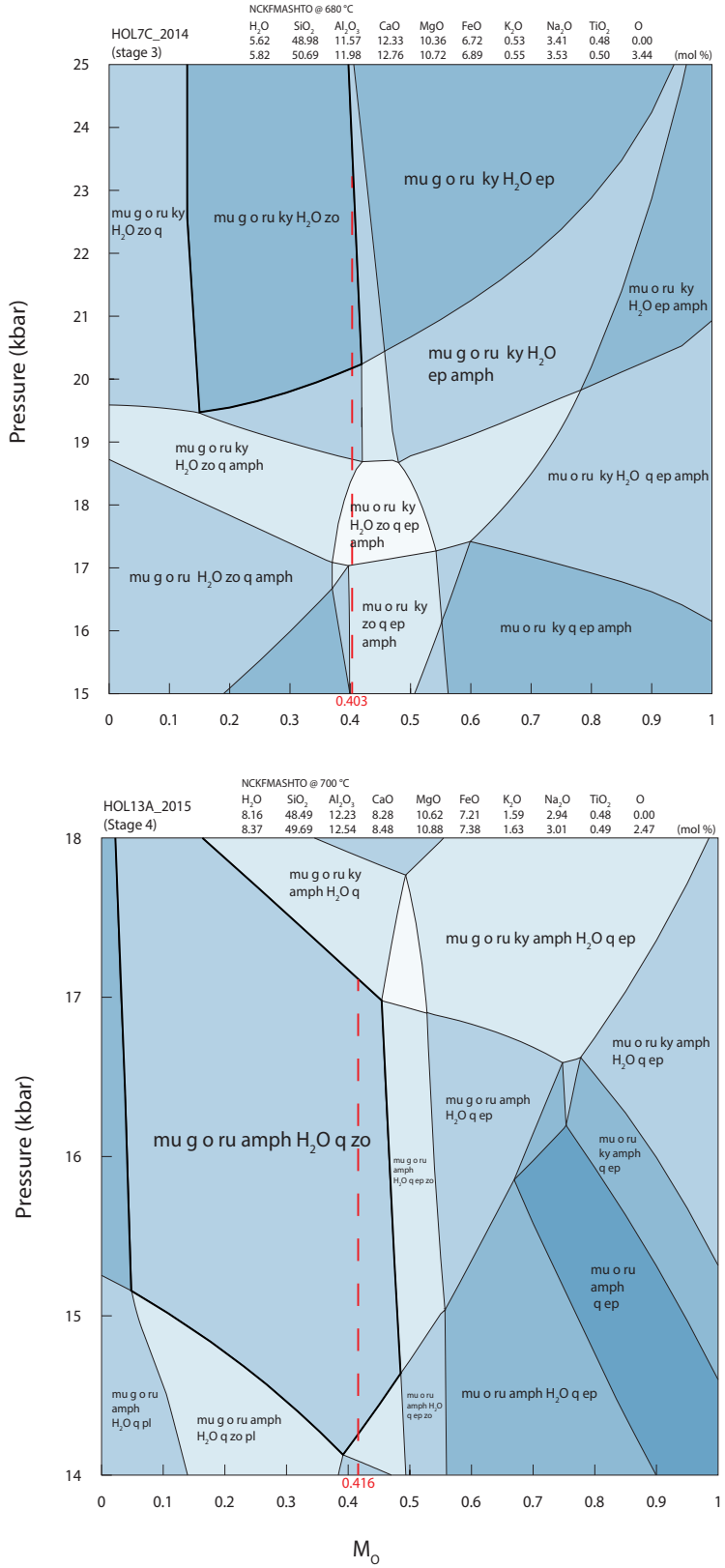

Figure S1.4. Calculated $P–M_O$ for HOL7C_2014 (at 680 °C) and HOL13A_2015 (at 700 °C). For both samples, the calculated fields spans over a large area in $P–T$ space, especially at higher pressure. Peak field for HOL7C_2014 lies in a range of ~ 0.15–0.42 and > 19.5 kbar while HOL13A_2015 extends in the range of ~0.02– 0.49 and >14.2 kbar. Measured M_O values, represented by the red dashed line, for both samples lie in the peak fields.

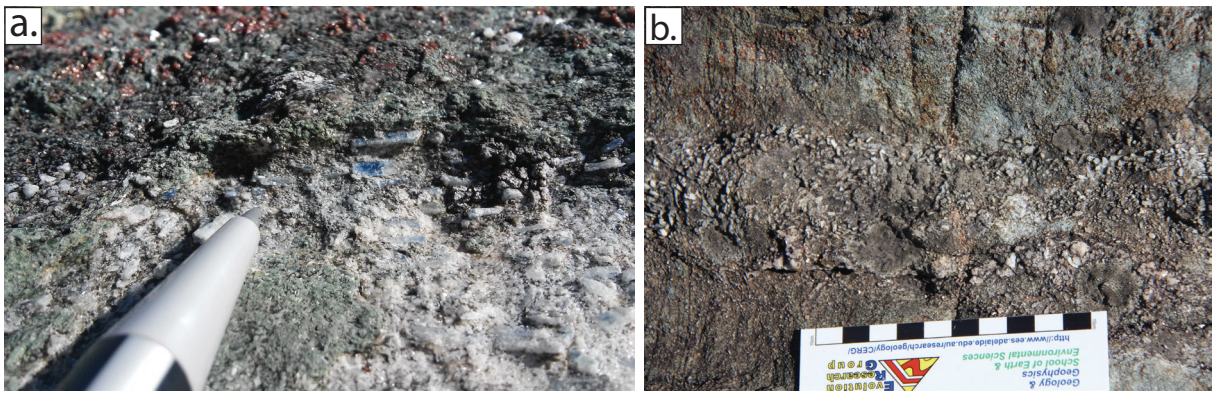

Figure S1.5. Field photograph of kyanite blades in rock type representing stage 2 of deformation.

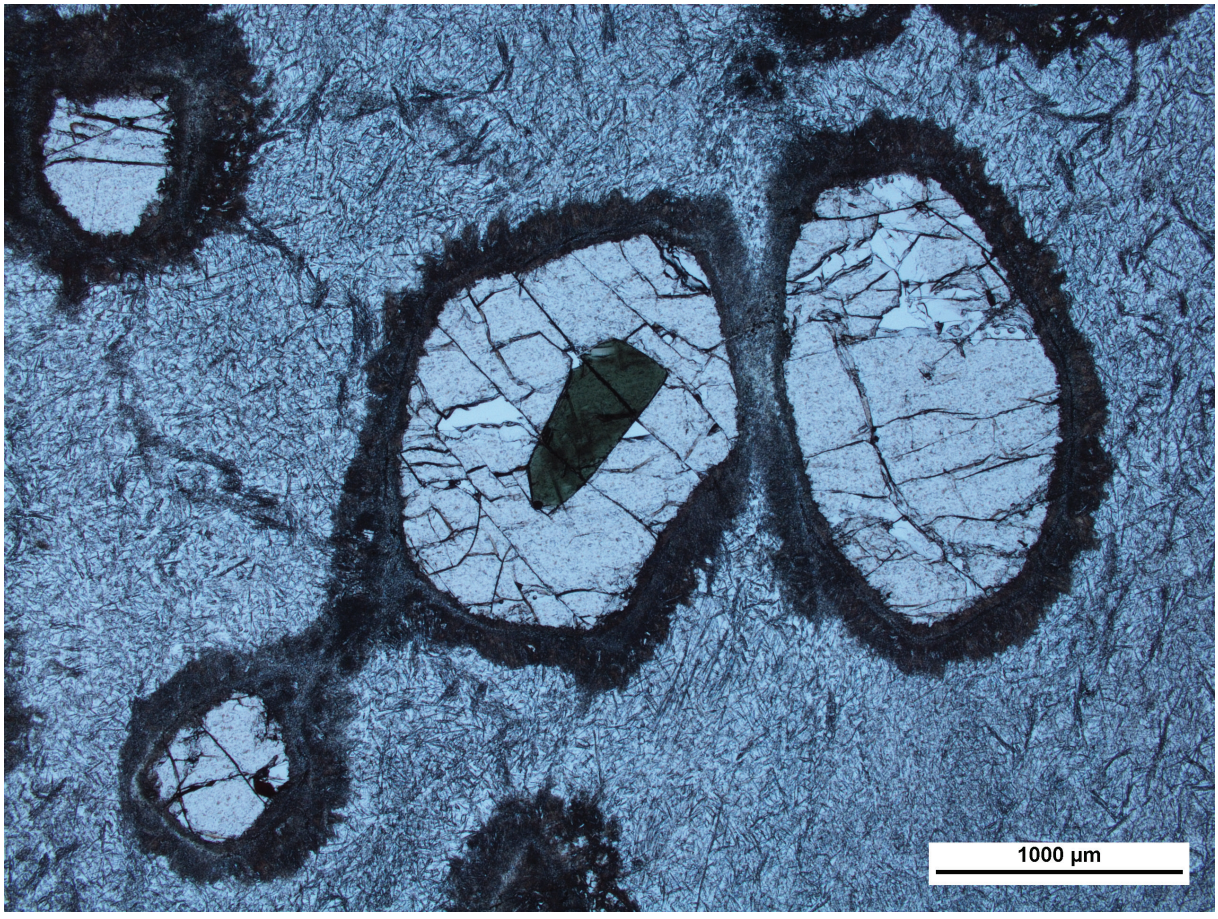

Figure S1.6. Photomicrograph of euhedral spinel inclusion in garnet in partially hydrated sample, HOL4B_2014.

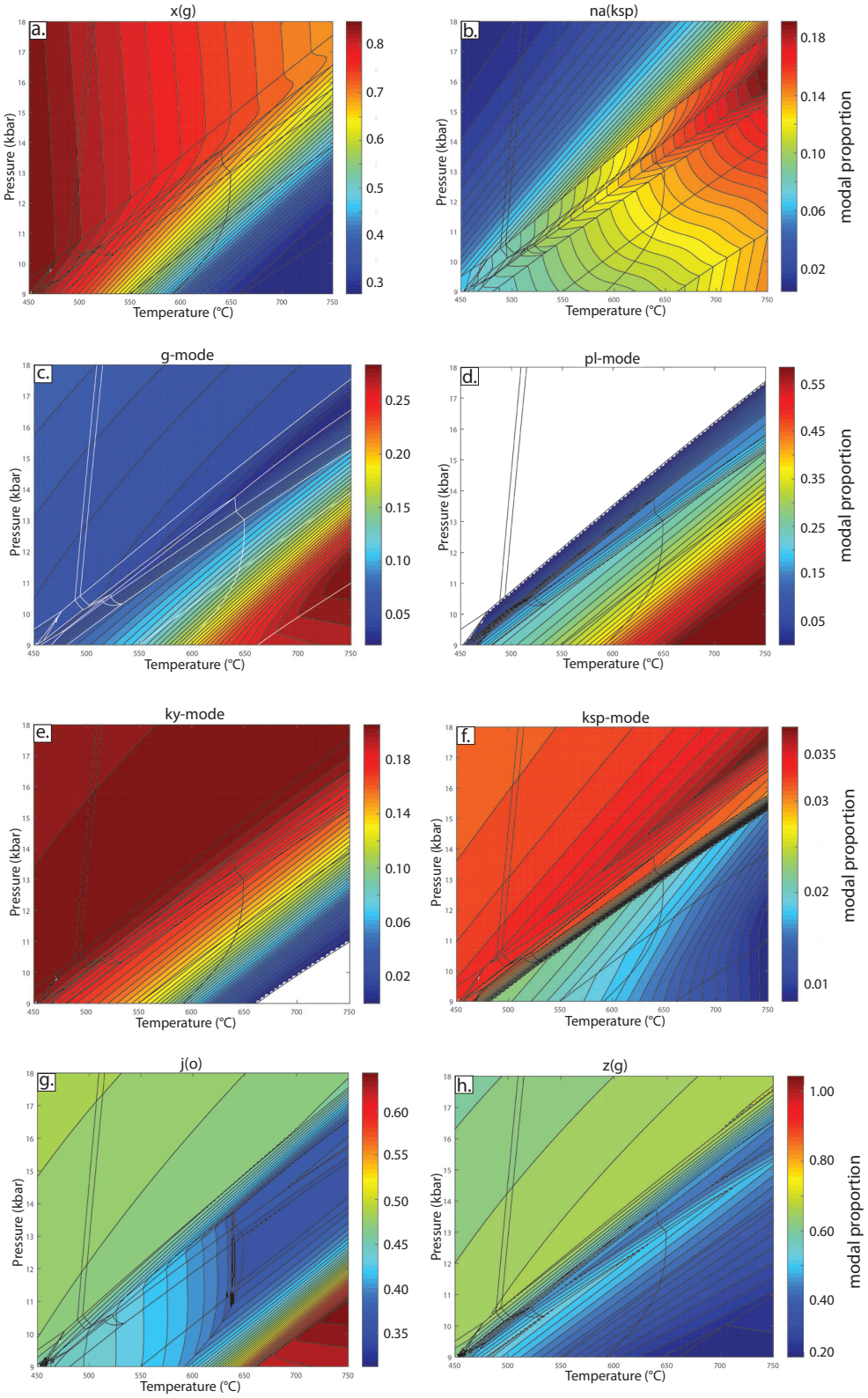

Figure S1.7. TCInvestigator output contours for (a) *x*(garnet) and (b) *na*(K-feldspar) which were used to constrain *P–T* conditions for sample HOL2A_2015. (c) garnet abundance, (d) plagioclase abundance, (e) kyanite abundance, (f) K-feldspar abundance. (g) *j*(omphacite), and (h) *z*(garnet) showing modal proportions varying parallel to the peak field boundary. Cold colours show low abundances and warmer colours represent higher abundances.

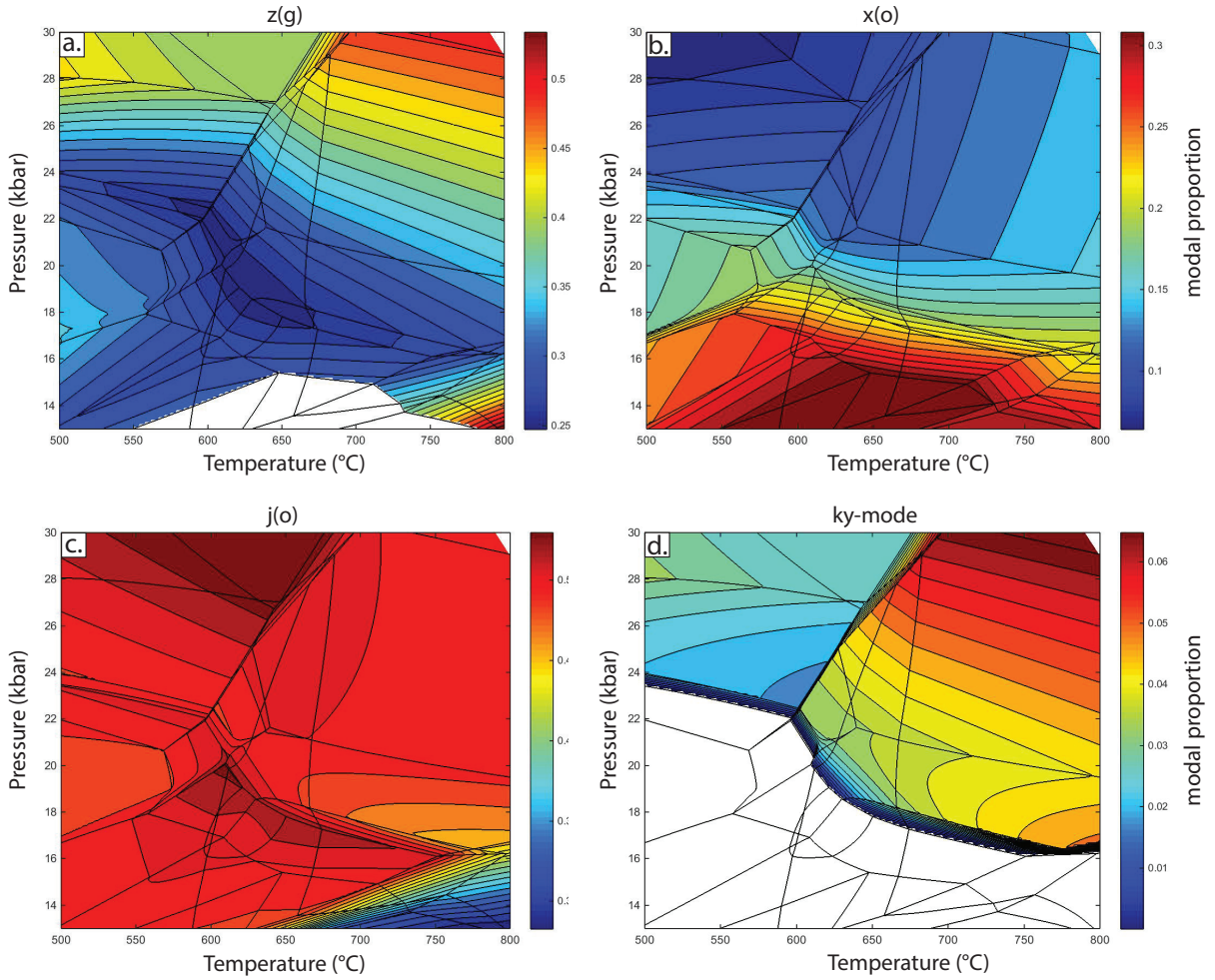

Figure S1.8. TCInvestigator output contours for (a) *z*(garnet), (b) *x*(omphacite), (c) *j*(omphacite) and (d) kyanite abundance that were used to constrain the *P–T* conditions for sample HOL7C_2014. Cold colours show low abundances and warmer colours represent higher abundances.

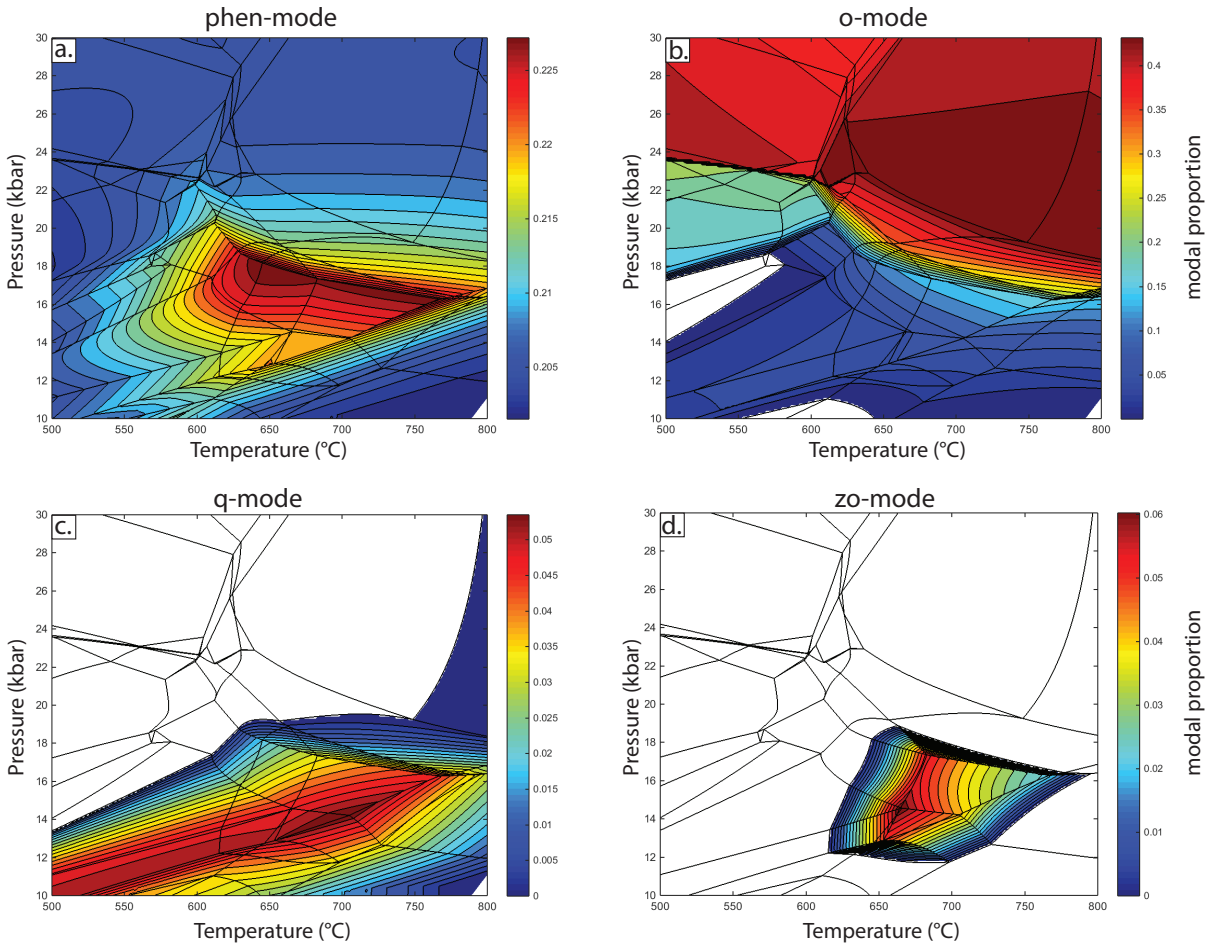

Figure S1.9. TCInvestigator output contours for (a) phengite abundance. (b) omphacite abundance, (c) quartz abundance, and (d) zoisite abundance that were used to constrain the *P–T* conditions for sample HOL13A_2015. Cold colours show low abundances and warmer colours represent higher abundances.

Appendix 2

Supplementary material for Chapter 3:
$\delta^{18}O$ and δD isotopic constraints on Holsnøy Island

Appendix S2.1

Sample preparation

The analysed garnet grains for sample HOL14-7C were cut from thin sections in small circular chips. Each chip was mounted in a 25 mm epoxy disc, with a UWG-2 standard (Valley *et al.*, 1995; Vielzeuf *et al.*, 2005a; Page *et al.*, 2010) positioned adjacent to them. Both the sample and standards were located within 5 mm of the centre. Each mount was ground using a Struers MD-1200. They were then polished using a combination of 9 μm, 3 μm and 1 μm cloths on magnetic discs. At each stage of the polishing process, the mount was visually inspected using a high-resolution reflected light microscope to monitor scratches, uneven polish and rounding of the grain edges. Once polishing was complete, the mount was imaged using reflected and transmitted light, and finally coated with 30 nm of high-purity gold.

Calculating $\delta^{18}O$ values

Yield- and background-corrected $^{18}O/^{16}O$ raw ratios (R_{raw}) were drift-corrected using a linear regression:

$$R_{drift} = R_{raw} - mx, \tag{1}$$

where m is the slope of the regression and x is the analysis number for the session, scaled to ensure that the intercept (c) crosses the x-axis at $x = 0$. The raw and drift-corrected data are presented in Table 5. The drift-corrected ratios were expressed as raw delta values (V-SMOW) using:

$$\delta^{18}O_{drift} = 1000 \left(\frac{R_{drift}}{0.0020246} - 1 \right). \tag{2}$$

The instrumental mass fractionation (α) was then calculated as the σ_{drift}^{-2} (see below) weighted average of all estimates α_i of the $\delta^{18}O_{drift}$ values for the bracketing standards using:

$$\alpha_i = \frac{1 + \left(\frac{\delta^{18}O_{drift}}{1000} \right)}{1 + \left(\frac{\delta^{18}O_{std}}{1000} \right)}, \tag{3}$$

where $\delta^{18}O_{std}$ is the $\delta^{18}O$ value of the standard material relative to V-SMOW (5.80 ‰; Valley *et al.*, 1995; Vielzeuf *et al.*, 2005a; Paget *et al.*, 2010). The $\delta^{18}O$ value of each sample spot relative to V-SMOW was obtained by adjusting for instrumental mass fractionation using:

$$\delta^{18}\mathrm{O}_{\mathrm{sample}} = 1000\left\{\frac{1+\left(\frac{\delta^{18}\mathrm{O}_{\mathrm{drift}}}{1000}\right)}{\alpha}-1\right\}. \quad (4)$$

The $\delta^{18}O_{sample}$ values were then corrected for cation composition following the method of Page *et al.* (2010). Instrumental bias relative to UWG-2 was assessed in three separate analytical sessions under similar operating conditions. A matrix-corrected $\delta^{18}O$ value, based on the molar fraction of grossular + uvarovite ($X_{gross + uvar}$), was then calculated using:

$$\delta^{18}\mathrm{O}_{\mathrm{corr}} = \delta^{18}\mathrm{O}_{\mathrm{sample}} - \left(AX^2 + BX + C\right), \quad (5)$$

where $A = -8.61 \pm 0.27$, $B = 12.98 \pm 0.27$ and $C = -1.30 \pm 0.07$.

Error propagation

The propagated error associated with drift correction was determined using the following:

$$\sigma_{R_{\mathrm{drift}}} = \sqrt{\sigma_i^2 + \sigma_{\mathrm{reg}}^2}, \quad (6)$$

where σ_i is the internal precision (standard error of the mean of the 20 cycles for a single analysis i) and σ_{reg} is the standard error of the estimate of the regression, given by:

$$\sigma_{\mathrm{reg}} = \sqrt{x^2\sigma_m^2 + \sigma_c^2 + 2x\rho\sigma_m\sigma_c}, \quad (7)$$

where σ_m and σ_c are the standard errors associated with the estimation of m and c respectively, and ρ is the correlation coefficient between analysis number and R_{raw}. The uncertainty of $\delta^{18}O_{drift}$ is given by:

$$\sigma_{\mathrm{drift}} = \sqrt{\left(\frac{1000}{0.0020052}\cdot\sigma_{R_{\mathrm{drift}}}\right)^2}. \quad (8)$$

The uncertainty of individual α_i estimates is given by:

$$\sigma_{\alpha i} = \sqrt{\left[\frac{1}{\left(1000+\delta^{18}\mathrm{O}_{\mathrm{std}}\right)}\cdot\sigma_{\mathrm{drift}}\right]^2 + \left\{-\sigma_{\mathrm{std}}\left[\frac{1+\left(\frac{\delta^{18}\mathrm{O}_{\mathrm{drift}}}{1000}\right)}{\left(1000+\delta^{18}\mathrm{O}_{\mathrm{std}}\right)^2}\right]\right\}^2}, \quad (9)$$

where σ_{std} is the uncertainty of the reference value for the UWG-2 standard (0.01 ‰). The uncertainty associated with α (σ_α) is the weighted mean standard error of the individual

estimates α_i obtained from the drift-corrected UWG-2 standards. The propagated uncertainty for the $\delta^{18}O$ value of each sample spot is given by:

$$\sigma_{\text{sample}} = \sqrt{\left(\frac{1}{\alpha}\cdot\sigma_{\text{drift}}\right)^2 + \left[\sigma_\alpha\left(\frac{-1000}{\alpha^2} - \frac{\delta^{18}\text{O}_{\text{sample}}}{\alpha^2}\right)\right]^2}. \quad (10)$$

Finally, the uncertainty associated with the cation composition correction scheme was calculated using:

$$\sigma_{\text{corrected}} = \sqrt{\sigma_{\text{sample}}^2 + \left(X^2\sigma_A\right)^2 + \left(X\sigma_B\right)^2 + \sigma_C^2 + 2\rho\left[X^3\sigma_A\sigma_B + X\sigma_B\sigma_C + X^2\sigma_A\sigma_C\right]}. \quad (11)$$

REFERENCES

Valley, J.W., Kitchen, N., Kohn, M.J., Niendorf, C.R. & Spicuzza, M.J., 1995. UWG-2, a garnet standard for oxygen isotope ratios: strategies for high precision and accuracy with laser heating. Geochimica et Cosmochimica Acta, **59**, 5223–5231.

Vielzeuf, D., Champenois, M., Valley, J.W., Brunet, F. & Devidal, J.L., 2005a. SIMS analyses of oxygen isotopes: matrix effects in Fe–Mg–Ca garnets. Chemical Geology, **223,** 208–226.

Page, F. Z., Kita, N. T. & Valley, J. W., 2010. Ion microprobe analysis of oxygen isotopes in garnets of complex chemistry. Chemical Geology, **270**, 9–19.

Appendix 3

Supplementary material for Chapter 4:
Trace element and Sm–Nd constraints

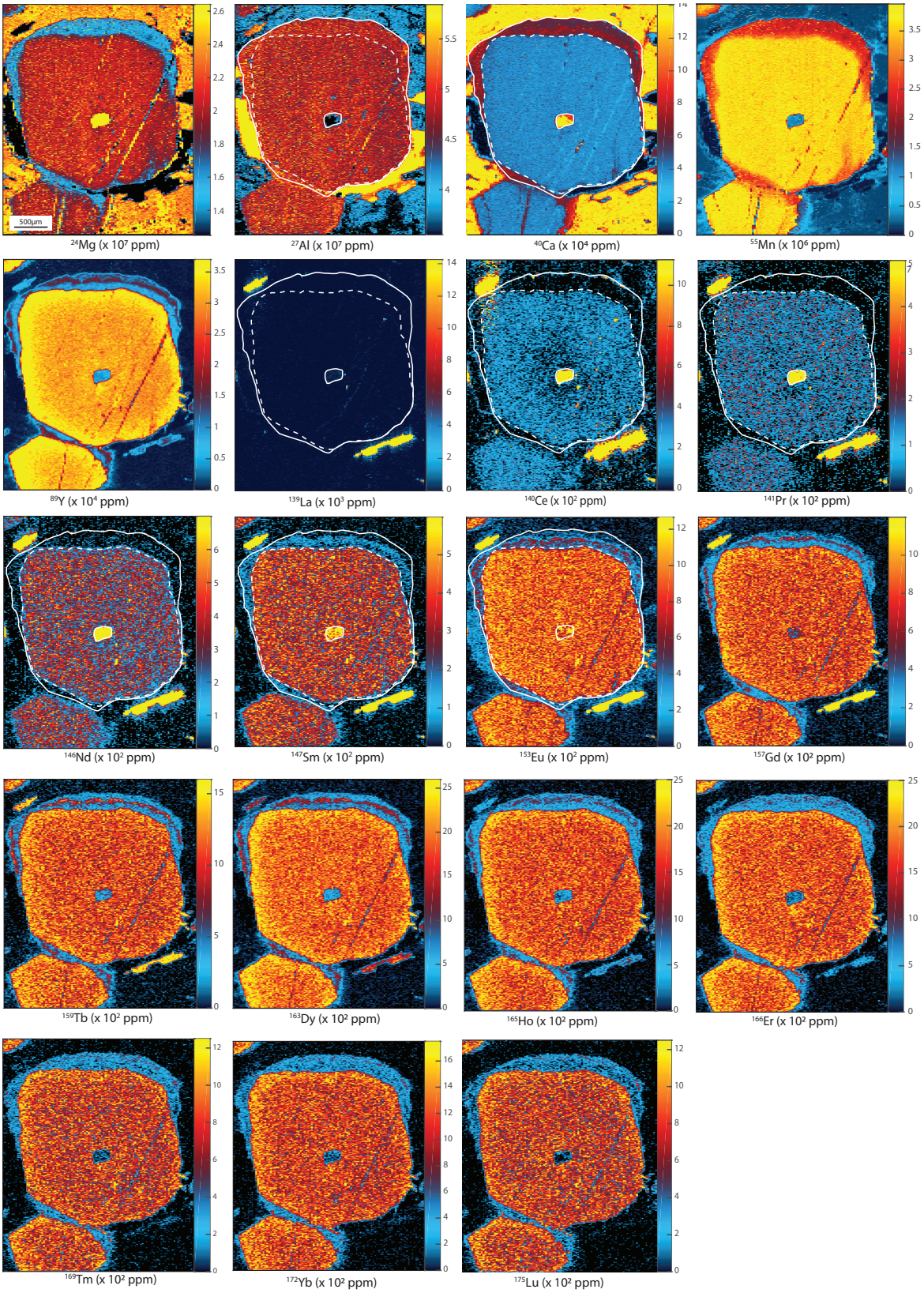

Figure S3.1. LA-ICP-MS maps qualitative maps showing elemental distribution and concentration in a zoned garnet grain in eclogite sample, HOL14–7C. Dotted line represents the core-rim boundary. Warmer colours represent higher concentrations. Maps were processed in *XMapTools*, and concentrations are presented in ppm.

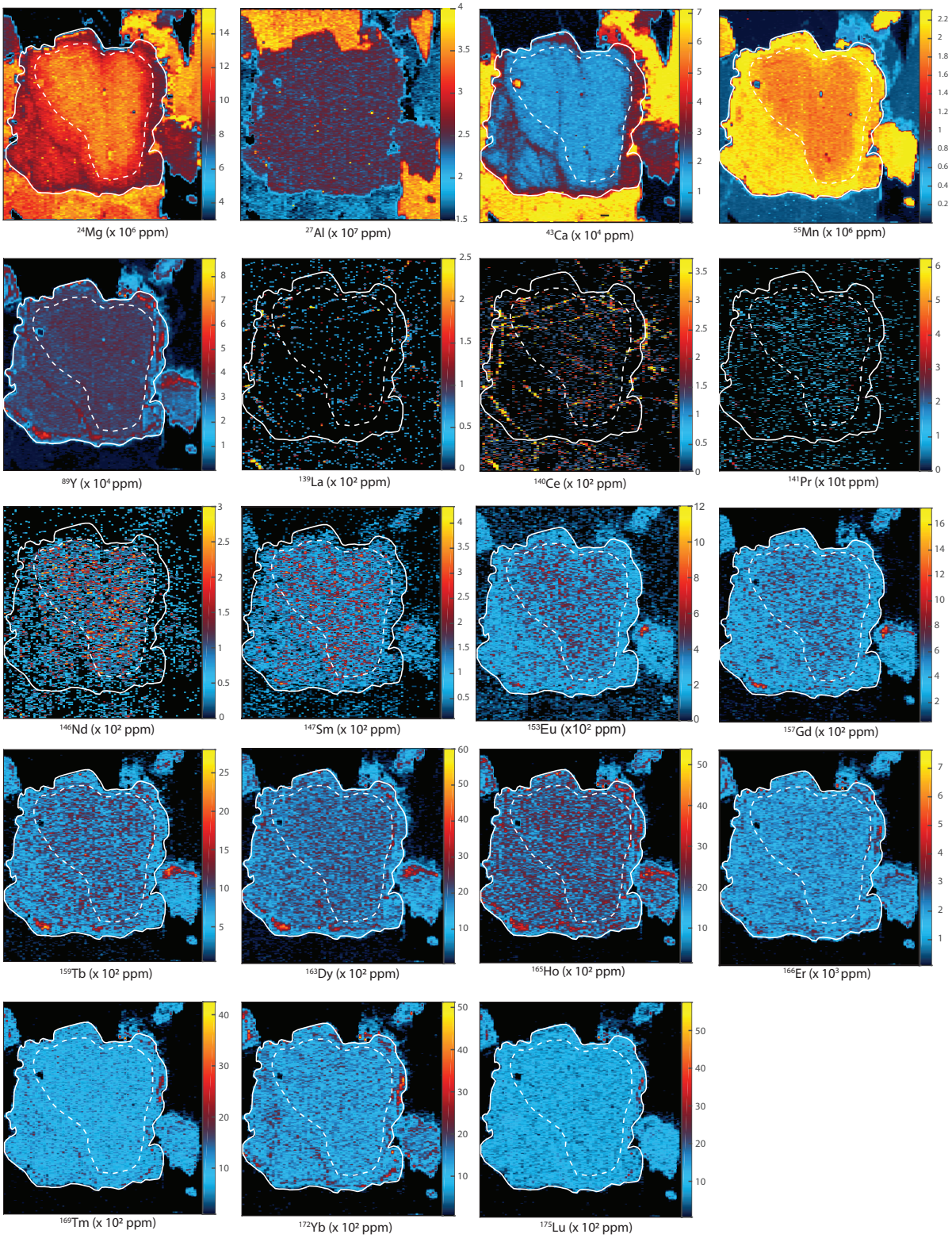

Figure S3.2. LA-ICP-MS maps qualitative maps showing elemental distribution and concentration in a zoned garnet grain in R-eclogite sample, HOL15–13E. Dotted line represent the core-rim boundary. Warmer colours represent higher concentrations. Maps were processed in *XMapTools*, and concentrations are presented in ppm.

Table 3.1. NIST612 and GSD-1D standard values for trace element analyses

	Na	Mg	Al	Si	K	Ti	V	Cr	Mn	Fe	Rb	Sr	Y	Zr	Nb	La	Ce	Pr	Nd	Sm	Eu	Gd	Tb	Dy	Ho	Er	Tm	Yb	Lu	Hf	Ta
G_NIST612_1	94860	57.69	10141	3.16E+05	53.1	39.4	39.25	35.6	38.19	58.5	29.04	77.54	39.85	38.83	37.82	36	38	37.3	35.92	37.74	37.19	38.9	37.04	35.92	38.36	39.87	37.9	40.3	37	36.3	35.3
G_NIST612_2	95590	57.41	10132	3.16E+05	52.48	40.2	39.12	35.9	38.42	58.6	29.2	77.73	39.41	38.41	37.64	36.1	38.05	37.07	35.4	37.78	36.8	38.86	36.84	35.84	38.04	39.42	37.3	39.6	37	35.8	35.24
G_NIST612_3	96480	Below l	10200	3.17E+05	Below LC	38.7	39.06	34.7	38.35	58.2	29.3	77.78	39.98	38.88	38.08	36.4	38.88	38.04	35.95	38.09	35.77	39.77	37.31	36.57	38.5	40.19	36.5	39.3	37	36.2	36.57
G_NIST612_4	96040	57.13	10205	3.14E+05	52.56	39	38.65	34.24	38.27	54.4	29.23	77.75	39.85	38.86	37.92	36.5	38.63	37.8	36.43	38.29	36	39.61	37.41	36.38	38.54	39.96	36.5	39.5	37	36	36.25
G_NIST612_5	95030	Below l	10159	3.12E+05	52.65	Below	38.58	35.3	38.29	Below LO	29.32	77.8	39.91	38.7	37.4	36.4	38.64	37.65	36.07	38.07	36.21	39.52	37	36.23	38.02	39.55	37.3	38.3	37	35.7	36.21
G_NIST612_6	95500	56.35	10163	3.14E+05	52.96	40.6	38.72	35	38.24	56.3	29.04	77.31	39.83	38.53	37.92	36.3	38.62	37.61	35.98	37.96	35.83	39.51	36.78	35.82	37.78	39.59	36.8	38.7	37	35.2	36.07
G_NIST612_7	96180	Below l	10226	3.14E+05	51.43	40.3	38.76	34.9	38.1	Below LO	29.06	77.79	39.8	38.89	37.64	36.4	38.55	37.71	36.02	38.3	37.23	39.93	37.24	36.1	38.18	39.72	37	39.6	37	36.2	36.5
G_NIST612_8	95770	56.84	10209	3.13E+05	52.43	39.5	38.58	34.5	38.46	56.4	28.95	77.33	39.69	38.62	37.6	36.3	38.44	37.49	35.96	38.15	36.84	39.69	36.9	36.11	38.24	39.69	36.8	39.2	37	35.7	36.35
G_NIST612_9	95220	56.75	10180	3.12E+05	52.62	38.2	38.29	34.9	37.87	57.2	28.7	77.25	39.83	38.57	37.32	36.1	38.13	37.25	36.38	38.13	36	39.46	36.78	35.58	37.9	39.4	37.6	39	37	35.8	35.84
G_NIST612_10	96310	56.41	10254	3.16E+05	52.27	39.3	38.92	35.2	38.62	58.5	28.99	77.57	40	39	37.73	36.3	38.6	37.64	36.14	38.11	36.51	39.92	37.17	35.93	38.26	40.03	37.5	39.2	37	36.2	36.57
G_NIST612_11	95320	Below l	10210	3.13E+05	51.83	38.8	38.54	35	Below	Below LO	28.82	77.41	40.18	38.69	37.14	36.3	38.28	37.43	36.23	37.98	36.38	39.64	37.35	36.13	38.27	39.78	37.1	39	37	36.1	36.11
G_NIST612_12	95160	56.52	10218	3.12E+05	51.84	39.2	38.61	34.69	38.36	56.3	28.9	77.43	39.34	38.48	37.17	35.9	38.09	37.47	35.92	37.88	36.45	39.38	36.97	35.95	38.16	39.54	36.9	39.2	37	35.5	35.86
G_NIST612_13	94090	Below l	10111	3.09E+05	52.02	37.6	38.42	34.2	Below	Below LO	28.77	77.18	39.73	38.36	37.26	36.3	37.9	37.2	35.65	37.94	37.24	39.46	36.96	35.75	37.98	39.66	37.7	40.1	37	35.6	35.73
G_NIST612_14	94760	55.95	10152	3.11E+05	52.95	39.5	38.45	35.3	38.02	56	29.15	77.5	39.84	39.18	37.24	36	38.26	37.34	36.35	37.97	36.96	39.41	37.07	36.04	37.99	39.78	37.5	40	37	35.6	35.85
G_NIST612_15	94780	Below l	10151	3.12E+05	53	39	38.22	34.7	38.05	Below LO	28.87	77.24	40.31	38.89	37.56	36.3	38.35	37.6	36.16	38.26	36.2	39.44	37.39	35.97	38.29	40.15	36.3	38.9	37	36.2	36.57
G_NIST612_16	94980	56.16	10187	3.12E+05	52.75	38.8	38.58	35	38.34	58.9	29.01	78.03	40.48	39.18	37.55	36.4	38.44	37.63	36.42	38.48	35.98	39.61	37.58	36.26	38.61	40.05	36.5	38.7	37	35.8	36.27
G_NIST612_17	94150	Below l	10141	3.10E+05	Below LC	Below	37.99	34.9	37.99	Below LO	28.95	77.67	40.06	39.02	37.29	36.1	38.26	37.31	36.32	38.09	36.35	39.44	37.05	35.72	37.96	39.82	37.4	39.4	37	35.8	35.97
G_NIST612_18	95250	56.76	10201	3.12E+05	52.04	37.6	38.59	35	38.15	60.4	29.27	77.58	40.17	38.94	37.71	36.3	38.45	37.61	36.38	38.05	36.27	39.76	37.32	36.31	38.37	39.87	37.5	39.3	37	36.2	36.06
G_NIST612_19	94370	Below l	10140	3.10E+05	Below LC	39.3	38.52	33.54	38.24	Below LO	28.8	77.15	40.03	39.08	37.57	36	38.04	37.48	35.98	38.05	36.02	39.94	37.23	36.25	38.16	39.67	37.2	38.9	37	36	36.13
G_NIST612_20	93970	55.45	10103	3.08E+05	51.61	39.3	38.03	34.7	37.69	56.3	28.81	77.4	39.79	38.99	36.98	36.1	37.98	37.26	36.1	37.88	36.1	39.22	37.05	36.09	38.05	39.93	37.1	39	37	35.7	36.08
G_NIST612_21	93890	Below l	10084	3.08E+05	51.25	39.3	38.32	34.9	37.94	57.8	28.84	77.12	39.78	39.04	37.15	35.8	37.87	37.3	36.09	37.91	36.37	39.43	37.03	36.16	37.99	40.19	37.2	39.3	37	35.8	35.71
G_NIST612_22	94610	55.75	10170	3.10E+05	51.83	38	38.36	35.7	38.03	55.7	28.9	77.57	39.8	39.09	37.15	35.9	37.96	37.21	36.14	38.26	36.32	39.3	37.24	35.96	38.2	40.19	37.2	38.9	37	36.1	36.05
G_NIST612_23	94270	Below l	10167	3.10E+05	Below LC	Below	38.2	34	38.11	Below LO	28.64	77.05	39.85	38.47	37.27	35.8	37.8	37.11	35.77	37.79	36.68	39.6	37.02	36.08	38.01	39.44	37.4	39.5	37	36.4	35.46
G_NIST612_24	94120	56.11	10164	3.10E+05	51.28	39.1	38.05	34.6	37.97	57.2	28.82	76.72	40.07	38.89	37.05	35.8	37.99	37.29	36.26	37.44	36.27	38.99	37.09	35.87	38	39.93	37.4	39.3	37	35.7	35.91
G_NIST612_25	94160	Below l	10171	3.10E+05	Below LC	39	37.9	35.75	38.22	Below LO	28.32	77.68	40.18	39.06	37.03	36.1	37.79	37.29	36.35	38.06	36.76	39.73	37.27	36.25	38.01	40.04	37.3	40	37	36.6	35.79
G_NIST612_26	94440	56.07	10208	3.10E+05	51.17	38.9	38.41	33.22	37.89	57.7	28.51	77.67	40.18	39.1	36.81	36.1	38.02	37.26	35.89	38.42	36.4	39.4	37.16	35.96	38.27	40.03	37.3	39.5	37	35.9	35.75
G_NIST612_27	93670	Below l	10073	3.08E+05	52.1	38.1	38.02	34.66	Below	Below LO	28.37	77.33	40.08	38.74	37.17	36	37.75	37.07	35.97	38.08	35.31	39.57	37.07	35.75	38.01	39.79	36.8	37.9	37	35.4	35.75
G_NIST612_28	93780	55.52	10136	3.09E+05	51.09	38.4	38.61	35.1	37.76	57.5	28.72	76.67	39.94	38.85	37.08	35.9	38.13	37.32	36.11	37.85	35.57	39.5	37.2	35.6	38.02	39.9	36.7	38.3	37	35.7	35.62
G_NIST612_29	93420	Below l	10123	3.08E+05	50.57	37.8	38.16	34.3	Below	Below LO	28.92	77.54	40.07	38.99	36.79	35.9	38.28	37.41	36.07	38.68	37.18	40.04	37.26	36.53	38.2	40.07	38.6	40.6	37	35.6	36.2
G_NIST612_30	93050	54.75	10053	3.06E+05	51.03	37.7	37.66	33.4	37.44	55.2	28.55	76.77	39.96	38.88	36.5	35.9	37.8	37.25	35.67	37.95	36.6	39.38	37.11	36.01	38.08	39.87	37.7	40	37	35.7	36.1
G_NIST612_31	92640	Below l	10069	3.07E+05	51.28	38.5	37.89	34.27	37.85	Below LO	28.69	77.56	40.13	38.87	36.76	36.1	38.03	37.41	36.12	38.26	35.82	39.82	37.36	35.94	38.34	40.24	37.4	40	37	36	36.16
G_NIST612_32	93690	55.15	10105	3.09E+05	51.27	39.1	37.98	34.3	38.09	59.2	28.22	77.72	40.18	39.11	37.19	36.2	38.25	37.65	36.38	37.87	36.27	39.74	37.57	35.96	38.38	40.35	37.6	40	37	36.3	36.03

	Na	Mg	Al	Si	K	Ti	V	Cr	Mn	Fe	Rb	Sr	Y	Zr	Nb	La	Ce	Pr	Nd	Sm	Eu	Gd	Tb	Dy	Ho	Er	Tm	Yb	Lu	Hf	Ta
G_GSD_1G_1	26320	21550	70260	2.48E+05	25100	7464	43.97	42.7	219.4	1.03E+05	37.17	69.32	41.8	41.32	41.61	38.7	40.74	44.24	43.5	46.83	40.98	49.94	46.48	50.65	48.49	39.52	49	50.9	51	38.9	39.15
G_GSD_1G_2	26270	21630	70560	2.47E+05	24810	7441	43.83	41.8	219.5	1.03E+05	36.51	69.32	41.69	41.92	41.98	38.8	41.07	44.53	44.7	47.54	41.02	50.24	47.04	50.82	49.17	40	49	50.8	52	38.7	39.38
G_GSD_1G_3	29980	22060	7.12E+04	2.76E+05	28500	7590	48	43.9	234.9	1.10E+05	41.8	68.7	41.4	44.1	45.6	39.1	41.4	45.5	45.6	49.1	41	50.3	47.3	50.7	48.9	40	49	52	51	38.9	40.4
G_GSD_1G_4	26560	21790	71010	2.49E+05	25140	7419	44.26	43.1	219.9	1.03E+05	37.04	69.35	42.25	42.5	41.7	39.4	41.6	45.32	44.77	47.97	41.12	51.66	47.34	51.46	49.41	40.63	49.1	51	52	39.4	40.47
G_GSD_1G_5	26750	21630	71380	2.50E+05	25310	7404	43.67	41.3	216.5	1.02E+05	37.61	69.51	41.85	41.87	42.11	39	41.19	45.03	44.22	47.4	40.77	50.37	46.89	51.91	48.98	40.12	48.8	50.7	51	39.2	39.89
G_GSD_1G_6	3.11E+04	22740	7.34E+04	2.81E+05	2.95E+04	7720	49.8	42.8	240.1	1.12E+05	43.9	70.8	42.8	42.3	46.9	40.6	43.4	47.6	47.6	50.1	41.8	50.9	48.6	52.5	49.8	41.7	49.7	51.7	53	40.4	43
G_GSD_1G_7	26460	21650	70890	2.46E+05	25070	7420	44.07	41.4	220.2	1.03E+05	37.01	69.75	42.58	42.54	42.17	39.4	41.88	45.4	45.02	48.11	41.04	50.95	47.23	51.44	49.09	40.4	49	51.1	51	38.7	39.9
G_GSD_1G_8	26170	21590	70510	2.44E+05	24880	7392	43.21	42.6	218.7	1.03E+05	36.69	69.83	42.05	41.82	41.95	39.3	41.61	45.18	45.1	48	40.86	51.22	46.94	51.19	49.08	40.26	48.9	50.6	52	38.8	40.14
G_GSD_1G_9	3.13E+04	22900	7.39E+04	2.82E+05	3.02E+04	7780	49.4	48.5	243.9	1.14E+05	45.2	72.4	43.3	44.1	45.2	41.2	43.7	47.8	47.6	50.4	41.9	53.5	48.4	52.8	50.5	41.9	49.8	52.2	53	42.5	42.6
G_GSD_1G_10	26370	21660	71050	2.45E+05	24920	7424	43.72	41.2	219.3	1.03E+05	36.55	69.38	41.76	42.12	41.64	38.9	41.64	45.22	45.02	48.08	40.96	50.33	46.83	50.88	48.87	39.77	48.9	50.8	51	38.7	40.08
G_GSD_1G_11	26240	21600	70550	2.44E+05	24690	7374	43.42	40.9	218.6	1.03E+05	36.47	68.85	41.85	42.13	41.45	39.2	41.47	45.25	45.08	48.63	40.96	50.84	47.06	51.26	48.91	40.58	49.1	51	52	39.1	40.13
G_GSD_1G_12	3.15E+04	22890	7.42E+04	2.82E+05	2.99E+04	7690	48.3	45.1	240.1	1.13E+05	45.4	70.3	42.4	44.2	46.5	40.9	43.3	47.9	46	49	41.8	53.2	47.8	53.3	50.1	41.3	49	50.8	52	40.1	43
G_GSD_1G_13	26730	21810	70890	2.49E+05	25040	7396	43.49	41.6	218.2	1.03E+05	37.14	68.91	41.35	41.52	41.54	39	41.34	44.76	44.27	47.2	40.95	50.36	46.79	50.96	48.51	39.68	49	50.9	51	38.7	40.12
G_GSD_1G_14	26460	21730	70780	2.47E+05	24970	7391	43.8	41	217.9	1.03E+05	36.59	68.37	42.05	41.94	41.63	39	41.11	44.85	44.96	48.07	41.01	51.32	46.82	51.21	48.98	40.09	48.8	50.8	52	39.2	40.14
G_GSD_1G_15	3.14E+04	22970	7.42E+04	2.83E+05	2.97E+04	7660	49	43.9	243	1.13E+05	44	71.1	42.5	43.2	45.8	40.7	43.4	47	46.6	50.3	41.2	52.8	48.5	52.7	50.7	40.9	50	51.8	53	40.3	43.2
G_GSD_1G_16	26690	21720	71040	2.48E+05	25230	7430	43.58	42.8	219	1.03E+05	37.18	68.89	42.06	41.48	41.65	38.7	41.09	44.56	44.42	48.04	40.93	50.64	46.5	50.63	48.68	39.54	49	50.9	51	38.6	39.39
G_GSD_1G_17	26680	21790	71300	2.48E+05	25350	7432	44.24	42.7	220.6	1.03E+05	36.97	69.57	42.16	41.88	42.01	39	41.29	45.01	44.63	47.66	41.02	50.37	47.05	51.39	49.04	39.83	49	50.9	52	39.1	39.92
G_GSD_1G_18	30180	22120	7.15E+04	2.71E+05	28690	7500	47.7	42.5	234.3	1.10E+05	42.6	67.4	41.4	42.3	45	39	41.9	44.75	45.1	47.9	41.1	52.1	46.9	51.2	48.9	40	49.3	50.8	51	38.2	41.8
G_GSD_1G_19	26340	21500	70580	2.46E+05	25020	7429	43.85	41.1	218	1.03E+05	36.91	69.16	42.01	41.81	41.75	39.1	41.05	44.82	44.28	47.49	40.98	50.4	46.68	50.51	48.66	39.92	49	50.7	51	39	39.48
G_GSD_1G_20	26430	21630	70780	2.47E+05	25140	7436	43.7	42.4	219.9	1.03E+05	37.35	69.5	42.21	42.4	41.69	39.2	41.2	44.98	45.14	48.08	40.92	50.33	46.97	51.34	49.08	39.98	48.9	51.1	52	39.1	39.89
G_GSD_1G_21	3.11E+04	22630	7.37E+04	2.80E+05	29710	7780	48.3	45.5	239.3	1.12E+05	44.7	72	43.2	42.1	47	40	43.8	47.2	47.5	48.9	41.7	52.7	48.5	51.3	50.7	41.5	49.7	51.3	53	40.1	42.6
G_GSD_1G_22	26590	21670	71140	2.48E+05	25240	7503	43.89	41.4	219.7	1.04E+05	37.09	70.27	41.98	41.89	42.33	39.2	41.68	45.28	45.07	47.78	40.94	50.54	47.24	51.25	49.3	40.45	49	50.9	52	38.9	40.19
G_GSD_1G_23	26430	21700	70740	2.44E+05	25090	7391	43.8	41.2	217.8	1.03E+05	36.9	68.93	42.28	41.96	41.87	39	41.38	45.06	44.85	47.7	41.02	51.12	47.09	51.62	49.03	39.97	49	50.9	52	39.3	40.24
G_GSD_1G_24	3.06E+04	22460	7.28E+04	2.76E+05	29330	7660	47.4	48.3	240.4	1.10E+05	45.1	70.8	42.7	43.6	44.9	39.6	43.2	46.9	45.8	48.5	41.2	52.1	48.2	52.2	50.1	40.8	48.9	50.8	53	40.1	43.1
G_GSD_1G_25	26630	21820	70940	2.48E+05	25120	7438	43.99	43.8	219.9	1.04E+05	37.32	69.7	42.07	42.02	41.89	39.1	41.5	45.03	44.29	47.67	40.98	50.43	46.69	50.95	48.69	40.03	49	50.8	51	38.7	39.71
G_GSD_1G_26	26350	21590	70690	2.46E+05	25050	7429	43.64	41.2	218.2	1.03E+05	37.11	69.34	41.77	41.88	41.84	39	41.34	45.12	44.24	47.93	40.97	50.65	47.12	51.46	49.13	40.24	49	51	51	38.7	39.77
G_GSD_1G_27	3.11E+04	22380	7.31E+04	2.76E+05	2.95E+04	7640	48.8	44.4	236.9	1.11E+05	45.1	70.3	42.6	43.1	46	39.6	43	46.3	45.5	48.2	41.5	53.1	48.5	52.6	49.3	40.9	49.5	50.9	53	40	42.9
G_GSD_1G_28	26680	21560	70970	2.47E+05	25390	7405	43.55	41.6	219.8	1.03E+05	37.08	69.64	41.64	41.72	42.02	39.2	41.38	44.99	44.92	47.55	41.05	50.12	46.65	50.95	48.95	39.89	49	50.9	51	39	40.1
G_GSD_1G_29	26260	21610	70530	2.45E+05	25020	7381	43.39	40.7	217.4	1.03E+05	36.91	69.46	42.07	41.94	41.88	38.9	41.02	44.78	44.28	47.62	40.8	50.83	47.05	50.98	48.99	40.4	48.9	50.7	52	39	40.12
G_GSD_1G_30	3.07E+04	22380	7.24E+04	2.71E+05	2.92E+04	7730	48.2	45.4	235.9	1.09E+05	43.5	71.5	42.4	44.8	43.7	39.8	42.4	45.9	45.8	50.2	41.7	52.7	48.1	53.1	49.8	40.8	49.7	51.9	52	40.7	43.2
G_GSD_1G_31	26360	21650	71030	2.46E+05	25090	7449	44.17	42.3	219	1.03E+05	37.31	68.87	41.71	42.1	41.44	38.9	41.06	44.66	44.33	47.81	40.92	50.32	46.93	51.1	48.75	39.56	49	50.9	51	38.8	40.02
G_GSD_1G_32	26690	21710	71170	2.48E+05	25500	7416	43.76	43.6	220.7	103390	37.45	69.82	41.95	42.04	42.15	39.1	41.41	45.11	45.21	48.56	41.05	50.86	47.19	51.5	49.15	40.3	49	50.9	52	39.5	40.13
G_GSD_1G_33	3.03E+04	22400	7.25E+04	2.71E+05	2.87E+04	7730	47	44.1	238.4	1.09E+05	42.7	70.4	42.5	43.9	45.4	40.8	43.2	46.3	47	46.1	41.1	51.4	47.4	53.1	50.1	40.8	49.4	51.6	53	39.8	43.1
G_GSD_1G_34	26440	21550	70650	2.47E+05	25110	7369	43.68	42.6	217.6	1.02E+05	37.04	69.47	41.54	41.81	41.62	38.6	40.94	44.37	43.75	47.05	40.93	50.01	46.45	50.53	48.53	39.73	48.9	50.7	51	38.2	39.12
G_GSD_1G_35	26540	21740	71050	2.47E+05	24930	7433	43.5	40.5	219.1	1.02E+05	36.84	69.25	41.74	41.61	41.61	39	41.25	44.9	44.91	47.68	41.01	50.74	46.67	50.83	48.87	40.11	49	51.1	51	39.1	39.59
G_GSD_1G_36	30090	22120	7.16E+04	2.71E+05	28370	7680	48.6	48.3	236.5	1.09E+05	41.6	69.2	43.5	43	44.4	39.8	42.4	46.3	46	48.3	41.3	50.9	47.8	52.9	49.9	39.7	49.3	50.8	52	39	42.2
G_GSD_1G_37	26410	21800	70980	2.47E+05	25020	7454	44	42.4	217.6	1.03E+05	36.81	69.21	42.15	42.09	41.71	38.9	41.18	44.85	43.94	47.33	40.95	50.48	46.81	50.85	48.63	39.8	48.9	50.9	51	38.5	39.81
G_GSD_1G_38	26490	21810	71270	2.49E+05	25100	7482	44.12	41.6	220	1.04E+05	36.92	69.56	42.36	42.63	41.97	39.2	41.59	45.21	45.09	47.72	40.98	50.97	47.58	51.68	49.58	40.65	49	50.8	52	39.8	40.1
G_GSD_1G_39	3.03E+04	22430	7.27E+04	2.74E+05	28700	7790	47.4	41.8	237.9	1.09E+05	42.8	70.7	42.1	42.5	45.4	40.5	42.5	46.9	45.4	48.1	41.6	53.2	48.2	51.9	50.1	39.7	49.2	52	52	41.2	41.4
G_GSD_1G_40	26250	21670	70710	2.45E+05	24800	7444	43.49	41.5	216.8	1.03E+05	36.41	69.38	42.2	41.86	41.77	39	41.06	44.78	44.33	48.05	41.02	51.09	46.9	50.83	48.86	39.95	48.9	51.1	51	38.9	39.74
G_GSD_1G_41	26040	21420	70400	2.45E+05	24660	7359	43.31	42.9	217.2	101580	36.16	68.76	41.82	41.87	41.61	39	41.16	44.74	44.39	47.83	40.94	50.5	46.84	51.28	48.82	40.32	49.1	50.8	52	38.7	39.59
G_GSD_1G_42	3.05E+04	22130	7.21E+04	2.72E+05	28850	7600	47.3	42	232.9	1.08E+05	43.7	70.3	41.2	41.1	45	39	42.26	45.6	45.5	48.9	41.4	51.1	47.2	52.2	49.1	40.1	48.9	51.3	51	41.1	42.7
G_GSD_1G_43	26150	21380	69780	2.44E+05	24620	7356	43.02	41.7	216.8	1.02E+05	36.53	69.15	41.78	41.51	41.23	38.8	40.81	44.39	44.46	47.34	40.89	50.09	46.79	50.73	48.69	39.86	48.9	50.5	51	38.5	39.59
G_GSD_1G_44	26600	21860	71380	2.49E+05	25100	7536	44.13	41.1	221.9	1.04E+05	36.97	70.73	42.63	42.48	42.07	39.7	42.02	45.71	45.56	48.25	41.05	51.26	47.61	51.85	49.99	40.73	49	51.1	52	39.8	40.58
G_GSD_1G_45	3.08E+04	22820	7.38E+04	2.76E+05	29090	7830	49.5	45	245.3	1.11E+05	43.5	71.2	43.8	44.1	47.5	41	43.6	47.7	47.1	50.6	41.3	55.2	49.6	53.6	51.7	41.8	49.8	52.7	54	40.5	43.6
G_GSD_1G_46	26460	21600	70310	2.47E+05	25210	7372	44.7	41.1	218.6	1.04E+05	37.01	69.16	41.65	41.6	41.74	38.6	41.27	45.09	44.86	47.61	41.04	50.63	46.4	50.74	48.43	39.88	49.1	50.8	51	38.6	39.32
G_GSD_1G_47	26930	21720	70230	2.49E+05	25180	7339	44.12	41.5	218.9	1.04E+05	37.9	68.67	41.84	41.15	41.61	39.1	41.77	44.76	44.71	47.19	40.74	50.11	46.54	50.74	48.53	39.7	48.7	50.6	51	38.6	39.66
G_GSD_1G_48	3.05E+04	22550	7.34E+04	2.76E+05	28880	7810	48.1	48.4	238	1.11E+05	43.7	71.4	42.9	45.1	45.5	41	43.5	47.3	47.5	48.8	41.8	52.6	49	53.8	51.8	42	50.3	54.2	54	41.5	43.6

Table 3.2. Dwell time for each mass for LA-ICP-MS trace elements maps.

Trace Element Maps		
Mass	Element	Integrated time/Mass (sec)
7	Li	0.01
23	Na	0.002
24	Mg	0.002
27	Al	0.002
29	Si	0.002
31	P	0.002
43	Ca	0.005
49	Ti	0.005
51	V	0.005
53	Cr	0.005
55	Mn	0.002
57	Fe	0.002
88	Sr	0.01
89	Y	0.008
90	Zr	0.008
139	La	0.008
140	Ce	0.008
141	Pr	0.008
146	Nd	0.01
147	Sm	0.015
153	Eu	0.015
157	Gd	0.015
159	Tb	0.01
163	Dy	0.01
165	Ho	0.008
166	Er	0.008
169	Tm	0.008
172	Yb	0.008
175	Lu	0.008
178	Hf	0.005
232	Th	0.005
238	U	0.005
Sampling period (sec)		0.285
Acquisiton time (sec)		70.395

Table 3.3. GSD-1D and NIST610 standard values for trace element maps

	Li	Na	Mg	Al	Si	P	Ti	V	Cr	Mn	Fe	Sr	Y	Zr	La	Ce	Pr	Nd	Sm	Eu	Gd	Tb	Dy	Ho	Er	Tm	Yb	Lu	Hf	Th	U
G_GSD_1G_1	40.88	24800	21360	70200	232600	784	7350	43	38.8	211.4	98500	69.4	41.28	42.26	38.22	39.96	43.77	43.9	46.82	40.61	49.4	46.26	50.75	48.41	39.31	48.3	51	50.55	37.32	39.59	38.8
G_GSD_1G_2	41	24740	21260	69300	232700	790	7300	43.42	40.7	211.1	97700	69	41.48	41.22	38.59	40.59	43.94	43.2	47.2	40.33	50.5	46.4	50.68	48.49	39.77	48.47	50.9	51.65	38.14	40.55	39.6
G_GSD_1G_3	41.44	24700	21180	69900	234300	813	7340	42.6	38.9	211.6	99100	68.4	41.41	41.41	38.37	40.27	43.54	43.7	46.6	40.04	49.4	45.63	49.4	47.89	38.94	47.78	49.75	49.9	37.8	39.73	39.6
G_GSD_1G_4	40.7	24580	21270	68800	231700	783	7310	42.05	39.7	216.7	95500	67.6	40.71	40.51	38.22	40.44	43.42	43.7	47	40.18	49.1	45.49	49.68	48.1	38.78	48	50.23	50.16	37.84	40.36	39.6
G_GSD_1G_5	42.2	26340	21640	71900	239200	799	7530	43.1	41.4	218	102400	70.4	41.85	41.49	38.72	41.4	44.88	43.94	47.84	40.85	50	46.55	51.35	48.78	39.59	48.52	50.6	51.09	38.19	40.2	40.9
G_GSD_1G_6	41.8	25400	21630	70400	239900	826	7490	43.6	39.3	215.3	99300	69.1	41.82	41.24	38.51	41.18	44.66	44.5	47.5	40.78	50.2	46.74	50.5	48.38	39.5	49.15	49.9	51.4	39	40.95	40.5
G_GSD_1G_7	42.6	25370	21660	68600	234500	797	7300	43.9	42.1	212	101200	68.6	40.83	40.3	37.98	40.3	44	44.1	46.6	39.86	49.5	45.6	48.9	47.61	38.57	47.2	49.1	49.2	37.8	39.95	39.5
G_GSD_1G_8	41.8	25490	21540	69200	231500	781	7320	43.3	40.6	217.1	99650	68.5	41.57	40.9	38.51	40.9	45	44.5	46.8	40.65	49.6	45.9	50.7	48.1	39.68	47.78	49.8	50.25	38.6	40.28	40.8
G_GSD_1G_9	40.58	25060	21150	70000	234700	810	7430	43	39.3	217.3	99100	69	41.22	41.5	38.07	40.8	44.2	43.5	47.5	40.61	49.6	45.7	50.3	47.64	39.2	48.1	49.5	50.02	37.1	39.9	39.5
G_GSD_1G_10	41.3	25030	21240	71000	234700	799	7420	43.4	39.7	214.7	99400	68.9	41.61	41.6	38.19	40.78	44.12	44	47.56	40.49	50.29	46.54	50.4	48.79	39.81	48.61	50.9	51.84	38.25	40.58	39.9
G_NIST610_1	435.6	88300	470.8	10130	300200	337	451.8	457.1	398.2	451.1	489	528	492.8	478.2	455.7	464	456.4	448.1	468.3	465.1	476	453.7	446.9	462.3	481.7	443.9	469.2	454.9	429.2	491.5	452
G_NIST610_2	437.1	90400	468.7	10110	302900	347	455.6	458.2	397.7	450.8	483	523.5	488.5	471.2	453.4	462.4	458.8	446.3	466.6	464.5	478.6	457.5	448.7	468.1	483.5	448.6	467.8	456.3	430.1	490.2	456
G_NIST610_3	438.9	93300	468.1	10120	300700	343	457.8	469.8	404.7	453.5	Below LO	530.6	500.1	475.5	459.7	466.6	461.7	450.6	471.9	467.9	481.8	461.9	452.2	472.7	489.8	449.6	470.8	461.1	432.1	487.6	450
G_NIST610_4	440.7	93300	466.9	10100	297900	352	456	464.6	402.1	452	494	527.7	499.9	475.3	458	465.6	462.9	450.4	471	468	483	464.9	453.2	474.1	489	456.1	470.7	464.7	431.9	494.1	458
G_NIST610_5	425.9	89200	Below L	10190	293900	339	457	436.4	387.3	450.2	Below LO	525.7	496.6	478.5	461.4	464.2	465	452.6	476.1	467.3	484.4	468	456.4	480.2	491.4	456.2	475.6	470	442.4	493.4	456
G_NIST610_6	426.3	90300	462.2	10260	297900	331	458.9	445.9	395.6	451.7	469	530.2	501.7	478.1	463	465.2	467.8	456	480.5	470.9	492.2	476.7	462.5	486.4	498.3	464.1	478.1	474.9	448.3	501.6	460
G_NIST610_7	446.7	95000	463.5	10117	295600	338	459.1	470.2	397.8	449.4	Below LO	531	514.6	479.4	461.3	467.5	472	452.5	480.1	470.5	489.1	472.8	458.5	484.5	501.1	460.3	473.9	472.5	445.6	517.7	456
G_NIST610_8	447.1	94200	468.3	10250	299600	345	467	464.3	396.7	455.5	488	533.2	511.1	481.2	461.4	465.5	474.5	454.3	477.8	468.5	488.6	473.2	458.5	485.8	497.5	460.3	474	476.7	443.9	514.2	459
G_NIST610_9	433.9	92600	Below L	10260	301000	350	452	438.9	401.7	449.1	Below LO	530.7	492.9	471.9	458.9	463.5	469.4	450	472.1	467.9	483	469.8	448.7	476.8	492.4	455.8	468	463.7	426	484	461
G_NIST610_10	445.4	93000	466.9	10401	304900	348	456.4	446.6	395.2	458.6	476	530.1	498.4	475.8	459.5	466.1	467.8	450.7	472.4	466.6	484.1	469.4	453.3	481.1	492.9	457.5	472.9	472.7	429.7	499.6	462

Table 3.4. Mass balance calculations for granulite sample HOL14-7A

HOL14–7A	*Desnity 3.1 g/cm³*													
Mineral	**Mineral SG**	**Abundance**	**Mass fraction**											
Garnet	3.65	0.3	0.3532											
Plagioclase	2.62	0.45	0.3803											
Clinopyroxene	3.18	0.25	0.2565											
Measured REE														
	La	Ce	Pr	Nd	Sm	Eu	Gd	Tb	Dy	Ho	Er	Tm	Yb	Lu
Garnet	0.05068	0.15499	0.57792	1.77872	6.78932	14.30460	11.61492	11.92241	12.90464	13.00920	13.14257	12.97987	13.25941	13.12117
plagioclase	9.31275	3.48137	1.68856	0.95296	0.10919	3.59132	0.02760	0.00000	0.00000	0.00000	0.00000	0.00000	0.00000	0.00000
clinopyroxene	11.55607	18.24451	25.41101	28.25165	21.43856	21.47745	10.12318	5.40451	3.24147	1.81687	1.19741	0.76102	0.47270	0.28084
Calculated mineral contribution														
Garnet	0.0179	0.0547	0.2041	0.6283	2.3982	5.0528	4.1027	4.2113	4.5583	4.5952	4.6423	4.5848	4.6836	4.6347
plagioclase	3.5418	1.3240	0.6422	0.3624	0.0415	1.3659	0.0105	0.0000	0.0000	0.0000	0.0000	0.0000	0.0000	0.0000
clinopyroxene	2.9636	4.6788	6.5167	7.2452	5.4980	5.5079	2.5961	1.3860	0.8313	0.4659	0.3071	0.1952	0.1212	0.0720
Calculated whole-rock														
	6.5233	6.0576	7.3630	8.2359	7.9376	11.9265	6.7093	5.5973	5.3895	5.0611	4.9494	4.7800	4.8048	4.7068
Measured whole-rock														
	10.00	7.46	8.25	8.38	6.49	11.84	5.23	4.31	3.96	3.64	3.49	3.65	3.75	3.15

Table 3.5. Mass balance calculations for eclogite sample HOL14-7C

HOL14–7C	*Density 3.58 g/cm³*													
Mineral	**Mineral SG**	**Abundance**	**Mass fraction**											
Garnet	3.65	0.27	0.2752793											
Omphacite	3.34	0.24	0.2239106											
Phengite	2.76	0.07	0.0539665											
Zoisite	3.36	0.14	0.1313966											
Amphibole	2.9	0.28	0.2268156											
Measured REE														
	La	**Ce**	**Pr**	**Nd**	**Sm**	**Eu**	**Gd**	**Tb**	**Dy**	**Ho**	**Er**	**Tm**	**Yb**	**Lu**
Garnet	0.0078	0.1451	0.5492	1.7750	6.9101	12.9059	11.8139	11.9770	12.9635	12.8136	12.8876	12.8192	12.6935	12.6135
Omphacite	0.0019	0.0082	0.0097	0.0206	0.0438	0.2900	0.1724	0.1721	0.1704	0.1276	0.0853	0.0188	0.0371	0.0137
Phengite	0.0290	0.0000	0.0000	0.0000	0.0425	6.7806	0.1147	0.0000	0.0000	0.0000	0.0000	0.0000	0.0000	0.0000
Zoisite	61.4130	50.0537	53.5766	54.1310	38.7446	52.4072	17.6611	7.7685	3.9138	1.6401	0.8342	0.3864	0.2229	0.1830
Amphibole	0.0018	0.0047	0.0044	0.0220	0.2968	1.3539	1.3707	1.7362	1.7177	1.4657	1.2915	1.0590	0.9971	0.8950
Calculated mineral contribution														
Garnet	0.0021	0.0399	0.1512	0.4886	1.9022	3.5527	3.2521	3.2970	3.5686	3.5273	3.5477	3.5288	3.4943	3.4722
Omphacite	0.0004	0.0018	0.0022	0.0046	0.0098	0.0649	0.0386	0.0385	0.0382	0.0286	0.0191	0.0042	0.0083	0.0031
Phengite	0.0016	0.0000	0.0000	0.0000	0.0023	0.3659	0.0062	0.0000	0.0000	0.0000	0.0000	0.0000	0.0000	0.0000
Zoisite	8.0695	6.5769	7.0398	7.1126	5.0909	6.8861	2.3206	1.0208	0.5143	0.2155	0.1096	0.0508	0.0293	0.0240
Amphibole	0.0004	0.0011	0.0010	0.0050	0.0673	0.3071	0.3109	0.3938	0.3896	0.3324	0.2929	0.2402	0.2262	0.2030
Calculated whole-rock														
	8.07	6.62	7.19	7.61	7.07	11.18	5.93	4.75	4.51	4.10	3.97	3.82	3.76	3.70
Measured whole-rock														
	13.13	9.17	10.15	10.38	8.18	12.99	6.93	5.17	4.57	4.47	4.38	3.65	3.71	3.41

Table 3.6. Mass balance calculations for granulite sample HOL15-

HOL15–15	*Desnity 3.1 g/cm³*													
Mineral	**Mineral SG**	**Abundance**	**Mass fraction**											
Garnet	3.65	0.6	0.7065											
Plagioclase	2.62	0.3	0.2535											
Clinopyroxene	3.18	0.1	0.1026											
Measured REE in mineral														
	La	Ce	Pr	Nd	Sm	Eu	Gd	Tb	Dy	Ho	Er	Tm	Yb	Lu
Garnet	0.0074	0.0790	0.3471	1.1522	2.4757	7.1501	2.4637	1.5670	1.3128	0.9645	0.8790	0.7538	0.6639	0.6298
Plagioclase	9.9950	5.4184	2.7127	1.5676	0.0850	2.6614	0.0407	0.0014	0.0012	0.0000	0.0000	0.0000	0.0000	0.0000
Clinopyroxene	68.0976	53.8805	39.3298	24.9521	5.5529	10.0658	1.7825	0.6003	0.2701	0.1165	0.0865	0.0495	0.0348	0.0093
Calculated mineral contribution														
Garnet	0.0052	0.0558	0.2452	0.8140	1.7489	5.0512	1.7405	1.1070	0.9274	0.6814	0.6210	0.5325	0.4690	0.4449
Plagioclase	2.5342	1.3738	0.6878	0.3975	0.0216	0.6748	0.0103	0.0004	0.0003	0.0000	0.0000	0.0000	0.0000	0.0000
Clinopyroxene	6.9855	5.5271	4.0345	2.5596	0.5696	1.0326	0.1829	0.0616	0.0277	0.0120	0.0089	0.0051	0.0036	0.0010
Calculated whole-rock														
	9.5250	6.9567	4.9675	3.7710	2.3401	6.7586	1.9336	1.1690	0.9554	0.6933	0.6299	0.5376	0.4726	0.4459
Measured whole-rock														
	5.83	4.39	4.01	3.18	1.86	4.94	1.05	0.86	0.60	0.47	0.60	0.00	0.36	0.52

Table 3.7. Mass balance calculations for R-eclogite sample HOL15-13B

HOL15–13B	*Density 3.21 g/cm³*													
Mineral	**Mineral SG**	**Abundance**	**Mass fraction**											
Garnet	3.65	0.11	0.1251											
Omphacite	3.34	0.17	0.1769											
Phengite	2.76	0.36	0.3095											
Zoisite	3.36	0.07	0.0733											
Amphibole	2.9	0.17	0.1536											
Measured REE in mineral														
	La	Ce	Pr	Nd	Sm	Eu	Gd	Tb	Dy	Ho	Er	Tm	Yb	Lu
Garnet	0.0000	0.0238	0.1624	0.8192	4.3207	8.6159	10.3758	12.6078	15.5731	17.0642	17.9250	17.6077	17.4059	16.2161
Omphacite	0.0063	0.0212	0.0365	0.0788	0.2208	0.5287	0.5294	0.6569	0.5223	0.3995	0.2811	0.2051	0.0645	0.0761
Phengite	0.0222	0.0022	0.0000	0.0000	0.0281	4.9126	0.1163	0.0000	0.0000	0.0000	0.0000	0.0000	0.0000	0.0000
Zoisite	20.7902	18.5998	20.9489	22.2644	18.8312	27.1264	10.6863	5.8966	3.2388	1.4101	0.5542	0.1096	0.1008	0.0866
Amphibole	0.0037	0.0083	0.0052	0.0159	0.2057	0.4072	0.7715	1.1718	1.8130	2.0552	2.1446	2.0839	2.0630	1.9760
Calculated mineral contribution														
Garnet	0.0000	0.0030	0.0203	0.1025	0.5404	1.0777	1.2978	1.5770	1.9478	2.1344	2.2420	2.2023	0.2755	2.0283
Omphacite	0.0011	0.0038	0.0065	0.0139	0.0391	0.0935	0.0936	0.1162	0.0924	0.0707	0.0497	0.0363	0.0064	0.0135
Phengite	0.0069	0.0007	0.0000	0.0000	0.0087	1.5206	0.0360	0.0000	0.0000	0.0000	0.0000	0.0000	0.0000	0.0000
Zoisite	1.5233	1.3628	1.5349	1.6313	1.3798	1.9876	0.7830	0.4320	0.2373	0.1033	0.0406	0.0080	0.0006	0.0063
Amphibole	0.0003	0.0013	0.0008	0.0024	0.0316	0.0625	0.1185	0.1800	0.2784	0.3156	0.3294	0.3201	0.0492	0.3035
Calculated whole-rock														
	1.5316	1.3715	1.5625	1.7502	1.9996	4.7419	2.3289	2.3052	2.5560	2.6240	2.6617	2.5667	0.3316	2.3516
Measured whole-rock														
	1.40	1.54	1.95	2.25	2.26	0.92	2.49	2.63	3.02	3.08	3.03	3.02	3.33	2.69

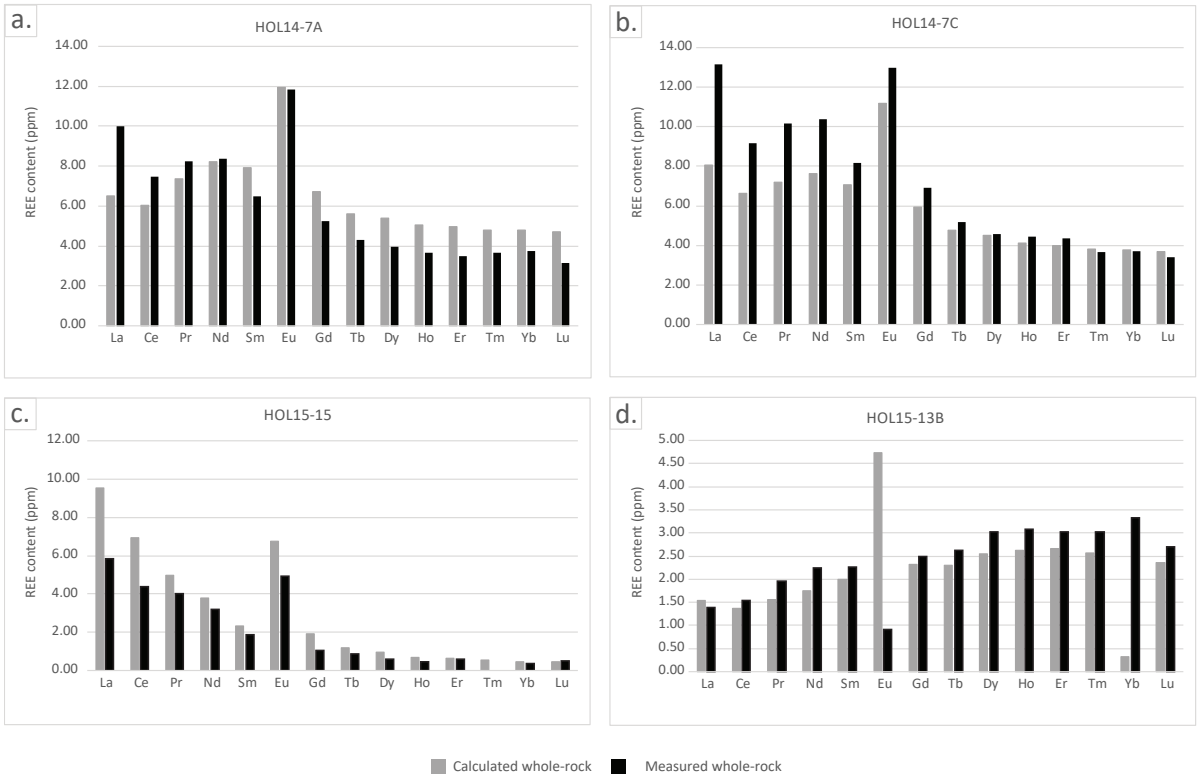

Figure S3.3. Calculated whole rock compositions based on mass balance calculations vs measured whole-rock compositions.

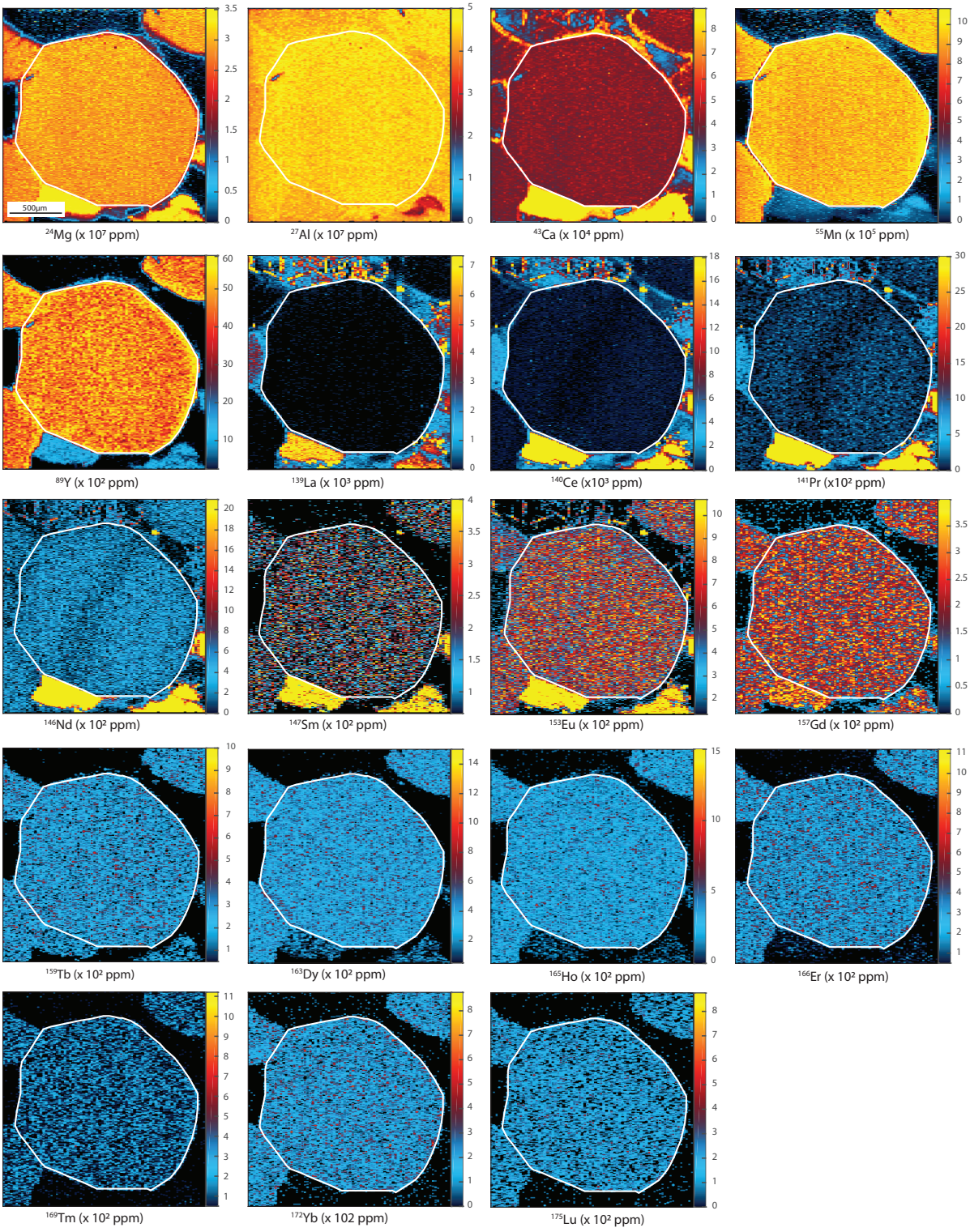

Figure S3.4. LA-ICP-MS maps qualitative maps showing elemental distribution and concentration in a zoned garnet grain in granulite sample, HOL15–15. Dotted line represents the core-rim boundary. Warmer colours represent higher concentrations. Maps were processed in *XMapTools*, and concentrations are presented in ppm.

Appendix 4

Supplementary material for Chapter 5:
Extreme exhumation rates: evidence of tectonic overpressure

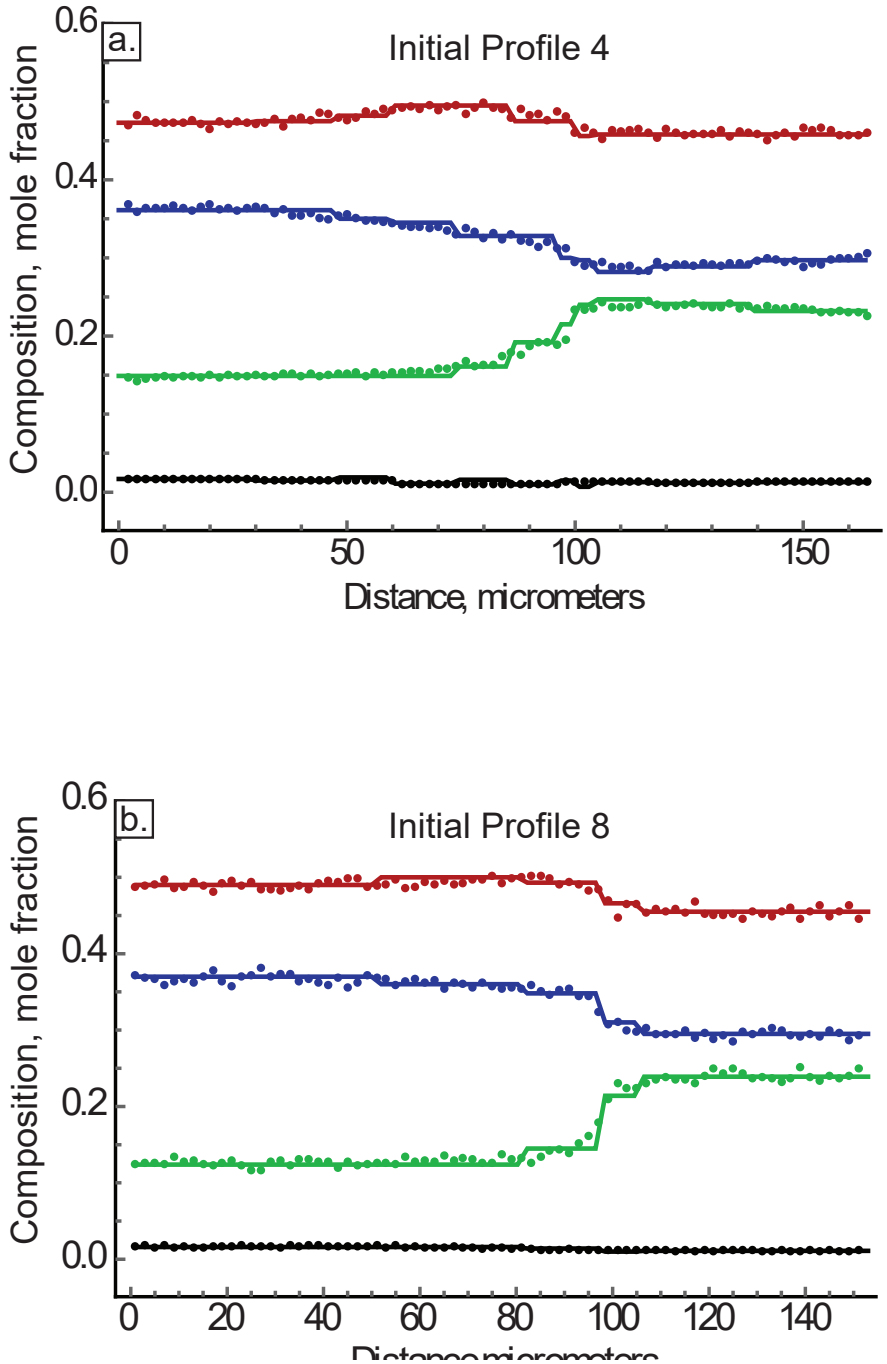

Figure S4.1. Stepped initial for a) Profile 4 and b) Profile 8

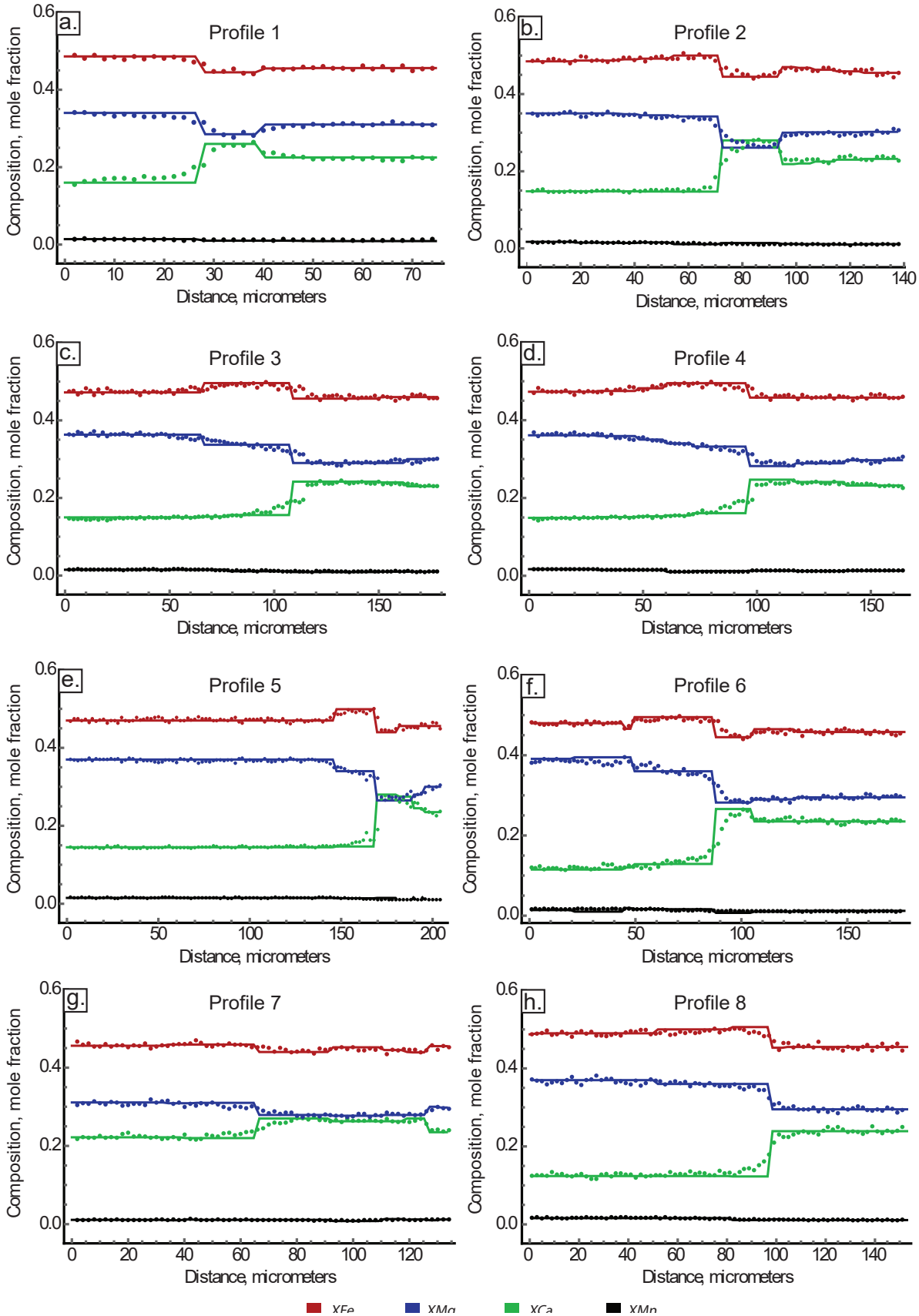

Figure S4.2. Initial profile for all 8 profiles modelled for durations of exhumation.

Appendix 5

Supplementary material for:
Extra work

Geophysical Research Abstracts
Vol. 20, EGU2018-12117, 2018
EGU General Assembly 2018

Hydrating the Earth's deep, dry crust

Chris Clark (1), Martin Hand (2), Timmons Erickson (1), and Steve Reddy (1)
(1) Curtin University, Perth, Australia (c.clark@curtin.edu.au), (2) University of Adelaide, Adelaide, Australia

The transformation of dry granulites to wet eclogites and amphibolites in the Bergen Arcs of western Norway a classic locality of deep crustal fluid-catalysed metamorphism and deformation. In this study we will focus on the transition between essentially unreacted dry granulite and its reacted hydrous products, i.e. at the hydration interface. We will assess the role of deformation microstructures in assisting fluid infiltration into nominally impermeable lower crustal rocks, the role and potential sources of fluids in driving mineral reactions and thus weakening the rock strength, and the interplay between these mechanisms. The granuilte protolith consists of a Precambrian anorthosite – gabbro assemblage of plagioclase and coronas of garnet around clinopyroxene. In thin section a thin (~75 μm) rim of pargasite amphibole can be seen between the garnet and plagioclase, while the rim of amphibole is thicker (600 μm) when between the clinopyroxene and plagioclase. Plagioclase is coarse grained (mms in diameter) and displays prominent growth twins within the undeformed regions of the granulite. However, within a sheared domain of the granulite the grain size has been significantly reduced (max diameter = 74 μm) as has the growth twinning. Within the retrogressed granulite sample a reduction in the grain size of the plagioclase can be seen in the shear fabric, this corresponds with the development of a crystal preferred orientation (CPO) and the breakdown of the garnet and/or clinopyroxene to amphibole of pargasite composition. Within the amphibolite facies shear zone the amphibole and epidote have developed a strong CPO aligned with the foliation and lineation of the shear zone, while the CPO of the plagioclase is much weaker. Zircons within the shear zone show a range of recrystallization textures consistent with dynamic recrystallization dominated by dislocation creep and dissolution reprecipitation modication of the zircon crystal structure. The zircons likely developed during high-T metamorphism and were subsequently modified during Caledonian orogenesis.

Hydrating the deep, dry crust:

Chris Clark[1], Timmons Erickson[1], Kamini Bhowany[1], Martin Hand[2] and Steve Reddy[1]

Curtin University 1 THE INSTITUTE FOR GEOSCIENCE RESEARCH (TIGeR)
THE UNIVERSITY of ADELAIDE 2

Introduction and aims of the study

An investigation of the feedbacks generated between lower crust–derived fluids and deformation microstructures formed within retrogressed granulites from the Bergen Arcs on the west coast of Norway was undertaken. The aim of the study is to assess the P–T conditions and deformation microstructures that form during fluid infiltration into nominally impermeable lower crustal rocks. The overarching aim of this study is to link the physical properties of the fluid affected rock systems to the broader scale geophysical response of the crust 100's of Myrs after a fluid flow event.

In order to achieve these aims the first part of the study involves sampling granulite facies rocks that have been subsequently modified within a shear zone near Isdal, Norway. The granulite protolith is made up of a Precambrian anorthosite – gabbro assemblage of plagioclase and coronas of garnet around clinopyroxene. Local alteration of the granulite to eclogite and amphibolite occured during the Caledonian orogen and has been attributed to the infiltration of fluids during the high strain event (Mukai et al., 2014 - JPet). These textural relationships offer the opportunity to study the active mechanisms during hydration of the lower crust and evaluate the relationships of solid-state diffusion, dissolution-reprecipitation and dynamic recrystallization.

Geologic Setting and Methods

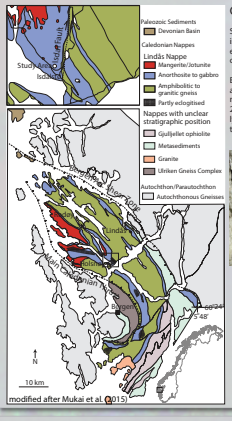

Samples were selected from within and adjacent to the shear zone along route 565 on the island of Radøy within the Bergen Arcs region of Western Norway. Two samples were selected; a retrogressed granulite which exhibits white plagioclase grains in the field and a piece of shear zone with a well developed foliation and lineation.

EBSD data was collected at Curtin University's Microscopy and Microanalysis Facility using a Tescan Mira 3 field emission gun SEM with an accelerating voltage of 20 kV. Large area maps (LAMs) were collected from a deformed domain within the regressed granulite (type 2) and from within the amphibolite shear zone (type 3). The shear zone sample was analysed such that the lineation (340°, 75°) was aligned with the x direction of the SEM acquisition surface.

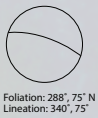

Foliation: 288°, 75° N
Lineation: 340°, 75°

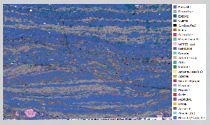

P–T conditions of shear zone formation

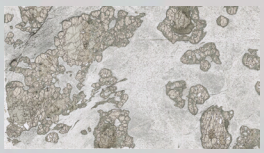

Initiation of shear zone:a thin (~75 µm) rim of pargasite amphibole can be seen between the garnet and plagioclase, while the rim of amphibole is thicker (600 µm) when between the clinopyroxene and plagioclase. Plagioclase is coarse grained (mm's in diameter) and is breaking down to form bundles of clinozoisite. The trace element pattern of garnet from this sample displays an unusual hump, interpreted to reflect the growth of garnet during the breakdown of plagioclase. FoV is 50 x 25 mm.

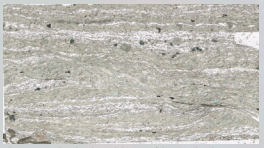

Shear zone:within the sheared domain of the granulite the grain size has been significantly reduced (max diameter = 74 µm) as has the growth twinning. The plagioclase from the sheared domain also displays a weak crystallographic preferred orientation (CPO) which does not appear to be inherited from the 'parent' grains. Within the strained domain there is also an increase in the reaction of garnet to pargasite, which also displays a strong CPO. New garnet is formed at the expense of plagioclase as is evident in the trace element patterns that are characteristic of eclogite facies garnet i.e. flat HREE and no Eu anomaly and is significantly different to the REE pattern of the granulite. Rutile, kyanite, zoisite and epidote are also present. Epidote contains a strong CPO. FoV is 50 x 25 mm.

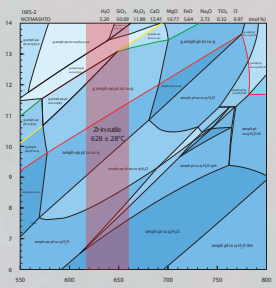

PseudosectionA P–T pseudosection in the NCFMASHTO system was constructed in THERMOCALC using the DS6 Holland & Powell dataset. A restricted field above kyanite-in and below omphacite-in constrains P to between 12-13 kbar and T to 600–650. Zr-in-rutile thermometry refines the T to 628 ± 28°C and P to between 12–13 kbar and T to 600-650. Zr-in-rutile thermometry refines the T to 628 ± 28°C.

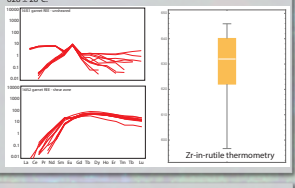

Shear zone microstructures

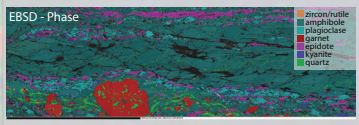

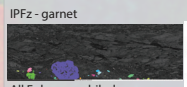

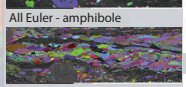

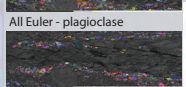

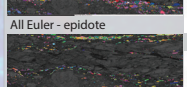

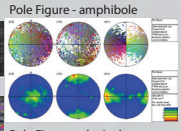

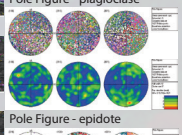

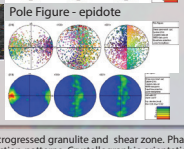

EBSD maps and pole figures of the retrogressed granulite and shear zone. Phase maps are produced by indexed diffraction patterns. Crystallographic orientation maps are either given an all Euler colour scheme or an inverse pole figure (IPF) Z scheme. Pole figures of the principle crystallographic directions or planes are coloured with All Euler, and are contoured to highlight the development of a crystal preferred orientation.

Retrogressed granulite microstructures

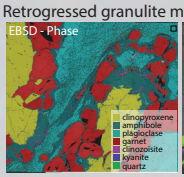

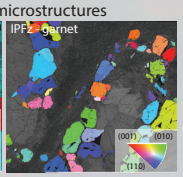

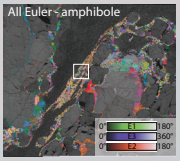

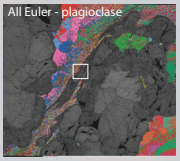

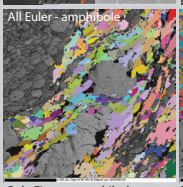

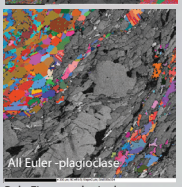

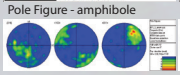

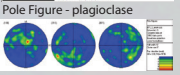

Comparison with Holsnøy eclogite shear zones

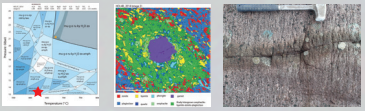

Recently, Bhowany et al (JMG, 2018) applied phase equilibria modelling to constrain the P–T conditions during the formation of eclogite facies shear zones on the nearby island of Holsnøy. They suggested the shear zones represent fluid ingress at peak conditions of 21 kbar and 700 °C, some 8 kbar higher-P and ~50 °C hotter. Putnis et al (JPet, 2018) speculated that the timing of shearing at Isdal and the formation of eclogite shear zones may have been simultaneous and relfect local perturbations in the stress field at the grain scale. While this mechanism may lead to variations in the recorded pressures we do not believe this variation could lead to the observed differences in the temperatures predicted for the assemblages. Our findings are consistent with the hypothesis that the eclogite facies and Isdal shear zones formed in response to fluid infiltration at different depths in the crust and the pressure differences record differences in burial depth, not local grain-scale driven variations. To test the differences in timing will require further investigation via high-precision geochronology.

Conclusions and future work

(1) Within the retrogressed granulite sample a reduction in the grain size of the plagioclase can be seen in the shear fabric, this corresponds with the development of a crystal preferred orientation and the breakdown of the garnet and/or clinopyroxene to amphibole of pargasite composition.

(2) Within the shear zone the amphibole and epidote have developed a strong CPO aligned with the foliation and lineation of the shear zone, while the CPO of the plagioclase is much weaker. The amphibole fabric is consistent with (100) [001] slip; in agreement with experimental and natural observations of plasticity in amphibole.

(3) Pseudosection modelling and Zr-in-rutile thermometry constrain the conditions of shearing to pressures of between 12-13 kbar and temperatures of 628 ± 28°C, i.e. eclogite facies conditions, consistent with trace element chemistry of garnet.

(4) The formation of the eclogite shear zones at Isdal and the Holsnøy examples occured at different crustal levels and further high-precision geochronology will yield information about the burial and exhumation rates during the Caledonian Orogeny.

Future work will focus on the timing of syn-deformational garnet growth via Lu–Hf garnet geochronology and experimental determinations of conductivity of granulite and shear zone in order to better understand changes in conductivity and the implications for imaging deep fossil fluid rock interactions in buried terranes.

Acknowledgments

This work has been supported by the Australian Research Council's Discovery Project 160104637 and the ARC Centre of Excellence Core to Cunst Fluid Systems. The ARC (LE130100053), Curtin University, University of Western Australia and CSIRO are acknowledged for funding the Tescan Mira3 FEG-SEM housed in the John De Laeter Centre's Microscopy and Microanalysis Facility

Geophysical Research Abstracts
Vol. 19, EGU2017-5921, 2017
EGU General Assembly 2017

Rehydration reactions and microstructure development in lower crustal granulites from the Bergen Arcs, Norway

Timmons Erickson (1), Steven Reddy (1), Chris Clark (1), Martin Hand (2), Kamini Bhowany (2), and Alex Prent (1)

(1) The Institute for Geoscience Research, Department of Applied Geology, Curtin University, Perth, Australia (timmons.erickson@gmail.com), (2) School of Physical Sciences, University of Adelaide, Adelaide, Australia

An investigation of the feedbacks generated between lower crust–derived fluids and deformation microstructures formed within retrogressed granulites from the Bergen Arcs on the west coast of Norway will be presented. We hope to assess the role of deformation microstructures in assisting fluid infiltration into nominally impermeable lower crustal rocks, the role of fluids in driving mineral reactions and thus weakening the rock strength, and the interplay between these mechanisms.

Granulite wall–rock adjacent to an amphibolite facies shear zone near Isdal, Norway has been sectioned, texturally mapped using electron backscatter diffraction (EBSD) and chemically mapped using energy dispersive x-ray spectrometry (EDS). The granuilte protolith is made up of a Precambrian anorthosite – gabbro assemblage of plagioclase and coronas of garnet around clinopyroxene. Local alteration of the granulite to eclogite and amphibolite occurred during the Caledonian orogen and has been attributed to the infiltration of fluids during the high strain event (Mukai et al., 2014).

In thin section a thin (~75 μm) rim of pargasite amphibole can be seen between the garnet and plagioclase, while the rim of amphibole is thicker (600 μm) when between the clinopyroxene and plagioclase. Plagioclase is coarse grained (mms in diameter) and displays prominent growth twins within the undeformed regions of the granulite. However, within a sheared domain of the granulite the grain size has been significantly reduced (max diameter = 74 μm) as has the growth twinning. The plagioclase from the sheared domain also displays a crystallographic preferred orientation (CPO) which does not appear to be inherited from the 'parent' grains. Within the strained domain there is also an increase in the reaction of garnet to pargasite, which also displays a strong CPO.

These textural relationships offer the opportunity to study the active mechanisms during hydration of the lower crust and evaluate the relationships of solid-state diffusion, dissolution-reprecipitation and dynamic recrystallization with one another.

Mukai, H., Austrheim, H., Putnis, C. V., and Putnis, A., 2014, Textural Evolution of Plagioclase Feldspar across a Shear Zone: Implications for Deformation Mechanism and Rock Strength: Journal of Petrology, v. 55, no. 8, p. 1457-1477.